

# A mixture model to take into account diluted gas in liquid flow: applications to aluminium electrolysis

Présentée le 20 mai 2022

Faculté des sciences de base  
Groupe Picasso  
Programme doctoral en mathématiques

pour l'obtention du grade de Docteur ès Sciences

par

## **Emile Tryphon Pierre SOUTTER**

Acceptée sur proposition du jury

Prof. F. Nobile, président du jury  
Prof. M. Picasso, Prof. J. Rappaz, directeurs de thèse  
Dr N. Chailly, rapporteuse  
Prof. R. Touzani, rapporteur  
Prof. S. DeParis, rapporteur



Si vita praevideret, desineret esse vita, ac sine sapore esse.  
If life were predictable it would cease to be life, and be without flavor.

Eleanor Roosevelt

To my family...



# Remerciements

Je voudrais remercier en premier lieu mes deux directeurs de thèse, Marco Picasso et Jacques Rappaz, qui m'ont proposé ce travail de doctorat. Je remercie Jacques pour sa disponibilité constante, nos nombreuses discussions constructives, son investissement considérable et ses attentives relectures. Je remercie Marco de m'avoir accueilli dans son groupe avec toujours une bonne ambiance, pour sa grande disponibilité, ses précieux conseils de présentation, les nombreuses discussions de maths et d'autres sujets et sa confiance. J'aurais difficilement pu rêver de meilleurs directeurs de thèse, ce fut un grand plaisir de travailler avec vous.

Je remercie les professeurs Rachid Touzani de l'université de Clermond-Ferrand, Simone Deparis de l'EPFL et la Dr. Nadia Chailly de Rio Tinto Aluminium d'avoir accepté de faire partie de mon jury de thèse, d'avoir pris le temps de lire ce document et pour leurs retours constructifs. Un grand merci également au professeur Fabio Nobile d'avoir accepté d'assumer le rôle de président de ce jury.

Je remercie l'entreprise Rio Tinto Aluminium Péchiney pour avoir financé ce travail et en particulier toute l'équipe de modélisation au LRF (Laboratoire de Recherche des Fabrications) de Saint-Jean-de-Maurienne. Merci à Michel Flück et Thomas, mon premier collègue de bureau, qui m'ont initié aux intrigues et astuces du logiciel Alucell. De même un grand merci à Alexandre et Julien d'Ycoor Systems pour m'avoir dépanné plus d'une fois au niveau de petites subtilités de ce côté-là.

Merci à toute l'équipe du groupe de Marco, pour la bonne ambiance et les nombreux cafés et cookie breaks : Léo, Sam, Boris (quasi partie du groupe aha), Paride, Maude, ainsi qu'aux collègues qui sont partis au cours de mon doctorat : Sylvain, Diane, Dimitrios et Arwa. Finalement merci aussi à quelques doctorants de maths qui prennent les cafés rituels à sat, Guillaume, Bruno, Quentin, Adélie, David, et bien d'autres. Je remercie encore finalement toute l'équipe administrative de maths qui font tenir l'ensemble de la structure avec qui j'ai partagé plus d'une pause de midi : Ariane, Anna, Valérie, Sara, Virginie, Anne et Maroussia. Merci encore à tous les gens que j'ai croisés ces quatre dernières années à l'EPFL et qui ont contribué de près ou de loin, à rendre l'expérience top.

Special thanks à mes 4 potes de la coloc Arthur, Ben, Gaetan et Martin, avec qui on a passé de sacrés moments, qui je l'espère vont se renouveler dans les années à venir, ainsi que toute

## Acknowledgements

---

l'équipe qui a gravité ces dernières années là autour, dont la liste est trop longue, mais qui ont toujours su faire de pures soirées qui permettent, pour un instant, de déconnecter du quotidien pour le cosmos.

Encore merci à mes amis de l'EPFL qui traînent toujours par là, mes potes du beach et du volley, ceux du kite, spécial dédicace à Ben et à ses plans foireux à Dakhla, et l'équipe du théâtre de "Frédéric", et à tous les autres potes autour de Lausanne avec qui j'ai partagé de bons moments ces dernières années, allant du jeu de société à la soirée déguisée. Encore merci à tous ceux qui comptent mais que la place de cette page et le temps pour lequel je dois rendre ce document me limitent à ces quelques lignes.

Finalement merci à ma famille, papa, maman, Math et Jack, qui ont toujours su en même temps me soutenir dans mes choix et en même temps les accepter de manière très décomplexée. Merci à ma copine, Elise, d'être aussi exceptionnelle, de me supporter encore et encore, dans les difficultés, les rires, les moments de fatigue comme de bonheur ;) Merci à tous!

*Lausanne, January 26, 2022*

# Abstract

Aluminium is a metal sought in the industry because of its various physical properties. It is produced by an electrolysis reduction process in large cells. In these cells, a large electric current goes through the electrolytic bath and the liquid aluminium. This electric current generates electromagnetic forces that set the bath and the aluminium into motion. Moreover, large quantities of carbon dioxide gas are produced through chemical reactions in the electrolytic bath: the presence of these gases alleviates the density of the liquid bath and changes the dynamics of the flow. Accurate knowledge of this fluid flow is essential to improve the efficiency of the whole process. The purpose of this thesis is to study and approximate the interaction of carbon dioxide with the fluid flow in the aluminium electrolysis process.

In the first chapter of this work, a mixture-averaged model is developed for mixtures of gas and liquid. The model is based on the conservation of mass and momentum equations of the two phases, liquid and gas. By combining these equations, a system is established that takes into account the velocity of the liquid-gas mixture, the pressure, the gas velocity and the local gas concentration as unknowns.

In the second chapter, a simplified problem is studied theoretically. It is shown that under the assumption that the gas concentration is small, the problem is well-posed. Moreover, we prove a priori error estimates of a finite element approximation of this problem. In the third chapter, we compare this liquid-gas model with a water column reactor experiment.

Finally, the last chapter shows that the fluid flow is changed in aluminium electrolysis cells when we take into account the density of the bath reduced by carbon dioxide. These changes are quantified as being of the order of 30% and explain partially the differences between previous models and observations from Rio Tinto Aluminium engineers.

**Keywords** Numerical simulations, Finite element methods, Partial differential equations, Aluminium electrolysis, Mixture model, Diluted gas, Fluid with varying density



# Résumé

L'aluminium est un métal très prisé par l'industrie à cause de ses propriétés physiques particulières. Il est produit notamment par un procédé d'électrolyse dans des cuves de grandes dimensions. Dans ces cuves, un important courant électrique traverse le bain électrolytique et l'aluminium liquide. Ces courants électriques génèrent des forces électromagnétiques qui mettent le bain et l'aluminium en mouvement. De plus, d'importantes quantités de gaz carbonique sont produites à travers les réactions chimiques dans le bain électrolytique : la présence d'un tel gaz va alléger le bain liquide et changer la dynamique des écoulements. Une bonne connaissance de ces écoulements est essentielle pour améliorer l'efficacité de tout le procédé. L'objet de cette thèse est l'étude et la simulation de l'interaction du gaz carbonique avec les écoulements des fluides dans le cadre du procédé d'électrolyse de l'aluminium.

Dans le premier chapitre de cette thèse, on développe un modèle de mélange moyen de gaz et de liquide. Le modèle se base sur les équations de conservation de la masse et de la quantité de mouvement des deux phases, liquide et gaz. En combinant ces équations, on établit un système qui admet la vitesse du mélange liquide-gaz, la pression, la vitesse du gaz et la concentration locale de gaz comme inconnues.

Dans le second chapitre, on étudie théoriquement un problème simplifié. On montre que sous l'hypothèse que la concentration de gaz est faible et ne présente pas de variation abrupte, le problème est bien-posé. De plus, on prouve des estimations d'erreur à priori pour une approximation numérique par des éléments finis. Au troisième chapitre, on compare le modèle de mélange liquide-gaz avec une expérience de réacteur de colonne d'eau.

Finalement, le dernier chapitre montre que les écoulements sont changés dans des cuves d'électrolyse d'aluminium lorsque l'on prend en compte la densité du bain allégé par du gaz carbonique. Ces changements sont quantifiés comme étant de l'ordre de 30% et expliquent en partie les différences constatées entre les précédents modèles et les observations des ingénieurs de Rio Tinto Aluminium.

**Mots-clés** Simulations numériques, Méthode des éléments finis, Équations aux dérivées partielles, Électrolyse de l'aluminium, Modèle de mélange, Gaz dissous, Fluide avec densité variable



# Zusammenfassung

Aluminium ist in der Industrie ein beliebtes Material auf Grund seiner physikalischen Eigenschaften und wird typischerweise durch einen elektrolytischen Reduktionsprozess in großen Zellen hergestellt. In diesen Zellen fließt ein starker elektrischer Strom durch ein elektrolytisches Bad und durch flüssiges Aluminium, was starke elektromagnetische Kräfte erzeugt, welche wiederum das Bad und das flüssige Aluminium in Bewegung setzen. Des Weiteren werden große Mengen Kohlendioxid durch chemische Prozesse im elektrolytischen Bad erzeugt. Dies reduziert die Dichte des Bades und führt zu einer Veränderung der Fluidodynamik. Eine genaue Kenntnis dieser Dynamik ist vonnöten um die Effektivität des gesamten Prozesses zu verbessern. Der Zweck dieser Dissertation ist, den Einfluss des Kohlendioxids auf die Fluidodynamik im Aluminiumelektrolyseprozess zu studieren.

Im ersten Teil dieser Arbeit wird ein Modell für Gemische aus Gasen und Flüssigkeiten entwickelt, welches gemittelte Mischungsverhältnisse nutzt. Dieses Modell basiert auf Erhaltungsgleichungen für den Impuls und die Masse der beiden Phasen. In dem man diese verbindet, erhält man ein System aus partiellen Differenzialgleichungen, welche die Geschwindigkeit des Gemisches, den Druck, die Geschwindigkeit des Gases und die lokale Konzentration des Gases in Verbindung setzt.

Im zweiten Teil wird ein vereinfachtes Problem theoretisch behandelt. Es wird gezeigt, dass das Problem, unter der Annahme dass die Konzentration des Gases gering ist, wohl-gestellt ist. Des Weiteren werden a priori Fehlerschätzer für Finite Elemente Verfahren für dieses Problem bewiesen. Im dritten Teil werden numerische Experimente des Modells mit Experimenten aus einem Blasesäulenreaktor verglichen.

Im letzten Teil wird gezeigt, dass sich die Fluidodynamik in den Elektrolysezellen ändert, wenn die Reduktion der Dichte durch das Kohlendioxid berücksichtigt wird. Diese Veränderungen betragen bis zu 30 % und erklären zum Teil die Unterschiede zwischen vorhergehenden numerischen Modellen und den Beobachtungen der Rio Tinto Aluminium Ingenieure.

**Schlüsselwörter** Numerische Simulationen, Finite Elemente Verfahren, Partielle Differenzialgleichungen, Aluminiumelektrolyse, Mischungsverhältnis, gemittelte Modelle, verdünntes Gas, kompressible Fluid



# Notations

The following contains the different symbols used throughout the document

## Related to physics

$\rho$	Density of the mixture of liquid and gas [ $kg/m^3$ ]
$\mathbf{u}$	Velocity vector field of the mixture [ $m/s$ ]
$t$	Time [ $s$ ]
$\boldsymbol{\tau}$	Stress tensor of the mixture of liquid and gas [ $kg/m^2s^2$ ]
$p$	Pressure [ $kg/ms^2$ ]
$\mu$	Dynamic viscosity of the mixture [ $kg/ms$ ]
$\mathbf{F}$	Vector field of external forces [ $kg/ms^2$ ]
$\epsilon(\mathbf{u})$	Shear rate tensor [ $1/s$ ]
$\mathbf{u}_g$	Gas velocity [ $m/s$ ]
$\mathbf{u}_l$	Liquid velocity [ $m/s$ ]
$p_g$	Gas pressure [ $kg/ms^2$ ]
$p_l$	Liquid pressure [ $kg/ms^2$ ]
$\rho_g$	Gas density [ $kg/m^3$ ]
$\rho_l$	Liquid density [ $kg/m^3$ ]
$\mu_g$	Gas dynamic viscosity [ $kg/ms$ ]
$\alpha_g$	Gas volumetric ratio [–]
$\mu_l$	Liquid dynamic viscosity [ $kg/ms$ ]
$\alpha_l$	Liquid volumetric ratio [–]
$\boldsymbol{\tau}_g$	Gas stress tensor [ $kg/m^2s^2$ ]

## Notations

---

$\boldsymbol{\tau}_l$	Liquid stress tensor [ $kg/m^2s^2$ ]
$F_g$	External forces applying to the gas [ $kg/ms^2$ ]
$F_l$	External forces applying to the liquid [ $kg/ms^2$ ]
$\mathbf{g}$	Earth's gravitational acceleration field [ $m/s^2$ ]
$\mathbf{f}_g$	Interface momentum exchange force from the liquid to the gas [ $kg/ms^2$ ]
$\mathbf{f}_l$	Interface momentum exchange force from the gas to the liquid [ $kg/ms^2$ ]
$D$	Drag coefficient [ $kg/m^3s$ ]
$p_c$	Capillary pressure [ $kg/ms^2$ ]
$\mathbf{r}$	Reynolds Stress tensor [ $kg/m^2s^2$ ]
$K$	Gas diffusion coefficient [ $m^2/s$ ]
$\dot{\alpha}_{source}$	Gas source term [ $1/s$ ]
$p_0$	Value of the pressure imposed at the outflow [ $kg/ms^2$ ]
$d$	Bubble average diameter [ $m$ ]
$F_{S,1bubble}$	Stokes drag force for a single bubble [ $kgm/s^2$ ]
$F_S$	Stokes drag force [ $kg/m^2s^2$ ]
$Re_b$	Reynolds bubble number[-]
$F_D$	Drag force [ $kgm/s^2$ ]
$C_D$	Dimensionless drag coefficient [-]
$F_A$	Archimède force [ $kgm/s^2$ ]
$\xi$	Normal component of the stress tensor through the outflow [ $kg/ms^2$ ]
$\mu_L$	Laminar viscosity [ $kg/ms$ ]
$\mu_T$	Turbulent viscosity [ $kg/ms$ ]
$C_T$	Turbulent parameter [ $m^2$ ]
$\mu_{init}$	Dynamic viscosity of the mixture during initialisation [ $kg/ms$ ]
$K_L$	Linear diffusion coefficient [ $m^2/s$ ]
$K_T$	Turbulent diffusion coefficient [ $m^2/s$ ]
$K_0$	Diffusion for reference solution [ $m^2/s$ ]

$\mathbf{j}$	Electric current density [ $A/m^2$ ]
$\mathbf{B}$	Magnetic field or magnetic flux density [ $kg/As^2$ ]
$H$	Height of the interface compared to initial position [ $m$ ]
$\rho_{al}$	Liquid aluminium density [ $kg/m^3$ ]
$\rho_{el}$	Liquid electrolyte bath density [ $kg/m^3$ ]
$\mu_{al}$	Liquid aluminium dynamic viscosity [ $kg/ms$ ]
$\mu_{el}$	Liquid electrolyte bath dynamic viscosity [ $kg/ms$ ]
$V_{alu}$	Volume of aluminium [ $m^3$ ]
$\psi$	Jump of the viscous force along the normal through the interface [ $kg/ms^2$ ]
$\mathbf{E}$	Electric field [ $mkg/As^3$ ]
$\mathbf{H}$	Magnetic field [ $A/m$ ]
$\mu_0$	Magnetic permeability of vacuum [ $kgm/A^2s^2$ ]
$\mu_r$	Relative magnetic permeability [-]
$\sigma$	Electric conductivity [ $A^2s^3/m^3kg$ ]
$V$	Electric potential [ $kgm^2/s^3A$ ]
$\eta_F$	Faraday efficiency factor of an aluminium reduction cell [-]
ACD	Distance between the interface and the anodes [ $m$ ]

**Symbols**

$\Omega$	Lipschitz domain in $\mathbb{R}^d$
$d$	Space dimensions, typically $d = 2, 3$
$\mathbf{x}$	Point in $\mathbb{R}^d$ . $\mathbf{x} = (x_1, x_2, \dots, x_d)$
$\partial\Omega$	Lipschitz boundary of $\Omega$ in $\mathbb{R}^{d-1}$
$\partial$	Partial derivative
$\otimes$	Outer product
$\mathbf{I}$	Identity matrix
div	Divergence operator
$\nabla$	Gradient operator

## Notations

---

$\Gamma_{in}$	Inflow surface
$\Gamma_{out}$	Outflow surface
$\Gamma_0$	Boundary $\partial\Omega$ without $\Gamma_{out}$
$\emptyset$	Empty set
$\mathbf{n}(P)$	Unit normal vector to the surface $\partial\Omega$ at the point $P \in \partial\Omega$
$\mathbf{t}_1(P), \mathbf{t}_2(P)$	Unit tangent vectors to the surface $\partial\Omega$ at the point $P \in \partial\Omega$
$\mathbf{V}$	Velocity space
$L$	Pressure space
$N$	Number of algorithm iterations
$N_g$	Number of gas sub-algorithm iterations
$S$	Normal stress tensor on the outflow space
$\mathcal{F}$	Linear operator of Navier-Stokes weak form
$D\mathcal{F}$	Gâteaux derivative of $\mathcal{F}$
$\mathcal{G}_\theta$	Linear operator of gas velocity weak form
$D\mathcal{G}_\theta$	Gâteaux derivative of $\mathcal{G}_\theta$
$\theta$	Reynolds regime parameter
$h$	Mesh size
$h_K$	Diameter of tetrahedron $K$
$\mathcal{T}_h$	Conformal mesh of $\Omega$ in triangles or tetrahedra of size $h$
$\partial\mathcal{T}_h$	The triangles or edges of $\mathcal{T}_h$ that are on $\partial\Omega$
$\partial W_h$	Piecewise linear finite element space associated with $\partial\mathcal{T}_h$
$W_h$	Piecewise linear finite element space associated with $\mathcal{T}_h$
$W_h$	Piecewise linear finite element space associated with mesh $\mathcal{T}_h$
$\mathbf{V}_h$	Finite element space $\mathbb{P}_1$ for the velocities
$\mathbb{P}_1(K, T)$	Set of polynomials of degree one on element $K, T$
$\varphi_j$	Linear basis function
$L_h$	Finite element space $\mathbb{P}_1$ for the pressure

$N_h$	Number of nodes of mesh $\mathcal{T}_h$
$S_h$	Finite element space $\mathbb{P}_1$ for the normal stress tensor on the outflow
$\mathbf{u}_h$	Finite element approximation of the mixture velocity
$V_{bubble,h}$	Bubble space function
$\mathbf{u}_{g,h}$	Finite element approximation of the mixture velocity
$p_h$	Finite element approximation of the pressure
$\alpha_{g,h}$	Finite element approximation of the gas volumetric ratio
$\rho_h$	Finite element approximation of the density
$\xi_h$	Finite element approximation of the normal stress tensor on the outflow
$\Delta t$	Time-step for the advection-diffusion equation
$C_S$	Stabilisation coefficient for the advection-diffusion equation
$N_{Ne}$	Number of Newton iterations
$L^p(\Omega)$	Lebesgue space of degree $p$
$W^{m,p}(\Omega)$	Sobolev space of $L^p$ functions with weak $k$ derivatives in $L^p$ , for all $1 \leq k \leq m$
$H^m(\Omega)$	Sobolev space $W^{m,2}(\Omega)$
$H_0^m(\Omega)$	Closure of all $C^\infty$ functions with compact support in $H^m(\Omega)$
$L_0$	Pressure space : zero average functions in $L^2(\Omega)$
$\mathbf{U}$	Velocity space : vector space, with each component in $H_0^1(\Omega)$
$\hookrightarrow$	Sobolev embedding
$D(\Omega)$	Space of $C^\infty$ functions with compact support in $\Omega$
$\pi_h, \Pi_h$	Lagrange interpolant
$\mathbf{U}_h$	Finite element space $\mathbb{P}_1$ for the velocity in the domain $\Omega$
$\beta$	Coefficient of the pressure stabilisation term
$\mathbf{w}_h$	Finite element approximation of $\rho \mathbf{u}_h$
$h_0$	Upper bound for the size of the mesh $h$
$r_h, R_h$	Clément interpolant
$\mathbf{u}^*$	Velocity solution of the dual problem

## Notations

---

$P^*$	Pressure solution of the dual problem
$e_i$	Error indicator in a norm defined by $i$
$r_i$	Rate of convergence in a norm defined by $i$
$O(h), O(h^2)$	Big O notation for $h, h^2$
$N_{iter}$	Number of iteration for the gmres solver
$H_{initial}$	Initial height of the water in the cylinder
$D_c$	Diameter of the water-column
$n_{sp}$	Number of spargers injecting the gas in the water-column
$r_{sp}$	Radius of a sparger injecting the gas in the water-column
$H_{cylinder}$	Height of the water in the cylinder at equilibrium
$\bar{\alpha}_g$	Average volumetric ratio of gas in the fluid $\Omega$
$\Phi_{in}$	Superficial gas velocity
$\Omega_{prod}$	Subregion of $\Omega$ , production region where $\dot{\alpha}_{source} > 0$
$H_s$	Height of $\Omega_{prod}$
$r_s$	Radius of $\Omega_{prod}$
$TOL$	Tolerance of the algorithm
$\Delta_\infty$	Relative difference in $L^\infty$ norm in domain $\Omega$
$\Delta_0$	Relative difference in $L^2$ norm in domain $\Omega$
$u_{h,ref}, u_{ref}$	Reference solution
$H_{data}$	Height of the measurements device for experimental data
$\Omega_{al}$	Domain of the liquid aluminium
$\Omega_{el}$	Domain of the liquid electrolyte bath
$\Gamma$	Interface between the electrolyte and the aluminium
$[\cdot]$	Jump operator through the interface
$\tilde{\Gamma}$	Fictitious interface between the electrolyte and the anodes
$f.$	Friction coefficient
$Z$	Space for the jump of the viscous force along the normal $\psi$

$L_{al}$	Pressure space in the aluminium domain
$L_{el}$	Pressure space in the electrolyte domain
$V_g$	Space for the gas velocity in the electrolyte domain
$\mathcal{L}_{el}$	Finite element space $\mathbb{P}_1$ for the pressure in the electrolyte domain
$\mathcal{L}_{al}$	Finite element space $\mathbb{P}_1$ for the pressure in the aluminium domain
$A_h$	Finite element space $\mathbb{P}_1$ for the gas ratio in the electrolyte domain
$\mathcal{S}_{h,fe}$	Finite element space $\mathbb{P}_1$ for the jump of the normal viscous force on the interface
$\mathcal{S}_{h,fe}$	Finite element space $\mathbb{P}_1$ for the normal viscous force on the outflow $\Gamma_{out}$
$\Delta_{L^2,\Omega}, \Delta_{L^\infty,\Gamma}$	Relative difference in $L^2, L^\infty$ norm in domain $\Omega, \Gamma$



# Contents

<b>Acknowledgements</b>	<b>i</b>
<b>Abstract</b>	<b>iii</b>
<b>Introduction</b>	<b>1</b>
0.1 Aluminium electrolysis process . . . . .	2
0.2 Aim of this work . . . . .	6
<b>1 A mixture model for a dilute dispersion of gas in a liquid</b>	<b>7</b>
1.1 Navier-Stokes equations with varying density . . . . .	7
1.2 Derivation of a mixture model from conservation equations . . . . .	8
1.3 Introduction of a gas production term in the system . . . . .	11
1.4 Boundary conditions with outflow . . . . .	12
1.5 The stationary model . . . . .	13
1.6 On a drag force model . . . . .	15
1.6.1 Derivation of a Drag force in the Stokes regime . . . . .	15
1.6.2 Turbulent Drag Force . . . . .	16
1.7 Simplified models . . . . .	17
1.7.1 An explicit formula for the gas velocity . . . . .	17
1.7.2 Connection with the velocity of a single bubble of gas in a fluid . . . . .	18
1.7.3 Boussinesq approximation of Navier-Stokes equation . . . . .	19
1.8 Weak formulation of the stationary system . . . . .	20
1.8.1 Weak form of Navier-Stokes equations . . . . .	20
1.8.2 Weak form of the gas momentum equation . . . . .	22
1.8.3 Weak form of the gas mass equation . . . . .	23
1.9 Algorithm to solve the stationary problem . . . . .	23
1.10 Linearisation of the equations . . . . .	25
1.11 Finite Element approximation of the stationary model . . . . .	28
<b>2 Mathematical analysis of a simplified model</b>	<b>33</b>
2.1 Sobolev spaces notation . . . . .	34
2.2 Weak formulation . . . . .	34
2.3 Numerical approximation of the simplified model . . . . .	38
2.4 Numerical experiments for the simplified problem . . . . .	47

## Contents

---

2.4.1	Numerical experiment on a rectangle . . . . .	47
2.4.2	Numerical experiment on a cube . . . . .	49
<b>3</b>	<b>Comparison with a water-column experiment</b>	<b>51</b>
3.1	Introduction to water-column experiments . . . . .	51
3.2	Setup of the experiment . . . . .	51
3.3	Setup of the gas source term . . . . .	53
3.4	Algorithm setup . . . . .	54
3.4.1	Boundary conditions . . . . .	54
3.4.2	Mesh . . . . .	55
3.4.3	Initial conditions . . . . .	55
3.4.4	Stop criteria . . . . .	58
3.5	Numerical results . . . . .	58
3.5.1	Reference solution . . . . .	58
3.5.2	Influence of the mesh size . . . . .	62
3.5.3	Influence of the drag coefficient . . . . .	62
3.5.4	Comparison of simplified models . . . . .	68
3.5.5	Sensitivity to gas diffusion and to gas viscosity . . . . .	70
3.5.6	Comparison with experimental data . . . . .	73
3.6	Conclusion . . . . .	76
<b>4</b>	<b>Application to aluminium electrolysis</b>	<b>77</b>
4.1	The fluid flow model in aluminium electrolysis . . . . .	77
4.1.1	Notations . . . . .	77
4.1.2	Hydrodynamic equations: two immiscible fluids . . . . .	78
4.1.3	Principles of an algorithm to solve the hydrodynamic equations coupled to the interface . . . . .	80
4.1.4	Partially sliding boundary conditions for the fluid in aluminium electroly- sis cells and weak formulation . . . . .	81
4.1.5	Electromagnetic effects . . . . .	83
4.1.6	Gas dynamics . . . . .	85
4.2	Space discretization and algorithm . . . . .	88
4.2.1	Meshes along the iterations . . . . .	88
4.2.2	Iterative algorithm without gas . . . . .	90
4.2.3	Iterative algorithm with gas . . . . .	91
4.2.4	Initialisation of the algorithms . . . . .	93
4.3	Two aluminium reduction cell domains . . . . .	94
4.3.1	Reference solution . . . . .	98
4.4	Numerical experiments : numerical parameters . . . . .	99
4.4.1	Distribution of the computational time through an iteration on an indus- trial cell . . . . .	99
4.4.2	Influence of Newton iterations $N_{Ne}$ on a small cell . . . . .	100
4.4.3	Influence of gas iteration $N_g$ and time-step $\Delta t$ on a small cell . . . . .	101

4.4.4	Comparison with a fine mesh on a small cell . . . . .	103
4.4.5	Conclusion about the numerical parameters . . . . .	106
4.5	Numerical experiments on the smaller simplified electrolysis cell: physical parameters . . . . .	106
4.5.1	Boundary conditions and friction coefficients . . . . .	106
4.5.2	Influence of the drag coefficient . . . . .	112
4.5.3	Influence of the turbulent gas diffusion . . . . .	114
4.5.4	Influence of the gas viscosity . . . . .	116
4.5.5	Conclusion . . . . .	116
4.6	Numerical results on an industrial AP32 electrolysis cell . . . . .	118
4.6.1	Effects of the gas . . . . .	118
4.6.2	Source term geometry and model . . . . .	127
4.6.3	Influence of the gas with variable conductivity . . . . .	128
4.6.4	Comparison with simplified gas velocity model . . . . .	129
4.6.5	Conclusion . . . . .	130
<b>5</b>	<b>Conclusion</b>	<b>133</b>
	<b>Bibliography</b>	<b>135</b>
<b>A</b>	<b>Appendix</b>	<b>141</b>
A.1	Proof of the independence of the gas velocity with respect to the choice of the constant for the pressure $p$ . . . . .	141
A.2	Gmsh simple code to generate a cylinder . . . . .	143
A.3	Python code for chapter 2 : Stokes experiment . . . . .	145
	<b>Curriculum Vitae</b>	<b>147</b>



# Introduction

This research work is motivated by the industrial process of aluminium electrolysis [Hyd21] and is financially supported by Rio Tinto Aluminium.

Aluminium is the chemical element of atomic number thirteen, which has low density, silver colour, is resistant to corrosion and has important malleability. Aluminium is very much appreciated by industry, in its pure form or alloyed with other metals, particularly in construction, transport, aeronautics, packaging and electronics.

Aluminium is the most abundant metal in the earth's crust, about 8% of its mass. It is not present in pure form, but in minerals that contain oxides of aluminum, notably alumina  $Al_2O_3$ . One of the main mineral forms of aluminum is bauxite, which is composed of about 50% alumina, as well as silicates, iron oxides and other impurities in smaller quantities. Mostly mined in Australia, South America and Asia, bauxite is processed using the alumina extraction process (Bayer process) to obtain alumina. This process has remained practically the same for a century, and is problematic because of the release of the bauxite residue called "red mud" very harmful for the environment. Recently some new technologies have emerged in order to obtain alumina with reduced environmental impact [Bor+16]. It takes about four tons of bauxite to produce one ton of aluminum with the Bayer process.

According to [Das12], the aluminium production industry has a carbon footprint amounting to 1.7% of global emissions from all sources and an electric current consumption representing 3% of the total worldwide, therefore huge efforts are done to enhance the process efficiency, both for economical and ecological reasons.

Finally, the Hall-Héroult process of aluminum electrolysis is an expensive and complex process, which extracts aluminum from alumina; it will be described in more details in this thesis. In this process, large quantities of carbon dioxide are produced. The purpose of this thesis is to predict the global effect of the carbon dioxide gas on the fluid flow with numerical simulations, in order to optimise the industrial process.

## 0.1 Aluminium electrolysis process

The Hall-Héroult electrolysis process allows to make pure aluminium from alumina  $Al_2O_3$ . Discovered simultaneously and independently in 1886 by Paul Héroult and Charles Hall, it is actively used today; for more details we refer to the work of [Grj+77; Hau13]. Aluminium reduction occurs in huge cells, composed of various parts. A schematic representation of a cell is given in Figure 1.

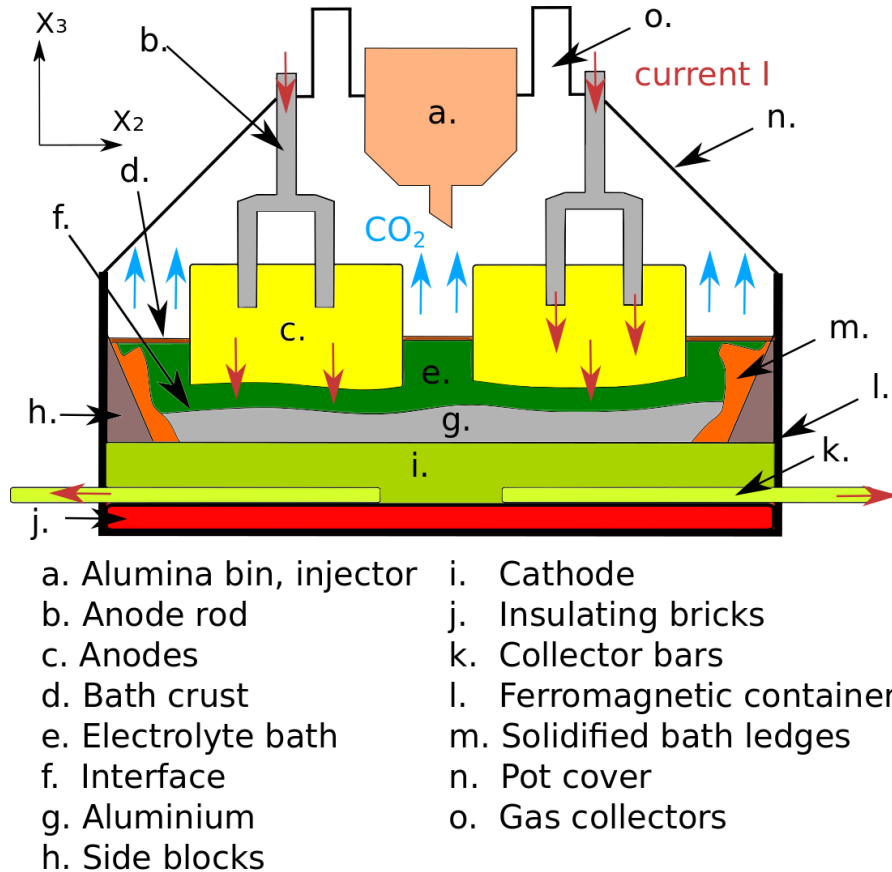


Figure 1 – Representation of the structure of the elements inside an aluminium electrolysis cell, transverse cut. Inspired from [KHP19].

An outer steel shell contains the whole setup. On the top of the cell the current  $I$  is injected through anode rods (Fig 1.b), and then through the anodes made of carbon (Fig 1.c), the electrolyte (Fig 1.e), the aluminium (Fig 1.g) and the cathode (Fig 1.i). Under the cathode, the iron bars, called collector bars (Fig 1.k), transport the electric current out of the cell. On the bottom, some layers of insulating bricks (Fig 1.j) are used to reduce heat losses. The liquid molten electrolysis bath and liquid aluminium are in a container made of carbon, and form a two immiscible phase system separated by an interface (Fig 1.d). The bottom part of the container is called cathode, although from a chemical point of view the cathode also includes liquid aluminium.

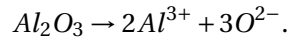
## 0.1. Aluminium electrolysis process

---

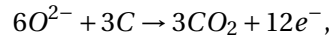
The electric current heats the bath presenting a high electric resistance by Joule effect: at high temperatures the bath and aluminium are liquid, and they are separated because of their different densities, the aluminium having a density around 10% higher than the bath density.

The temperature required for all these elements to be liquid and the chemical reactions to work properly is around 950°C. The temperature of the whole system is set such that a solid layer of bath forms close to the side blocks of the cells (Fig 1.h): these solid layers of bath are called bath ledges (Fig 1.m) and allows the thermal isolation of the cell while also protecting the cell against the corrosion of the bath.

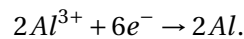
Chemical reactions occur in the molten bath. Alumina  $Al_2O_3$  is inserted at controlled pace in the bath through an injector (Fig 1.a) that is required to pierce the bath crust (Fig 1.d) formed at the surface. The chemical challenge to separate aluminium and oxygen in the alumina  $Al_2O_3$  can be overcome using in particular cryolite  $Na_3AlF_6$  and Aluminium fluoride  $AlF_3$ , that act as flux to dissolve the aluminium. Alumina is dissolved in ions of aluminium by the reaction:



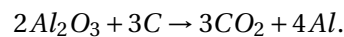
Second, the carbon of the anodes react with the oxygen ions, and form carbon dioxide gas  $CO_2$  by the transformation:



thus the anodes are slowly consumed, and need to be changed regularly. The lifespan of an anode is a month in industrial context. A cell containing typically between twenty and forty anodes (Figure 2), an anode is changed every day in an industrial cell on average. Recent developments aim to reduce the aluminium carbon footprint by using inert anodes [Yas+20] instead of carbon anodes, diminishing the total carbon dioxide produced. Finally, the aluminium ions are reduced in Aluminium through the main reaction:



As gravity drags the aluminium at the bottom of the cell, it is pumped out of the cell regularly, through a tap hole (illustrated in Figure 2). The overall reduction reaction is:



The carbon dioxide  $CO_2$  represents 90% of the gas produced in the reduction chemical reactions. In addition, some gases such as hydrogen fluoride  $HF$ ,  $CF_4$  (PFC-14, tetrafluoromethane) and  $C_2F_6$  (PFC-116, hexafluoroethane) are generated, mostly from secondary reaction with the cryolite. All the gases escape the bath mainly through the channels between the anodes, and are collected through gas collectors (Fig 1.o) in a gas treatment center (GTC). The gases are then filtered in the GTC: in particular the hydrogen fluoride  $HF$ , highly toxic, is recycled by fluorating fresh alumina. The carbon dioxide being the less threatening of the different gases, it is released in the wild, unfortunately contributing to the greenhouse effects.

## Introduction

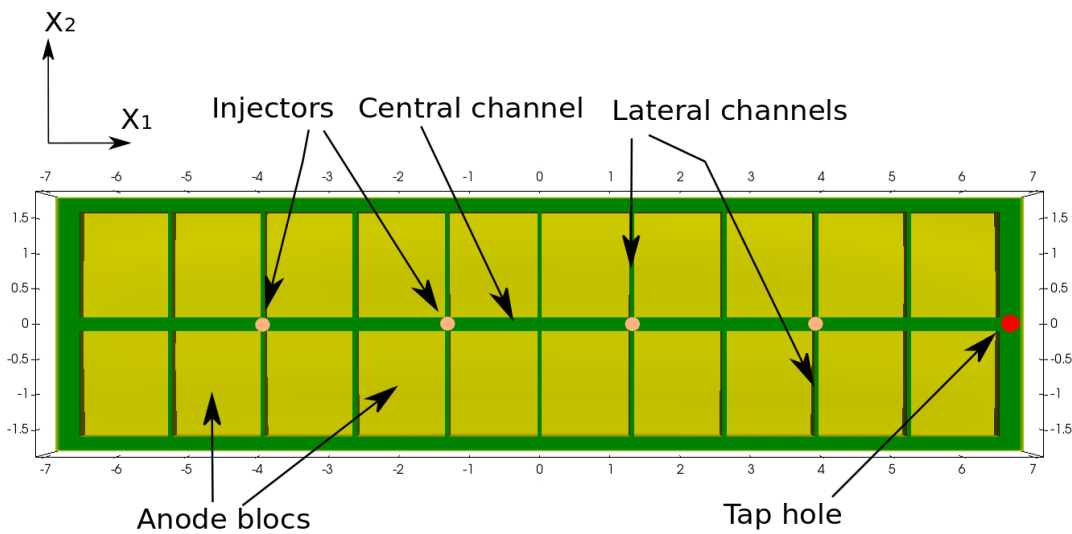


Figure 2 – Scheme of the liquid region in an industrial cell seen from above.

In order for this process to work at industrial scale, a typical aluminium reduction cell measures about  $14[m]$  of length for  $3[m]$  of width, shown in Figure 2. The anodes are arranged in two parallel lines, where the distance between the two lines is called central channel. A huge electric current in the range of  $320[kA]$  is used, and to reduce the energy cost, the resistance generated by the electrolytic bath has to be as low as possible. For this reason, the distance between the anode surface and the aluminium-bath interface, called ACD<sup>1</sup>, is chosen between  $20[mm]$  and  $40[mm]$ . Figure 3 shows a factory with several industrial cells in series.

The huge electric current in a cell and its neighbours generate important electromagnetic forces (Lorentz forces). These forces will put the electrolytic bath and the liquid aluminium into movement, leading the interface between them to move as well. It is critical that the interface does not move too much, because oscillations of the interface would reduce the ACD locally: in the extreme case where the aluminium would touch the anode, a shortcut would happen. This situation has to be avoided at all costs, as it would destabilise the system, as well as the neighbouring cells.

Thus, the movement of the fluids in the aluminium reduction cells and their numerical modelling are of paramount importance. The problem is especially challenging because of the coupling between the magneto hydrodynamics and the free interface. Reference works can be found in [GBL03; BE15], in [MR96; Sne85; DFR98] regarding the interface stability or in several EPFL PhD thesis [Pai06; Ste09; Flo13; Roc16].

The software Alucell<sup>2</sup> [Ste09], allows to compute a stationary state numerical approximation

<sup>1</sup>for Anode-Cathode-Distance.

<sup>2</sup>The software Alucell, co-proprerty of EPFL and Rio Tinto Aluminium, is developed by EPFL and YcoorSystems SA (Sierre, Switzerland). The source code is written in C++ and Fortran, and uses a native script language to implement algorithm related to the numerical modelling of aluminium electrolysis.

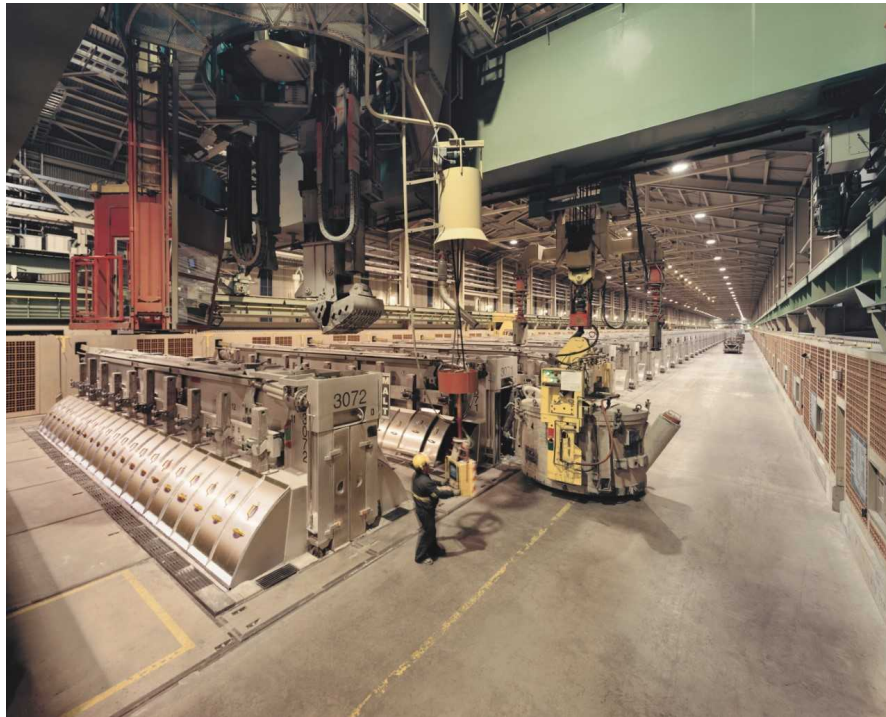


Figure 3 – View of a hall with several aluminium electrolysis cells in serie. Siphoning of aluminium is done on the right. Photo courtesy of Rio Tinto Aluminium.

of the fluid flow and the interface. Several new functionalities have been added since: the ferromagnetic effects[DF89], the thermal effects[Flo13; Saf05], alumina dissolution[Hof11; Hil19] and different turbulence models[Roc16].

Furthermore, the movements of the gas modify the fluid flow, making the multi-physics at stake even more complex. Similarly to recent models[Ein+17; SLL19; Zha+17], the purpose of this thesis is to develop a model to take into account the global effect of the gas in numerical simulations coupling the magneto-hydrodynamics and the free surface, and implement it in the software Alucell.

Furthermore, an accurate prediction of the fluid velocity fields is also important in order to study the transport of the alumina through the electrolysis cell. The concentration of alumina should be balanced homogeneously through the whole cell to optimise the process. If the concentration is too high, the alumina might solidify in aggregates and disturb the flow. If the concentration is too low, the current efficiency decreases leading to the so-called anode effect: in addition to carbon dioxide, more  $CF_4$  (PFC-14, tetrafluoromethane) and  $C_2F_6$  (PFC-116, hexafluoroethane) are generated, resulting in a layer of gas under the anode, insulating the anode even more, leading to an increased voltage.

Numerical experiments indicate under-estimated velocities in the channels, leading for instance to a wrong prediction of the alumina concentration. Taking into account the change of

density due to the gas distribution will change the fluid flow, and hopefully, gives numerical results closer to reality.

### 0.2 Aim of this work

The aim of this thesis consists into studying a model of diluted gas in numerical magneto-hydrodynamics simulations, in order to evaluate how the liquid flow is modified by the density composed of a mixture of gas and liquid. In particular, an algorithm is introduced in the software Alucell in order to reach a stationary solution, with respect to the different magneto-hydrodynamics unknowns, including the unknowns associated with the gas model. This document is structured as follows:

In chapter 1, the mixture model that is going to be used in this thesis is presented. The model takes its root in the coupling of the equations of conservation of mass and momentum for respectively the gas phase and liquid phase. A few physical assumptions, in particular the fact that the pressure of liquid, gas and mixture is the same, are considered. Two models of drag forces are described, and a further simplified model of the gas velocity is introduced. In addition, the weak formulation associated with the problem, as well as its corresponding finite element approximations are presented. Finally, an iterative algorithm to reach a stationary solution is described.

In chapter 2, extra assumptions are used to further simplify the model, and develop theoretical results. The paramount assumption is that the gas density  $\rho_g \alpha_g$  is given as an input data, and is not an unknown. In this case, it is shown that as long as the gas density satisfies some regularity and bounds, the problem is well-posed. Moreover, a finite element approximation of the problem is considered, and we proved that the standard a priori error estimates for the velocity and the pressure can be recovered.

In chapter 3, the model is compared with a water-column experiment. While this situation differs completely from the aluminium electrolysis context, it allows to show that the behaviour of the model is correct. In this context, the liquid is not driven by external forces (electromagnetic forces) but is solely put into movement because of the gas density distribution. The proposed stationary approach of chapter 1 is compared with experimental data collected from [Gem+18; BRJ06] in this context.

Finally, in chapter 4, the magneto-hydrodynamics equations are presented. The algorithm of chapter 1 is applied to the aluminium electrolysis process. The behaviour of the model with variations of the different parameters are presented and discussed. The results show that the velocity fields are indeed modified in the channels.

# 1 A mixture model for a dilute dispersion of gas in a liquid

In this chapter a model of a two phase flow consisting of a gaseous phase diluted into a liquid phase is presented. In order to introduce such a model, the general Navier-Stokes equations with varying density are recalled. To establish this model, the equations of conservation of mass and momentum for each phase are combined, and the resulting equations form a system of Navier-Stokes equations with varying density. The model is expressed in Eulerian form, thus the gas bubbles are not represented in this model. The model is based on [RL16; Pan06].

We denote  $\mathbf{x} = (x_1, x_2, x_3)$  any point of  $\mathbb{R}^3$  and  $\Omega \subset \mathbb{R}^3$  the computational domain containing the liquid, with boundary  $\partial\Omega$ .

## 1.1 Navier-Stokes equations with varying density

Navier-Stokes equations describe the motion of viscous fluids. They arise from two conservation laws, namely the conservation of the momentum of the fluid:

$$\frac{\partial(\rho \mathbf{u})}{\partial t} + \operatorname{div}(\rho \mathbf{u} \otimes \mathbf{u}) = \operatorname{div}(\boldsymbol{\tau}) + \mathbf{F}, \quad (1.1)$$

and the conservation of the mass of the fluid:

$$\frac{\partial \rho}{\partial t} + \operatorname{div}(\rho \mathbf{u}) = 0, \quad (1.2)$$

where  $\rho$  is the density of the fluid,  $\mathbf{u}$  its velocity,  $\boldsymbol{\tau}$  the stress tensor and  $\mathbf{F}$  the density of body forces applied to the fluid. The stress tensor is written as:

$$\boldsymbol{\tau} = -p\mathbf{I} - \frac{2}{3}\mu \operatorname{div}(\mathbf{u})\mathbf{I} + 2\mu \boldsymbol{\epsilon}(\mathbf{u}), \quad (1.3)$$

where  $p$  is the pressure of the fluid and  $\mu$  the viscosity of the fluid. Also

$$\boldsymbol{\epsilon}(\mathbf{u}) = \frac{1}{2}(\nabla \mathbf{u} + \nabla \mathbf{u}^T), \quad \text{with } (\nabla \mathbf{u})_{i,j} = \frac{\partial u_i}{\partial x_j}, \quad 1 < i, j < 3,$$

## Chapter 1. A mixture model for a dilute dispersion of gas in a liquid

---

is the shear rate tensor. In equation (1.1),  $\mathbf{u} \otimes \mathbf{u}$  is the tensor given by  $(\mathbf{u} \otimes \mathbf{u})_{i,j} = u_i u_j$ , and the divergence of a tensor  $\boldsymbol{\tau}$  is defined as  $(\text{div}(\boldsymbol{\tau}))_i = \sum_{j=1}^3 \partial \tau_{i,j} / \partial x_j$ ,  $1 < i < 3$ . When the unknowns are the velocity  $\mathbf{u}$ , the pressure  $p$  and the density  $\rho$ , the system of equations (1.1)-(1.2) is incomplete, an additional scalar equation is required: for instance in the case of a perfect gas, that would be an equation linking  $p$  and  $\rho$ . We will see in this chapter that  $\rho$  depends on the quantity of gas introduced in the fluid. Since:

$$\text{div}(\rho \mathbf{u} \otimes \mathbf{u}) = \text{div}(\rho \mathbf{u}) \mathbf{u} + (\rho \mathbf{u} \cdot \nabla) \mathbf{u},$$

this equation together with (1.2) gives the non-conservative form of equations (1.1) and (1.2):

$$\rho \frac{\partial \mathbf{u}}{\partial t} + (\rho \mathbf{u} \cdot \nabla) \mathbf{u} = \text{div}(\boldsymbol{\tau}) + \mathbf{F}, \quad (1.4)$$

$$\frac{\partial \rho}{\partial t} + \text{div}(\rho \mathbf{u}) = 0, \quad (1.5)$$

where  $\boldsymbol{\tau}$  is defined by relation (1.3). When the density is constant, the following relation holds instead of (1.5):

$$\text{div}(\mathbf{u}) = 0,$$

and then the viscous stress tensor  $\boldsymbol{\tau}$  in (1.3) simplifies to:

$$\boldsymbol{\tau} = -p\mathbf{I} + 2\mu\boldsymbol{\epsilon}(\mathbf{u}).$$

### 1.2 Derivation of a mixture model from conservation equations

Consider a domain  $\Omega$  and a final time  $T > 0$ . The model described in this section relies on a mixture between an incompressible gas and an incompressible liquid, as developed by [Pan06; RL16]. Start by considering two different phases, the liquid denoted by  $l$  and the diluted gas phase denoted by  $g$ . Then we write  $\mathbf{u}_k, p_k, \rho_k, \mu_k$  and  $\alpha_k$  the velocity field, pressure, density, viscosity and volumetric fraction of each phase  $k \in \{l, g\}$  respectively. In particular the volumetric fraction of each phase represents the percentage in volume of each phase at a given location of the domain. Each phase  $k$  satisfies the equations of conservation of momentum and mass:

$$\frac{\partial(\alpha_k \rho_k \mathbf{u}_k)}{\partial t} + \text{div}(\alpha_k \rho_k \mathbf{u}_k \otimes \mathbf{u}_k) = \text{div}(\boldsymbol{\tau}_k) + \alpha_k \rho_k \mathbf{g} + \mathbf{f}_k + \mathbf{F}_k, \quad (1.6)$$

$$\frac{\partial(\alpha_k \rho_k)}{\partial t} + \text{div}(\alpha_k \rho_k \mathbf{u}_k) = 0, \quad (1.7)$$

with the viscous tensor of each phase  $\boldsymbol{\tau}_k = -p_k \alpha_k \mathbf{I} - 2/3 \mu_k \text{div}(\mathbf{u}_k) \mathbf{I} + 2\mu_k \boldsymbol{\epsilon}(\mathbf{u}_k)$ ,  $\mathbf{F}_k$  the external forces,  $\alpha_k \rho_k \mathbf{g}$  the gravity force and  $\mathbf{f}_k$  the interface momentum exchange terms applied to each phase  $k$ . The total conservation of volume implies:

$$\alpha_g + \alpha_l = 1,$$

## 1.2. Derivation of a mixture model from conservation equations

which expresses the fact that the two phases fill the space. The interface momentum exchange terms take the following form:

$$\mathbf{f}_l = p_l \nabla \alpha_l + D \alpha_g \alpha_l (\mathbf{u}_g - \mathbf{u}_l),$$

$$\mathbf{f}_g = p_g \nabla \alpha_g + D \alpha_g \alpha_l (\mathbf{u}_l - \mathbf{u}_g),$$

where the first term represents the effect of pressure force and the second term the drag force exerted by the other component, proportional to the difference of velocities.

**Remark 1.** The drag coefficient  $D$  is discussed later in Section 1.6. From now we keep this coefficient as general as possible.

The mixture is defined as the general substance composed of a part of liquid and a part of gas. The population of gaseous bubbles diluted in the liquid is considered as a continuous phase  $\alpha_g$  as in Figure 1.1. Then equations that describe directly the behaviour of the velocity and density of the mixture can be derived. The momentum and mass conservation equations for

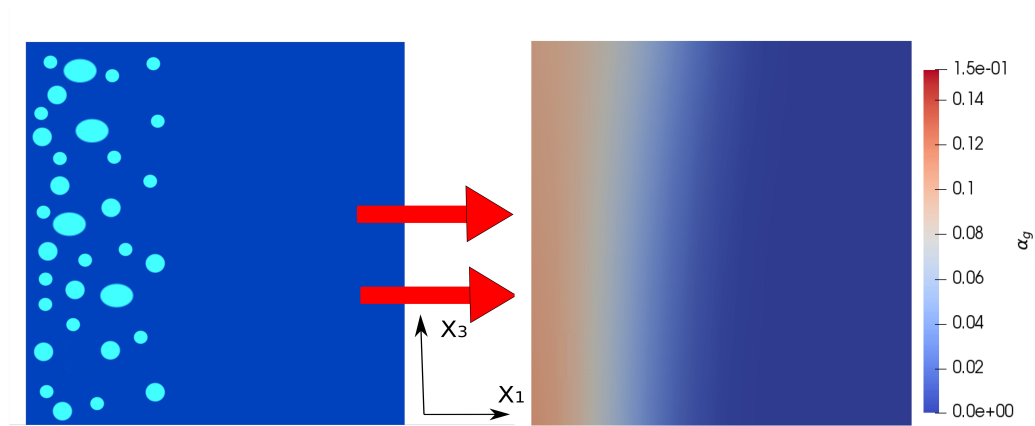


Figure 1.1 – The population of small gas bubbles diluted in the liquid is described with a continuous phase, the volumetric ratio of gas  $\alpha_g$ .

the mixture are obtained by summing the corresponding equations for each component. In particular the density of the mixture  $\rho$  is defined by:

$$\rho = \alpha_g \rho_g + \alpha_l \rho_l = \alpha_g \rho_g + (1 - \alpha_g) \rho_l. \quad (1.8)$$

The velocity of the mixture  $\mathbf{u}$  is defined by:

$$\rho \mathbf{u} = \alpha_g \rho_g \mathbf{u}_g + (1 - \alpha_g) \rho_l \mathbf{u}_l. \quad (1.9)$$

Summing equations (1.6)-(1.7) for the gaseous phase  $k = g, l$  leads to:

$$\frac{\partial(\rho \mathbf{u})}{\partial t} + \text{div}(\rho \mathbf{u} \otimes \mathbf{u}) = \text{div}(\boldsymbol{\tau} + \mathbf{r}) + \rho \mathbf{g} + \mathbf{F} - p_c \nabla \alpha_g, \quad (1.10)$$

$$\frac{\partial \rho}{\partial t} + \operatorname{div}(\rho \mathbf{u}) = 0, \quad (1.11)$$

where:

$$\mathbf{r} = -\frac{\alpha_g \rho_g}{(1 - \alpha_g) \rho_l} \rho (\mathbf{u}_g - \mathbf{u}) \otimes (\mathbf{u}_g - \mathbf{u}) \text{ is the Reynolds stress tensor,} \quad (1.12)$$

$$\boldsymbol{\tau} = \boldsymbol{\tau}_g + \boldsymbol{\tau}_l = -p \mathbf{I} - 2/3 \mu \operatorname{div}(\mathbf{u}) \mathbf{I} + 2\mu \boldsymbol{\epsilon}(\mathbf{u})$$

is the stress tensor of the mixture: it is not possible to compose it as the sum of the liquid tensor and the gas tensor as a tensor depending only on the mixture velocity  $\mathbf{u}$ . Therefore it is rewritten as its classical formulation, where the viscosity of the mixture  $\mu$  has to be described with adequate constitutive physical law. The total pressure is given with:

$$p = \alpha_g p_g + (1 - \alpha_g) p_l, \quad (1.13)$$

and  $p_c$  is the capillary pressure defined as the difference of pressures between each phase  $p_c = p_l - p_g$ . Using the different definitions, several variables can be eliminated. Indeed, as  $\alpha_l = 1 - \alpha_g$ ,  $\rho$  depends only on  $\alpha_g$  thanks to (1.8). The liquid velocity  $\mathbf{u}_l$  can be written, thanks to (1.9), as:

$$\mathbf{u}_l = \frac{1}{\rho_l \alpha_l} (\rho \mathbf{u} - \alpha_g \rho_g \mathbf{u}_g). \quad (1.14)$$

### Assumptions to close the model

Different hypothesis are introduced in order to obtain a close system of equations. Consider that the densities of each phase  $\rho_g$  and  $\rho_l$  are constant, that the density of the gas is significantly lower  $\rho_g \ll \rho_l$ , and also that the volumetric ratio of gas  $\alpha_g$ , as the diluted phase, is smaller than the ratio of liquid. In the case of low velocities, the Reynolds stress tensor (1.12)  $\mathbf{r}$  can be neglected.

The drag force can be rewritten using (1.14):

$$D\alpha_g \alpha_l (\mathbf{u}_l - \mathbf{u}_g) = D\alpha_g (1 - \alpha_g) \left( \frac{\rho}{(1 - \alpha_g) \rho_l} \mathbf{u} - \frac{\alpha_g \rho_g}{(1 - \alpha_g) \rho_l} \mathbf{u}_g - \mathbf{u}_g \right) = D\alpha_g \frac{\rho}{\rho_l} (\mathbf{u} - \mathbf{u}_g).$$

An additional law is required for the capillary pressure  $p_c$  to close the model. In this thesis we consider that the surface tensions effects are neglected, so the capillary pressure  $p_c = 0$ , and therefore consider a unique pressure  $p = p_g = p_l$ . Finally no external force is exerted on the gas,  $\mathbf{F}_g = 0$  and positive gas diffusion coefficient  $K > 0$  is included in the model to take into account the gas diffusion in the applications, especially in aluminium electrolysis. Then rewriting (1.6)(1.7) for the gas  $k = g$  and (1.10)(1.11) with these assumptions, the following system can be deduced:

$$\rho_g \frac{\partial(\alpha_g \mathbf{u}_g)}{\partial t} + \operatorname{div}(\alpha_g \rho_g \mathbf{u}_g \otimes \mathbf{u}_g) + D\alpha_g \frac{\rho}{\rho_l} \mathbf{u}_g - \operatorname{div}(\boldsymbol{\tau}_g) + p \nabla \alpha_g = \alpha_g \rho_g \mathbf{g} + D\alpha_g \frac{\rho}{\rho_l} \mathbf{u}, \quad (1.15)$$

### 1.3. Introduction of a gas production term in the system

$$\frac{\partial \alpha_g}{\partial t} + \operatorname{div}(\alpha_g \mathbf{u}_g - K \nabla \alpha_g) = 0, \quad (1.16)$$

$$\frac{\partial(\rho \mathbf{u})}{\partial t} + \operatorname{div}(\rho \mathbf{u} \otimes \mathbf{u}) = \operatorname{div}(\boldsymbol{\tau}) + \rho \mathbf{g} + \mathbf{F}, \quad (1.17)$$

$$\frac{\partial \rho}{\partial t} + \operatorname{div}(\rho \mathbf{u}) = 0, \quad (1.18)$$

with:

$$\boldsymbol{\tau}_g = -p \alpha_g \mathbf{I} - 2/3 \mu_g \operatorname{div}(\mathbf{u}_g) \mathbf{I} + 2 \mu_g \epsilon(\mathbf{u}_g), \quad (1.19)$$

$$\boldsymbol{\tau} = -p \mathbf{I} - 2/3 \mu \operatorname{div}(\mathbf{u}) \mathbf{I} + 2 \mu \epsilon(\mathbf{u}),$$

$$\rho = \alpha_g \rho_g + (1 - \alpha_g) \rho_l.$$

Then (1.15)-(1.18) forms a system of equations for the unknowns  $\mathbf{u}_g$ ,  $\alpha_g$ ,  $\mathbf{u}$  and  $p$ , with the different inputs given:  $\rho_g$ ,  $\rho_l$ ,  $\mu_g$ ,  $D$ ,  $\mu$ ,  $K$  and  $\mathbf{F}$ . Appropriate initial and boundary conditions are then required.

### 1.3 Introduction of a gas production term in the system

A particular attention is given to mass conservation of gas (1.16). Notice that if:

$$\mathbf{u}_g \cdot \mathbf{n} = 0 \text{ on } \partial\Omega, \quad (1.20)$$

with  $\mathbf{n}$  being the unit normal vector to the external boundary of  $\Omega$ , there is no influx nor outflux of gas out of the domain  $\Omega$ . It is completed with the condition for  $\alpha_g$ :

$$K \nabla \alpha_g \cdot \mathbf{n} = 0 \text{ on } \partial\Omega, \quad (1.21)$$

which represents the fact that the gas system is isolated, there is no gas diffusion through the boundary  $\partial\Omega$ . Therefore the initial quantity of gas is conserved if (1.20)(1.21) hold.

However in aluminium electrolysis the initial state of the system is not known, but the rate of production of the system can be computed, as the quantity of gas produced in the domain  $\Omega$  per unit time is known. A first method could be to model the rate of production as an inflow, i.e an incoming flux on a part of the boundary  $\Gamma_{in} \subset \partial\Omega$ , where  $\Gamma_{in} = \{\mathbf{x} \in \partial\Omega : \mathbf{u}_g \cdot \mathbf{n} < 0\}$ .

The use of an inflow can lead to various issues: the paramount one being that it requires to fix both unknowns  $\mathbf{u}_g$  and  $\alpha_g$  on the inflow  $\Gamma_{in}$ , and that in some practical cases fixing these boundary conditions lead to severe numerical issues<sup>1</sup>. A different approach is proposed in this thesis to introduce gas into the system: thanks to a volumetric source term, rewriting

<sup>1</sup>In particular the boundary conditions on the inflow would be to impose a gas velocity going down, where the gas velocity goes naturally up everywhere because of gravity in this model. The composition of this boundary condition and the model result in ill-posed model in our experience

(1.16) as:

$$\frac{\partial \alpha_g}{\partial t} + \operatorname{div}(\alpha_g \mathbf{u}_g - K \nabla \alpha_g) = \dot{\alpha}_{source}. \quad (1.22)$$

Here the positive source term  $\dot{\alpha}_{source} \geq 0$  has the dimension of a frequency. The quantity  $\rho_g \dot{\alpha}_{source}$  represents the mass of gas produced in the domain per unit volume per unit time.

If we require (1.22) to reach a stationary solution, then integrating (1.22) over  $\Omega$ , and integrating by part taking into account (1.21) gives compatibility condition:

$$\int_{\Omega} \dot{\alpha}_{source} dx = \int_{\partial\Omega} \alpha_g \mathbf{u}_g \cdot \mathbf{n} ds = \int_{\Gamma_{out}} \alpha_g \mathbf{u}_g \cdot \mathbf{n} ds, \quad (1.23)$$

where we denote:

$$\begin{aligned} \Gamma_{out} &= \{\mathbf{x} \in \partial\Omega : \mathbf{u}_g \cdot \mathbf{n} \neq 0\}, \\ \partial\Omega &= \Gamma_{out} \cup \Gamma_0, \\ \Gamma_0 &= \{\mathbf{x} \in \partial\Omega : \mathbf{u}_g \cdot \mathbf{n} = 0\}. \end{aligned}$$

Notice that it is necessary that  $\Gamma_{out} \neq \emptyset$  as long as the source term  $\dot{\alpha}_{source}$  is positive if a stationary state exists: otherwise the problem would be ill-posed. In practice  $\Gamma_{out}$  is an outflow surface through which the gas is expelled out of  $\Omega$ .

## 1.4 Boundary conditions with outflow

The introduction of an outflow of gas in the model induces different changes. For every point  $P$  on the boundary  $\partial\Omega$ , let  $\mathbf{n}(P)$ ,  $\mathbf{t}_1(P)$  and  $\mathbf{t}_2(P)$  denote the external unitary normal vector outgoing the surface  $\partial\Omega$  at point  $P$  the two unit basis vectors tangent to  $\partial\Omega$  such that  $(\mathbf{n}(P), \mathbf{t}_1(P), \mathbf{t}_2(P))$  form an orthonormal system. The boundary conditions on the mixture velocity  $\mathbf{u}$  are the following:

$$\mathbf{u} = \mathbf{0}, \text{ on } \Gamma_0, \quad (1.24)$$

$$\mathbf{u} \cdot \mathbf{n} = 0, \text{ on } \Gamma_{out}, \quad (1.25)$$

$$(\boldsymbol{\tau} \cdot \mathbf{n}) \cdot \mathbf{t}_i = 0 \text{ on } \Gamma_{out}, \quad i = 1, 2. \quad (1.26)$$

The two conditions (1.24-1.25) ensure that  $\mathbf{u} \cdot \mathbf{n} = 0$  yields for the whole boundary  $\partial\Omega$ , thus the mixture is confined in the domain  $\Omega$ .

**Remark 2.** In (1.26) the chosen notation is that the product  $(\boldsymbol{\tau} \cdot \mathbf{n})$  represents a matrix product between a  $3 \times 3$  matrix  $(\boldsymbol{\tau})$  and a  $3 \times 1$  vector, resulting in a vector  $3 \times 1$ :

$$(\boldsymbol{\tau} \cdot \mathbf{n})_i = \sum_{j=1}^3 \tau_{i,j} n_j.$$

The second  $\cdot$  with the vector  $\mathbf{t}_i$  here denotes the standard scalar product.

**Remark 3.** One immediately notices that since  $\mathbf{u} \cdot \mathbf{n} = 0$  holds on the whole frontier and if the gas velocity  $\mathbf{u}_g$  can be such that  $\mathbf{u}_g \cdot \mathbf{n} > 0$  on  $\Gamma_{out}$ , then the definition (1.9) implies that some liquid velocity  $\mathbf{u}_l$  is coming into the domain,  $\mathbf{u}_l \cdot \mathbf{n} \neq 0$  on  $\Gamma_{out}$ . However :

$$\mathbf{u}_l = -\frac{\alpha_g \rho_g}{(1 - \alpha_g) \rho_l} \mathbf{u}_g \text{ is very small on } \Gamma_{out} \text{ when } \rho_g / \rho_l \ll 1, \mathbf{u} = \mathbf{0}, \alpha_g \ll 1,$$

and it is reasonable not to take it into account. (in the frame of aluminium electrolysis  $\rho_g / \rho_l < 1/200$ )

The pressure  $p$  in equations (1.15) and (1.17) is defined up to a constant. This constant is determined for instance by imposing that:

$$\int_{\Omega} p dx = 0, \quad (1.27)$$

that is,  $p$  belongs to the space of zero average function. The boundary conditions for the gas velocity  $\mathbf{u}_g$  are:

$$\mathbf{u}_g = 0, \text{ on } \Gamma_0, \quad (1.28)$$

$$(\boldsymbol{\tau}_g \cdot \mathbf{n}) \cdot \mathbf{n} = \alpha_g p_0, \text{ on } \Gamma_{out}, \quad (1.29)$$

Here  $p_0$  is such that:

$$\int_{\Gamma_{out}} (\boldsymbol{\tau}_g \cdot \mathbf{n}) \cdot \mathbf{n} ds = \int_{\Gamma_{out}} \alpha_g (\boldsymbol{\tau} \cdot \mathbf{n}) \cdot \mathbf{n} ds$$

that is to say

$$p_0 = \frac{\int_{\Gamma_{out}} (\boldsymbol{\tau} \cdot \mathbf{n}) \cdot \mathbf{n} ds}{\int_{\Gamma_{out}} ds}. \quad (1.30)$$

that is the scalar  $p_0$  is the average of  $(\boldsymbol{\tau} \cdot \mathbf{n}) \cdot \mathbf{n}$  on the outflow surface  $\Gamma_{out}$ . The last condition is:

$$(\boldsymbol{\tau}_g \cdot \mathbf{n}) \cdot \mathbf{t}_i = 0, \text{ on } \Gamma_{out}, i = 1, 2. \quad (1.31)$$

With this definition, the constant  $p_0$  can be seen as a virtual pressure imposed on the outflow. The pressure  $p$  may be defined with (1.27) or any other condition, the gas velocity  $\mathbf{u}_g$  resulting from equation (1.15) and boundary conditions (1.28-1.31) is independent of the choice of this constant, see Appendix A.1.

## 1.5 The stationary model

In the applications, the stationary solution of the equations are of primary interest, as it gives key insights of the average behaviour of the system. Such an average system is obtained through time evolution, up to a point when the solution does not evolve anymore, which is

## Chapter 1. A mixture model for a dilute dispersion of gas in a liquid

---

considered as a steady state. Numerical experiments show that the time scale of the different equations are not the same: in the applications, the time scale of the gas equation (1.22) is much faster than the others. Consequently, an efficient method to reach a steady state is to consider this last equation as a time-evolution one ( see 1.33 below), while solving the others under their stationary form. Therefore, the following problem is considered: find the unknowns  $\mathbf{u}_g, \alpha_g, \mathbf{u}$  and  $p$  in  $\Omega$  satisfying:

$$\operatorname{div}(\alpha_g \rho_g \mathbf{u}_g \otimes \mathbf{u}_g) + D\alpha_g \frac{\rho}{\rho_l} \mathbf{u}_g - \operatorname{div}(\boldsymbol{\tau}_g) = p \nabla \alpha_g + \alpha_g \rho_g \mathbf{g} + D\alpha_g \frac{\rho}{\rho_l} \mathbf{u}, \quad (1.32)$$

$$\frac{\partial \alpha_g}{\partial t} + \operatorname{div}(\alpha_g \mathbf{u}_g - K \nabla \alpha_g) = \dot{\alpha}_{source}, \quad (1.33)$$

$$\operatorname{div}(\rho \mathbf{u} \otimes \mathbf{u}) = \operatorname{div}(\boldsymbol{\tau}) + \rho \mathbf{g} + \mathbf{F}, \quad (1.34)$$

$$\operatorname{div}(\rho \mathbf{u}) = 0, \quad (1.35)$$

where we recall the definitions of  $\boldsymbol{\tau}, \rho$  and  $\boldsymbol{\tau}_g$  given by (1.3), (1.8) and (1.19):

$$\boldsymbol{\tau} = -p \mathbf{I} - 2/3 \mu \operatorname{div}(\mathbf{u}) \mathbf{I} + 2\mu \boldsymbol{\epsilon}(\mathbf{u}),$$

$$\rho = \alpha_g \rho_g + (1 - \alpha_g) \rho_l,$$

$$\boldsymbol{\tau}_g = -p \alpha_g \mathbf{I} - 2/3 \mu_g \operatorname{div}(\mathbf{u}_g) \mathbf{I} + 2\mu_g \boldsymbol{\epsilon}(\mathbf{u}_g),$$

with the appropriate boundary conditions defined in (1.21)(1.24-1.31):

$$K \nabla \alpha_g \cdot \mathbf{n} = 0, \text{ on } \partial\Omega,$$

$$\mathbf{u} = \mathbf{0}, \text{ on } \Gamma_0,$$

$$\mathbf{u} \cdot \mathbf{n} = 0, \text{ on } \Gamma_{out},$$

$$(\boldsymbol{\tau} \cdot \mathbf{n}) \cdot \mathbf{t}_i = 0 \text{ on } \Gamma_{out}, \quad i = 1, 2,$$

$$\int_{\Omega} p \, dx = 0,$$

$$\mathbf{u}_g = \mathbf{0}, \text{ on } \Gamma_0,$$

$$(\boldsymbol{\tau}_g \cdot \mathbf{n}) \cdot \mathbf{n} = \alpha_g p_0 \text{ on } \Gamma_{out},$$

$$p_0 = \frac{\int_{\Gamma_{out}} (\boldsymbol{\tau} \cdot \mathbf{n}) \cdot \mathbf{n} \, ds}{\int_{\Gamma_{out}} ds},$$

$$(\boldsymbol{\tau}_g \cdot \mathbf{n}) \cdot \mathbf{t}_i = 0 \text{ on } \Gamma_{out}, \quad i = 1, 2.$$

In addition, the stationary system can be completed with :

$$\int_{\Omega} \dot{\alpha}_{source} dx = \int_{\Gamma_{out}} \alpha_g \mathbf{u}_g \cdot \mathbf{n} ds. \quad (1.36)$$

**Remark 4.** Condition (1.36) is not satisfied for all time  $t$ . However, it is a necessary condition when the solution is stationary, therefore it can be used in practice as an indicator that the solution may be close to a steady state.

**Remark 5.** In this model, the velocity of the mixture  $\mathbf{u}$  is very close to the liquid velocity  $\mathbf{u}_l$ , similarly to (1.14) :

$$(\mathbf{u} - \mathbf{u}_l) = \left( \frac{\alpha_g \rho_g}{\rho} \mathbf{u}_g + \left( \frac{(1 - \alpha_g) \rho_l}{\rho} - 1 \right) \mathbf{u}_l \right), \quad (1.37)$$

which is also very small when  $\rho_g / \rho_l \ll 1$  and  $\alpha_g \ll 1$ .

## 1.6 On a drag force model

Consider equation (1.32), in which the Drag force is given in compact form as:

$$D \frac{\rho}{\rho_l} \alpha_g (\mathbf{u} - \mathbf{u}_g) = D(1 - \alpha_g) \alpha_g (\mathbf{u}_l - \mathbf{u}_g) \quad (1.38)$$

We are going to look more into details what is the Drag coefficient  $D$ : first a simple law is derived in the so-called "Stokes" case, where some assumptions hold in the linear regime and we will also state a more general Drag force that is used in the literature. We will see that both forces are equivalent when the Reynolds number associated with the gas bubble flow is low.

### 1.6.1 Derivation of a Drag force in the Stokes regime

First the case of small spherical bubbles and small velocities is considered: with these assumptions, the Stokes drag force applying on an individual spherical bubble of gas in the surrounding fluid is described as Stokes force :

$$\mathbf{F}_{S,1bubble} = 3\pi\mu_L d (\mathbf{u}_l - \mathbf{u}_g), \quad (1.39)$$

where  $d$  is the diameter of the bubble and  $\mu_L$  the viscosity of the surrounding flow. It is then convenient to sum the force on the population of bubbles, considering that the volume of  $1[m^3]$  holds  $n$  bubbles given by  $n = r \frac{6\alpha_g}{d^3\pi}$ , where  $r$  is a packing factor: in the cases of spheres, its value is  $r = \frac{\pi}{3\sqrt{2}}$ . Therefore, the drag term would be:

$$\mathbf{F}_S = D\alpha_l \alpha_g (\mathbf{u}_l - \mathbf{u}_g) = n\alpha_l \mathbf{F}_{S,1bubble} = 18 \frac{\alpha_g \alpha_l \mu_L r}{d^2} (\mathbf{u}_l - \mathbf{u}_g) = 18 \frac{\alpha_g \rho \mu_L r}{d^2 \rho_l} (\mathbf{u} - \mathbf{u}_g), \quad (1.40)$$

where relation (1.14) was used in the last equality. The liquid volumetric ratio  $\alpha_l$  is usually close to one, which is why it is usually neglected in the classical Stokes formula (1.39). In this thesis,

this factor will be considered all the time. This expression shows that the bubble diameter is paramount for the drag Force as the dependency is  $\propto d^{-2}$ . In our model, a constant bubble diameter is considered as the average diameter of the population of bubbles. In the Stokes regime, the drag coefficient is then:

$$D = \frac{18\mu_L r}{d^2}. \quad (1.41)$$

### 1.6.2 Turbulent Drag Force

The turbulence associated with a flow of bubble in a fluid is measured through the value of the dimensionless Reynolds bubble number  $Re_b$ :

$$Re_b = \frac{\rho_l |\mathbf{u}_l - \mathbf{u}_g| d}{\mu_L}. \quad (1.42)$$

An interesting approach is to consider one of the most general formulation for the Drag force exerted on an object [LL59]:

$$|\mathbf{F}_D| = \frac{C_D \rho_l |\mathbf{U}|^2 S}{2}, \quad (1.43)$$

where  $\mathbf{U}$  is the difference of velocity between the object and the surroundings,  $S$  the area of a cross-section transverse to the direction of the flux, and  $C_D$  an dimensionless drag coefficient. Applied to a spherical bubble of gas of diameter  $d$  in a fluid, it can be written:

$$\mathbf{F}_{D,1bubble} = C_D \frac{\pi d^2 \rho_l}{8} (\mathbf{u}_l - \mathbf{u}_g) |\mathbf{u}_l - \mathbf{u}_g|. \quad (1.44)$$

$C_D$  is the dimensionless drag coefficient. When considering not a single bubble, but a dispersed population of bubble at different Reynolds numbers, a lot of different laws for the coefficient  $C_D$  exist in the literature: usually the coefficient is a function depending on the Reynolds number, and possibly on the geometry of the bubbles. In our model, all the aspects linked to the variations of the geometry of the bubbles are neglected, and the bubbles are considered as spheres with constant average diameter  $d$ . The model of Drag coefficient of Schiller will be considered [Sch33]:

$$C_D = \max\left(\frac{24}{Re_b} [1 + 0.15 Re_b^{0.687}], 0.44\right), \quad (1.45)$$

Notice that when the bubble Reynolds number  $Re_b \ll 1$  is small, injecting  $C_D = \frac{24}{Re_b}$  in (1.44) gives exactly the same expression as the Stokes Drag force in (1.39). Thus, using the same reasoning as to obtain the force in (1.40), one gets:

$$\mathbf{F}_D = \max\left([1 + 0.15 Re_b^{0.687}], \frac{0.44 Re_b}{24}\right) \mathbf{F}_S = f(Re_b) \mathbf{F}_S. \quad (1.46)$$

Therefore, the difference between the Stokes drag force  $\mathbf{F}_S$  and the more general form of the Drag force  $\mathbf{F}_D$  depends on a function labeled  $f(Re_b)$  which can be expressed directly with

the Reynolds bubble number. In the applications, the Reynolds bubble number is most of the time low and the Stokes approximation is sufficient. However, we will see that in some cases, the more general expression of the Drag force is useful. With the model (1.46), the drag coefficient is:

$$D = \max\left(\left[1 + 0.15Re_b^{0.687}\right], \frac{0.44Re_b}{24}\right) \frac{18\mu_L r}{d^2}. \quad (1.47)$$

Notice that the Stokes regime (1.41) is the inferior bound of expression (1.47).

## 1.7 Simplified models

In this section, simpler models are presented and derived, with additional assumptions. These models are easier to implement and to solve than the full model described in section 1.5, therefore can be useful in practice, but take poorly into account boundary conditions. A first simplification consists to eliminate the gas velocity from the system with additional assumptions. A second simple model arises similarly when eliminating the gas velocity assuming its velocity corresponds to the velocity of a single bubble in a flow at low Reynolds number. We will see that these two models are very similar. Lastly, we will talk about the Boussinesq approximation, which consists to take into account the variation of the density only through the gravity force.

### 1.7.1 An explicit formula for the gas velocity

Notice that using  $\text{div}(-\alpha_g p \mathbf{I}) + p \nabla \alpha_g = -\alpha_g \nabla p$ , equation (1.32) can be written as:

$$\text{div}(\alpha_g \rho_g \mathbf{u}_g \otimes \mathbf{u}_g) = \text{div}(2\mu_g (\epsilon(\mathbf{u}_g) - \text{div}(\mathbf{u}_g) \mathbf{I}/3)) - \alpha_g \nabla p + \alpha_g \rho_g \mathbf{g} + \frac{D\alpha_g \rho}{\rho_l} (\mathbf{u} - \mathbf{u}_g). \quad (1.48)$$

If only the last three terms are taken into account (we neglect the viscous and convective terms), one gets:

$$-\alpha_g \nabla p + \alpha_g \rho_g \mathbf{g} + \frac{D\alpha_g \rho}{\rho_l} (\mathbf{u} - \mathbf{u}_g) = 0. \quad (1.49)$$

Dividing by  $\alpha_g$ , re-arranging and using the Stokes expression (1.41) for the Drag coefficient  $D$  gives:

$$\mathbf{u}_g = \mathbf{u} - \frac{d^2 \rho_l}{18\mu_r \rho} (\nabla p - \rho_g \mathbf{g}) = \mathbf{u}_l - \frac{d^2}{18\mu_r \alpha_l} (\nabla p - \rho_g \mathbf{g}). \quad (1.50)$$

The last equality can be obtained using (1.38). Using one of the direct explicit relation (1.50) for  $\mathbf{u}_g$  allows to eliminate  $\mathbf{u}_g$ , and under these assumptions, system (1.32)-(1.35) is turned into another problem:

$$\rho = \alpha_g \rho_g + (1 - \alpha_g) \rho_l,$$

$$\text{div}(\rho \mathbf{u} \otimes \mathbf{u}) = \text{div}(\boldsymbol{\tau}) + \rho \mathbf{g} + \mathbf{F}, \quad (1.34)$$

$$\operatorname{div}(\rho \mathbf{u}) = 0, \quad (1.35)$$

$$\frac{\partial \alpha_g}{\partial t} + \operatorname{div} \left( \alpha_g \left( \mathbf{u} - \frac{d^2 \rho_l}{18 \mu r \rho} (\nabla p - \rho_g \mathbf{g}) \right) - K \nabla \alpha_g \right) = \dot{\alpha}_{source}, \quad (1.51)$$

with appropriate boundary conditions for the unknowns  $\mathbf{u}$ ,  $p$  and  $\alpha_g$ .

### 1.7.2 Connection with the velocity of a single bubble of gas in a fluid

Consider the situation of a single bubble of gas in a fluid. The velocity of the fluid  $\mathbf{u}$  satisfies equations of momentum and mass (1.34)-(1.35) for a constant density  $\rho = \rho_l$ . The motion of this bubble is described by two forces: the Archimedes force  $\mathbf{F}_A$  lifting up the bubble in the direction oppose to gravity  $\mathbf{g}$  and the drag force  $\mathbf{F}_D$  exerted on the bubble by the surrounding fluid, putting the bubble in movement in the same direction as the fluid.

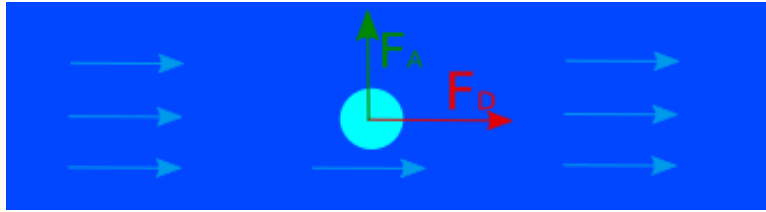


Figure 1.2 – A bubble suddenly produced in a fluid in motion from left to right : the two dominant forces are  $\mathbf{F}_A$  and  $\mathbf{F}_D$ .

The Archimedes force is defined by:

$$\mathbf{F}_A = -\frac{4}{3}\pi\left(\frac{d}{2}\right)^3(\rho_l - \rho_g)\mathbf{g}, \quad (1.52)$$

where  $d$  is the diameter of the bubble. Obviously, if the density  $\rho_g$  is equal to  $\rho_l$ , the resulting force is zero. For a spherical bubble in a non turbulent regime at low velocity, the drag force exerted on the bubble by the fluid is known as the Stokes drag law [Sto51; GM11]:

$$\mathbf{F}_D = 6\pi\mu(d/2)(\mathbf{u} - \mathbf{u}_g). \quad (1.53)$$

Taking into account these different forces, a simple model consists in looking at the equilibrium of the forces exerted on the bubble: The Archimedes force will put into motion the bubble with an ascending velocity, up to a limit vertical velocity given when the Archimedes force is in balance with the Drag force (and gravity force) opposing this ascending movement.

When the forces balance each other:

$$\mathbf{F}_D + \mathbf{F}_A = \mathbf{0}, \quad (1.54)$$

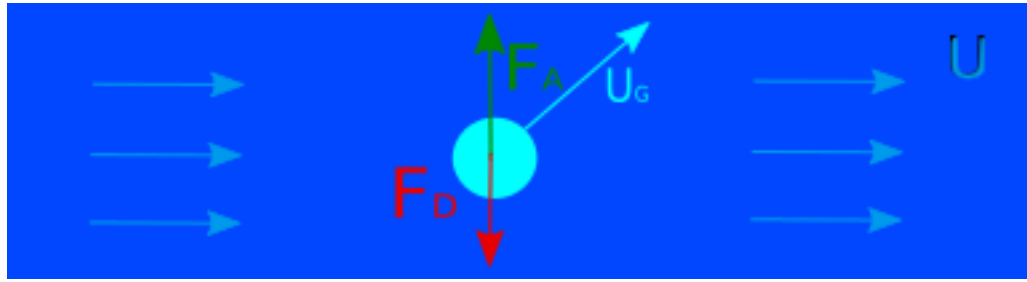


Figure 1.3 – When the forces are balanced, the resulting limit velocity corresponds to the velocity of the fluid with an additional vertical component.

which simplifies and gives the limit velocity of the bubble:

$$\mathbf{u}_g = \mathbf{u} - \frac{d^2}{18\mu}(\rho_l - \rho_g)\mathbf{g}. \quad (1.55)$$

This relation is very similar to (1.50), up to factors  $\alpha_l$ ,  $r$  and instead of the force  $\rho_l \mathbf{g}$ , the gradient of the pressure  $\nabla p$  is used in (1.50).

**Remark 6.** One major drawback of both equations (1.50) and (1.55) is that they can not take into account well boundary conditions of the problem<sup>2</sup>, however they can be computed very easily and taken as a reference order of magnitude of the expected solutions in a wide range of applications.

### 1.7.3 Boussinesq approximation of Navier-Stokes equation

Consider equations (1.34) and (1.35) for the unknowns  $\mathbf{u}$  and  $p$ . As the density  $\rho$  is

$$\rho = (1 - \alpha_g)\rho_l + \alpha_g\rho_g,$$

if  $\alpha_g \ll 1$ , the density is the constant  $\rho_l$  with a small perturbation. Then the first order development in  $\rho$  of these equations is the Boussinesq approximation [Bou77], i.e solve the following system for the unknowns  $\mathbf{u}$  and  $p$ :

$$(\rho_l \mathbf{u} \cdot \nabla) \mathbf{u} - \operatorname{div}(2\mu\epsilon(\mathbf{u})) + \nabla p = \mathbf{F} + \rho \mathbf{g}, \quad (1.56)$$

$$\operatorname{div}(\mathbf{u}) = 0. \quad (1.57)$$

The Boussinesq approximation can be useful in practice: for a quick implementation and fast results, in some cases it is enough to take into account the variations of the density  $\rho$  only in the gravity force. Another advantage for fast implementation is that combining the Boussinesq approximation with the relation (1.55) to eliminate  $\mathbf{u}_g$  results into the following simplified

<sup>2</sup>For example, if an obstacle blocks the ascending direction of the bubbles.

system:

$$\rho = \alpha_g \rho_g + (1 - \alpha_g) \rho_l,$$

$$\frac{\partial \alpha_g}{\partial t} + \operatorname{div} \left( \alpha_g \left( \mathbf{u} - \frac{d^2}{18\mu} (\rho_l \mathbf{g} - \rho_g \mathbf{g}) \right) - K \nabla \alpha_g \right) = \dot{\alpha}_{source}, \quad (1.51)$$

$$\operatorname{div}(\rho_l \mathbf{u} \otimes \mathbf{u}) = \operatorname{div}(\boldsymbol{\tau}) + \rho \mathbf{g} + \mathbf{F}, \quad (1.56)$$

$$\operatorname{div}(\mathbf{u}) = 0, \quad (1.57)$$

Notice that in (1.56-1.51),  $\mathbf{u}$  as well as  $\mathbf{u}_g = \mathbf{u} - \frac{d^2}{18\mu} (\rho_l \mathbf{g} - \rho_g \mathbf{g})$  are divergence-free, which is easier to treat and implement especially for the equation of advection-diffusion (1.51). In the applications, numerical schemes conserving in particular the mass and other properties with such velocity fields have been designed for example for the transport of the alumina in the aluminium [Hil19; Hof11].

## 1.8 Weak formulation of the stationary system

In the following, the weak formulation for each equation of the stationary model is presented, including the relevant boundary conditions. The regularity in space of the unknowns  $\mathbf{u}, p, \mathbf{u}_g, \alpha_g$  will not be mentioned except in chapter 2 when some theoretical results of existence are established.

### 1.8.1 Weak form of Navier-Stokes equations

First notice that using  $\operatorname{div}(\rho \mathbf{u}) = 0$ , one gets:

$$\operatorname{div}(\rho \mathbf{u} \otimes \mathbf{u}) = (\rho \mathbf{u} \cdot \nabla) \mathbf{u} + \operatorname{div}(\rho \mathbf{u}) \mathbf{u} = (\rho \mathbf{u} \cdot \nabla) \mathbf{u}. \quad (1.58)$$

Consider now for  $\mathbf{u}$  the space satisfying (1.24):

$$\mathbf{V} = \{ \mathbf{v} : (x_1, x_2, x_3) \in \Omega \rightarrow \mathbf{v}(x_1, x_2, x_3) \in \mathbb{R}^3 : \mathbf{v} = \mathbf{0} \text{ on } \Gamma_0 \}, \quad (1.59)$$

where  $\partial\Omega = \Gamma_{out} \cup \Gamma_0$ , and  $\Gamma_{out}$  is the outflow part of the boundary where the gas escapes out of the domain. Consider a regular vector function  $\mathbf{v} \in \mathbf{V}$ , we multiply (1.34) by  $\mathbf{v}$ , and integrating over  $\Omega$ , one gets, using (1.58):

$$\int_{\Omega} (\rho \mathbf{u} \cdot \nabla) \mathbf{u} \cdot \mathbf{v} dx - \int_{\Omega} \operatorname{div}(\boldsymbol{\tau}) \cdot \mathbf{v} dx = \int_{\Omega} (\mathbf{F} + \rho \mathbf{g}) \cdot \mathbf{v} dx. \quad (1.60)$$

## 1.8. Weak formulation of the stationary system

Then, integrating by part the expression with the stress tensor yields, as  $\boldsymbol{\tau}$  is symmetric:

$$\int_{\Omega} \operatorname{div}(\boldsymbol{\tau}) \cdot \mathbf{v} dx = \int_{\Omega} \sum_{i=1}^3 \sum_{j=1}^3 \frac{\partial}{\partial x_j} (\tau_{ij}) v_i dx = - \int_{\Omega} \sum_{i=1}^3 \sum_{j=1}^3 \tau_{ij} \frac{\partial v_i}{\partial x_j} dx + \int_{\partial\Omega} \sum_{i=1}^3 \sum_{j=1}^3 \tau_{ij} v_i \mathbf{n}_j ds.$$

So:

$$\int_{\Omega} \operatorname{div}(\boldsymbol{\tau}) \cdot \mathbf{v} dx = - \int_{\Omega} \boldsymbol{\tau} : \boldsymbol{\epsilon}(\mathbf{v}) dx + \int_{\partial\Omega} (\boldsymbol{\tau} \cdot \mathbf{n}) \cdot \mathbf{v} ds. \quad (1.61)$$

Explicitly, the first term in (1.61) corresponds to:

$$\int_{\Omega} \boldsymbol{\tau} : \boldsymbol{\epsilon}(\mathbf{v}) dx = 2 \int_{\Omega} \mu \boldsymbol{\epsilon}(\mathbf{u}) : \boldsymbol{\epsilon}(\mathbf{v}) dx - 2/3 \int_{\Omega} \mu \operatorname{div}(\mathbf{u}) \operatorname{div}(\mathbf{v}) dx - \int_{\Omega} p \operatorname{div}(\mathbf{v}) dx. \quad (1.62)$$

Notice the tensor product  $\boldsymbol{\epsilon}(\mathbf{u}) : \boldsymbol{\epsilon}(\mathbf{v})$  is given by

$$\boldsymbol{\epsilon}(\mathbf{u}) : \boldsymbol{\epsilon}(\mathbf{v}) = \sum_{i,j=1}^d \boldsymbol{\epsilon}(\mathbf{u})_{i,j} \boldsymbol{\epsilon}(\mathbf{v})_{i,j}, \quad (1.63)$$

and  $|\boldsymbol{\epsilon}(\mathbf{u})| = (\boldsymbol{\epsilon}(\mathbf{u}) : \boldsymbol{\epsilon}(\mathbf{u}))^{1/2}$ . The same notation is adopted for  $\boldsymbol{\tau} : \boldsymbol{\epsilon}(\mathbf{v})$ ,  $\nabla \mathbf{u} : \nabla \mathbf{v}$ . Furthermore, notice that the second term in (1.61) can be decomposed in the Cartesian system defined by  $(\mathbf{n}, \mathbf{t}_1, \mathbf{t}_2)$ , which together with the boundary conditions (1.24-1.26) and (1.59) give:

$$\begin{aligned} \int_{\partial\Omega} (\boldsymbol{\tau} \cdot \mathbf{n}) \cdot \mathbf{v} ds &= \int_{\partial\Omega} (\boldsymbol{\tau} \cdot \mathbf{n}) \cdot \mathbf{n} (\mathbf{v} \cdot \mathbf{n}) ds + \int_{\partial\Omega} (\boldsymbol{\tau} \cdot \mathbf{n}) \cdot \mathbf{t}_1 (\mathbf{v} \cdot \mathbf{t}_1) ds \\ &+ \int_{\partial\Omega} (\boldsymbol{\tau} \cdot \mathbf{n}) \cdot \mathbf{t}_2 (\mathbf{v} \cdot \mathbf{t}_2) ds = \int_{\Gamma_{out}} (\boldsymbol{\tau} \cdot \mathbf{n}) \cdot \mathbf{n} (\mathbf{v} \cdot \mathbf{n}) ds. \end{aligned} \quad (1.64)$$

Let us define  $\xi = (\boldsymbol{\tau} \cdot \mathbf{n}) \cdot \mathbf{n}$ ,  $\xi \in S$  with:

$$S = \{s : (x_1, x_2, x_3) \in \partial\Omega \rightarrow s(x_1, x_2, x_3) \in \mathbb{R} : s = 0 \text{ on } \Gamma_0\}, \quad (1.65)$$

then multiply the condition (1.25) by a function  $\sigma \in S$  and integrating over  $\partial\Omega$  results into:

$$\int_{\Gamma_{out}} \sigma (\mathbf{u} \cdot \mathbf{n}) ds = 0, \quad (1.66)$$

also let the space with zero average function be:

$$L = \left\{ f : (x_1, x_2, x_3) \in \Omega \rightarrow f(x_1, x_2, x_3) \in \mathbb{R} : \int_{\Omega} f dx = 0 \right\}, \quad (1.67)$$

and multiply (1.35) with a function  $q \in L$  to obtain:

$$\int_{\Omega} \operatorname{div}(\rho \mathbf{u}) q dx = 0. \quad (1.68)$$

## Chapter 1. A mixture model for a dilute dispersion of gas in a liquid

---

Finally a weak formulation of equations (1.34-1.35) with boundary conditions (1.24-1.27) consists into looking for  $(\mathbf{u}, p, \xi) \in \mathbf{V} \times L \times S$  such that:

$$\begin{aligned} & \int_{\Omega} (\rho \mathbf{u} \cdot \nabla) \mathbf{u} \cdot \mathbf{v} dx + \int_{\Omega} 2\mu \left( \epsilon(\mathbf{u}) : \epsilon(\mathbf{v}) - \frac{1}{3} \operatorname{div}(\mathbf{u}) \operatorname{div}(\mathbf{v}) \right) dx \\ & - \int_{\Omega} p \operatorname{div}(\mathbf{v}) dx - \int_{\Gamma_{out}} \xi (\mathbf{v} \cdot \mathbf{n}) ds = \int_{\Omega} (\mathbf{F} + \rho \mathbf{g}) \cdot \mathbf{v} dx, \\ & \int_{\Omega} \operatorname{div}(\rho \mathbf{u}) q dx = 0, \\ & \int_{\Gamma_{out}} \sigma (\mathbf{u} \cdot \mathbf{n}) ds = 0, \end{aligned} \quad (1.69)$$

for all  $(\mathbf{v}, q, \sigma) \in \mathbf{V} \times L \times S$ . Notice that the variable  $\xi$  is the normal part of the viscous forces through the boundary  $\Gamma_{out}$ , and acts as a Lagrange multiplier to ensure the condition  $(\mathbf{u} \cdot \mathbf{n})$  on  $\Gamma_{out}$ .

### 1.8.2 Weak form of the gas momentum equation

For  $\rho_g > 0$  a constant and  $\alpha_g$  a regular function, with  $\mathbf{u}_g \in \mathbf{V}$ , one gets:

$$\operatorname{div}(\rho_g \alpha_g \mathbf{u}_g \otimes \mathbf{u}_g) = (\rho_g \alpha_g \mathbf{u}_g \cdot \nabla) \mathbf{u}_g + \operatorname{div}(\rho_g \alpha_g \mathbf{u}_g) \mathbf{u}_g. \quad (1.70)$$

To treat the term  $\operatorname{div}(\rho_g \alpha_g \mathbf{u}_g) \mathbf{u}_g$ , we choose to consider the stationary form of equation (1.33) neglecting the diffusive term, thus  $\partial \alpha_g / \partial t = 0$  and  $K = 0$  in (1.33) gives:

$$\operatorname{div}(\alpha_g \mathbf{u}_g) = \dot{\alpha}_{source} \quad (1.71)$$

Then injecting (1.71) in (1.70) reads:

$$\operatorname{div}(\rho_g \alpha_g \mathbf{u}_g \otimes \mathbf{u}_g) = (\rho_g \alpha_g \mathbf{u}_g \cdot \nabla) \mathbf{u}_g + \operatorname{div}(\rho_g \alpha_g \mathbf{u}_g) \mathbf{u}_g = (\rho_g \alpha_g \mathbf{u}_g \cdot \nabla) \mathbf{u}_g + (\rho_g \dot{\alpha}_{source}) \mathbf{u}_g. \quad (1.72)$$

Furthermore, the equality (1.61) for  $\boldsymbol{\tau}$  holds as well for  $\boldsymbol{\tau}_g$ . As in (1.64), the border integral of the gas viscous tensor can be split in the  $(\mathbf{n}, \mathbf{t}_1, \mathbf{t}_2)$  coordinate system, and using boundary conditions (1.28-1.29) with  $\xi = (\boldsymbol{\tau} \cdot \mathbf{n}) \cdot \mathbf{n} \in S$ , it holds:

$$\begin{aligned} & \int_{\partial\Omega} (\boldsymbol{\tau}_g \cdot \mathbf{n}) \cdot \mathbf{v} ds = \int_{\partial\Omega} (\boldsymbol{\tau}_g \cdot \mathbf{n}) \cdot \mathbf{n} (\mathbf{v} \cdot \mathbf{n}) ds + \int_{\partial\Omega} (\boldsymbol{\tau}_g \cdot \mathbf{n}) \cdot \mathbf{t}_1 (\mathbf{v} \cdot \mathbf{t}_1) ds \\ & + \int_{\partial\Omega} (\boldsymbol{\tau}_g \cdot \mathbf{n}) \cdot \mathbf{t}_2 (\mathbf{v} \cdot \mathbf{t}_2) ds = \int_{\Gamma_{out}} (\boldsymbol{\tau}_g \cdot \mathbf{n}) \cdot \mathbf{n} (\mathbf{v} \cdot \mathbf{n}) ds = \int_{\Gamma_{out}} \alpha_g p_0 (\mathbf{v} \cdot \mathbf{n}) ds. \end{aligned} \quad (1.73)$$

Of course,  $p_0$  is the average of  $\xi$  on  $\Gamma_{out}$ :

$$p_0 = \frac{\int_{\Gamma_{out}} (\boldsymbol{\tau} \cdot \mathbf{n}) \cdot \mathbf{n} ds}{\int_{\Gamma_{out}} ds} = \frac{\int_{\Gamma_{out}} \xi ds}{\int_{\Gamma_{out}} ds},$$

## 1.9. Algorithm to solve the stationary problem

Then multiplying the gas momentum equation (1.32) by a regular function  $\mathbf{v}_g \in \mathbf{V}$ , and using (1.70)(1.73), an equivalent formulation of equation (1.32) with boundary conditions (1.28-1.29) consists into looking for  $\mathbf{u}_g \in \mathbf{V}$  such that:

$$\begin{aligned} & \int_{\Omega} (\rho_g \alpha_g \mathbf{u}_g \cdot \nabla) \mathbf{u}_g \cdot \mathbf{v}_g dx + \int_{\Omega} (\rho_g \dot{\alpha}_{source}) \mathbf{u}_g \cdot \mathbf{v}_g dx - \int_{\Gamma_{out}} \alpha_g p_0 (\mathbf{v}_g \cdot \mathbf{n}) ds \\ & + \int_{\Omega} 2\mu_g \left( \epsilon(\mathbf{u}_g) : \epsilon(\mathbf{v}_g) - \frac{1}{3} \operatorname{div}(\mathbf{u}_g) \operatorname{div}(\mathbf{v}_g) \right) dx + \int_{\Omega} D \frac{\rho}{\rho_l} \alpha_g \mathbf{u}_g \cdot \mathbf{v}_g dx = \int_{\Omega} \alpha_g p \operatorname{div}(\mathbf{v}_g) dx \\ & + \int_{\Omega} p \nabla \alpha_g \cdot \mathbf{v}_g dx + \int_{\Omega} \alpha_g \rho_g \mathbf{g} \cdot \mathbf{v}_g dx + \int_{\Omega} D \frac{\rho}{\rho_l} \alpha_g \mathbf{u} \cdot \mathbf{v}_g dx, \end{aligned} \quad (1.74)$$

for all  $\mathbf{v}_g \in \mathbf{V}$ .

### 1.8.3 Weak form of the gas mass equation

Finally, we need to treat a weak form for the equation of mass conservation of the gas (1.33). In particular, Multiplying equation (1.33) by any regular function  $\omega : (x_1, x_2, x_3) \rightarrow \omega(x_1, x_2, x_3) \in \mathbb{R}$  results in:

$$\int_{\Omega} \frac{\partial \alpha_g}{\partial t} \omega dx + \int_{\Omega} \operatorname{div}(\alpha_g \mathbf{u}_g) \omega dx - \int_{\Omega} \operatorname{div}(K \nabla \alpha_g) \omega dx = \int_{\Omega} \dot{\alpha}_{source} \omega dx. \quad (1.75)$$

Integrating by part yields:

$$- \int_{\Omega} \operatorname{div}(K \nabla \alpha_g) \omega dx = \int_{\Omega} K \nabla \alpha_g \nabla \omega dx - \int_{\partial \Omega} K \nabla \alpha_g \cdot \mathbf{n} \omega ds. \quad (1.76)$$

Using (1.76) and boundary condition (1.21) that allows to get rid of the boundary term leads to the following weak formulation of (1.33) with boundary condition (1.21). We are looking for  $\alpha_g : (x_1, x_2, x_3) \rightarrow \alpha_g(x_1, x_2, x_3) \in \mathbb{R}$  satisfying:

$$\int_{\Omega} \frac{\partial \alpha_g}{\partial t} \omega dx + \int_{\Omega} \operatorname{div}(\alpha_g \mathbf{u}_g) \omega dx + \int_{\Omega} K \nabla \alpha_g \nabla \omega dx = \int_{\Omega} \dot{\alpha}_{source} \omega dx, \quad (1.77)$$

for all  $\omega : (x_1, x_2, x_3) \rightarrow \omega(x_1, x_2, x_3) \in \mathbb{R}$ . Notice that choosing  $\omega = 1$  together with the stationary condition  $\partial \alpha_g / \partial t = 0$  leads to the balance of mass (1.23).

## 1.9 Algorithm to solve the stationary problem

An iterative algorithm is required to solve the whole system of equations regrouping the weak formulations of the Navier-Stokes system (1.69), the gas momentum system (1.74) and the gas mass equation (1.77). Let  $n$  denotes  $n$ -th iteration of the algorithm and assume that  $\{\mathbf{u}_g\}_n, \{\alpha_g\}_n, \{p\}_n, \{\xi\}_n$  and  $\{\mathbf{u}\}_n$  are known.

The following algorithm gives the step to obtain the unknowns at stage  $n + 1$ , so to compute

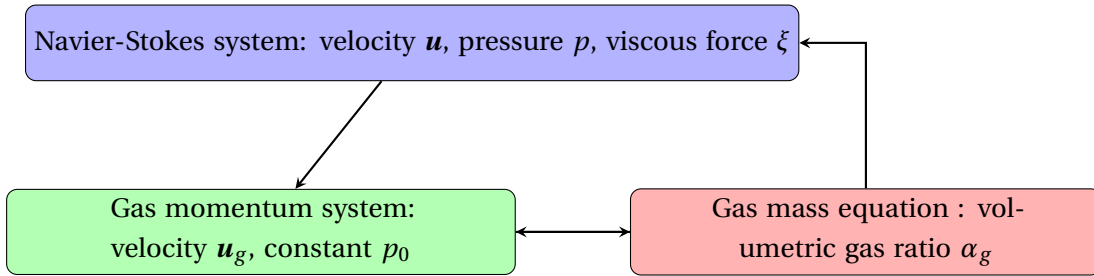
## Chapter 1. A mixture model for a dilute dispersion of gas in a liquid

$\{\mathbf{u}_g\}_{n+1}, \{\alpha_g\}_{n+1}, \{p\}_{n+1}, \{\xi\}_{n+1}$  and  $\{\mathbf{u}\}_{n+1}$ :

1. Using (1.8) compute  $\rho = \{\alpha_g\}_n \rho_h + (1 - \{\alpha_g\}_n) \rho_l$  as input and solve Navier-Stokes equations (1.69) in order to obtain  $\{\mathbf{u}\}_{n+1}, \{p\}_{n+1}, \{\xi\}_{n+1}$ .
2. Let  $N_g$  be another positive integer and  $\Delta t$  a positive time-step. Then perform a sub-sequences algorithm: that is consider the sub-sequences  $\{\alpha_g\}_{n,k}$  and  $\{\mathbf{u}_g\}_{n,k}$ , where  $k = 0, \dots, N_g$  denotes the iteration number of the sub-sequences. The following steps are performed  $N_g$  times allowing to pass from the sub-sequences  $\{\alpha_g\}_{n,k}$  and  $\{\mathbf{u}_g\}_{n,k}$  to the next sub-sequences  $\{\alpha_g\}_{n,k+1}$  and  $\{\mathbf{u}_g\}_{n,k+1}$ :
  - (a) Take  $\{\mathbf{u}\}_{n+1}, \{p\}_{n+1}, \{\xi\}_{n+1}$  and  $\{\alpha_g\}_{n,k}$  as input in system (1.74) and solve it in order to get  $\{\mathbf{u}_g\}_{n,k+1}$ .
  - (b) Use  $\{\mathbf{u}_g\}_{n,k+1}$  as input and solve (1.77) with a time discretization scheme to obtain  $\{\alpha_g\}_{n,k+1}$ , with time-step  $\Delta t$ . This time discretization should be seen as a continuation method to reach a stationary solution. For simplicity the implicit Euler scheme can be considered, i.e find  $\{\alpha_g\}_{n,k+1} \in A$  such that for all  $\omega \in A$ , we have:

$$\int_{\Omega} \frac{\{\alpha_g\}_{n,k+1} - \{\alpha_g\}_{n,k}}{\Delta t} \omega dx + \int_{\Omega} \operatorname{div}(\{\alpha_g\}_{n,k+1} \{\mathbf{u}_g\}_{n,k+1}) \omega dx + \int_{\Omega} K \nabla \{\alpha_g\}_{n,k+1} \nabla \omega dx = \int_{\Omega} \dot{\alpha}_{source} \omega dx$$

3. Then the values of the sub-sequences at number  $k = N_g$  are taken to update the sequences of the main algorithm:  $\{\mathbf{u}_g\}_{n,N_g} \rightarrow \{\mathbf{u}_g\}_{n+1}$ , and  $\{\alpha_g\}_{n,N_g} \rightarrow \{\alpha_g\}_{n+1}$ .



Repetitions of steps 1. to 3. are performed up to a fixed number of iteration  $N$  or up to a stop criteria. At this stage, one can assess at which point the solution is stationary by checking if the following ratio is close to 1:

$$r = \frac{\int_{\Gamma_{out}} \alpha_g \mathbf{u}_g \cdot \mathbf{n} ds}{\int_{\Omega} \dot{\alpha}_{source} dx},$$

that is the production of gas in the domain  $\Omega$  corresponds to the outflow escaping out through the boundary  $\Gamma_{out}$ .

## 1.10 Linearisation of the equations

In the applications of algorithm (1.9), three important non-linearities have to be addressed:

1. The effective viscosity  $\mu$  in Navier-Stokes problem (1.69) is composed of two terms, the constant laminar viscosity  $\mu_L$  and the turbulent viscosity  $\mu_T$  which takes into account the average diffusion due to the turbulence:

$$\mu = \mu_L + \mu_T. \quad (1.78)$$

The turbulent viscosity  $\mu_T$  follows a Smagorinski-kind model [Pop01] described in [Roc16], and can be written:

$$\mu_T = C_T \rho |\epsilon(\mathbf{u})|, \quad (1.79)$$

with  $C_T$  a constant turbulent parameter<sup>3</sup>. The shear rate tensor  $\epsilon(\mathbf{u})$  is defined in (1.1) and  $|\epsilon(\mathbf{u})| = \sqrt{\sum_{i,j} (\epsilon_{i,j}(\mathbf{u}))^2}$ . Thus the term  $2\mu(\epsilon(\mathbf{u}) : \epsilon(\mathbf{v}) - \frac{1}{3} \text{div}(\mathbf{u}) \text{div}(\mathbf{v}))$  in (1.69) is non-linear with respect to  $\mathbf{u}$ .

The viscosity used in the drag coefficient  $D$  in (1.41) will not include the turbulent viscosity, only the laminar viscosity  $\mu_L$ .

2. The standard convective term  $(\rho \mathbf{u} \cdot \nabla) \mathbf{u}$  is a second non linearity in the Navier-Stokes equation with respect to  $\mathbf{u}$ , as well as the term  $(\alpha_g \rho_g \mathbf{u}_g \cdot \nabla) \mathbf{u}_g$  in the gas momentum equation (1.74).
3. If the general drag force (1.47) is used for the drag coefficient in the gas momentum equation (1.74), the weak formulation for  $\mathbf{u}_g$  is non-linear.

In the following the Newton method to solve these non-linearities is detailed.

**Remark 7.** When considering the complete model, the non-linear interactions between the different equations (1.69)-(1.74)- (1.77) are such that it is not useful to solve very accurately the non-linearities specific to each of the different equations. (a low number of Newton iteration for one of these equations is enough as it is useless to spend computational power when the solution is far away). However, the Newton method will be useful when getting closer to the stationary solution.

Taking into account the two first non-linearities, let us consider the weak form (1.69) of Navier-Stokes equation. In the following, assume  $\mathbf{V}$  to be the space for the velocity  $\mathbf{u}$  or  $\mathbf{u}_g$ ,  $L$  the space for the pressure  $p$  and  $S$  the space for  $\xi$ , as in section 1.8. The linearisation of the weak form of the equations in section 1.8 can be computed with a formal calculation. With  $\rho$  given as fixed input, the following operator  $\mathcal{F} : [\mathbf{V} \times L \times S] \rightarrow [\mathbf{V} \times L \times S]'$ , where  $[\mathbf{V} \times L \times S]'$  denotes

<sup>3</sup>In the literature, the dimension of  $C_T$  is the unit of a distance squared  $l^2$ . The length is chosen as a characteristic length of the problem, or in some cases, the mesh size  $h$ . In this thesis it is regrouped as one unique constant.

the dual of  $[V \times L \times S]$ :

$$\begin{aligned}
 \langle \mathcal{F}(\mathbf{u}, p, \xi), (\mathbf{v}, q, \sigma) \rangle = & \int_{\Omega} 2(\mu_L + C_T \rho |\epsilon(\mathbf{u})|) \left( \epsilon(\mathbf{u}) : \epsilon(\mathbf{v}) - \frac{1}{3} \operatorname{div}(\mathbf{u}) \operatorname{div}(\mathbf{v}) \right) dx \\
 & + \int_{\Omega} (\rho \mathbf{u} \cdot \nabla) \mathbf{u} \cdot \mathbf{v} dx - \int_{\Omega} p \operatorname{div}(\mathbf{v}) dx - \int_{\Gamma_{out}} \xi (\mathbf{v} \cdot \mathbf{n}) ds \\
 & - \int_{\Omega} (\mathbf{F} + \rho \mathbf{g}) \cdot \mathbf{v} dx + \int_{\Omega} \operatorname{div}(\rho \mathbf{u}) q dx + \int_{\Gamma_{out}} \sigma (\mathbf{u} \cdot \mathbf{n}) ds.
 \end{aligned} \tag{1.80}$$

The Gateaux derivative of  $\mathcal{F}$  in  $(\mathbf{u}, p, \xi)$  in the direction  $(\mathbf{w}, r, s)$  exists for all  $(\mathbf{v}, q, \sigma) \in V \times L \times S$  and is:

$$\begin{aligned}
 \langle D\mathcal{F}(\mathbf{u}, p, \xi)(\mathbf{w}, r, t); (\mathbf{v}, q, \sigma) \rangle = & \int_{\Omega} 2(\mu_L + C_T \rho |\epsilon(\mathbf{u})|) \left( \epsilon(\mathbf{w}) : \epsilon(\mathbf{v}) - \frac{1}{3} \operatorname{div}(\mathbf{w}) \operatorname{div}(\mathbf{v}) \right) dx \\
 & + \int_{\Omega} 2(C_T \rho) \frac{\epsilon(\mathbf{w}) : \epsilon(\mathbf{u})}{|\epsilon(\mathbf{u})|} \left( \epsilon(\mathbf{u}) : \epsilon(\mathbf{v}) - \frac{1}{3} \operatorname{div}(\mathbf{u}) \operatorname{div}(\mathbf{v}) \right) dx \\
 & + \int_{\Omega} (\rho \mathbf{w} \cdot \nabla) \mathbf{u} \cdot \mathbf{v} dx + \int_{\Omega} (\rho \mathbf{u} \cdot \nabla) \mathbf{w} \cdot \mathbf{v} dx - \int_{\Omega} r \operatorname{div}(\mathbf{v}) dx \\
 & - \int_{\Gamma_{out}} t (\mathbf{v} \cdot \mathbf{n}) ds + \int_{\Omega} \operatorname{div}(\rho \mathbf{w}) q dx + \int_{\Gamma_{out}} \sigma (\mathbf{w} \cdot \mathbf{n}) ds.
 \end{aligned} \tag{1.81}$$

The relation (1.81) holds directly for the linear terms. For the term  $(\rho \mathbf{u} \cdot \nabla) \mathbf{u}$ , it is clear that for  $K : V \rightarrow V'$  with  $\langle K(\mathbf{u}), \mathbf{v} \rangle = \int_{\Omega} (\rho \mathbf{u} \cdot \nabla) \mathbf{u} \cdot \mathbf{v} dx$ , it directly follows:

$$\lim_{t \rightarrow 0} \frac{K(\mathbf{u} + t\mathbf{w}) - K(\mathbf{u})}{t} = \int_{\Omega} (\rho \mathbf{w} \cdot \nabla) \mathbf{u} \cdot \mathbf{v} dx + \int_{\Omega} (\rho \mathbf{u} \cdot \nabla) \mathbf{w} \cdot \mathbf{v} dx. \tag{1.82}$$

Only the viscous terms are left, and if  $V : V \rightarrow V'$  defined with

$\langle V(\mathbf{u}), \mathbf{v} \rangle = \int_{\Omega} 2(C_T \rho |\epsilon(\mathbf{u})|) \left( \epsilon(\mathbf{u}) : \epsilon(\mathbf{v}) - \frac{1}{3} \operatorname{div}(\mathbf{u}) \operatorname{div}(\mathbf{v}) \right) dx$ , the derivative can be written:

$$\begin{aligned}
 \lim_{t \rightarrow 0} \frac{V(\mathbf{u} + t\mathbf{w}) - V(\mathbf{u})}{t} = & \int_{\Omega} 2(C_T \rho |\epsilon(\mathbf{u})|) \left( \epsilon(\mathbf{w}) : \epsilon(\mathbf{v}) - \frac{1}{3} \operatorname{div}(\mathbf{w}) \operatorname{div}(\mathbf{v}) \right) dx \\
 & + \int_{\Omega} 2C_T \rho \left( \lim_{t \rightarrow 0} \frac{|\epsilon(\mathbf{u} + t\mathbf{w})| - |\epsilon(\mathbf{u})|}{t} \right) \left( \epsilon(\mathbf{u}) : \epsilon(\mathbf{v}) - \frac{1}{3} \operatorname{div}(\mathbf{u}) \operatorname{div}(\mathbf{v}) \right) dx.
 \end{aligned} \tag{1.83}$$

Finally, the following holds:

$$\lim_{t \rightarrow 0} \frac{|\epsilon(\mathbf{u} + t\mathbf{w})| - |\epsilon(\mathbf{u})|}{t} = \lim_{t \rightarrow 0} \frac{|\epsilon(\mathbf{u} + t\mathbf{w})|^2 - |\epsilon(\mathbf{u})|^2}{t(|\epsilon(\mathbf{u} + t\mathbf{w})| + |\epsilon(\mathbf{u})|)} = \frac{\epsilon(\mathbf{w}) : \epsilon(\mathbf{u})}{|\epsilon(\mathbf{u})|}. \tag{1.84}$$

This concludes the proof of (1.81).

**Remark 8.** This development is taken from [Roc16](pages 36-37) addressing the incompressible Navier-Stokes equation case for different turbulent models, though there was a mistake of a factor 2 in the original document (and in the numerical method), corrected here.

Second, consider the gas velocity formulation (1.74) with a non linear Drag term (1.47). Thus, define the operator  $\mathcal{G}_\theta : \mathbf{V} \rightarrow \mathbf{V}'$  defined, for given and fixed  $\alpha_g, p, \mathbf{u}, \xi, \mu_g, \mu_L$  and parameter  $\theta \in \{0, 1\}$  as inputs<sup>4</sup>, and the drag coefficient given by (1.47):

$$\begin{aligned}
 \langle \mathcal{G}_\theta(\mathbf{u}_g), \mathbf{v} \rangle = & \int_{\Omega} (\rho_g \alpha_g \mathbf{u}_g \cdot \nabla) \mathbf{u}_g \cdot \mathbf{v} dx + \int_{\Omega} (\rho_g \dot{\alpha}_{source}) \mathbf{u}_g \cdot \mathbf{v} dx - \int_{\Gamma_{out}} \alpha_g p_0 (\mathbf{v} \cdot \mathbf{n}) ds \\
 & + \int_{\Omega} 2\mu_g \left( \epsilon(\mathbf{u}_g) : \epsilon(\mathbf{v}) - \frac{1}{3} \operatorname{div}(\mathbf{u}_g) \operatorname{div}(\mathbf{v}) \right) dx - \int_{\Omega} p \nabla \alpha_g \cdot \mathbf{v} dx - \int_{\Omega} \alpha_g p \operatorname{div}(\mathbf{v}) dx \\
 & - \int_{\Omega} \alpha_g \rho_g \mathbf{g} \cdot \mathbf{v} dx + \theta \int_{\Omega} [1 + 0.15 Re_b^{0.687}] \frac{18\mu_L r}{d^2} \frac{\rho}{\rho_l} \alpha_g (\mathbf{u}_g - \mathbf{u}) \cdot \mathbf{v} dx \\
 & + (1 - \theta) \int_{\Omega} \frac{0.44 Re_b}{24} \frac{18\mu_L r}{d^2} \frac{\rho}{\rho_l} \alpha_g (\mathbf{u}_g - \mathbf{u}) \cdot \mathbf{v} dx, \\
 Re_b(\mathbf{u}_g) = & \frac{\rho_l |\mathbf{u} - \mathbf{u}_g| d}{\mu_L}.
 \end{aligned} \tag{1.85}$$

Let us compute formally the Gateaux derivative of  $\mathcal{G}$  in  $(\mathbf{u}_g)$  in the direction  $(\mathbf{w})$  exists for all  $\mathbf{v} \in \mathbf{V}$ :

$$\begin{aligned}
 \langle D\mathcal{G}_\theta(\mathbf{u}_g)(\mathbf{w}), \mathbf{v} \rangle = & \int_{\Omega} (\rho_g \alpha_g \mathbf{w} \cdot \nabla) \mathbf{u}_g \cdot \mathbf{v} dx + \int_{\Omega} (\rho_g \alpha_g \mathbf{u}_g \cdot \nabla) \mathbf{w} \cdot \mathbf{v} dx + \int_{\Omega} (\rho_g \dot{\alpha}_{source}) \mathbf{w} \cdot \mathbf{v} dx \\
 & + \int_{\Omega} 2\mu_g \left( \epsilon(\mathbf{w}) : \epsilon(\mathbf{v}) - \frac{1}{3} \operatorname{div}(\mathbf{w}) \operatorname{div}(\mathbf{v}) \right) dx \\
 & + \theta \int_{\Omega} [1 + 0.15 Re_b^{0.687}] \frac{18\mu_L r}{d^2} \frac{\rho}{\rho_l} \alpha_g (\mathbf{w}) \cdot \mathbf{v} dx \\
 & + (1 - \theta) \int_{\Omega} \frac{0.44 Re_b}{24} \frac{18\mu_L r}{d^2} \frac{\rho}{\rho_l} \alpha_g (\mathbf{w}) \cdot \mathbf{v} dx, \\
 & + \theta \int_{\Omega} [0.150.687 Re_b^{0.687-1}] \frac{\mathbf{w} \cdot (\mathbf{u}_g - \mathbf{u})}{|\mathbf{u}_g - \mathbf{u}|} \frac{18r\rho}{d} \alpha_g (\mathbf{u}_g - \mathbf{u}) \cdot \mathbf{v} dx \\
 & + (1 - \theta) \int_{\Omega} \frac{0.44}{24} \frac{\mathbf{w} \cdot (\mathbf{u}_g - \mathbf{u})}{|\mathbf{u}_g - \mathbf{u}|} \frac{18r\rho}{d} \alpha_g (\mathbf{u}_g - \mathbf{u}) \cdot \mathbf{v} dx, \\
 Re_b(\mathbf{u}_g) = & \frac{\rho_l |\mathbf{u} - \mathbf{u}_g| d}{\mu_L}.
 \end{aligned} \tag{1.86}$$

The assumption (1.86) is directly verified for the linear and constant term with respect to  $\mathbf{u}_g$ . The derivative of  $(\rho_g \alpha_g \mathbf{u}_g \cdot \nabla) \mathbf{u}_g$  is directly obtained using (1.82) with  $\rho = \alpha_g \rho_g$  and  $\mathbf{u} = \mathbf{u}_g$ . The only terms left are the non linear drag force terms. First take the operator  $T_1 : \mathbf{V} \rightarrow \mathbf{V}'$  defined with:

$$\langle T_1(\mathbf{u}_g), \mathbf{v} \rangle = \int_{\Omega} [1 + 0.15 Re_b^{0.687}] \frac{18\mu_L r}{d^2} \frac{\rho}{\rho_l} \alpha_g (\mathbf{u}_g - \mathbf{u}) \cdot \mathbf{v} dx. \tag{1.87}$$

<sup>4</sup>The value of  $\theta$  will be 1 or 0 depending on the regime, given by the Reynolds number, in (1.47).

Then:

$$\begin{aligned} \lim_{t \rightarrow 0} \frac{T_1(\mathbf{u}_g + t\mathbf{w}) - T_1(\mathbf{u}_g)}{t} &= \int_{\Omega} [1 + 0.15 Re_b^{0.687}] \frac{18\mu_L r}{d^2} \frac{\rho}{\rho_l} \alpha_g(\mathbf{w}) \cdot \mathbf{v} dx \\ &+ \int_{\Omega} \left( \lim_{t \rightarrow 0} \left[ 0.15 \frac{Re_b(\mathbf{u}_g + t\mathbf{w})^{0.687} - Re_b(\mathbf{u}_g)^{0.687}}{t} \right] \right) \frac{18\mu_L r}{d^2} \frac{\rho}{\rho_l} \alpha_g(\mathbf{u}_g - \mathbf{u}) \cdot \mathbf{v} dx, \end{aligned} \quad (1.88)$$

and with the chain rule:

$$\lim_{t \rightarrow 0} \left[ 0.15 \frac{Re_b(\mathbf{u}_g + t\mathbf{w})^{0.687} - Re_b(\mathbf{u}_g)^{0.687}}{t} \right] = 0.15 \cdot 0.687 Re_b^{0.687-1} \lim_{t \rightarrow 0} \frac{Re_b(\mathbf{u}_g + t\mathbf{w}) - Re_b(\mathbf{u}_g)}{t}.$$

This last limit gives:

$$\begin{aligned} \lim_{t \rightarrow 0} \frac{Re_b(\mathbf{u}_g + t\mathbf{w}) - Re_b(\mathbf{u}_g)}{t} &= \lim_{t \rightarrow 0} \frac{\rho_l d}{\mu_L} \frac{|\mathbf{u}_g + t\mathbf{w} - \mathbf{u}| - |\mathbf{u}_g - \mathbf{u}|}{t} = \\ \lim_{t \rightarrow 0} \frac{\rho_l d}{\mu_L} \frac{|\mathbf{u}_g + t\mathbf{w} - \mathbf{u}|^2 - |\mathbf{u}_g - \mathbf{u}|^2}{t(|\mathbf{u}_g + t\mathbf{w} - \mathbf{u}| + |\mathbf{u}_g - \mathbf{u}|)} &= \frac{\rho_l d}{\mu_L} \frac{\mathbf{w} \cdot (\mathbf{u}_g - \mathbf{u})}{|\mathbf{u}_g - \mathbf{u}|}. \end{aligned} \quad (1.89)$$

Injecting this result in (1.88) gives the first term in the proposition. The second term can be treated with the definition of  $T_2 : \mathbf{V} \rightarrow \mathbf{V}'$ :

$$\langle T_2(\mathbf{u}_g), \mathbf{v} \rangle = \int_{\Omega} \frac{0.44 Re_b}{24} \frac{18\mu_L r}{d^2} \frac{\rho}{\rho_l} \alpha_g(\mathbf{u}_g - \mathbf{u}) \cdot \mathbf{v} dx. \quad (1.90)$$

The derivative of  $T_2$  writes:

$$\begin{aligned} \lim_{t \rightarrow 0} \frac{T_2(\mathbf{u}_g + t\mathbf{w}) - T_2(\mathbf{u}_g)}{t} &= \int_{\Omega} \frac{0.44 Re_b}{24} \frac{18\mu_L r}{d^2} \frac{\rho}{\rho_l} \alpha_g(\mathbf{w}) \cdot \mathbf{v} dx \\ &+ \int_{\Omega} \frac{0.44}{24} \left( \lim_{t \rightarrow 0} \frac{Re_b(\mathbf{u}_g + t\mathbf{w}) - Re_b(\mathbf{u}_g)}{t} \right) \frac{18\mu_L r}{d^2} \frac{\rho}{\rho_l} \alpha_g(\mathbf{u}_g - \mathbf{u}) \cdot \mathbf{v} dx = \\ &\int_{\Omega} \frac{0.44 Re_b}{24} \frac{18\mu_L r}{d^2} \frac{\rho}{\rho_l} \alpha_g(\mathbf{w}) \cdot \mathbf{v} dx \\ &+ \int_{\Omega} \frac{0.44}{24} \left( \frac{\rho_l d}{\mu_L} \frac{\mathbf{w} \cdot (\mathbf{u}_g - \mathbf{u})}{|\mathbf{u}_g - \mathbf{u}|} \right) \frac{18\mu_L r}{d^2} \frac{\rho}{\rho_l} \alpha_g(\mathbf{u}_g - \mathbf{u}) \cdot \mathbf{v} dx, \end{aligned} \quad (1.91)$$

where the limit (1.89) was used in the second equality. Taking into account this last equality proves (1.86).

## 1.11 Finite Element approximation of the stationary model

Let us assume that  $\Omega$  is a polyhedral domain and introduce a conformal tetrahedral space discretization. For any  $h > 0$ , let  $\mathcal{T}_h$  be a conformal regular mesh of  $\Omega$  [Cia02a] in tetrahedra  $K$  having diameter  $h_K \leq h$ . Also assume that the triangulation  $\partial\mathcal{T}_h$  of the surface  $\partial\Omega$  of  $\Omega$  into triangles is such that each of this triangle is one of the faces of elements  $K \in \mathcal{T}_h$ . Let us define

## 1.11. Finite Element approximation of the stationary model

---

the piecewise linear finite element space:

$$W_h = \left\{ v \in C^0(\bar{\Omega}) : v|_K \in \mathbb{P}_1(K), \forall K \in \mathcal{T}_h \right\}, \quad (1.92)$$

where  $\mathbb{P}_1(K)$  denotes the set of polynomials of degree 1 on  $K$ . Let  $P_1, P_2, \dots, P_{N_h}$  be the nodes of the tetrahedral mesh  $\mathcal{T}_h$ , and let  $\varphi_1, \varphi_2, \dots, \varphi_{N_h}$  the finite element basis of  $W_h$ , with  $\varphi_i(P_j) = \delta_{ij}$ . In addition, the following definition of the conforming bubble  $\varphi_b^K$  basis function for every element  $K$  is : let, for the tetrahedron  $K$ ,  $\varphi_i^K$ ,  $i = 1, 2, 3, 4$  be the four finite element linear basis functions on tetrahedron  $K$ . Also the discretized equivalent of spaces (1.59)(1.67) are:

$$\mathbf{V}_h = W_h^3 \cap \mathbf{V}, \quad L_h = W_h \cap L. \quad (1.93)$$

Then define :

$$\varphi_b^K = (256) \prod_{i=1}^4 \varphi_i^K. \quad (1.94)$$

The bubble basis function allows to define the bubble space function :

$$V_{bubble,h} = \left\{ \mathbf{v}_h : \Omega \rightarrow \mathbb{R}^3 \mid \mathbf{v}_h = \sum_{K \in \mathcal{T}_h} \mathbf{v}_K^b \varphi_b^K, \mathbf{v}_K^b \in \mathbb{R}^3 \right\}, \quad (1.95)$$

This additional bubble space is used to ensure stabilisation of the Navier-Stokes problem, as an equivalent method as the PSPG (Pressure Stabilized Petrov Galerkin) methods [BW90]. The approximated solution  $\mathbf{u}_h$  of  $\mathbf{u}$  is then discretized as:

$$\mathbf{u}_h \in (\mathbf{V}_h \oplus V_{bubble,h}), \mathbf{u}_h = \sum_{j=1}^{N_1} \mathbf{u}_j \varphi_j + \sum_{K \in \mathcal{T}_h} \mathbf{u}_K^b \varphi_b^K. \quad (1.96)$$

Then let the piecewise linear finite element space:

$$\partial W_h = \left\{ v \in C^0(\partial\Omega) : v_T \in \mathbb{P}_1(T), \forall T \in \partial\mathcal{T}_h \right\}, \quad (1.97)$$

where  $\mathbb{P}_1(T)$  denotes the set of polynomials of degree 1 on the triangle  $T$ , and then let:

$$S_h = \partial W_h \cap S \quad (1.98)$$

be the discretized finite element space of  $S(1.65)$  on  $\Gamma_{out}$ . Then:

- The approximated Navier-Stokes system of (1.69) consists into looking for  $(\mathbf{u}_h, p_h, \xi_h) \in$

$\mathbf{V}_h \oplus V_{bubble,h} \times L_h \times S_h$  such that :

$$\begin{aligned}
 & \int_{\Omega} (\rho_h \mathbf{u}_h \cdot \nabla) \mathbf{u}_h \cdot \mathbf{v} dx + \int_{\Omega} 2\mu \left( \epsilon(\mathbf{u}_h) : \epsilon(\mathbf{v}) - \frac{1}{3} \operatorname{div}(\mathbf{u}_h) \operatorname{div}(\mathbf{v}) \right) dx \\
 & - \int_{\Omega} p_h \operatorname{div}(\mathbf{v}) dx - \int_{\Gamma_{out}} \xi_h(\mathbf{v} \cdot \mathbf{n}) ds = \int_{\Omega} (\mathbf{F} + \rho_h \mathbf{g}) \cdot \mathbf{v} dx, \\
 & \int_{\Omega} \operatorname{div}(\rho_h \mathbf{u}_h) q dx = 0, \\
 & \int_{\Gamma_{out}} \sigma(\mathbf{u}_h \cdot \mathbf{n}) ds = 0,
 \end{aligned} \tag{1.99}$$

$\forall (\mathbf{v}, q, \sigma) \in \mathbf{V}_h \oplus V_{bubble,h} \times L_h \times S_h$ . Here  $\rho_h$  is defined as its continuous equivalent  $\rho$  (1.8), as  $\rho_h = \alpha_{g,h} \rho_g + (1 - \alpha_{g,h}) \rho_l$ .

- The approximated gas velocity system of (1.74) consists into looking for  $(\mathbf{u}_{g,h}) \in \mathbf{V}_h$  such that :

$$\begin{aligned}
 & \int_{\Omega} (\rho_g \alpha_{g,h} \mathbf{u}_{g,h} \cdot \nabla) \mathbf{u}_{g,h} \cdot \mathbf{v}_g dx + \int_{\Omega} (\rho_g \dot{\alpha}_{source}) \mathbf{u}_{g,h} \cdot \mathbf{v}_g dx \\
 & - \int_{\Gamma_{out}} (\alpha_{g,h} p_0)(\mathbf{v}_g \cdot \mathbf{n}) ds + \int_{\Omega} 2\mu_g \left( \epsilon(\mathbf{u}_{g,h}) : \epsilon(\mathbf{v}_g) - \frac{1}{3} \operatorname{div}(\mathbf{u}_{g,h}) \operatorname{div}(\mathbf{v}_g) \right) dx \\
 & = \int_{\Omega} \alpha_{g,h} (p_h) \operatorname{div}(\mathbf{v}_g) dx + \int_{\Omega} (p_h) \nabla \alpha_{g,h} \cdot \mathbf{v}_g dx + \int_{\Omega} \alpha_{g,h} \rho_g \mathbf{g} \cdot \mathbf{v}_g dx \\
 & + \int_{\Omega} D \frac{\rho_h}{\rho_l} \alpha_{g,h} (\mathbf{u}_h - \mathbf{u}_{g,h}) \cdot \mathbf{v}_g dx,
 \end{aligned} \tag{1.100}$$

$\forall \mathbf{v}_g \in \mathbf{V}_h$ .

- The approximated gas transport equation of (1.77) consists into looking for  $\alpha_{g,h} \in W_h$  such that:

$$\begin{aligned}
 & \int_{\Omega} \frac{\alpha_{g,h}^{r+1} - \alpha_{g,h}^r}{\Delta t} \omega dx + \int_{\Omega} \operatorname{div}(\alpha_{g,h} \mathbf{u}_{g,h}) \omega dx + \int_{\Omega} K \nabla \alpha_{g,h} \nabla \omega dx \\
 & + \frac{h C_S}{2|\mathbf{u}_{g,h}|} \int_{\Omega} (\mathbf{u}_{g,h} \cdot \nabla \omega) (\operatorname{div}(\alpha_{g,h} \mathbf{u}_{g,h}) - \dot{\alpha}_{source}) dx = \int_{\Omega} \dot{\alpha}_{source} \omega dx,
 \end{aligned} \tag{1.101}$$

$\forall \omega \in W_h$ . The term  $\partial \alpha_{g,h} / \partial t$  has been discretized using an implicit Euler scheme: let a fixed time-step  $\Delta t > 0$ : the temporal discretization of  $(0, \infty)$  is uniform and  $t_n = n \Delta t$ , for all  $n \in \mathbb{N}$ . Here  $\Delta t$  is a numerical parameter. Here the coefficient  $C_S$  is the coefficient of the stabilisation term. This latter term is of the same kind as a SUPG [QV08] but is instead the whole term  $\operatorname{div}(\alpha_{g,h} \mathbf{u}_{g,h}) - \dot{\alpha}_{source}$  is used instead of only  $\mathbf{u}_{g,h} \cdot \nabla \alpha_{g,h}$ .

### Computation of the integrals

The integrals in (1.99-1.101) are computed exactly, with the exceptions of a few terms. In particular the integrals of  $\int_{\Omega} \operatorname{div}(\alpha_{g,h} \mathbf{u}_{g,h}) \omega dx$  in (1.101) and  $\int_{\Omega} \operatorname{div}(\rho_h \mathbf{u}_h) q dx$  are computed as a "finite element group formulation" [Kuz10]. In both cases,  $\alpha_{g,h} \mathbf{u}_{g,h}$  and  $(\rho_h \mathbf{u}_h)$  are

## 1.11. Finite Element approximation of the stationary model

projected on  $V_h$ , and then the integral is performed exactly.

### Newton's method

In order to solve the non linearities in system (1.99) with respect to  $\mathbf{u}_h$  and of system (1.100) with respect to  $\mathbf{u}_{g,h}$ , the definition and results of section 1.10 are used. For the Navier-Stokes equations (1.99), with  $\rho_h$  given and a viscosity which takes the form  $\mu = \mu_L + \mu_T = \mu_L + C_T \rho_h |\epsilon(\mathbf{u}_h)|$ , the idea is to approach  $(\mathbf{u}_h, p_h, \xi_h) \in \mathbf{V}_h \oplus V_{bubble,h} \times L_h \times S_h$  such that (see (1.80)):

$$\langle \mathcal{F}(\mathbf{u}_h, p_h, \xi_h), (\mathbf{v}, q, \sigma) \rangle = 0, \quad (1.102)$$

for all  $(\mathbf{v}, q, \sigma) \in \mathbf{V}_h \oplus V_{bubble,h} \times L_h \times S_h$ . Then Newton's method can be written: build a sequence  $\{\mathbf{u}_h^m, p_h^m, \xi_h^m\}$  such that:

$$\langle \mathcal{F}(\mathbf{u}_h^m, p_h^m, \xi_h^m), (\mathbf{v}, q, \sigma) \rangle + \langle D\mathcal{F}(\mathbf{u}_h^m, p_h^m, \xi_h^m)(\mathbf{u}_h^{m+1} - \mathbf{u}_h^m, p_h^{m+1} - p_h^m, \xi_h^{m+1} - \xi_h^m); (\mathbf{v}, q, \sigma) \rangle = 0,$$

with the definition of the jacobian in (1.81). The initial point with  $m = 0$  is given with the precedent iteration in algorithm (1.9). Then for  $m = 0, 1, \dots, N_{Ne}$ , the system is solved successively  $N_{Ne}$  times,  $N_{Ne}$  being the number of Newton iteration.

The same method is applied with the non-linearity in the gas momentum equation (1.100), with  $\alpha_{g,h}$  and  $\mathbf{u}_h$  given as inputs. In order to find  $\mathbf{u}_{g,h} \in \mathbf{V}_h$  such that:

$$\langle \mathcal{G}_\theta(\mathbf{u}_{g,h}), \mathbf{v} \rangle = 0, \quad (1.103)$$

for all  $\mathbf{v} \in \mathbf{V}_h$ , use (1.86), and build a sequence  $\{\mathbf{u}_{g,h}^m\}$  with:

$$\langle \mathcal{G}_\theta(\mathbf{u}_{g,h}^m), \mathbf{v} \rangle + \langle D\mathcal{G}_\theta(\mathbf{u}_{g,h}^m)(\mathbf{u}_{g,h}^{m+1} - \mathbf{u}_{g,h}^m); \mathbf{v} \rangle = 0, \quad (1.104)$$

where again the index  $m = 0, \dots, N_{Ne}$  is the Newton iteration to solve the part 2b in the algorithm (1.9), with the value at  $m = 0$  given with the precedent iteration.

### Explicit example of Newton's method for the gas velocity system

Assume that we are at iteration  $k$  at stage 2b of the algorithm described in section 1.9 and that the drag coefficient follows the non-linear model (1.47):

$$D = \left( \theta \left[ 1 + 0.15 Re_b^{0.687} \right] + (1 - \theta) \frac{0.44 Re_b}{24} \frac{18 \mu_L r}{d^2} \right), \theta = \begin{cases} 1 & \text{if } \left[ 1 + 0.15 Re_b^{0.687} \right] \geq \frac{0.44 Re_b}{24}, \\ 0 & \text{if } \left[ 1 + 0.15 Re_b^{0.687} \right] < \frac{0.44 Re_b}{24}, \end{cases}$$

$$Re_b(\mathbf{u}_{g,h}) = \frac{\rho_l |\mathbf{u}_h - \mathbf{u}_{g,h}| d}{\mu_L}.$$

The discretization in finite elements is (1.100), where all the quantities  $\alpha_{g,h}$ ,  $\mathbf{u}_{g,h}$ ,  $\mathbf{u}_h$  and  $p_h$  from the precedent iteration are known. For Newton iterations  $m = 1, \dots, N_{Ne}$ , where  $N_{Ne}$  is

## Chapter 1. A mixture model for a dilute dispersion of gas in a liquid

the number of Newton iterations, here for  $\mathbf{u}_{g,h}$ . The  $m$ -th iteration of  $\mathbf{u}_{g,h}$  is denoted  $\mathbf{u}_{g,h}^m$ . The linearisation of (1.100) and then one step of the Newton method consists into the following laborious expression: look for  $\mathbf{u}_{g,h}^{m+1} \in \mathbf{V}_h$  such that:

$$\begin{aligned}
& \int_{\Omega} (\rho_g \alpha_{g,h} \mathbf{u}_{g,h}^{m+1} \cdot \nabla) \mathbf{u}_{g,h}^m \cdot \mathbf{v}_{g,h} dx + \int_{\Omega} (\rho_g \alpha_{g,h} \mathbf{u}_{g,h}^m \cdot \nabla) \mathbf{u}_{g,h}^{m+1} \cdot \mathbf{v}_{g,h} dx + \int_{\Omega} (\rho_g \dot{\alpha}_{source}) \mathbf{u}_{g,h}^{m+1} \cdot \mathbf{v}_g dx \\
& - \int_{\Gamma_{out}} (\alpha_{g,h} p_0) (\mathbf{v}_g \cdot \mathbf{n}) ds + \int_{\Omega} 2\mu_g \left( \epsilon(\mathbf{u}_{g,h}^{m+1}) : \epsilon(\mathbf{v}_g) - \frac{1}{3} \operatorname{div}(\mathbf{u}_{g,h}^{m+1}) \operatorname{div}(\mathbf{v}_g) \right) dx \\
& + \theta \int_{\Omega} [1 + 0.15 Re_b^{0.687}] \frac{18\mu_L r}{d^2} \frac{\rho_h}{\rho_l} \alpha_{g,h} \mathbf{u}_{g,h}^{m+1} \cdot \mathbf{v} dx + (1-\theta) \int_{\Omega} \frac{0.44}{24} \frac{\mathbf{u}_{g,h}^{m+1} \cdot (\mathbf{u}_{g,h}^m - \mathbf{u}_h)}{|\mathbf{u}_{g,h}^m - \mathbf{u}_h|} \frac{18r\rho_h}{d} \alpha_{g,h} (\mathbf{u}_{g,h}^m - \mathbf{u}_h) \cdot \mathbf{v} dx \\
& + \theta \int_{\Omega} [(0.15)0.687 Re_b^{0.687-1}] \frac{\mathbf{u}_{g,h}^{m+1} \cdot (\mathbf{u}_{g,h}^m - \mathbf{u}_h)}{|\mathbf{u}_{g,h}^m - \mathbf{u}_h|} \frac{18r\rho_h}{d} \alpha_{g,h} (\mathbf{u}_{g,h}^m - \mathbf{u}_h) \cdot \mathbf{v} dx \\
& + (1-\theta) \int_{\Omega} \frac{0.44 Re_b}{24} \frac{18\mu_L r}{d^2} \frac{\rho_h}{\rho_l} \alpha_{g,h} \mathbf{u}_{g,h}^{m+1} \cdot \mathbf{v} dx, \\
& = \int_{\Omega} \alpha_{g,h} p_h \operatorname{div}(\mathbf{v}_g) dx + \int_{\Omega} p_h \nabla \alpha_{g,h} \cdot \mathbf{v}_g dx + \int_{\Omega} \alpha_{g,h} \rho_g \mathbf{g} \cdot \mathbf{v}_g dx \\
& + \theta \int_{\Omega} [1 + 0.15 Re_b^{0.687}] \frac{18\mu_L r}{d^2} \frac{\rho_h}{\rho_l} \alpha_{g,h} \mathbf{u}_h \cdot \mathbf{v} dx + (1-\theta) \int_{\Omega} \frac{0.44 Re_b}{24} \frac{18\mu_L r}{d^2} \frac{\rho_h}{\rho_l} \alpha_{g,h} \mathbf{u}_h \cdot \mathbf{v} dx \\
& + (1-\theta) \int_{\Omega} \frac{0.44}{24} \frac{\mathbf{u}_{g,h}^m \cdot (\mathbf{u}_{g,h}^m - \mathbf{u}_h)}{|\mathbf{u}_{g,h}^m - \mathbf{u}_h|} \frac{18r\rho_h}{d} \alpha_{g,h} (\mathbf{u}_{g,h}^m - \mathbf{u}_h) \cdot \mathbf{v} dx \\
& + \theta \int_{\Omega} [(0.15)0.687 Re_b^{0.687-1}] \frac{\mathbf{u}_{g,h}^m \cdot (\mathbf{u}_{g,h}^m - \mathbf{u}_h)}{|\mathbf{u}_{g,h}^m - \mathbf{u}_h|} \frac{18r\rho_h}{d} \alpha_{g,h} (\mathbf{u}_{g,h}^m - \mathbf{u}_h) \cdot \mathbf{v} dx, \\
Re_b(\mathbf{u}_{g,h}^m) &= \frac{\rho_l |\mathbf{u}_h - \mathbf{u}_{g,h}^m| d}{\mu_L}, \theta = \begin{cases} 1 & \text{if } [1 + 0.15 Re_b^{0.687}] \geq \frac{0.44 Re_b}{24}, \\ 0 & \text{if } [1 + 0.15 Re_b^{0.687}] < \frac{0.44 Re_b}{24}, \end{cases}
\end{aligned}$$

$\forall \mathbf{v}_g \in \mathbf{V}_h$ . The same can be applied for the Navier-Stokes equation (1.99) to obtain the explicit Newton step. (see [Roc16] for reference) If the chosen drag coefficient model is the linear law independent of  $\mathbf{u}_g$ , i.e  $D = 18\mu_L r / d^2$ , then the drag force is linear with respect to  $\mathbf{u}_g$  and the Newton's step is useful only for the convective term  $(\rho_g \alpha_{g,h} \mathbf{u}_{g,h} \cdot \nabla) \mathbf{u}_{g,h}$ .

## 2 Mathematical analysis of a simplified model

In this chapter, the well-posedness of a simplified model is proved when the volumetric ratio of gas  $\alpha_g$  is given as an input and is small enough. In addition a priori estimates on this simplified problem are given for a stabilized finite element approximation. Most of the arguments presented are rephrased from [SRP21]. In the frame of the industrial process, the goal is to find a stationary solution as rapidly as possible. Numerical investigations have shown that an efficient strategy is to perform one time step of (1.33) in order to obtain a new  $\alpha_g$ , then to solve the stationary equations (1.32)(1.34)(1.35) to obtain  $\mathbf{u}$ ,  $p$  and  $\mathbf{u}_g$ . We therefore study the well-posedness of (1.32)(1.34)(1.35),  $\alpha_g$  being a known quantity.

It is assumed that  $\Omega$  is an open bounded domain in  $\mathbb{R}^d$ ,  $d = 2, 3$ , with Lipschitz boundary  $\partial\Omega$ . The convective terms  $\operatorname{div}(\alpha_g \rho_g \mathbf{u}_g \otimes \mathbf{u}_g)$  in (1.32) and  $\operatorname{div}(\rho \mathbf{u} \otimes \mathbf{u})$  in (1.34) are disregarded; in the applications their effects are of secondary importance; they could be treated as perturbations as in [CR97] or incorporated in the definition of the stress tensor as in [Gat+21]. Equations(1.32)(1.34)(1.35) then simplify to:

$$-\operatorname{div}(\boldsymbol{\tau}) = \rho \mathbf{g} + \mathbf{F}, \quad (2.1)$$

$$\operatorname{div}(\rho \mathbf{u}) = 0, \quad (2.2)$$

$$-\operatorname{div}(\boldsymbol{\tau}_g) = p \nabla \alpha_g + \alpha_g \rho_g \mathbf{g} + D \alpha_g \frac{\rho}{\rho_l} (\mathbf{u} - \mathbf{u}_g), \quad (2.3)$$

where  $\boldsymbol{\tau}$ ,  $\boldsymbol{\tau}_g$  and  $\rho$  is given by:

$$\boldsymbol{\tau} = -p \mathbf{I} - 2/d \mu \operatorname{div}(\mathbf{u}) \mathbf{I} + 2\mu \boldsymbol{\epsilon}(\mathbf{u}), \quad (2.4)$$

$$\boldsymbol{\tau}_g = -p \alpha_g \mathbf{I} - 2/d \mu_g \operatorname{div}(\mathbf{u}_g) \mathbf{I} + 2\mu_g \boldsymbol{\epsilon}(\mathbf{u}_g). \quad (2.5)$$

$$\rho = \alpha_g \rho_g + (1 - \alpha_g) \rho_l, \quad (2.6)$$

For the sake of simplicity we assume that  $\mu_g, D, \rho_l > \rho_g$  and  $\mu$  are positive constants and set  $\mathbf{u}_g = \mathbf{u} = 0$  on  $\partial\Omega$ . Thus in this simplified problem there is no outflow surface  $\Gamma_{out}$  (and associated quantities  $\xi$  and  $p_0$ ).

## 2.1 Sobolev spaces notation

The notations for Sobolev spaces with their associated semi-norms and norms are the following. Let  $K \subset \Omega$  be an open sub-domain of  $\Omega$  with Lipschitz boundary  $\partial K$ . For a d-index  $s = (s_1, s_2) \in \mathbb{N}^2$  if  $d = 2$  or  $s = (s_1, s_2, s_3) \in \mathbb{N}^3$  if  $d = 3$ , and for a differentiable function  $g : \mathbb{R}^d \rightarrow \mathbb{R}$ , we denote by  $|s| = \sum_{i=1}^d s_i$  and  $D^s g = \partial^{|s|} g / (\prod_{i=1}^d \partial x_i^{s_i})$ . For  $1 \leq p < \infty$  and  $0 \leq m$ :

$$W^{m,p}(K) = \{g \in L^p(K) : D^s g \in L^p(K), 1 \leq |s| \leq m\},$$

and in the case where  $m = 0$ ,  $W^{0,p}(K) = L^p(K)$ . We will also use

$$|g|_{m,p,K} = \left( \sum_{|s|=m} \|D^s g\|_{L^p(K)}^p \right)^{1/p} \text{ and } \|g\|_{m,p,K} = \left( \sum_{|s| \leq m} \|D^s g\|_{L^p(K)}^p \right)^{1/p}.$$

When  $p = 2$  we will use the notations  $H^m(K) = W^{m,2}(K)$  and for  $g \in H^m(K)$ , the semi-norms  $|g|_{m,K} = |g|_{m,2,K}$  and norms  $\|g\|_{m,K} = \|g\|_{m,2,K}$ . When  $K = \Omega$ ,  $H_0^m(\Omega)$  will denote the closure of all  $C^\infty$  functions with compact support  $D(\Omega)$  in  $H^m(\Omega)$ . In this space, semi-norm  $|\cdot|_{m,\Omega}$  and norm  $\|\cdot\|_{m,\Omega}$  are equivalent. If  $\mathbf{u} \in H^m(\Omega)^d$ , we will denote by  $|\mathbf{u}|_{m,\Omega} = (\sum_{i=1}^d |u_i|_{m,\Omega}^2)^{1/2}$  and  $\|\mathbf{u}\|_{m,\Omega} = (\sum_{i=1}^d \|u_i\|_{m,\Omega}^2)^{1/2}$ . Finally, we will denote by

$$L_0 = \left\{ v \in L^2(\Omega) : \int_{\Omega} v \, dx = 0 \right\}, \text{ and } \mathbf{U} = H_0^1(\Omega)^d.$$

## 2.2 Weak formulation

The weak form of Equation (2.1) and (2.2) is given by  $(\mathbf{u}, p) \in \mathbf{U} \times L_0$  satisfying:

$$\begin{aligned} \int_{\Omega} 2\mu \left( \epsilon(\mathbf{u}) : \epsilon(\mathbf{v}) - \frac{1}{d} \operatorname{div} \mathbf{u} \operatorname{div} \mathbf{v} \right) dx \\ - \int_{\Omega} p \operatorname{div} \mathbf{v} \, dx = \int_{\Omega} (\rho \mathbf{g} + \mathbf{F}) \cdot \mathbf{v} \, dx, \end{aligned} \quad \forall \mathbf{v} \in \mathbf{U}, \quad (2.7)$$

$$\int_{\Omega} \operatorname{div}(\rho \mathbf{u}) q \, dx = 0, \quad \forall q \in L_0. \quad (2.8)$$

A weak form of (2.3) is  $\mathbf{u}_g \in \mathbf{U}$  such that:

$$\begin{aligned} \int_{\Omega} 2\mu_g \left( \epsilon(\mathbf{u}_g) : \epsilon(\mathbf{v}) - \frac{1}{d} \operatorname{div} \mathbf{u}_g \operatorname{div} \mathbf{v} \right) dx + \int_{\Omega} D \frac{\alpha_g \rho}{\rho_l} \mathbf{u}_g \cdot \mathbf{v} \, dx \\ = \int_{\Omega} p \nabla \alpha_g \cdot \mathbf{v} \, dx + \int_{\Omega} \alpha_g p \operatorname{div} \mathbf{v} \, dx + \int_{\Omega} \alpha_g (\rho_g \mathbf{g} + D \frac{\rho}{\rho_l} \mathbf{u}) \cdot \mathbf{v} \, dx, \end{aligned} \quad \forall \mathbf{v} \in \mathbf{U}. \quad (2.9)$$

We assume that  $\mathbf{g} \in \mathbb{R}^d$ ,  $\mathbf{F} \in L^2(\Omega)^d$  and also that  $\alpha_g \in W^{1,3}(\Omega) \cap L^\infty(\Omega)$  is known and is such that  $0 \leq \alpha_g \leq 1$ . Using (2.6) and  $0 \leq \alpha_g \leq 1$ , it is obvious that  $\rho \in W^{1,3}(\Omega) \cap L^\infty(\Omega)$ ,  $\rho_g \leq \rho \leq \rho_l$ , and

$$\frac{\partial \rho}{\partial x_i} = \frac{\partial \alpha_g}{\partial x_i} (\rho_g - \rho_l).$$

A similar problem corresponding to Equations (2.7) and (2.8) is considered in [Ber+92; Ern96], and in a first part of this analysis, we adapt some arguments of [Ber+92].

**Lemma 1** (Isomorphic mapping). *Assume  $0 \leq \alpha_g \leq 1$  and  $\alpha_g \in W^{1,3}(\Omega)$ . The mapping  $\mathbf{u} \in \mathbf{U} \rightarrow \rho \mathbf{u} \in \mathbf{U}$  (with  $\rho$  given by (2.6)) is an isomorphism. There exists two positive constants  $\gamma_1, \gamma_2$  such that for every  $\mathbf{u} \in \mathbf{U}$ :*

$$|\mathbf{u}|_{1,\Omega} \leq \gamma_1 (1 + |\alpha_g|_{1,3,\Omega}) |\rho \mathbf{u}|_{1,\Omega}, \quad (2.10)$$

$$|\rho \mathbf{u}|_{1,\Omega} \leq \gamma_2 (1 + |\alpha_g|_{1,3,\Omega}) |\mathbf{u}|_{1,\Omega}. \quad (2.11)$$

*In dimension  $d = 2$ , it is sufficient that  $\alpha_g \in W^{1,2+k}(\Omega)$ ,  $k > 0$ , instead of  $\alpha_g \in W^{1,3}(\Omega)$ . Then there exists two positive constants  $\gamma_3, \gamma_4$  such that for every  $\mathbf{u} \in \mathbf{U}$ :*

$$|\mathbf{u}|_{1,\Omega} \leq \gamma_3 (1 + |\alpha_g|_{1,2+k,\Omega}) |\rho \mathbf{u}|_{1,\Omega}, \quad (2.12)$$

$$|\rho \mathbf{u}|_{1,\Omega} \leq \gamma_4 (1 + |\alpha_g|_{1,2+k,\Omega}) |\mathbf{u}|_{1,\Omega}. \quad (2.13)$$

*Proof.* Let  $\mathbf{u}$  be in  $\mathbf{U}$  and let us compute de partial derivatives of  $\mathbf{w} = \rho \mathbf{u}$ . We verify that  $\nabla \mathbf{w} = \rho \nabla \mathbf{u} + \mathbf{u} \otimes \nabla \rho$  with the notation  $(\mathbf{a} \otimes \mathbf{b})_{i,j} = a_i b_j$ . At this point, we recall a useful Sobolev's embedding theorem [Cia02b]. In dimension  $d$ , for all integers  $m \geq 0$  and all  $1 \leq p \leq \infty$ ,

$$W^{m,p}(\Omega) \hookrightarrow L^{p^*}(\Omega) \text{ with } \frac{1}{p^*} = \frac{1}{p} - \frac{m}{d}, \text{ if } m < \frac{d}{p}. \quad (2.14)$$

Another useful theorem is the Kondrasov theorem which includes the compact injection:

$$W^{m,p}(\Omega) \hookrightarrow^c L^q(\Omega) \text{ for all } q \in [1, \infty[, \text{ if } m = \frac{d}{p}. \quad (2.15)$$

By using (2.6) we have  $\rho_g \leq \rho \leq \rho_l$  and  $\nabla \rho = (\rho_g - \rho_l) \nabla \alpha_g$ .

Hölder inequalities imply

$$\|\nabla \mathbf{w}\|_{0,\Omega} \leq \rho_l \|\nabla \mathbf{u}\|_{0,\Omega} + C \|\mathbf{u}\|_{0,6,\Omega} \|\nabla \alpha_g\|_{0,3,\Omega}, \quad (2.16)$$

and

$$\|\nabla \mathbf{w}\|_{0,\Omega} \leq \rho_l \|\nabla \mathbf{u}\|_{0,\Omega} + C_2 \|\mathbf{u}\|_{0,(4+2k)/k,\Omega} \|\nabla \alpha_g\|_{0,2+k,\Omega}, \quad (2.17)$$

where  $C, C_2$  are constants independent of derivatives of  $\alpha_g$ . With continuous embedding (2.14),  $d = 2, 3$ ,  $H_0^1(\Omega) \hookrightarrow L^6(\Omega)$  and we easily obtain (2.11) from (2.16). With the compact

## Chapter 2. Mathematical analysis of a simplified model

---

injection (2.15) and  $d = 2$ ,  $H_0^1(\Omega) \hookrightarrow L^{(4+2k)/k}(\Omega)$  and we obtain (2.13) from (2.17).

In order to obtain (2.10), and (2.12), the same technique is used with

$$\mathbf{u} = \frac{1}{\rho} \mathbf{w}, \frac{1}{\rho_l} \leq \frac{1}{\rho} \leq \frac{1}{\rho_g} \text{ and } \nabla \frac{1}{\rho} = -\frac{1}{\rho^2} (\rho_g - \rho_l) \nabla \alpha_g.$$

■

**Lemma 2** (Korn equality). *Assume  $\mathbf{u} \in \mathbf{U}$ . Then*

$$\int_{\Omega} |\epsilon(\mathbf{u})|^2 dx = \frac{1}{2} \int_{\Omega} (|\nabla \mathbf{u}|^2 + |\operatorname{div} \mathbf{u}|^2) dx.$$

*Proof.* Let  $\mathbf{u}, \mathbf{v} \in D(\Omega)^d$ . Then

$$\begin{aligned} \int_{\Omega} \epsilon(\mathbf{u}) : \epsilon(\mathbf{v}) dx &= \int_{\Omega} \frac{1}{4} \sum_{i,j=1}^d \left( \frac{\partial u_i}{\partial x_j} + \frac{\partial u_j}{\partial x_i} \right) \left( \frac{\partial v_i}{\partial x_j} + \frac{\partial v_j}{\partial x_i} \right) dx = \\ &= \int_{\Omega} \frac{1}{4} \sum_{i,j=1}^d \left( \frac{\partial u_i}{\partial x_j} \frac{\partial v_i}{\partial x_j} + \frac{\partial u_j}{\partial x_i} \frac{\partial v_j}{\partial x_i} + 2 \frac{\partial u_i}{\partial x_j} \frac{\partial v_j}{\partial x_i} \right) dx. \end{aligned}$$

Integrating two times by part the last term gives

$$\int_{\Omega} \frac{\partial u_i}{\partial x_j} \frac{\partial v_j}{\partial x_i} dx = - \int_{\Omega} \frac{\partial^2 v_j}{\partial x_i \partial x_j} u_i dx = \int_{\Omega} \frac{\partial v_j}{\partial x_j} \frac{\partial u_i}{\partial x_i} dx$$

and

$$\int_{\Omega} \epsilon(\mathbf{u}) : \epsilon(\mathbf{v}) dx = \frac{1}{2} \int_{\Omega} \nabla \mathbf{u} : \nabla \mathbf{v} dx + \frac{1}{2} \int_{\Omega} \operatorname{div} \mathbf{u} \operatorname{div} \mathbf{v} dx. \quad (2.18)$$

To complete the proof of this lemma, it is enough to remark that  $D(\Omega)^d$  is dense in  $\mathbf{U}$  and taking  $\mathbf{v} = \mathbf{u}$ . ■

In order to solve equations (2.7) and (2.8), choose  $\mathbf{w} = \rho \mathbf{u}$  and define two continuous bilinear forms  $a : \mathbf{U} \times \mathbf{U} \rightarrow \mathbb{R}$  and  $b : \mathbf{U} \times L_0 \rightarrow \mathbb{R}$  by:

$$a(\mathbf{w}, \mathbf{v}) = \int_{\Omega} 2\mu \left( \epsilon \left( \frac{\mathbf{w}}{\rho} \right) : \epsilon(\mathbf{v}) - \frac{1}{d} \operatorname{div} \left( \frac{\mathbf{w}}{\rho} \right) \operatorname{div}(\mathbf{v}) \right) dx, \quad (2.19)$$

$$\text{and } b(\mathbf{w}, q) = \int_{\Omega} \operatorname{div} \mathbf{w} q dx. \quad (2.20)$$

Remark that the bilinear form  $a$  is not symmetric and depends on  $\alpha_g$ . With the change of

variables  $\mathbf{w} = \rho \mathbf{u}$ , problem (2.7)-(2.8) is equivalent to find  $\mathbf{w} \in \mathbf{U}$  and  $p \in L_0$  satisfying

$$a(\mathbf{w}, \mathbf{v}) - b(\mathbf{v}, p) = \int_{\Omega} (\rho \mathbf{g} + \mathbf{F}) \cdot \mathbf{v} dx, \quad \forall \mathbf{v} \in \mathbf{U}, \quad (2.21)$$

$$b(\mathbf{w}, q) = 0 \quad \forall q \in L_0, \quad (2.22)$$

In order to analyse equation (2.9), we define the continuous bilinear form  $\ell : \mathbf{U} \times \mathbf{U} \rightarrow \mathbb{R}$  by:

$$\ell(\mathbf{u}, \mathbf{v}) = \int_{\Omega} 2\mu_g \left( \epsilon(\mathbf{u}) : \epsilon(\mathbf{v}) - \frac{1}{d} \operatorname{div} \mathbf{u} \operatorname{div} \mathbf{v} \right) dx + \int_{\Omega} D \frac{\alpha_g \rho}{\rho_l} \mathbf{u} \cdot \mathbf{v} dx. \quad (2.23)$$

We prove the following:

**Lemma 3** (Coercivity of bilinear form  $a$ ). *There exists  $\varepsilon > 0$  such that if  $\alpha_g \in W^{1,3}(\Omega)$ ,  $|\alpha_g|_{1,3,\Omega} \leq \varepsilon$  and  $0 \leq \alpha_g \leq 1$ , then the bilinear form  $a(\cdot, \cdot)$  is coercive on  $\mathbf{U}$ .*

*Proof.* Using Lemma 1, then  $\mathbf{w} = \rho \mathbf{u} \in \mathbf{U}$  and, if  $|\alpha_g|_{1,3,\Omega}$  is bounded, there exist two positive constants  $\beta_1 < \beta_2$  satisfying

$$\beta_1 \|\mathbf{u}\|_{1,\Omega} \leq \|\mathbf{w}\|_{1,\Omega} \leq \beta_2 \|\mathbf{u}\|_{1,\Omega}. \quad (2.24)$$

It is easy to verify that

$$\epsilon\left(\frac{\mathbf{w}}{\rho}\right) = \frac{1}{\rho} \epsilon(\mathbf{w}) - \frac{1}{2\rho^2} \left( \nabla \rho \otimes \mathbf{w} + \mathbf{w} \otimes \nabla \rho \right),$$

when  $(\mathbf{b} \otimes \mathbf{c})_{i,j} = b_i c_j$ . It follows that for  $\mathbf{v}, \mathbf{w} \in \mathbf{U}$

$$\begin{aligned} a(\mathbf{w}, \mathbf{v}) &= \int_{\Omega} \frac{2\mu}{\rho} \left( \epsilon(\mathbf{w}) : \epsilon(\mathbf{v}) - \frac{1}{d} \operatorname{div} \mathbf{w} \operatorname{div} \mathbf{v} \right) dx \\ &\quad - \int_{\Omega} \frac{\mu}{\rho^2} \left( (\nabla \rho \otimes \mathbf{w} + \mathbf{w} \otimes \nabla \rho) : \epsilon(\mathbf{v}) \right) dx \\ &\quad + \int_{\Omega} \frac{2\mu}{d\rho^2} \left( \mathbf{w} \cdot \nabla \rho \operatorname{div} \mathbf{v} \right) dx. \end{aligned} \quad (2.25)$$

By using Lemma 2 and Hölder inequality, there exists a constant  $C$  independent of  $\mathbf{w}$  and  $\nabla \alpha_g$  such that

$$a(\mathbf{w}, \mathbf{w}) \geq \frac{\mu}{\rho_g} \left( \|\mathbf{w}\|_{1,\Omega}^2 - C \|\nabla \rho\|_{0,3,\Omega} \|\mathbf{w}\|_{0,6,\Omega} \|\mathbf{w}\|_{1,\Omega} \right).$$

It is sufficient to remark that  $H_0^1(\Omega) \hookrightarrow L^6(\Omega)$  with continuous embedding (2.14), that  $\nabla \rho = (\rho_g - \rho_l) \nabla \alpha_g$ , that  $|\cdot|_{1,\Omega}$  is equivalent to  $\|\cdot\|_{1,\Omega}$  in  $H_0^1(\Omega)$ , in order to prove that if  $|\alpha_g|_{1,3,\Omega}$  is small enough, then the bilinear form  $a(\cdot, \cdot)$  is uniformly coercive on  $\mathbf{U}$ .  $\blacksquare$

**Proposition 1** (Well-posedness of the mixture problem). *There exists  $\varepsilon > 0$  such that if  $\alpha_g \in W^{1,3}(\Omega)$ ,  $|\alpha_g|_{1,3,\Omega} \leq \varepsilon$  and  $0 \leq \alpha_g \leq 1$ , then Problem (2.7)-(2.8), in which  $\rho$  is defined by (2.6), possesses a unique solution  $(\mathbf{u}, p) \in \mathbf{U} \times L_0$ . Moreover there exists a constant  $C$  such that  $\|\mathbf{u}\|_{1,\Omega} + \|p\|_{0,\Omega} \leq C$ .*

## Chapter 2. Mathematical analysis of a simplified model

*Proof.* The usual inf–sup condition on  $b(\cdot, \cdot)$ , together with the previous lemma implies (see [GR86], corollary 4.1 page 61, for instance) the existence and uniqueness of  $(\mathbf{w}, p) \in \mathbf{U} \times L_0$  for equations (2.21) and (2.22). By setting  $\mathbf{u} = \mathbf{w}/\rho$  and using (2.24), we can conclude. ■

**Proposition 2** (Well-posedness of the gas momentum equation). *There exists  $\varepsilon > 0$  such that if  $\alpha_g \in W^{1,3}(\Omega)$ ,  $|\alpha_g|_{1,3,\Omega} \leq \varepsilon$  and  $0 \leq \alpha_g \leq 1$ , then Problem (2.9) possesses a unique solution  $\mathbf{u}_g \in \mathbf{U}$ . Moreover there exists a constant  $C$  (independent of  $\alpha_g$ ) such that  $\|\mathbf{u}_g\|_1 \leq C$ .*

*Proof.* Clearly, using Lemma 2 and the hypotheses of this Proposition, the bilinear form  $\ell$  defined by (2.23) is coercive and continuous on  $\mathbf{U} \times \mathbf{U}$ .

In order to finish the proof of this Proposition, it remains to prove that the right member of (2.9) is bounded for every  $\mathbf{v} \in H_0^1(\Omega)$ ,  $\|\mathbf{v}\|_{1,\Omega} = 1$ .

By estimating the three integrals of the right member of (2.9), using Hölder inequalities and hypotheses of this Proposition, one successively obtains:

$$\begin{aligned} \left| \int_{\Omega} p \nabla \alpha_g \cdot \mathbf{v} dx \right| &\leq \varepsilon \|p\|_{0,\Omega} \|\mathbf{v}\|_{0,6,\Omega}; \\ \left| \int_{\Omega} \alpha_g p \operatorname{div} \mathbf{v} dx \right| &\leq \|p\|_{0,\Omega} \|\mathbf{v}\|_{1,\Omega}; \\ \left| \int_{\Omega} (\alpha_g \rho_g \mathbf{g} + D \frac{\alpha_g \rho}{\rho_l} \mathbf{u}) \cdot \mathbf{v} dx \right| &\leq (\rho_g |\mathbf{g}| + D \|\mathbf{u}\|_{0,\Omega}) \|\mathbf{v}\|_{0,\Omega}. \end{aligned}$$

Using again the embedding  $H_0^1(\Omega) \hookrightarrow L^6(\Omega)$ , the result of proposition 2 is proved. ■

In this section we have therefore proved that if  $\alpha_g : \Omega \rightarrow \mathbb{R}$  is given such that  $0 \leq \alpha_g \leq 1$ ,  $\alpha_g \in W^{1,3}(\Omega)$  with  $|\alpha_g|_{1,3,\Omega}$  small enough<sup>1</sup>, then Problem (2.7) to (2.9) has a unique solution.

### 2.3 Numerical approximation of the simplified model

Let us assume that  $\Omega$  is a polygonal ( $d = 2$ ) or polyhedral domain ( $d = 3$ ). For any  $h > 0$ , let  $\mathcal{T}_h$  be a conformal regular triangular/tetrahedral mesh of  $\bar{\Omega}$  with triangles/tetrahedra  $K \in \mathcal{T}_h$  with diameter  $h_K \leq h$ .

$$W_h = \{q \in C^0(\bar{\Omega}) : q|_K \in \mathbb{P}_1(K), \forall K \in \mathcal{T}_h\}, \quad (2.26)$$

where  $\mathbb{P}_1(K)$  denotes the set of polynomials of degree 1 on  $K$ . Let  $P_1, P_2, \dots, P_{N_h}$  be the nodes of the triangular/tetrahedral mesh  $\mathcal{T}_h$ , and let  $\varphi_1, \varphi_2, \dots, \varphi_{N_h}$  the finite element basis of  $W_h$ . If

<sup>1</sup>In 2D ( $d = 2$ ), if  $\alpha_g \in W^{1,s}(\Omega)$ ,  $s > 2$  with  $|\alpha_g|_{1,s,\Omega}$  small enough

### 2.3. Numerical approximation of the simplified model

$q \in C^0(\bar{\Omega})$  we denote by  $\pi_h q$  its Lagrange interpolation on  $W_h$ , i.e

$$\pi_h q = \sum_{j=1}^{N_h} q(P_j) \varphi_j.$$

Now we define the following finite element spaces:

$$\mathbf{U}_h = \mathbf{U} \cap W_h^d, \text{ and } L_h = L_0 \cap W_h.$$

For a function  $\mathbf{v} \in C^0(\bar{\Omega})^d$  such that  $\mathbf{v} = 0$  on  $\partial\Omega$ , we denote by  $\Pi_h \mathbf{v}$  its interpolation on  $\mathbf{U}_h$ , i.e.

$$\Pi_h \mathbf{v} = \sum_{j=1}^{N_h} \mathbf{v}(P_j) \varphi_j.$$

An approximation of Problems (2.7)(2.8) and (2.9) will be: find  $(\mathbf{u}_h, p_h, \mathbf{u}_{g,h}) \in \mathbf{U}_h \times L_h \times \mathbf{U}_h$  such that for every  $\mathbf{v} \in \mathbf{U}_h, q \in L_h$

$$\begin{aligned} & \int_{\Omega} 2\mu \left( \epsilon(\mathbf{u}_h) : \epsilon(\mathbf{v}) - \frac{1}{d} \operatorname{div} \mathbf{u}_h \operatorname{div} \mathbf{v} \right) dx \\ & - \int_{\Omega} p_h \operatorname{div} \mathbf{v} dx = \int_{\Omega} (\rho \mathbf{g} + \mathbf{F}) \cdot \mathbf{v} dx, \end{aligned} \quad (2.27)$$

$$\int_{\Omega} \operatorname{div} (\Pi_h(\rho \mathbf{u}_h)) q dx + \beta h^2 \int_{\Omega} \nabla p_h \cdot \nabla q dx = 0, \quad (2.28)$$

$$\begin{aligned} & \int_{\Omega} 2\mu_g \left( \epsilon(\mathbf{u}_{g,h}) : \epsilon(\mathbf{v}) - \frac{1}{d} \operatorname{div} \mathbf{u}_{g,h} \operatorname{div} \mathbf{v} \right) dx + \int_{\Omega} D \frac{\alpha_g \rho}{\rho_l} \mathbf{u}_{g,h} \cdot \mathbf{v} dx \\ & = \int_{\Omega} p_h \nabla \alpha_g \cdot \mathbf{v} dx + \int_{\Omega} \alpha_g p_h \operatorname{div} \mathbf{v} dx + \int_{\Omega} (\alpha_g \rho_g \mathbf{g} + D \frac{\alpha_g \rho}{\rho_l} \mathbf{u}_h) \cdot \mathbf{v} dx. \end{aligned} \quad (2.29)$$

It is well known that if the stabilization term  $\beta h^2 \int_{\Omega} \nabla p_h \cdot \nabla q dx$  in (2.28) is missing, the numerical method is not stable. Note that (2.28), we have replaced  $\rho \mathbf{u}_h$  by  $\Pi_h(\rho \mathbf{u}_h)$  to take into account quadrature formula.

**Remark 9.** In practice in this thesis, the inf sup condition is satisfied using an enriched bubble space for the velocity (see section 1.11). Here an analog of the pressure stabilized Petrov-Galerkin (PSPG) stabilisation is considered instead, in order to prove the results clearly. Several studies have shown the equivalence between both numerical methods from a theoretical aspect if  $\mathcal{T}_h$  is uniform, as well as in practice [BW90; Lau16].

In order to analyse Equations (2.27) (2.28), we proceed as in Lemma 1 by introducing the

## Chapter 2. Mathematical analysis of a simplified model

---

variable

$$\mathbf{w}_h = \Pi_h(\rho \mathbf{u}_h). \quad (2.30)$$

Clearly

$$\mathbf{u}_h = \Pi_h(\mathbf{w}_h / \rho), \quad (2.31)$$

so that setting

$$a_h(\mathbf{w}_h, \mathbf{v}) = \int_{\Omega} 2\mu \left( \epsilon(\Pi_h(\mathbf{w}_h / \rho)) : \epsilon(\mathbf{v}) - \frac{1}{d} \operatorname{div}(\Pi_h(\mathbf{w}_h / \rho)) \operatorname{div} \mathbf{v} \right) dx,$$

problem (2.27) (2.28) is equivalent to find  $\mathbf{w}_h \in \mathbf{U}_h$  and  $p_h \in L_h$  such that for every  $\mathbf{v} \in \mathbf{U}_h$  and  $q \in L_h$  we have

$$a_h(\mathbf{w}_h, \mathbf{v}) - b(\mathbf{v}, p_h) = \int_{\Omega} (\rho \mathbf{g} + \mathbf{F}) \cdot \mathbf{v} dx, \quad (2.32)$$

$$b(\mathbf{w}_h, q) + \beta h^2 \int_{\Omega} \nabla p_h \cdot \nabla q dx = 0. \quad (2.33)$$

In order to prove convergence of the solutions of (2.32) (2.33) towards that of (2.21) (2.22), three lemmas are established.

**Lemma 4** (Interpolation error). *Let  $\rho \in W^{2,3}(\Omega) \cap W^{1,\infty}(\Omega)$ . Then there exists a constant  $C$  such that*

$$\|\rho q - \Pi_h(\rho q)\|_{1,\Omega} \leq Ch \|q\|_{1,\Omega} \quad \forall q \in W_h. \quad (2.34)$$

*Proof.* Clearly, if  $\rho \in W^{2,3}(\Omega) \cap W^{1,\infty}(\Omega)$  and  $q \in W_h$ , then  $\rho q \in H^1(\Omega)$  and  $\rho q|_K \in H^2(K)$ ,  $\forall K \in \Gamma_h$ . It is well known (see [Cia02a]) that the following estimate holds:

$$\|\rho q - \pi_h(\rho q)\|_{1,\Omega}^2 \leq Ch^2 \sum_{K \in \Gamma_h} |\rho q|_{2,K}^2. \quad (2.35)$$

When  $q \in W_h$ , then  $\partial^2 q / \partial x_i \partial x_j = 0$  on  $K$  and

$$\frac{\partial^2(\rho q)}{\partial x_i \partial x_j} = \frac{\partial^2 \rho}{\partial x_i \partial x_j} q + \frac{\partial \rho}{\partial x_i} \frac{\partial q}{\partial x_j} + \frac{\partial \rho}{\partial x_j} \frac{\partial q}{\partial x_i}.$$

Consequently

$$\begin{aligned} \left\| \frac{\partial^2(\rho q)}{\partial x_i \partial x_j} \right\|_{0,K}^2 &\leq \left\| \frac{\partial^2 \rho}{\partial x_i \partial x_j} \right\|_{0,3,K}^2 \|q\|_{0,6,K}^2 + \left\| \frac{\partial \rho}{\partial x_i} \right\|_{0,\infty,K}^2 \left\| \frac{\partial q}{\partial x_j} \right\|_{0,K}^2 \\ &\quad + \left\| \frac{\partial \rho}{\partial x_j} \right\|_{0,\infty,K}^2 \left\| \frac{\partial q}{\partial x_i} \right\|_{0,K}^2 \\ &\leq C \left( |\rho|_{2,3,K}^2 \|q\|_{0,6,K}^2 + |\rho|_{1,\infty,K}^2 |q|_{1,K}^2 \right). \end{aligned}$$

Since  $\|q\|_{0,6,K} \leq C \|q\|_{1,K}$ , then (2.35) allows to conclude. ■

### 2.3. Numerical approximation of the simplified model

The equivalent discrete proposition of Lemma (1) can be stated.

**Lemma 5** (Isomorphism of the numerical mapping). *Assume  $0 \leq \alpha_g \leq 1$  and  $\alpha_g \in W^{2,3}(\Omega) \cap W^{1,\infty}(\Omega)$ . When  $\rho$  is given by (2.6), the application  $T_h : \mathbf{U}_h \rightarrow \mathbf{U}_h$  defined by*

$$T_h(\boldsymbol{\omega}) = \Pi_h(\rho\boldsymbol{\omega}), \quad \forall \boldsymbol{\omega} \in \mathbf{U}_h \quad (2.36)$$

is an isomorphism of  $\mathbf{U}_h$  uniformly in  $h$ , i.e, there exist two positive constants  $C_1$  and  $C_2$  such that

$$C_1 \|\boldsymbol{\omega}\|_{1,\Omega} \leq \|T_h(\boldsymbol{\omega})\|_{1,\Omega} \leq C_2 \|\boldsymbol{\omega}\|_{1,\Omega} \quad \forall \boldsymbol{\omega} \in \mathbf{U}_h. \quad (2.37)$$

Thus we have  $T_h^{-1}(\mathbf{u}) = \Pi_h(\rho^{-1}\mathbf{u}), \quad \forall \mathbf{u} \in \mathbf{U}_h$ .

*Proof.* Using Lemma 4:

$$\begin{aligned} \|\Pi_h(\rho\boldsymbol{\omega})\|_{1,\Omega} &\leq \|\Pi_h(\rho\boldsymbol{\omega}) - \rho\boldsymbol{\omega}\|_{1,\Omega} + \|\rho\boldsymbol{\omega}\|_{1,\Omega} \\ &\leq Ch \|\boldsymbol{\omega}\|_{1,\Omega} + \|\rho\|_{1,\infty,\Omega} \|\boldsymbol{\omega}\|_{1,\Omega}. \end{aligned}$$

The same applies to  $\rho^{-1}$  instead of  $\rho$ . ■

**Lemma 6** (Bound for the difference between  $a$  and  $a_h$ ). *Under the assumptions of Lemma 5, there exists a constant  $C > 0$  such that*

$$|a(\boldsymbol{\varphi}, \boldsymbol{\psi}) - a_h(\boldsymbol{\varphi}, \boldsymbol{\psi})| \leq Ch \|\boldsymbol{\varphi}\|_{1,\Omega} \|\boldsymbol{\psi}\|_{1,\Omega} \quad \forall \boldsymbol{\varphi}, \boldsymbol{\psi} \in \mathbf{U}_h.$$

*Proof.* By bi-linearity of  $a$  and  $a_h$  one gets  $\forall \boldsymbol{\varphi}, \boldsymbol{\psi} \in \mathbf{U}_h$ :

$$\begin{aligned} &|a(\boldsymbol{\varphi}, \boldsymbol{\psi}) - a_h(\boldsymbol{\varphi}, \boldsymbol{\psi})| = \\ &\left| 2\mu \int_{\Omega} \left( \epsilon \left( \frac{\boldsymbol{\varphi}}{\rho} - \Pi_h \left( \frac{\boldsymbol{\varphi}}{\rho} \right) \right) : \epsilon(\boldsymbol{\psi}) - \frac{1}{d} \operatorname{div} \left( \frac{\boldsymbol{\varphi}}{\rho} - \Pi_h \left( \frac{\boldsymbol{\varphi}}{\rho} \right) \right) \operatorname{div} \boldsymbol{\psi} \right) dx \right|. \end{aligned}$$

Using Lemma 4, there exists two constants  $C_1, C_2$  such that

$$|a(\boldsymbol{\varphi}, \boldsymbol{\psi}) - a_h(\boldsymbol{\varphi}, \boldsymbol{\psi})| \leq C_1 \left\| \frac{\boldsymbol{\varphi}}{\rho} - \Pi_h \left( \frac{\boldsymbol{\varphi}}{\rho} \right) \right\|_{1,\Omega} \|\boldsymbol{\psi}\|_{1,\Omega} \leq C_2 h \|\boldsymbol{\varphi}\|_{1,\Omega} \|\boldsymbol{\psi}\|_{1,\Omega}.$$

■

**Corollary 1** (Well-posedness of the approximated mixture problem). *Assume  $0 \leq \alpha_g \leq 1$  and  $\alpha_g \in W^{2,3}(\Omega) \cap W^{1,\infty}(\Omega)$ , and let  $\epsilon > 0$  be such as in Lemma (3). Then there exists  $h_0 > 0$  such that if  $h \leq h_0$ , Problem (2.32) (2.33) possesses a unique solution  $(\mathbf{w}_h, p_h) \in \mathbf{U}_h \times L_h$ . Moreover there exists a constant  $C$  (independent of  $h$ ) such that  $\|\mathbf{w}_h\|_{1,\Omega} + h \|\nabla p_h\|_{0,\Omega} \leq C$ .*

*Proof.* Under these assumptions, Lemma 6 and Lemma 3 imply that the bilinear form  $a_h(\cdot, \cdot)$  is uniformly coercive on  $\mathbf{U}_h$  when  $h \leq h_0$  is small enough, i.e there exists  $\kappa > 0$  such that if

## Chapter 2. Mathematical analysis of a simplified model

---

$h \leq h_0$

$$a_h(\boldsymbol{\varphi}, \boldsymbol{\varphi}) \geq \kappa \|\boldsymbol{\varphi}\|_{1,\Omega}^2, \quad \forall \boldsymbol{\varphi} \in \mathbf{U}_h. \quad (2.38)$$

Setting  $A((\mathbf{w}, p); (\mathbf{v}, q)) = a_h(\mathbf{w}, \mathbf{v}) - b(\mathbf{v}, p) + b(\mathbf{w}, q) + \beta h^2 \int_{\Omega} \nabla p \cdot \nabla q dx$ , it follows that  $A : (\mathbf{U}_h \times L_h) \times (\mathbf{U}_h \times L_h) \rightarrow \mathbb{R}$  is coercive on  $\mathbf{U}_h \times L_h$  provided with the norm  $\|\mathbf{w}\|_{1,\Omega} + h \|\nabla p\|_{0,\Omega}$ , i.e:

$$A((\mathbf{w}, p); (\mathbf{w}, p)) \geq \kappa \|\mathbf{w}\|_{1,\Omega}^2 + \beta h^2 \|\nabla p\|_{0,\Omega}^2, \quad \forall (\mathbf{w}, p) \in \mathbf{U}_h \times L_h.$$

The proof of this corollary is a consequence of the equivalence of Problem (2.32) (2.33) with  $A((\mathbf{w}_h, p_h); (\mathbf{v}, q)) = \int_{\Omega} (\rho \mathbf{g} + \mathbf{F}) \cdot \mathbf{v} dx$  for every  $(\mathbf{v}, q) \in \mathbf{U}_h \times L_h$ . ■

We now derive error estimates between  $(\mathbf{w}, p)$  and  $(\mathbf{w}_h, p_h)$  and, consequently, between  $\mathbf{u}$  and  $\mathbf{u}_h$ . To do this we assume that the solution of Problem (2.7) (2.8) satisfies

$$(\mathbf{u}, p) \in H^2(\Omega)^d \times H^1(\Omega). \quad (2.39)$$

Let us remark that if assumption (2.39) is true and if  $\alpha_g \in W^{2,3}(\Omega) \cap W^{1,\infty}(\Omega)$ , then  $(\mathbf{w}, p) \in H^2(\Omega)^d \times H^1(\Omega)$  when  $\mathbf{w} = \rho \mathbf{u}$ .

**Proposition 3** (A priori estimates for the mixture problem). *Under the assumptions of Corollary 1 and (2.39), there exists a constant  $C$  independent of  $h$  such that*

$$\|\mathbf{u} - \mathbf{u}_h\|_{1,\Omega} + h \|\nabla(p - p_h)\|_{0,\Omega} \leq Ch. \quad (2.40)$$

*Proof.* By subtraction of (2.32) to (2.21), we obtain for every  $\mathbf{v} \in \mathbf{U}_h$ :

$$a(\mathbf{w} - \mathbf{w}_h, \mathbf{v}) - b(\mathbf{v}, p - p_h) = a_h(\mathbf{w}_h, \mathbf{v}) - a(\mathbf{w}_h, \mathbf{v}), \quad (2.41)$$

and consequently:

$$\begin{aligned} & a(\mathbf{w} - \mathbf{w}_h, \mathbf{w} - \mathbf{w}_h) - b(\mathbf{w} - \mathbf{w}_h, p - p_h) \\ &= a(\mathbf{w} - \mathbf{w}_h, \mathbf{w} - \mathbf{v}) - b(\mathbf{w} - \mathbf{v}, p - p_h) + a_h(\mathbf{w}_h, \mathbf{v} - \mathbf{w}_h) - a(\mathbf{w}_h, \mathbf{v} - \mathbf{w}_h). \end{aligned} \quad (2.42)$$

By subtraction of (2.33) to (2.22), it yields for every  $q \in L_h$ :

$$b(\mathbf{w} - \mathbf{w}_h, q) - \beta h^2 (\nabla p_h, \nabla q)_{0,\Omega} = 0, \quad (2.43)$$

where  $(\nabla p_h, \nabla q)_{0,\Omega} = \int_{\Omega} \nabla p_h \cdot \nabla q dx$  denotes the scalar product in  $L^2(\Omega)^d$ . Consequently:

$$\begin{aligned} & b(\mathbf{w} - \mathbf{w}_h, p - p_h) + \beta h^2 \|\nabla(p - p_h)\|_{0,\Omega}^2 \\ &= b(\mathbf{w} - \mathbf{w}_h, p - q) + \beta h^2 (\nabla p, \nabla(p - p_h))_{0,\Omega} - \beta h^2 (\nabla p_h, \nabla(p - q))_{0,\Omega} \end{aligned} \quad (2.44)$$

### 2.3. Numerical approximation of the simplified model

By adding (2.42), (2.44), and by taking into account Lemmas 3, 6 and using:

$$\begin{aligned} |b(\mathbf{w} - \mathbf{v}, p - p_h)| &\leq \|\mathbf{w} - \mathbf{v}\|_{0,\Omega} \|\nabla(p - p_h)\|_{0,\Omega}, \\ \|\nabla(p_h)\|_{0,\Omega} &\leq \|\nabla(p - p_h)\|_{0,\Omega} + \|\nabla p\|_{0,\Omega}, \end{aligned}$$

we have the following estimate:

$$\begin{aligned} &\|\mathbf{w} - \mathbf{w}_h\|_{1,\Omega}^2 + h^2 \|\nabla(p - p_h)\|_{0,\Omega}^2 \\ &\leq C \left( \|\mathbf{w} - \mathbf{v}\|_{1,\Omega} \|\mathbf{w} - \mathbf{w}_h\|_{1,\Omega} + \|\mathbf{w} - \mathbf{v}\|_{0,\Omega} \|\nabla(p - p_h)\|_{0,\Omega} \right. \\ &\quad \left. + h \|\mathbf{w}_h\|_{1,\Omega} \|\mathbf{v} - \mathbf{w}_h\|_{1,\Omega} + \|\mathbf{w} - \mathbf{w}_h\|_{1,\Omega} \|p - q\|_{0,\Omega} \right. \\ &\quad \left. + h^2 \left( \|\nabla(p - p_h)\|_{0,\Omega} \left( 1 + \|\nabla(p - q)\|_{0,\Omega} \right) + \|\nabla(p - q)\|_{0,\Omega} \right) \right), \end{aligned}$$

for every  $(\mathbf{v}, q) \in \mathbf{U}_h \times L_h$ .

Setting  $\mathbf{v} = \Pi_h \mathbf{w}$ , and  $q = r_h(p)$  (here  $r_h : H^1(\Omega) \rightarrow L_h$  is a Clement's interpolation type; see for instance [Clé75],  $\|p - r_h(p)\|_{s,\Omega} \leq Ch^{1-s}$ ,  $s = 0, 1$ ) in this inequality and using the result of corollary 1 leads to

$$\begin{aligned} &\|\mathbf{w} - \mathbf{w}_h\|_{1,\Omega}^2 + h^2 \|\nabla(p - p_h)\|_{0,\Omega}^2 \\ &\leq Ch \left( \|\mathbf{w} - \mathbf{w}_h\|_{1,\Omega} + h \|\nabla(p - p_h)\|_{0,\Omega} + h \right). \end{aligned}$$

This inequality proves (2.40) when we set  $\mathbf{u} = \mathbf{w}/\rho$  and  $\mathbf{u}_h = \Pi_h(\mathbf{w}_h/\rho)$ . ■

In order to obtain an error estimate of  $\|p - p_h\|_{0,\Omega}$ , we proceed by duality like in [BD88].

**Proposition 4** (A priori estimate for the pressure). *Under the assumptions of Corollary 1 and (2.39), there exists a constant  $C$  such that*

$$\|p - p_h\|_{0,\Omega} \leq Ch. \tag{2.45}$$

*Proof.* We introduce the dual problem: find  $(\mathbf{W}, Q) \in \mathbf{U} \times L$  satisfying

$$a(\mathbf{v}, \mathbf{W}) - b(\mathbf{v}, Q) = 0 \quad \forall \mathbf{v} \in \mathbf{U}, \tag{2.46}$$

$$b(\mathbf{W}, q) = (p - p_h, q)_{0,\Omega} \quad \forall q \in L. \tag{2.47}$$

Of course we have

$$\|\mathbf{W}\|_{1,\Omega} + \|Q\|_{0,\Omega} \leq C \|p - p_h\|_{0,\Omega}. \tag{2.48}$$

## Chapter 2. Mathematical analysis of a simplified model

---

By taking  $q = p - p_h$  in (2.47), it follows

$$\|p - p_h\|_{0,\Omega}^2 = b(\mathbf{W}, p - p_h) = b(\mathbf{W} - R_h \mathbf{W}, p - p_h) + b(R_h \mathbf{W}, p - p_h),$$

where  $R_h \mathbf{W}$  is a Clement's interpolation of  $\mathbf{W}$  on  $\mathbf{V}_h$  ( $\|\mathbf{W} - R_h \mathbf{W}\|_{s,\Omega} \leq Ch^{1-s} \|\mathbf{W}\|_{1,\Omega}$ ,  $s = 0, 1$ ). So we have with an integration by part:

$$\|p - p_h\|_{0,\Omega}^2 \leq Ch \|\nabla(p - p_h)\|_{0,\Omega} \|\mathbf{W}\|_{1,\Omega} + |b(R_h \mathbf{W}, p - p_h)|$$

and by (2.48) and Proposition 3

$$\|p - p_h\|_{0,\Omega}^2 \leq Ch \|p - p_h\|_{0,\Omega} + |b(R_h \mathbf{W}, p - p_h)|. \quad (2.49)$$

It remains to estimate  $|b(R_h \mathbf{W}, p - p_h)|$ .

Relation (2.41) with Lemma 6 imply

$$\begin{aligned} |b(R_h \mathbf{W}, p - p_h)| &\leq |a(\mathbf{w} - \mathbf{w}_h, R_h \mathbf{W})| + |a_h(\mathbf{w}_h, R_h \mathbf{W}) - a(\mathbf{w}_h, R_h \mathbf{W})| \\ &\leq C \|\mathbf{w} - \mathbf{w}_h\|_{1,\Omega} \|R_h \mathbf{W}\|_{1,\Omega} + Ch \|\mathbf{w}_h\|_{1,\Omega} \|R_h \mathbf{W}\|_{1,\Omega} \leq Ch \|\mathbf{W}\|_{1,\Omega}. \end{aligned} \quad (2.50)$$

This last estimate with (2.48) and (2.49) lead to the conclusion. ■

In order to obtain an estimate for  $\|\mathbf{u} - \mathbf{u}_h\|_{0,\Omega}$ , we need to assume some extra hypothesis. Assuming that for any  $\mathbf{G}$  given in  $L^2(\Omega)^3$ , the unique solution  $(\mathbf{u}^*, P^*) \in \mathbf{U} \times L$  of the dual problem

$$\begin{aligned} a(\mathbf{v}, \mathbf{u}^*) - b(\mathbf{v}, P^*) &= (\mathbf{G}, \mathbf{v})_{0,\Omega}, \quad \forall \mathbf{v} \in \mathbf{U}, \\ b(\mathbf{u}^*, q) &= 0, \quad \forall q \in L, \end{aligned}$$

belongs to  $H^2(\Omega)^d \times H^1(\Omega)$ , and assuming that there exists  $C$  independent of  $\mathbf{G}$  satisfying:

$$\|\mathbf{u}^*\|_{2,\Omega} + \|P^*\|_{1,\Omega} \leq C \|\mathbf{G}\|_{0,\Omega}. \quad (2.51)$$

**Remark 10.** This hypothesis requires some regularity conditions on the domain shape and on the regularity of  $\alpha_g$ . For instance, this hypothesis holds if  $\alpha_g \in D(\Omega)$  and  $\Omega$  is convex.

Then we can formulate the following proposition:

**Proposition 5** (A priori estimate for the mixture velocity in  $L_2$  norm). *Under the hypothesis of Corollary 1 and (2.39), and that the condition (2.51) is satisfied, then there exists a constant  $C$  such that*

$$\|\mathbf{u} - \mathbf{u}_h\|_{0,\Omega} \leq Ch^2. \quad (2.52)$$

### 2.3. Numerical approximation of the simplified model

*Proof.* Let  $\mathbf{u}^* \in \mathbf{U}$  and  $P^* \in L$  given by

$$a(\mathbf{v}, \mathbf{u}^*) - b(\mathbf{v}, P^*) = (\mathbf{w} - \mathbf{w}_h, \mathbf{v})_{0,\Omega}, \quad \forall \mathbf{v} \in \mathbf{V}, \quad (2.53)$$

$$b(\mathbf{u}^*, q) = 0, \quad \forall q \in L. \quad (2.54)$$

Using (2.51) we have

$$\|\mathbf{u}^*\|_{2,\Omega} + \|P^*\|_{1,\Omega} \leq C \|\mathbf{w} - \mathbf{w}_h\|_{0,\Omega}. \quad (2.55)$$

Taking  $\mathbf{v} = \mathbf{w} - \mathbf{w}_h$  in (2.53),

$$\begin{aligned} \|\mathbf{w} - \mathbf{w}_h\|_{0,\Omega}^2 &= a(\mathbf{w} - \mathbf{w}_h, \mathbf{u}^*) - b(\mathbf{w} - \mathbf{w}_h, P^*) \\ &= a(\mathbf{w} - \mathbf{w}_h, \mathbf{u}^* - \Pi_h \mathbf{u}^*) - b(\mathbf{w} - \mathbf{w}_h, P^* - R_h P^*) \\ &\quad + a(\mathbf{w} - \mathbf{w}_h, \Pi_h \mathbf{u}^*) - b(\mathbf{w} - \mathbf{w}_h, R_h P^*), \end{aligned} \quad (2.56)$$

where  $R_h$  is a Clement's interpolation type. Since  $\|P^* - R_h P^*\|_{s,\Omega} \leq Ch^{1-s} \|P^*\|_{s,\Omega}$ ,  $s = 0, 1$  and referring to (2.55), we obtain

$$|a(\mathbf{w} - \mathbf{w}_h, \mathbf{u}^* - \Pi_h \mathbf{u}^*) - b(\mathbf{w} - \mathbf{w}_h, P^* - R_h P^*)| \leq Ch \|\mathbf{w} - \mathbf{w}_h\|_{1,\Omega} \|\mathbf{w} - \mathbf{w}_h\|_{0,\Omega}. \quad (2.57)$$

In order to treat the last part of (2.56), we use (2.41) and (2.43) to get

$$\begin{aligned} &|a(\mathbf{w} - \mathbf{w}_h, \Pi_h \mathbf{u}^*) - b(\mathbf{w} - \mathbf{w}_h, R_h P^*)| = \\ &\left| b(\Pi_h \mathbf{u}^*, p - p_h) + a_h(\mathbf{w}_h, \Pi_h \mathbf{u}^*) - a(\mathbf{w}_h, \Pi_h \mathbf{u}^*) - \beta h^2 (\nabla p_h, \nabla R_h P^*)_{0,\Omega} \right|. \end{aligned} \quad (2.58)$$

Using (2.54) and Proposition 3 in this expression we have

$$\begin{aligned} &|b(\Pi_h \mathbf{u}^*, p - p_h)| \leq |b(\Pi_h \mathbf{u}^* - \mathbf{u}^*, p - p_h)| + |b(\mathbf{u}^*, p - p_h)| \\ &\leq C \|\Pi_h \mathbf{u}^* - \mathbf{u}^*\|_{0,\Omega} \|\nabla(p - p_h)\|_{0,\Omega} \leq Ch^2 \|\mathbf{u}^*\|_{2,\Omega} \leq Ch^2 \|\mathbf{w} - \mathbf{w}_h\|_{0,\Omega}. \end{aligned} \quad (2.59)$$

Moreover

$$\begin{aligned} &|a_h(\mathbf{w}_h, \Pi_h \mathbf{u}^*) - a(\mathbf{w}_h, \Pi_h \mathbf{u}^*)| \\ &\leq |a_h(\mathbf{w}_h, \Pi_h \mathbf{u}^* - \mathbf{u}^*) - a(\mathbf{w}_h, \Pi_h \mathbf{u}^* - \mathbf{u}^*)| + |a_h(\mathbf{w}_h, \mathbf{u}^*) - a(\mathbf{w}_h, \mathbf{u}^*)| \\ &= \left| \int_{\Omega} 2\mu[\epsilon(\Pi_h(\mathbf{w}_h/\rho) - \mathbf{w}_h/\rho) : \epsilon(\Pi_h \mathbf{u}^* - \mathbf{u}^*)] dx \right. \\ &\quad \left. - \int_{\Omega} \left[ \frac{1}{d} \operatorname{div}(\Pi_h(\mathbf{w}_h/\rho) - \mathbf{w}_h/\rho) \operatorname{div}(\Pi_h \mathbf{u}^* - \mathbf{u}^*) \right] dx \right| \\ &\quad + \left| \int_{\Omega} 2\mu[\epsilon(\Pi_h(\mathbf{w}_h/\rho) - \mathbf{w}_h/\rho) : \epsilon(\mathbf{u}^*)] - \frac{1}{d} \operatorname{div}(\Pi_h(\mathbf{w}_h/\rho) - \mathbf{w}_h/\rho) \operatorname{div}(\mathbf{u}^*) \right] dx \right| \\ &\leq C \|\Pi_h(\mathbf{w}_h/\rho) - \mathbf{w}_h/\rho\|_{1,\Omega} \|\Pi_h \mathbf{u}^* - \mathbf{u}^*\|_{1,\Omega} + \|\Pi_h(\mathbf{w}_h/\rho) - \mathbf{w}_h/\rho\|_{0,\Omega} \|\mathbf{u}^*\|_{2,\Omega} \\ &\leq Ch^2 \|\mathbf{w}_h\|_{1,\Omega} \|\mathbf{u}^*\|_{2,\Omega} \leq Ch^2 \|\mathbf{w} - \mathbf{w}_h\|_{0,\Omega}. \end{aligned}$$

It follows that

$$|a(\mathbf{w} - \mathbf{w}_h, \Pi_h \mathbf{u}^*) - b(\mathbf{w} - \mathbf{w}_h, r_h P^*)| \leq Ch^2 \|\mathbf{w} - \mathbf{w}_h\|_{0,\Omega}. \quad (2.60)$$

Finally (2.56), (2.57), and (2.60) imply

$$\|\mathbf{w} - \mathbf{w}_h\|_{0,\Omega} \leq Ch^2. \quad (2.61)$$

Finally the estimate on  $\mathbf{u} - \mathbf{u}_h$  is obtained from the estimate on  $\mathbf{w} - \mathbf{w}_h$  by considering Lemma 5. ■

In order to finish this section, we establish an error estimate for  $\|\mathbf{u}_g - \mathbf{u}_{g,h}\|_{1,\Omega}$  by considering (2.9) and (2.29).

**Proposition 6** (A priori estimate for the gas velocity). *Under the hypothesis of Proposition 4, and if  $\mathbf{u}_g \in H^2(\Omega)^d$ , there exists a constant  $C$  independent of  $h \leq h_0$  such that*

$$\|\mathbf{u}_g - \mathbf{u}_{g,h}\|_{1,\Omega} \leq Ch. \quad (2.62)$$

*Proof.* Setting:

$$f(\mathbf{v}) = \int_{\Omega} p \nabla \alpha_g \cdot \mathbf{v} dx + \int_{\Omega} \alpha_g p \operatorname{div}(\mathbf{v}) dx + \int_{\Omega} (\alpha_g \rho_g \mathbf{g} + D \frac{\alpha_g \rho}{\rho_l} \mathbf{u}) \cdot \mathbf{v} dx,$$

and

$$f_h(\mathbf{v}) = \int_{\Omega} p_h \nabla \alpha_g \cdot \mathbf{v} dx + \int_{\Omega} \alpha_g p_h \operatorname{div}(\mathbf{v}) dx + \int_{\Omega} (\alpha_g \rho_g \mathbf{g} + D \frac{\alpha_g \rho}{\rho_l} \mathbf{u}_h) \cdot \mathbf{v} dx.$$

We have

$$\begin{aligned} |f(\mathbf{v}) - f_h(\mathbf{v})| &\leq C \{ \|p - p_h\|_{0,\Omega} \|\alpha_g\|_{1,3,\Omega} \|\mathbf{v}\|_{0,6,\Omega} \\ &\quad + \|p - p_h\|_{0,\Omega} \|\mathbf{v}\|_{1,\Omega} + \|\mathbf{u} - \mathbf{u}_h\|_{1,\Omega} \|\mathbf{v}\|_{1,\Omega} \} \end{aligned} \quad (2.63)$$

and a consequence of Propositions 4 and 3 is that

$$|f(\mathbf{v}) - f_h(\mathbf{v})| \leq Ch \|\mathbf{v}\|_{1,\Omega} \quad \forall \mathbf{v} \in \mathbf{U}. \quad (2.64)$$

Thanks to the continuous and bilinear form  $l(.,.)$  (2.23), Problems (2.9) and (2.29) can be written as

$$l(\mathbf{u}_g, \mathbf{v}) = f(\mathbf{v}) \quad \forall \mathbf{v} \in \mathbf{U}, \quad (2.65)$$

and

$$l(\mathbf{u}_{g,h}, \mathbf{v}) = f_h(\mathbf{v}) \quad \forall \mathbf{v} \in \mathbf{U}_h. \quad (2.66)$$

## 2.4. Numerical experiments for the simplified problem

Of course we have  $l(\mathbf{u}_g - \mathbf{u}_{g,h}, \mathbf{v}) = f(\mathbf{v}) - f_h(\mathbf{v})$ ,  $\forall \mathbf{v} \in \mathbf{V}_h$ , and if  $\mathbf{u}_g \in H^2(\Omega)^3$

$$\begin{aligned} |l(\mathbf{u}_g - \mathbf{u}_{g,h}, \mathbf{u}_g - \mathbf{u}_{g,h})| &= |l(\mathbf{u}_g - \mathbf{u}_{g,h}, \mathbf{u}_g - \Pi_h \mathbf{u}_g) + l(\mathbf{u}_g - \mathbf{u}_{g,h}, \Pi_h \mathbf{u}_g - \mathbf{u}_{g,h})| \\ &\leq |l(\mathbf{u}_g - \mathbf{u}_{g,h}, \mathbf{u}_g - \Pi_h \mathbf{u}_g)| + |f(\Pi_h \mathbf{u}_g - \mathbf{u}_{g,h}) - f_h(\Pi_h \mathbf{u}_g - \mathbf{u}_{g,h})|. \end{aligned} \quad (2.67)$$

Using (2.64), we finally have

$$l(\mathbf{u}_g - \mathbf{u}_{g,h}, \mathbf{u}_g - \mathbf{u}_{g,h}) \leq Ch \left( \|\mathbf{u}_g - \mathbf{u}_{g,h}\|_{1,\Omega} + \|\Pi_h \mathbf{u}_g - \mathbf{u}_{g,h}\|_{1,\Omega} \right).$$

With the coercivity of  $l(\cdot, \cdot)$  on  $\mathbf{U} \times \mathbf{U}$  we obtain the conclusion. ■

In this section, we have discussed the hypothesis required to obtain a priori estimates of the error in different norms for the numerical approximations  $\mathbf{u}_h$ ,  $p_h$  and  $\mathbf{u}_{g,h}$ .

## 2.4 Numerical experiments for the simplified problem

Numerical experiments are prepared when  $d = 2$  and  $d = 3$  to check the expected convergence rates with a given  $\alpha_g$ . Convergence is checked by computing the errors in the relevant norms and rates defined by:

$$e_i(m) = \|m - m_h\|_{i,\Omega}, \quad r_i(m) = \frac{\log(e_i(m)/\hat{e}_i(m))}{\log(\hat{h}/h)},$$

where  $m$  denotes the velocity, pressure,  $i = 0, 1$ ,  $e$  and  $\hat{e}$  denoting respectively the errors computed on two consecutive meshes  $\mathcal{T}_h$  and  $\mathcal{T}_{\hat{h}}$ .

Here the mathematical system described in (2.1) and (2.2) is solved with the numerical approximations (2.27) and (2.28), performed with the open source software Fenics [Aln+15]. The resolution was performed with a direct solver using PETSC [Abh+18]. The python code corresponding to these experiments is given in the Appendix (A.3).

### 2.4.1 Numerical experiment on a rectangle

Let  $\Omega = (0, 1)^2$ , discretized with  $N^2$  vertices cut into triangles. In this case  $\rho(x_1, x_2)$  is given by:

$$\rho(x_1, x_2) = 1 - \rho_1 \left( \frac{1}{2} \tanh \left( \gamma \left( x_2 - \frac{1}{2} \right) \right) + \frac{1}{2} \right),$$

and the right hand side of (2.1) is computed such that the velocity field  $\mathbf{u}(x_1, x_2)$  and the pressure  $p(x_1, x_2)$  are given by:

$$\mathbf{u}(x_1, x_2) = \frac{1}{\rho(x_1, x_2)} \begin{pmatrix} 4(x_2 - 1)x_2(x_1 - 1)^2 x_1^2 (x_2 - \frac{1}{2}) \\ -(4(x_1 - \frac{1}{2}))x_2^2 x_1 (x_2 - 1)^2 (x_1 - 1) \end{pmatrix}, \quad (2.68)$$

## Chapter 2. Mathematical analysis of a simplified model

---

$$p(x_1, x_2) = 1 \left( x_1 x_2 - \frac{1}{4} \right), \int_{\Omega} p(x_1, x_2) dx_1 dx_2 = 0. \quad (2.69)$$

The constants  $p_0, u_0$  are chosen to quantify the sensitivity of the model to variation of density. It can be checked that:

$$\operatorname{div}(\rho \mathbf{u}) = 0 \text{ in } \Omega \text{ and } \mathbf{u} = 0 \text{ on } \partial\Omega. \quad (2.70)$$

The results are reported in Tables 2.1 and 2.2 when  $\rho_1 = 0$  (constant density) and  $\rho_1 = 1, \gamma = 10$  (variable density). The result is observed in the  $H_1$  norm for  $\mathbf{u}$  and  $L_2$  norm for  $p$ . As predicted in Proposition 3, the  $H_1$  norm of the error of the velocity  $\mathbf{u}$  converges at linear rate. Finally, the convergence rate for the  $L_2$  norm of  $\mathbf{u}$  is very close to  $O(h^2)$ , as expected by proposition 5.

$N$	$e_0(p)$	$r_0(p)$	$e_1(u_m)$	$r_1(u)$	$e_0(u)$	$r_0(u)$
10	1.2475e-02	-	1.8051e-02	-	9.5680e-04	-
14	1.1593e-02	2.18e-01	1.4323e-02	6.88e-01	7.9796e-04	5.40e-01
20	9.6923e-03	5.02e-01	1.0996e-02	7.41e-01	6.4996e-04	5.75e-01
28	7.3793e-03	8.10e-01	8.1998e-03	8.72e-01	4.8666e-04	8.60e-01
40	4.9873e-03	1.10	5.6973e-03	1.02	3.1915e-04	1.18
56	3.1956e-03	1.32	3.8978e-03	1.13	1.9568e-04	1.45
80	1.8924e-03	1.47	2.5645e-03	1.17	1.0871e-04	1.65
113	1.1078e-03	1.55	1.7106e-03	1.17	5.8846e-05	1.78
160	6.3827e-04	1.59	1.1480e-03	1.15	3.0841e-05	1.86
226	3.6817e-04	1.59	7.8123e-04	1.11	1.5958e-05	1.91
320	2.1205e-04	1.59	5.3566e-04	1.09	8.1291e-06	1.94
452	1.2315e-04	1.57	3.7126e-04	1.05	4.1317e-06	1.96
640	7.1606e-05	1.56	2.5824e-04	1.04	2.0806e-06	1.97
905	4.1914e-05	1.55	1.8068e-04	1.03	1.0473e-06	1.98
1280	2.4622e-05	1.53	1.2678e-04	1.02	5.2588e-07	1.99

Table 2.1 – Results in 2D with constant density ( $\rho_1 = 0$ ).

As expected, the errors with a varying density are systematically more important than the incompressible case  $\rho = 1$  constant. The values of the error for various input densities are reported in Figure 2.1

## 2.4. Numerical experiments for the simplified problem

$N$	$e_0(p)$	$r_0(p)$	$e_1(u_m)$	$r_1(u)$	$e_0(u)$	$r_0(u)$
10	1.9882e-02	-	2.9164e-02	-	1.6887e-03	-
14	1.8678e-02	1.86e-01	2.3294e-02	6.68e-01	1.3733e-03	6.14e-01
20	1.5784e-02	4.72e-01	1.8042e-02	7.16e-01	1.0894e-03	6.49e-01
28	1.2184e-02	7.69e-01	1.3578e-02	8.45e-01	8.0851e-04	8.86e-01
40	8.3556e-03	1.06	9.4977e-03	1.00	5.3099e-04	1.18
56	5.4073e-03	1.29	6.5017e-03	1.13	3.2702e-04	1.44
80	3.2147e-03	1.46	4.2542e-03	1.19	1.8243e-04	1.64
113	1.8759e-03	1.56	2.8135e-03	1.20	9.8962e-05	1.77
160	1.0718e-03	1.61	1.8725e-03	1.17	5.1901e-05	1.86
226	6.1159e-04	1.62	1.2665e-03	1.13	2.6847e-05	1.91
320	3.4834e-04	1.62	8.6516e-04	1.10	1.3667e-05	1.94
452	2.0030e-04	1.60	5.9846e-04	1.07	6.9412e-06	1.96
640	1.1549e-04	1.58	4.1589e-04	1.05	3.4930e-06	1.97
905	6.7159e-05	1.56	2.9087e-04	1.03	1.7573e-06	1.98
1280	3.9252e-05	1.55	2.0408e-04	1.02	8.8203e-07	1.99

Table 2.2 – Results in 2D with variable density ( $\rho_1 = 0.5$ ,  $\gamma = 10$ ).

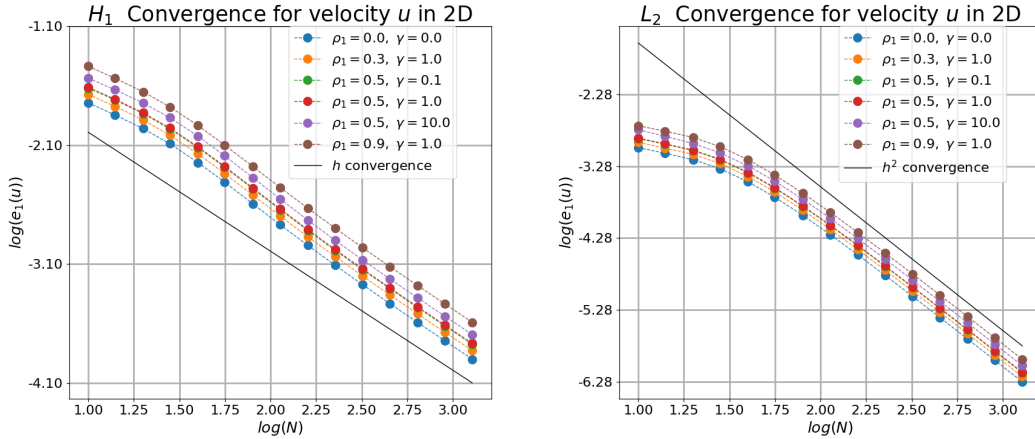


Figure 2.1 – Errors of the velocity for various input densities.

### 2.4.2 Numerical experiment on a cube

Let  $\Omega = (0, 1)^3$  discretized with  $N^3$  vertices cut into tetrahedrons. The density given by:

$$\rho(x_1, x_2, x_3) = 1 - \rho_1 \left( \frac{1}{2} \tanh \left( \gamma \left( x_3 - \frac{1}{2} \right) \right) + \frac{1}{2} \right),$$

the right hand side in (2.1) is computed such that the velocity field  $\mathbf{u}(x_1, x_2, x_3)$  and the pressure  $p(x_1, x_2, x_3)$  are given by:

$$\mathbf{u}(x_1, x_2, x_3) = \frac{1}{\rho(x_1, x_2, x_3)}$$

## Chapter 2. Mathematical analysis of a simplified model

$$\left( \begin{array}{l} (4(2x_2x_3 - x_2 - x_3 + 1))(x_2 - 1)x_2(x_1 - 1)^2(-x_3 + x_2)(x_3 - 1)x_1^2x_3 \\ -4(x_2 - 1)^2(-x_3 + x_1)x_2^2(x_1 - 1)(2x_1x_3 - x_1 - x_3 + 1)(x_3 - 1)x_1x_3 \\ (4(x_2 - 1))x_2(-x_2 + x_1)(x_1 - 1)(2x_1x_2 - x_1 - x_2 + 1)(x_3 - 1)^2x_1x_3^2 \end{array} \right),$$

$$p(x_1, x_2, x_3) = 1 \left( x_1x_2x_3 - \frac{1}{8} \right), \int_{\Omega} p(x_1, x_2, x_3) dx_1 dx_2 dx_3 = 0. \quad (2.71)$$

$$\operatorname{div}(\rho \mathbf{u}) = 0 \text{ in } \Omega \text{ and } \mathbf{u} = 0 \text{ on } \partial\Omega. \quad (2.72)$$

where again  $\rho_1, \gamma$  are parameters to quantify the sensitivity of the model to variation of density.

The numerical numbers of the errors and the convergence rates are given in Tables 2.3 and 2.4. As expected, the number of iterations of the gmres solver  $N_{iter}$  is  $O(1/h)$ .

$N$	$e_0(p)$	$r_0(p)$	$e_1(u)$	$r_1(u)$	$N_{iter}$
10	2.1659e-03	-	1.4218e-03	-	16
14	1.2639e-03	1.60	1.0299e-03	9.58e-01	22
20	8.6205e-04	1.07	7.6989e-04	8.16e-01	33
28	6.6104e-04	7.89e-01	5.8928e-04	7.95e-01	48
40	4.8304e-04	8.80e-01	4.2899e-04	8.90e-01	74
56	3.3334e-04	1.10	3.0383e-04	1.03	108
80	2.0911e-04	1.31e	2.0311e-04	1.13	185
113	1.2671e-04	1.45	1.3530e-04	1.18	294
160	7.4389e-05	1.53	8.9891e-05	1.18	497

Table 2.3 – Results in 3D with constant density ( $\rho_1 = 0$ ).

$N$	$e_0(p)$	$r_0(p)$	$e_1(u)$	$r_1(u)$	$N_{iter}$
10	2.4480e-03	-	2.1377e-03	-	15
14	1.6590e-03	1.16	1.6135e-03	8.36e-01	22
20	1.3048e-03	6.73e-01	1.2394e-03	7.40e-01	32
28	1.0656e-03	6.02e-01	9.6399e-04	7.47e-01	48
40	8.0283e-04	7.94e-01	7.1062e-04	8.55e-01	72
56	5.6394e-04	1.05e	5.0690e-04	1.00	104
80	3.5774e-04	1.28	3.3891e-04	1.13	185
113	2.1731e-04	1.44	2.2418e-04	1.20	291
160	1.2689e-04	1.55	1.4733e-04	1.20	521

Table 2.4 – Results in 3D with variable density ( $\rho_1 = 0.5, \gamma = 10$ ).

## 3 Comparison with a water-column experiment

In this chapter, the model presented in chapter 1 is applied to a water-column experiment. The results of our model are compared with some experimental data that can be found in [Gem19].

### 3.1 Introduction to water-column experiments

A cylindrical water-column reactor is filled with water up to an initial height  $H_{initial}$ . At the bottom, some gas is injected through small holes. As the gas bubbles ascend through the water column, the liquid starts to move, typically moving upwards in the centre of the column and downwards close to the outer wall of the cylinder. In the original paper [Gem+18], the evolution in time of the system is computed, and an average over a time sample of the physical quantities are compared with numerical results. On average and in an homogeneous regime, the solution can be approached by a steady-state method: our model aims to reproduce this solution, and to study the impact of the parameters on the solution.

In this kind of experiment, the liquid is put into motion by the presence of the gas injected in the domain. The drag coefficient and model of drag force is the paramount element influencing the hydrodynamics.

### 3.2 Setup of the experiment

The experiment (Figure 3.1) consists into a vertical cylindrical container of total height of  $3.25[m]$ , diameter  $D_c = 0.4[m]$  filled with water up to  $x_3 = H_{initial} = 4D_c = 1.6[m]$ . At the bottom of the cylinder, at  $x_3 = 0$ , different flows of gas (air) are injected through  $n_{sp} = 92$  perforated spargers with small holes of radius  $r_{sp} = 1[mm]$ , and injection velocity  $\mathbf{u}_{g,in}$ . The experimental data (profile of velocity  $\mathbf{u}$  and gas distribution  $\alpha_g$ ) are measured at  $x_3 = 1[m]$ .

Once the gas is progressively injected, the fluid in the column is put into movement, and after some time, the movement is expected to be close to stationary (in a regime with low gas

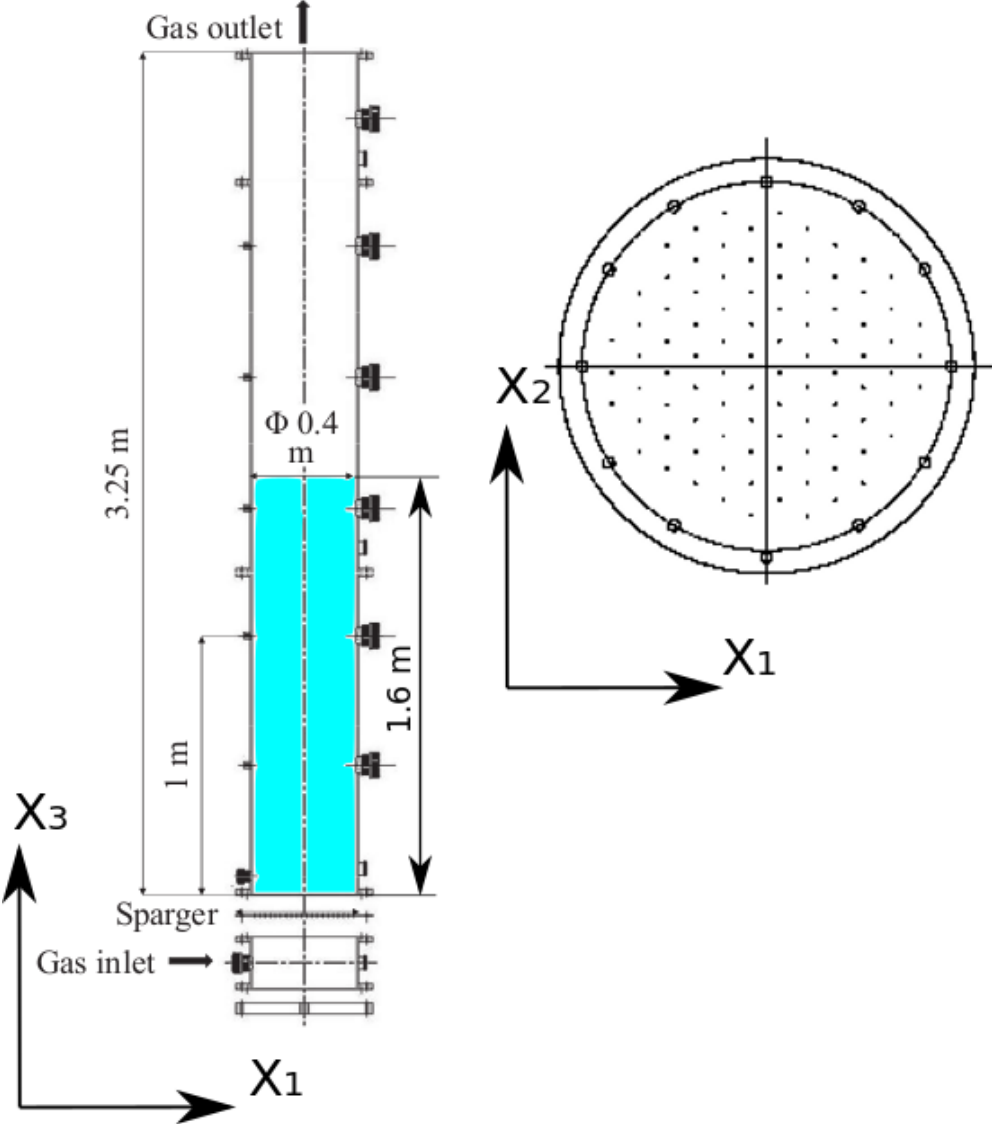


Figure 3.1 – Setup of the column from [Gem+18]: water-column (left), the small holes of the sparger (right).

volumetric ratio, low  $\Phi_{in}$  ). At the top surface the gas escapes through the outflow surface  $\Gamma_{out}$ . Measuring the new height of the mixture  $H_{cylinder}$  and comparing it to  $H_{initial}$  gives the average of volumetric ratio of gas in the column:

$$\frac{H_{cylinder} - H_{initial}}{H_{cylinder}} = \frac{\int_{\Omega} \alpha_g dx}{\int_{\Omega} dx} = \bar{\alpha}_g. \quad (3.1)$$

The measurements involve the average gas ratio  $\bar{\alpha}_g$ , the radial profile of the gas ratio  $\alpha_g$  and the radial profile of the mixture velocity  $\mathbf{u}$  at fixed height  $x_3 = 1[m]$ .

### 3.3 Setup of the gas source term

The primary parameter in this experiment is the amount of gas injected in the system (per unit of time), represented in our model by  $\dot{\alpha}_{source}$ . We chose to consider a relatively low amount of gas flow, leading to the homogeneous flow. When the amount of gas injected increases, the flow becomes turbulent and the regime is heterogeneous. The amount of gas and the average velocity at  $\Gamma_{in}$  is defined with the gas superficial velocity  $\Phi_{in}[m/s]$ :

$$\Phi_{in} = \frac{\int_{\Gamma_{in}} \alpha_g \mathbf{u}_g \cdot \mathbf{n} ds}{\int_{\Gamma_{in}} ds},$$

which corresponds to a volumetric source term  $\dot{\alpha}_{source}[1/s]$  satisfying:

$$\Phi_{in} = \frac{\int_{\Gamma_{in}} \alpha_g \mathbf{u}_g \cdot \mathbf{n} ds}{\int_{\Gamma_{in}} ds} = \frac{\int_{\Omega_{prod}} \dot{\alpha}_{source} dx}{\int_{\Gamma_{in}} ds}, \quad (3.2)$$

where  $\Omega_{prod} \subset \Omega$  is the volume,  $\dot{\alpha}_{source}$  is positive. In order to represent the fact that the production is performed at the inflow, the subregion  $\Omega_{prod}$  is close to the bottom of the water-column at a specific height  $H_s$ . The typical source term  $\dot{\alpha}_{source}$  is illustrated in Figure 3.2.

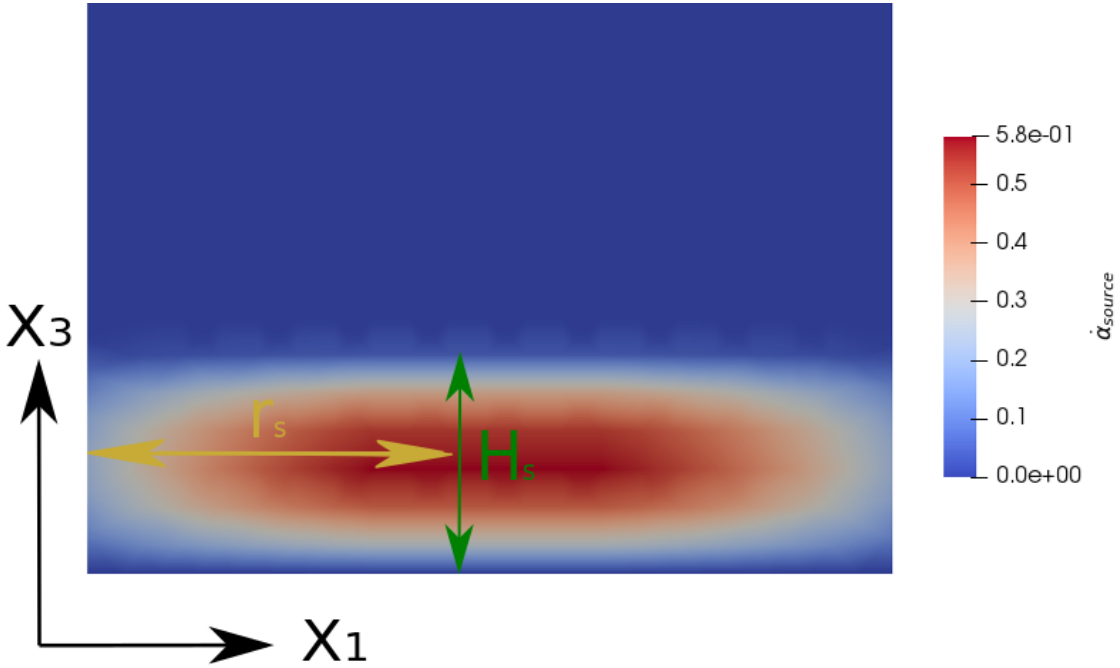


Figure 3.2 – Source term at the bottom of the water column, which decrease at a quadratic rate up to  $x_3 = H_s$ . The radial profile is set by  $r_s$ : the profile is also quadratic with respect to the radial position.

### 3.4 Algorithm setup

#### 3.4.1 Boundary conditions

In addition to the boundary conditions defined in section 1.4, the boundary at the bottom of the water column is denoted  $\Gamma_{in}$ , such that  $\partial\Omega = \Gamma_{out} \cup \Gamma_0 \cup \Gamma_{in}$ . The boundary conditions are modified such that:

$$K\nabla\alpha_g \cdot \mathbf{n} = 0, \text{ on } \partial\Omega, \quad (3.3)$$

$$\mathbf{u} \cdot \mathbf{n} = 0, \text{ on } \partial\Omega \setminus \Gamma_{in}, \quad (3.4)$$

$$(\boldsymbol{\tau} \cdot \mathbf{n}) \cdot \mathbf{t}_i = 0 \text{ on } \partial\Omega \setminus \Gamma_{in}, \quad i = 1, 2. \quad (3.5)$$

$$\mathbf{u} = \mathbf{0}, \text{ on } \Gamma_{in}, \quad (3.6)$$

$$(\boldsymbol{\tau}_g \cdot \mathbf{n}) \cdot \mathbf{n} = \alpha_g p_0, \text{ on } \Gamma_{out}, \quad (3.7)$$

$$\text{with : } p_0 = \frac{\int_{\Gamma_{out}} (\boldsymbol{\tau} \cdot \mathbf{n}) \cdot \mathbf{n} ds}{\int_{\Gamma_{out}} ds}, \quad (3.8)$$

$$(\boldsymbol{\tau}_g \cdot \mathbf{n}) \cdot \mathbf{t}_i = 0, \text{ on } \partial\Omega \setminus \Gamma_{in}, i = 1, 2. \quad (3.9)$$

$$\mathbf{u}_g \cdot \mathbf{n} = 0, \text{ on } \Gamma_0, \quad (3.10)$$

$$\mathbf{u}_g = \mathbf{0}, \text{ on } \Gamma_{in}. \quad (3.11)$$

The boundary conditions consist into a full sliding on the lateral wall of the cylinder, with a zero velocity at the bottom for both velocities  $\mathbf{u}$  and  $\mathbf{u}_g$ . Once the discretization is adapted to these boundary conditions, the algorithm can be used.

### 3.4.2 Mesh

The generation of the mesh is used with the gmsh open source software [GR09] with the Frontal-Delaunay algorithm for mesh generation, for both the surface and the volume, corresponding to [Sch97]. An example sample of the gmsh code generating the cylinder is given in the appendix A.2. A mesh contains 37'322 vertices and 203'394 elements is shown in Figure 3.4.3.

### 3.4.3 Initial conditions

Equipped with the discretized spaces corresponding to the boundary conditions, the finite element discretization detailed in section 1.11 can be applied together with the algorithm described in section 1.9.

The initialisation starts with the simplified lift (1.50) used for  $\mathbf{u}_{g,h}(k=0)$  as a starting point, i.e:

$$\mathbf{u}_{g,h}(k=0) = -\frac{d^2}{18\mu_L}((\rho_l - \rho_g)\mathbf{g}).$$

Let  $\Delta t > 0$  be a time-step. A first value of  $\alpha_{g,h}$  is obtained taking as input  $\mathbf{u}_{g,h}(k=0)$ ,  $\alpha_{g,h}^{r=0} = 0$ , and looking for  $\alpha_{g,h}^{r+1} \in W_h$ :

$$\begin{aligned} & \int_{\Omega} \frac{\alpha_{g,h}^{r+1} - \alpha_{g,h}^r}{\Delta t} \omega dx + \int_{\Omega} \operatorname{div}(\alpha_{g,h} \mathbf{u}_{g,h}) \omega dx + \int_{\Omega} K \nabla \alpha_{g,h} \nabla \omega dx \\ & + \frac{h C_S}{2|\mathbf{u}_{g,h}|} \int_{\Omega} (\mathbf{u}_{g,h} \cdot \nabla \omega) (\operatorname{div}(\alpha_{g,h} \mathbf{u}_{g,h}) - \dot{\alpha}_{source}) dx = \int_{\Omega} \dot{\alpha}_{source} \omega dx, \end{aligned} \quad (3.12)$$

for all  $\omega \in W_h$ . Equation (1.101) is solved successively for a number of iterations  $N_0$  such that the virtual total amount of time elapsed is  $T_0 = N_0 \Delta t = H_{cylinder} / \mathbf{u}_{g,h}(k=0)$ . Then  $\alpha_{g,h}(k=0)$ ,  $\mathbf{u}_{g,h}(k=0)$  and  $\mathbf{u}_h(k=0) = \mathbf{0}$  are given and the algorithm 1.9 can be started.

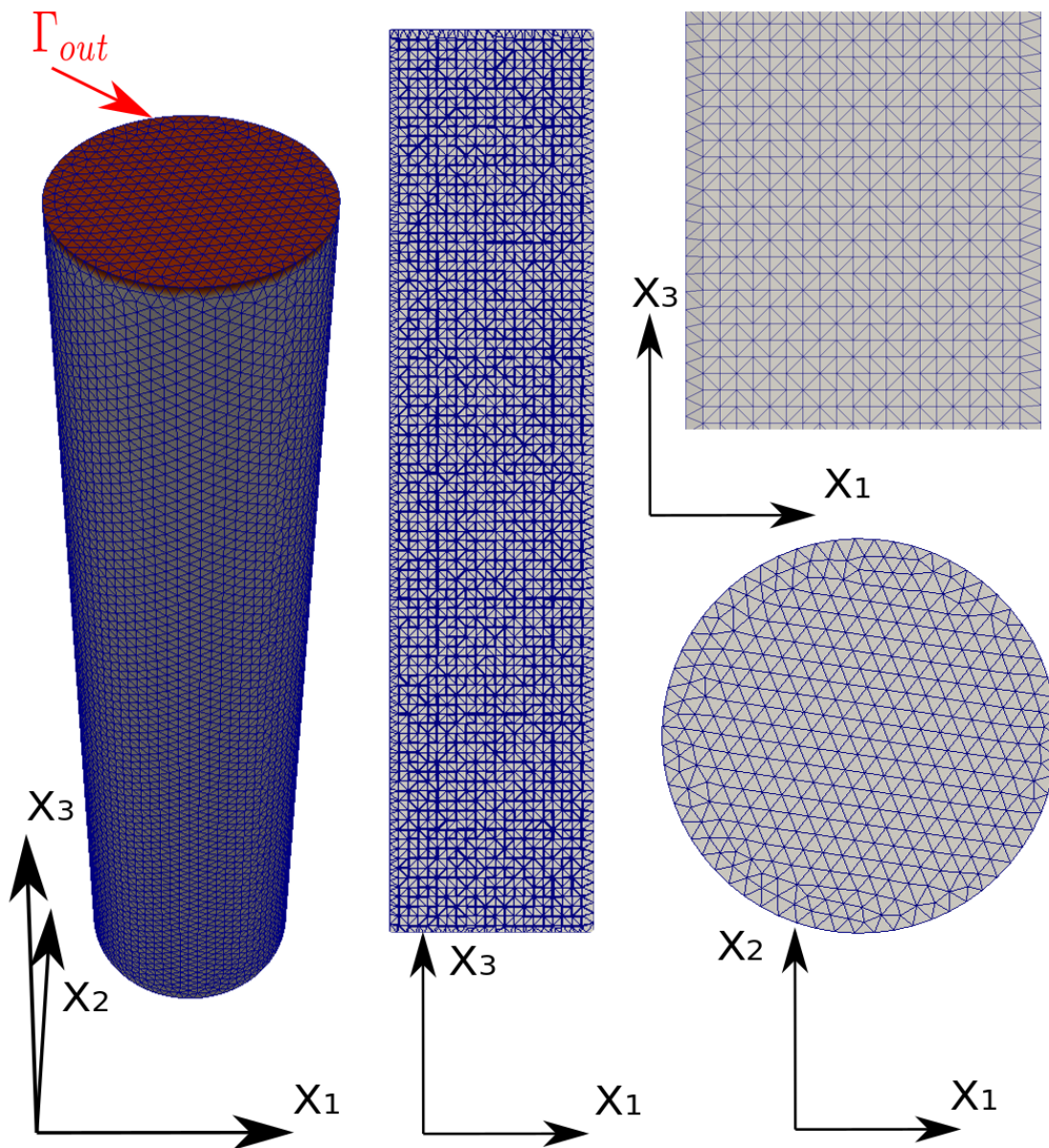


Figure 3.3 – Mesh of the water-column with mesh parameter of size  $h = 0.02$ . On the left a 3D view, then a cut in the middle in the  $x_2$ -plane at  $x_2 = 0.0$ , on the right a zoom on the mesh and below the mesh from above at  $x_3 = H_{cylinder}$ .

### Initialisation of the viscosity

If the viscous terms dominates the convective terms  $(\rho_h \mathbf{u}_h \cdot \nabla) \mathbf{u}_h$  in (3.13) and  $(\rho_g \alpha_{g,h} \mathbf{u}_{g,h} \cdot \nabla) \mathbf{u}_{g,h}$  in (3.14) (see details in chapter 1, (1.99)(1.100)) the resolution of the following system

of equations should converge, as long as the unknown  $\alpha_g$  is small.

$$\begin{aligned}
 & \int_{\Omega} (\rho_h \mathbf{u}_h \cdot \nabla) \mathbf{u}_h \cdot \mathbf{v} dx + \int_{\Omega} 2\mu \left( \epsilon(\mathbf{u}_h) : \epsilon(\mathbf{v}) - \frac{1}{3} \operatorname{div}(\mathbf{u}_h) \operatorname{div}(\mathbf{v}) \right) dx \\
 & - \int_{\Omega} p_h \operatorname{div}(\mathbf{v}) dx - \int_{\Gamma_{out}} \xi_h(\mathbf{v} \cdot \mathbf{n}) ds = \int_{\Omega} (\mathbf{F} + \rho_h \mathbf{g}) \cdot \mathbf{v} dx, \\
 & \int_{\Omega} \operatorname{div}(\rho_h \mathbf{u}_h) q dx = 0, \\
 & \int_{\Gamma_{out}} \sigma(\mathbf{u}_h \cdot \mathbf{n}) ds = 0,
 \end{aligned} \tag{3.13}$$

$$\begin{aligned}
 & \int_{\Omega} (\rho_g \alpha_{g,h} \mathbf{u}_{g,h} \cdot \nabla) \mathbf{u}_{g,h} \cdot \mathbf{v}_g dx + \int_{\Omega} (\rho_g \dot{\alpha}_{source}) \mathbf{u}_{g,h} \cdot \mathbf{v}_g dx \\
 & - \int_{\Gamma_{out}} (\alpha_{g,h} p_0)(\mathbf{v}_g \cdot \mathbf{n}) ds + \int_{\Omega} 2\mu_g \left( \epsilon(\mathbf{u}_{g,h}) : \epsilon(\mathbf{v}_g) - \frac{1}{3} \operatorname{div}(\mathbf{u}_{g,h}) \operatorname{div}(\mathbf{v}_g) \right) dx \\
 & = \int_{\Omega} \alpha_{g,h} (p_h) \operatorname{div}(\mathbf{v}_g) dx + \int_{\Omega} (p_h) \nabla \alpha_{g,h} \cdot \mathbf{v}_g dx + \int_{\Omega} \alpha_{g,h} \rho_g \mathbf{g} \cdot \mathbf{v}_g dx \\
 & + \int_{\Omega} D \frac{\rho_h}{\rho_l} \alpha_{g,h} (\mathbf{u}_h - \mathbf{u}_{g,h}) \cdot \mathbf{v}_g dx,
 \end{aligned} \tag{3.14}$$

In the present approach, the viscosity of the mixture  $\mu$  is given by:

$$\mu = \mu_L + \mu_T = \mu_L + C\rho l^2 |\epsilon(\mathbf{u}_h)| = \mu_L + C_T \rho |\epsilon(\mathbf{u}_h)|. \tag{3.15}$$

The laminar part of the viscosity is taken as  $\mu_L = 0.13[kg/ms]$ , from a calibration of the drag force (see 3.5.3). If the algorithm of section 1.9 starts initially with (3.15), the algorithm does not converge. An analysis shows that an artificially increased viscosity conditions the problem well for the initialisation of (3.13) in [KLS06]. Therefore, the algorithm of section 1.9 is split into two phases:

1. The problem is solved with a constant artificially increased viscosity  $\mu = \mu_{init} = 4.5[kg/ms]$  in (1.99). When this problem converges to a stationary solution, the next stage is computed.
2. Then, the turbulent model of Smagorinski (3.15) is used for the turbulent viscosity  $\mu_T = C_T \rho_h |\epsilon(\mathbf{u}_h)|$ , using as initialisation the solution of 1.

Then, the final solution considered is the solution obtained after the successive convergence of each one of the two phases: the number of iterations  $N$  reported is the sum of the iterations used in 1 and 2.

### 3.4.4 Stop criteria

The convergence is checked following a criteria between two iterations  $k$  and  $k + 1$ . In order to check the convergence to a steady solution, we chose to check the relative  $L^2$  discrepancy norm will be checked to be lower than some fixed tolerance  $TOL$ :

$$\max\left(\frac{\|\mathbf{u}^{k+1} - \mathbf{u}^k\|_{L^2(\Omega)}}{\|\mathbf{u}^{k+1}\|_{L^2(\Omega)}}, \frac{\|\alpha_g^{k+1} - \alpha_g^k\|_{L^2(\Omega)}}{\|\alpha_g^{k+1}\|_{L^2(\Omega)}}, \frac{\|\mathbf{u}_g^{k+1} - \mathbf{u}_g^k\|_{L^2(\Omega)}}{\|\mathbf{u}_g^{k+1}\|_{L^2(\Omega)}}\right) < TOL, \quad (3.16)$$

Notice that the norm above is not relevant to converge to a solution when one of this solution is zero: however, in the following numerical experiments it is not the case. In addition the following ratio is checked to be very close to one:

$$1 - TOL < \left| \frac{\int_{\Gamma_{out}} \alpha_g^{k+1} \mathbf{u}_g^{k+1} \cdot \mathbf{n} ds}{\int_{\Omega} \dot{\alpha}_{source} dx} \right| < 1 + TOL, \quad (3.17)$$

ensuring that the volumetric production of gas is indeed expelled out of the domain through  $\Gamma_{out}$ .

## 3.5 Numerical results

### 3.5.1 Reference solution

#### Numerical default parameters

By default the numerical and physical parameters presented in Table 3.1 will be used. The main parameters are the viscosities coefficients  $\mu_L$  and  $C_T$ . The viscosity  $\mu_L$  is scaled with respect to the drag force model in order to obtain an average gas distribution value  $\bar{\alpha}_g$  corresponding to experimental data. (see section 3.5.3 below) The coefficient  $C_T$  was scaled to obtain the correct order of magnitude of the velocity  $\mathbf{u}$ . The sensitivity of the results with some of these parameters is discussed in the following.

#### Typical solution

The solution obtained with parameters in Table 3.1 is the reference solution  $u_{h,ref}$ .

Name	Notation	Value	Cross-reference
Initial water height without gas	$H_{initial}$	1.6[m]	section 3.2
Experimental average $\alpha_g$	$\bar{\alpha}_g$ [%]	10.78	(3.1)
Height of the water with gas	$H_{cylinder}$	1.772[m]	(3.1)
Diameter of the water column	$D_c$	0.4[m]	section 3.2
Source height	$H_s$	$H_{cylinder}/16$ [m]	section 3.3
Source radius	$r_s$	0.2 [m]	section 3.3
Gas inflow	$\Phi_{in}$	0.03 [m/s]	section 3.3
Liquid density	$\rho_l$	1000 [kg/m <sup>3</sup> ]	(1.8)
Gas density	$\rho_g$	2.5 [kg/m <sup>3</sup> ]	(1.8)
Laminar viscosity	$\mu_L$	0.13 [kg/ms]	(3.15)
Artificial initial viscosity	$\mu_{init}$	4.5 [kg/ms]	initialisation (1)
Gas viscosity	$\mu_g$	0.13 [kg/ms]	section 3.5.5
Laminar diffusion coefficient	$K_L$	$2e-4$ [m <sup>2</sup> /s]	section 3.5.5
Turbulent diffusion coefficient	$K_T$	$2e-4$ [m <sup>2</sup> ]	section 3.5.5
Turbulent viscosity coefficient	$C_T$	$1e-2 D_c^2$ [m <sup>2</sup> ]	(3.15)
Bubble diameter	$d$	7.0 [mm]	section 3.5.3
Drag coefficient	$D$	$16\mu_L/d^2$	section 3.5.3
Time-step	$\Delta t$	2[s]	section 3.4.3
Gas iterations	$N_g$	10	section 3.4.3
Newton iterations	$N_{Ne}$	3	(1.102)
Tolerance of algorithm	TOL	$2e-3$	section 3.4.3, (3.16)
Element size	$h$	0.02 [m]	section 3.4.1

Table 3.1 – Default parameters.

This reference solution is shown in Figure 3.4 and Figure 3.5. The velocity is ascending in the middle of the water column and going down on the sides, while the gas volumetric ratio  $\alpha_g$  is slightly more concentrated in the middle. The gas velocity  $\mathbf{u}_g$  is ascending, with a stronger amplitude in the middle.

The difference between a numerical solution  $u_h$  and the reference solution  $u_{h,ref}$  will be quantified with:

$$\Delta_\infty(u_h) = 100 \frac{\|u_h - u_{h,ref}\|_{L^\infty(\Omega)}}{\|u_{h,ref}\|_{L^\infty(\Omega)}}, \quad (3.18)$$

$$\Delta_0(u_h) = 100 \frac{\|u_h - u_{h,ref}\|_{L^2(\Omega)}}{\|u_{h,ref}\|_{L^2(\Omega)}}. \quad (3.19)$$

The idea is that the difference in the  $\Delta_\infty$  norm illustrates if there is a localised difference in a particular area, where the  $\Delta_0$  norm reflects a global difference between two given solutions.

Chapter 3. Comparison with a water-column experiment

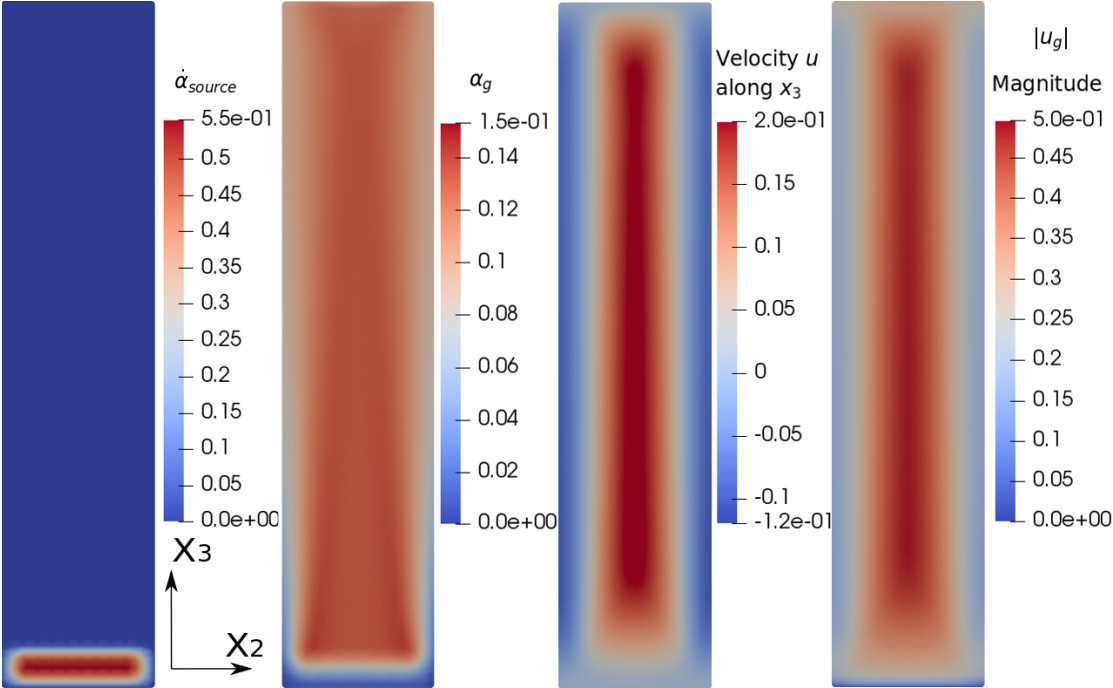


Figure 3.4 – Results in the middle of the water column at  $x_1 = 0$ . From left to right: the source term, the amount of gas  $\alpha_g$ , the vertical component of the velocity  $\mathbf{u}$  and the amplitude of the gas velocity  $\mathbf{u}_g$ .

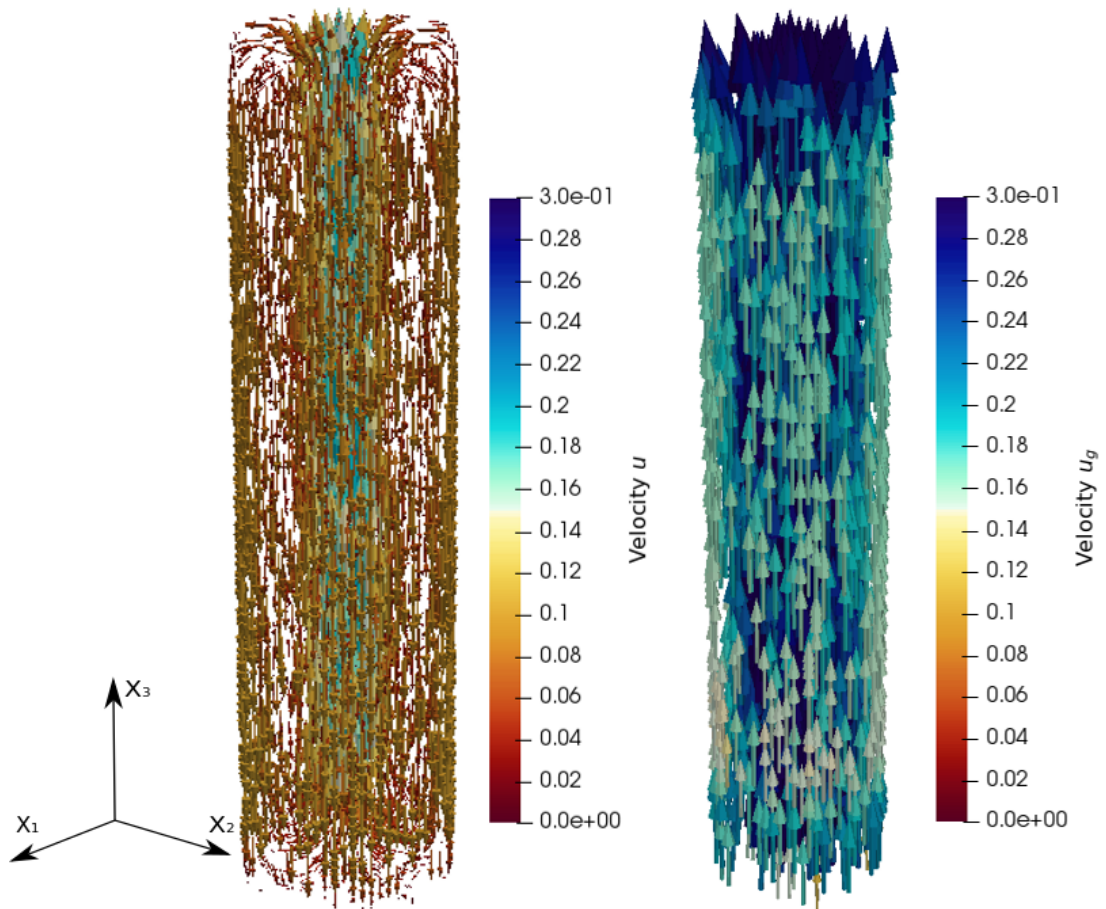


Figure 3.5 – Illustration of the velocity fields of the mixture  $\mathbf{u}$  on the left and gas velocity  $\mathbf{u}_g$  on the right.

### 3.5.2 Influence of the mesh size

A first simple experiment is performed with six sizes of mesh ranging from  $h = 0.04$  to  $h = 0.0075$ . Convergence can be observed in Table 3.2 and Figure 3.6. Accurate results are observed when the mesh size is  $h \leq 0.02[m]$ , thus the default setting is  $h = 0.02[m]$ .

$h[m]$	$\bar{\alpha}_g$ [%]	$\ \mathbf{u}\ _{L^\infty(\Omega)}$	$N$
0.04	10.30	0.25	28
0.03	10.23	0.23	27
0.02	10.21	0.22	13
0.015	10.21	0.22	13
0.01	10.23	0.22	13
0.0075	10.23	0.22	13

Table 3.2 – Results for different mesh sizes.  $\bar{\alpha}_g$  denotes the average gas distribution obtained, and  $N$  the number of iterations of the algorithm.

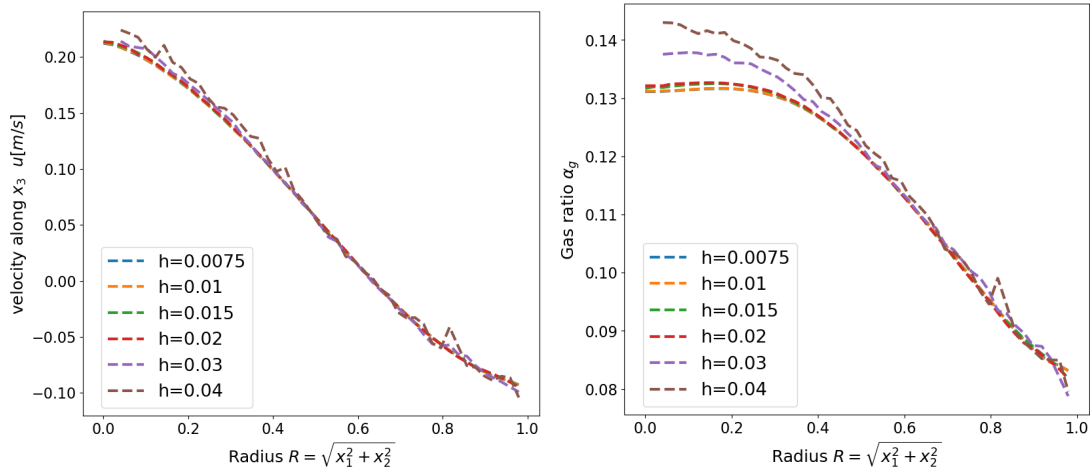


Figure 3.6 – Profile at  $x_3 = 1[m]$ : on the left the profile of the velocity  $\mathbf{u}$ , on the right the profile of the gas distribution  $\alpha_g$ .

### 3.5.3 Influence of the drag coefficient

The drag force is driving the interaction between the two phases liquid and gas. As such, depending on the model of Drag force, the constant viscosity  $\mu_L$  appearing in the Drag force can be calibrated with respect to the measurements of  $\alpha_g$ . The considered models of drag forces compared in this section are (see section 1.6):

Model 1

$$D = \frac{18\mu_L r}{d^2}, \text{ where } \mu_L = 0.13[kg/ms]. \quad (3.20)$$

In this first model, the only free parameter is the linear viscosity  $\mu_L$ . The average diameter of the bubbles is  $d$  and  $r$  is the packing sphere factor. The value  $\mu_L = 0.13[\text{kg}/\text{m}\cdot\text{s}]$  is the value that fits best the average gas distribution  $\bar{\alpha}_g$  with experimental data.

Model 2

$$D = \max\left(\left[1 + 0.15Re_b^{0.687}\right], \frac{0.44Re_b}{24}\right) \frac{18\mu_L r}{d^2}, \text{ where } \mu_L = 0.025[\text{kg}/\text{m}\cdot\text{s}], \quad (3.21)$$

$$Re_b = \frac{\rho_l |\mathbf{u} - \mathbf{u}_g| d}{\mu_L}.$$

Both models are similar when the Reynolds number is low. The drag coefficient as a function of  $\mu_L$  is reported in Figure 3.7.

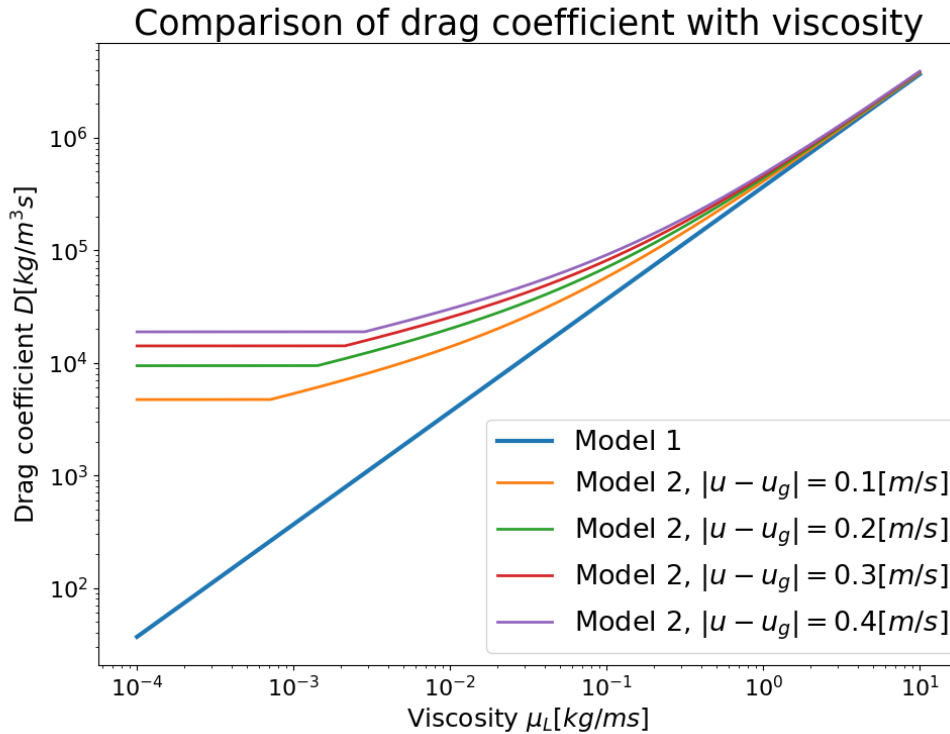


Figure 3.7 – Comparison of the amplitude of the drag coefficients  $D$  for the two models with respect to the viscosity, for  $\rho_l = 1000[\text{kg}/\text{m}^3]$  and  $d = 7[\text{mm}]$ , assuming different constant values of  $|\mathbf{u} - \mathbf{u}_g|$  for (3.21).

**Model 1, eq (3.20)**

The model (3.20) is considered with different values of the viscosity  $\mu_L$ . Results are reported in Figure 3.8. Note that the method does not converge to a stationary solution when  $\mu_L > 0.195[\text{kg}/\text{m}\cdot\text{s}]$ . As the drag coefficient increases, the gas velocity sticks more to the fluid flow, and therefore the lift decreases, the gas is expelled more slowly out of the domain,  $\alpha_g$  increases

### Chapter 3. Comparison with a water-column experiment

---

as illustrated in Figure 3.9. Table 3.3 quantifies the change of the results with different values of viscosity  $\mu_L$ : note that the relationship between  $\mu_L$  and  $\bar{\alpha}_g$  is close to linear.

$\mu_L [kg/ms]$	$\Delta_\infty(\mathbf{u}_h)$	$\Delta_\infty(\alpha_{g,h})$	$\Delta_\infty(\mathbf{u}_{g,h})$	$\Delta_0(\mathbf{u}_h)$	$\Delta_0(\alpha_{g,h})$	$\Delta_0(\mathbf{u}_{g,h})$	$\bar{\alpha}_g [\%]$
0.0325	45.3%	69.2%	156.0%	40.0%	69.4%	236.0%	3.08%
0.065	24.1%	43.1%	54.1%	19.2%	43.5%	79.2%	5.72%
0.13	0.0%	0.0%	0.0%	0.0%	0.0%	0.0%	10.21%
0.195	12.2%	33.8%	18.4%	7.6%	36.7%	26.6%	14.01%

Table 3.3 – Comparison of the model (3.20) with different values of  $\mu_L$ . Discrepancy with respect to the default value  $\mu_L = 0.13 [kg/ms]$ .

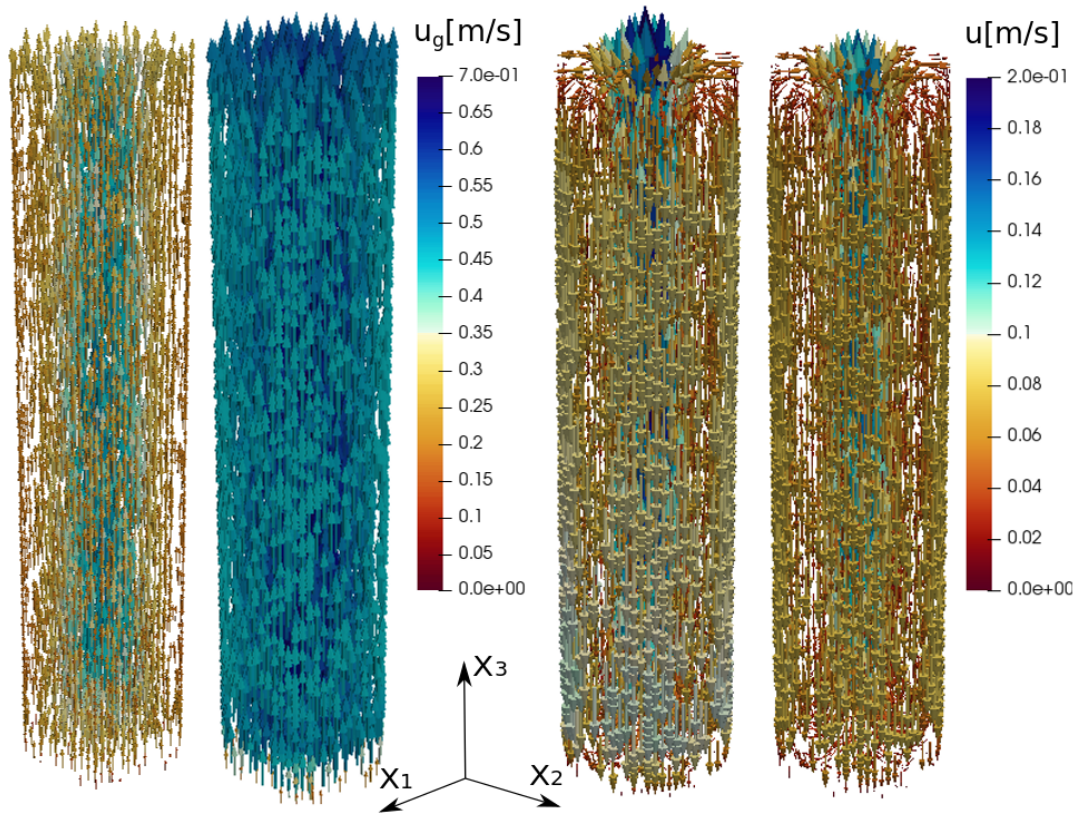


Figure 3.8 – The model (3.20): from the left to the right: gas velocity  $\mathbf{u}_g$  when  $\mu_L = 0.13$  [kg/ms], then  $\mu_L = 0.065$  [kg/ms]. Next the mixture velocity field  $\mathbf{u}$  obtained for  $\mu_L = 0.13$  [kg/ms] and  $\mu_L = 0.065$  [kg/ms].

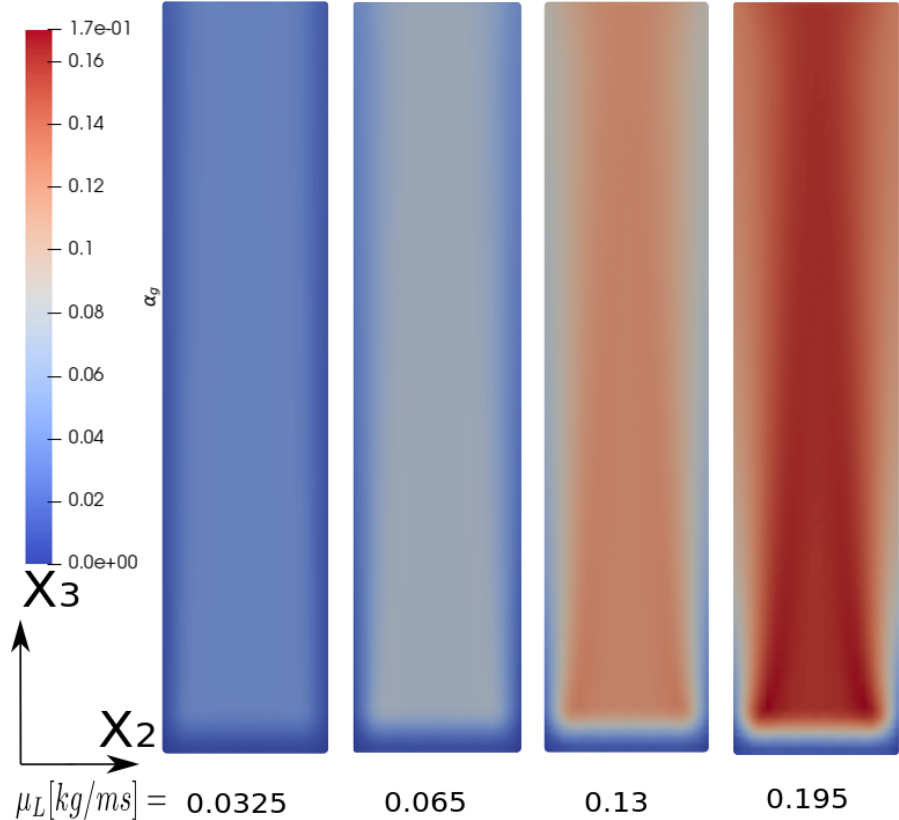


Figure 3.9 – The model (3.20): from the left to the right: the viscosity ranges from  $\mu_L = 0.0325[kg/ms]$  to  $\mu_L = 0.195[kg/ms]$ , and the associated solution  $\alpha_g$  increases as well.

**Model 2, eq (3.21)**

Next the comparison of different viscosity with the second Drag model (3.21) is reported quantitatively in Table 3.3. Similar results are obtained: for a lower value of  $\mu_L$ , the drag force decreases. Inversely, an important value of the viscosity implies that the gas velocity  $\mathbf{u}_g$  will stick more to the mixture velocity  $\mathbf{u}$ . For the second model, the relationship between  $\mu_L$  and  $\bar{\alpha}_g$  is not linear any more, and the results are less sensitive to the viscosity.

Finally in Figure 3.10, the two models are compared to obtain the same average value of  $\bar{\alpha}_g = 10.2\%$ , with values respectively of  $\mu_L = 0.13[kg/ms]$  and  $\mu_L = 0.025[kg/ms]$ . The second model (3.21) exhibits more gas at the bottom of the column, and less at the top. The vertical gas velocity is more important in the second model close to the wall.

$\mu_L[kg/ms]$	$\Delta_\infty(\mathbf{u}_h)$	$\Delta_\infty(\alpha_{g,h})$	$\Delta_\infty(\mathbf{u}_{g,h})$	$\Delta_0(\mathbf{u}_h)$	$\Delta_0(\alpha_{g,h})$	$\Delta_0(\mathbf{u}_{g,h})$	$\bar{\alpha}_g[\%]$
0.01	21.9%	20.9%	21.1%	15.2%	20.7%	27.0%	8.14%
0.02	6.9%	6.13%	5.5%	4.4%	6.0%	6.5%	9.63%
0.025	0%	0%	0%	0%	0%	0%	10.23%
0.04	32.1%	17.9%	13.8%	15.2%	15.5%	14.0%	11.8%
0.08	48.5%	49.9%	29.8%	29.1%	49.5%	33.8%	15.2%

Table 3.4 – Comparison of the model (3.21) with different values of  $\mu_L$ . Discrepancy with respect to the default value  $\mu_L = 0.025[kg/ms]$ .

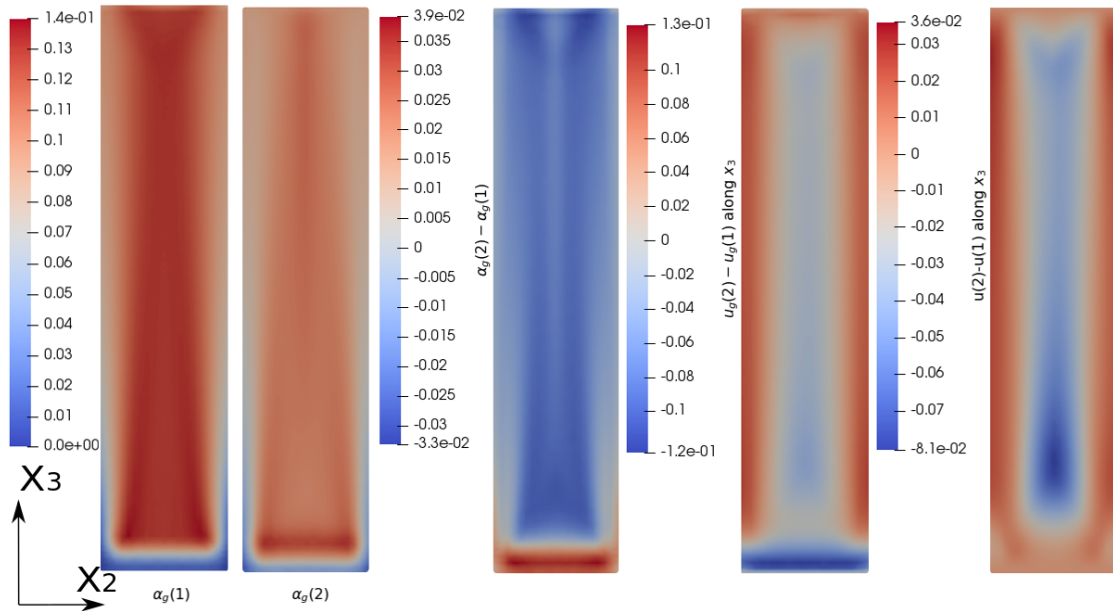


Figure 3.10 – Comparison between the two models (3.20) and (3.21).

As a conclusion, in this section, two models have been used: the first model (3.20) in the Stokes approximation, which corresponds to a Drag force that is linear with the respect to the difference of phase velocity  $\mathbf{u} - \mathbf{u}_g$ . The second model (3.21) considers a non-linear law that

### Chapter 3. Comparison with a water-column experiment

depends on the Reynolds number, and retrieves the first model when the Reynolds number is small. The constant viscosity  $\mu_L$  has been calibrated for each model to reproduce a correct average amplitude for the gas volumetric distribution  $\alpha_g$ . In the following, by default the first model (3.20) will be used.

#### 3.5.4 Comparison of simplified models

In this paragraph, the validity of the Boussinesq approximation (1.7.3) to obtain the velocity  $\mathbf{u}$  is verified. In addition, the resolution of the gas velocity  $\mathbf{u}_g$  in algorithm 1.9 (chapter 1) is compared in two cases:

A Use the standard formulation of this thesis (3.14), look for the gas velocity  $\mathbf{u}_g$ :

$$\begin{aligned}
 & \int_{\Omega} (\rho_g \alpha_{g,h} \mathbf{u}_{g,h} \cdot \nabla) \mathbf{u}_{g,h} \cdot \mathbf{v}_{g,h} dx + \int_{\Omega} (\rho_g \dot{\alpha}_{source}) \mathbf{u}_{g,h} \cdot \mathbf{v}_g dx \\
 & - \int_{\Gamma_{out}} (\alpha_{g,h} p_0) (\mathbf{v}_g \cdot \mathbf{n}) ds + \int_{\Omega} 2\mu_g \left( \epsilon(\mathbf{u}_{g,h}) : \epsilon(\mathbf{v}_g) - \frac{1}{3} \text{div}(\mathbf{u}_{g,h}) \text{div}(\mathbf{v}_g) \right) dx \\
 & = \int_{\Omega} \alpha_{g,h} (p_h) \text{div}(\mathbf{v}_g) dx + \int_{\Omega} (p_h) \nabla \alpha_{g,h} \cdot \mathbf{v}_g dx + \int_{\Omega} \alpha_{g,h} \rho_g \mathbf{g} \cdot \mathbf{v}_g dx \\
 & + \int_{\Omega} D \frac{\rho_h}{\rho_l} \alpha_{g,h} (\mathbf{u}_h - \mathbf{u}_{g,h}) \cdot \mathbf{v}_g dx, \forall \mathbf{v}_g
 \end{aligned} \tag{3.14}$$

B Use the approximation (1.50) for the gas velocity:

$$\mathbf{u}_{g,h} = \mathbf{u}_h - \frac{d^2}{18\mu_L} ((\rho_l - \rho_g) \mathbf{g}). \tag{3.22}$$

#### Sensitivity due to Boussinesq approximation

Table 3.5 show that the solutions with and without Boussinesq approximation differ only up to 2%. Therefore the Boussinesq approximation can be considered as very accurate. The number of iterations for the algorithm was similar.

Gaz condition	$\Delta_{\infty}(\mathbf{u}_h)$	$\Delta_{\infty}(\alpha_{g,h})$	$\Delta_{\infty}(\mathbf{u}_{g,h})$	$\Delta_{\infty}(\xi_h)$	$N_1$	$N_2$
A	2.2%	1.1%	1.0%	0.05%	12	13
B	2.2%	1.5%	1.0%	0.05%	13	14

Table 3.5 – Comparison with the Boussinesq approximation. The number of iterations of the algorithm does not change much. The number  $N_1$  is the number of iterations obtained with Boussinesq approximation and  $N_2$  without it.

#### Comparison with explicit gas velocity model

Comparisons between models *A* to *B* are reported in Table 3.6 and Figure 3.11. The results show almost no differences in the average behaviour, although they exhibit local differences located at the very bottom and at the top of the outflow. This can be explained because the boundary conditions are taken into account through the resolution of the finite element approximation in case *A* : on the contrary in case *B*, the velocity exhibit no change on the top surface, and is numerically imposed to zero at the bottom of the domain, resulting in a discrete discontinuity regarding  $\mathbf{u}_g$ . In conclusion, the explicit model is sufficient for a simple geometry such as a water-column, up to the boundary conditions that have to be carefully treated.

$\Delta_\infty(\mathbf{u}_h)$	$\Delta_\infty(\alpha_{g,h})$	$\Delta_\infty(\mathbf{u}_{g,h})$	$\Delta_0(\mathbf{u}_h)$	$\Delta_0(\alpha_{g,h})$	$\Delta_0(\mathbf{u}_{g,h})$
2.2%	18.9%	34.2%	1.2%	1.4%	3.2%

Table 3.6 – Difference with explicit model without Boussinesq approximation in  $L^\infty$  and  $L^2$  norms.

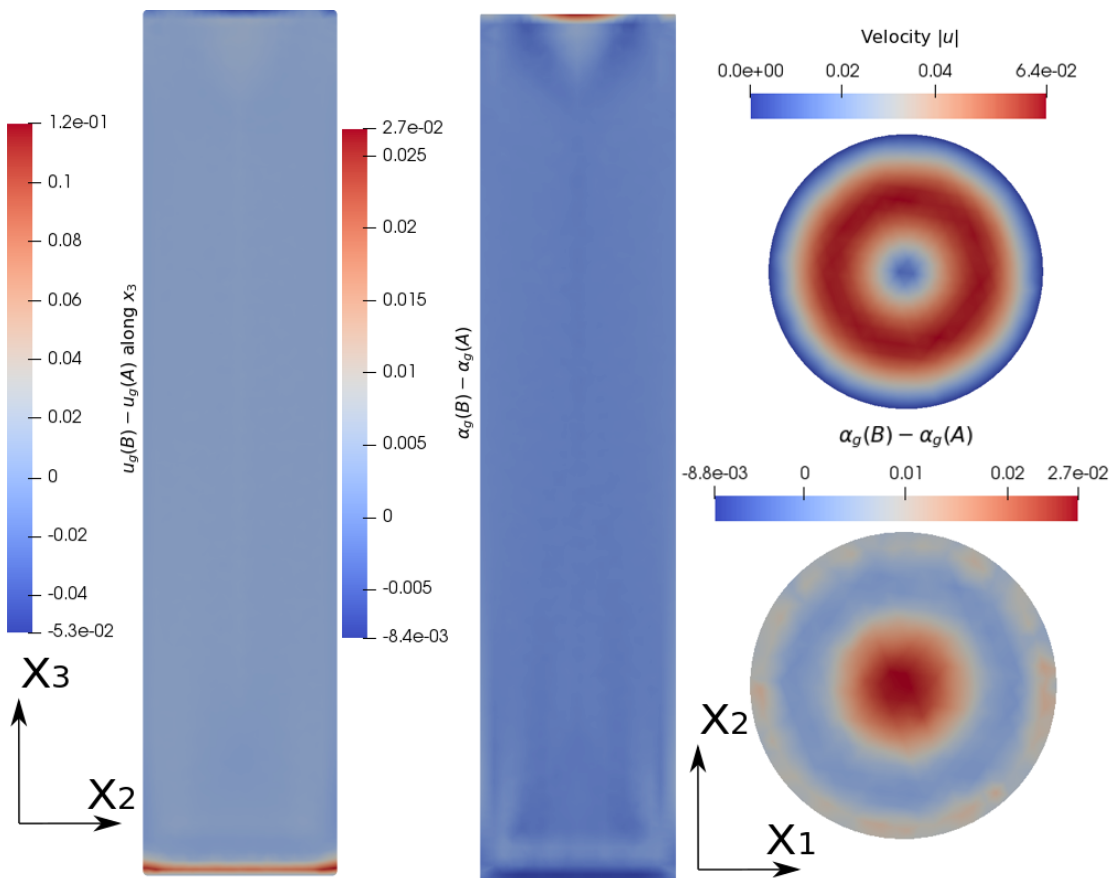


Figure 3.11 – Results in the middle of the water column at  $x_1 = 0$  on the left, and on the surface  $\Gamma_{out}$  on the right between cases *A* and *B*.

### 3.5.5 Sensitivity to gas diffusion and to gas viscosity

#### Gas viscosity

In this section, the gas viscosity is considered as constant, and the influence of a constant gas viscosity going from  $\mu_g = 1e-3[kg/ms]$  to  $\mu_g = 10[kg/ms]$  is measured. Table 3.7 quantifies the difference between the solutions with different gas viscosities.

Viscosity $\mu_g[kg/ms]$	$\Delta_\infty(\alpha_{g,h})$	$\Delta_\infty(\mathbf{u}_{g,h})$	$\Delta_0(\alpha_{g,h})$	$\Delta_0(\mathbf{u}_{g,h})$	$\bar{\alpha}_g[\%]$
1e-3	13.4%	50.2%	1.1%	4.1%	10.2%
1e-2	9.0%	16.6%	0.9%	2.3%	10.2%
1e-1	0.0%	0.0%	0.0%	0.0%	10.2%
1	11.0%	14.1%	2.5%	4.1%	10.2%
10	34.4%	27.3%	11.7%	16.1%	10.1%

Table 3.7 – Difference of results of simulations with different constant gas viscosities  $\mu_g[kg/ms]$ , with as reference the case  $\mu_g = 1e-1[kg/ms]$ .

The number of iterations  $N$  of the algorithm to converge was unchanged. In regards of those numbers, the gas viscosity  $\mu_g$  does not change much the results, except if  $\mu_g > 1[kg/ms]$ . In Figure 3.12, it is shown that an increase of the gas viscosity results on an increase on the gas vertical velocity close to the wall, and a small decrease in the centre of the water-column. Consequently, the gas ratio  $\alpha_g$  tends to increase in the centre, and decrease close to the wall. It is also observed that the difference between  $\mu_g = 1e-1[kg/ms]$  and  $\mu_g = 1e-3[kg/ms]$  is negligible, the visible change being only present close to the bottom of the column, where the boundary condition  $\mathbf{u}_g = \mathbf{0}$  is imposed. With  $\mu_g = 1e-4[kg/ms]$ , small oscillations on  $\mathbf{u}_g$  in this area prevented convergence.

The values in practice are in the order of magnitude of  $\mu_g \leq 0.5[kg/ms]$ . It can be observed that the solutions do not change much globally in the  $L^2$  norm when comparing  $\mu_g = 1e-1[kg/ms]$ ,  $1e-2[kg/ms]$  and  $1e-3[kg/ms]$ . In order to have a reasonable solution and avoid the oscillations close to the bottom observed if  $\mu_g$  is too low, the same value as the linear part of the liquid viscosity is considered by default  $\mu_g = \mu_L = 0.13[kg/ms]$ .

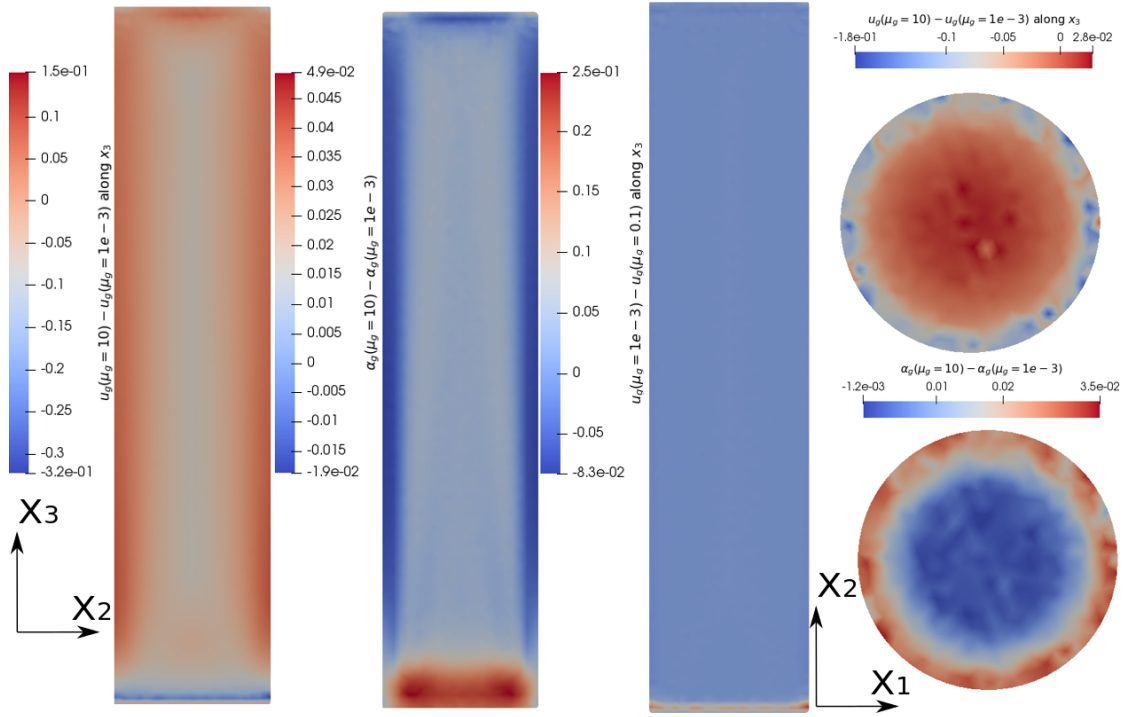


Figure 3.12 – On the left, results between solutions with different gas viscosities  $\mu_g$  in the middle of the water column at  $x_1 = 0$ . On the right, the difference is illustrated on  $\Gamma_{out}$ , viewed from above.

### Gas diffusion

On the other hand, the sensitivity to the gas diffusion with laminar coefficient  $K_L$  and turbulent coefficient  $K_T$  are compared in terms of amplitude in the expression of the diffusion:

$$K = K_L + K_T |\epsilon(\mathbf{u}_{g,h})|.$$

The default values are  $K_L = 2e - 4 [m^2/s]$  and  $K_T = 2e - 4 [m^2]$ . Quantification of the influence of the diffusion coefficient is given in Table 3.8. The changes are relatively important regarding the gas volumetric ratio  $\alpha_g$  and the velocity  $\mathbf{u}$ : it can be observed that a stronger diffusion leads to a slightly more important average gas value  $\bar{\alpha}_g$ .

Qualitative interpretation of the sensitivity of the gas diffusion can be done with Figure 3.13: the greater the diffusion is, more gas  $\alpha_g$  is present close to the wall of the water-column, and as a result, the convection movement of the velocity  $\mathbf{u}$  seems to be weaker as well in this area.

In this section, the effect of different gas viscosities and gas diffusion coefficients have been shown through different simulation results. If the viscosity  $\mu_g$  is too small (smaller than  $\mu_g = 1e - 3 [kg/ms]$ ) the algorithm does not converge, as small oscillations appear at the bottom of the water column. The impact in the results is relatively low for different gas viscosity, except if the viscosity is very important ( $\mu_g = 10$ ). The diffusion can have a relatively

### Chapter 3. Comparison with a water-column experiment

---

Diffusion	$\Delta_{\infty}(\mathbf{u}_h)$	$\Delta_{\infty}(\alpha_{g,h})$	$\Delta_{\infty}(\mathbf{u}_{g,h})$	$\Delta_0(\mathbf{u}_h)$	$\Delta_0(\alpha_{g,h})$	$\Delta_0(\mathbf{u}_{g,h})$	N	$\bar{\alpha}_g$ [%]
$K_0-K_0/8$	13.9%	37.3%	8.4%	16.8%	17.5%	8.4%	16	9.8%
$K_0-K_0/4$	12.8%	27.3%	6.4%	14.3%	12.7%	5.2%	15	9.8%
$K_0-K_0/2$	8.6%	14.0%	4.0%	8.7%	6.4%	3.0%	13	10.0%
$K_0-2K_0$	15.7%	13.4%	7.2%	12.1%	6.0%	4.0%	13	10.4%
$K_0-4K_0$	39.7%	25.8%	18.3%	28.5%	11.0%	9.0%	15	10.6%

Table 3.8 – Comparison of the stationary flow with different gas diffusion coefficients  $K$ , with reference case  $K_0$ .

stronger impact on the global behaviour, but that remains limited when considering the resulting velocity  $\mathbf{u}$ , except if the diffusion is especially high.

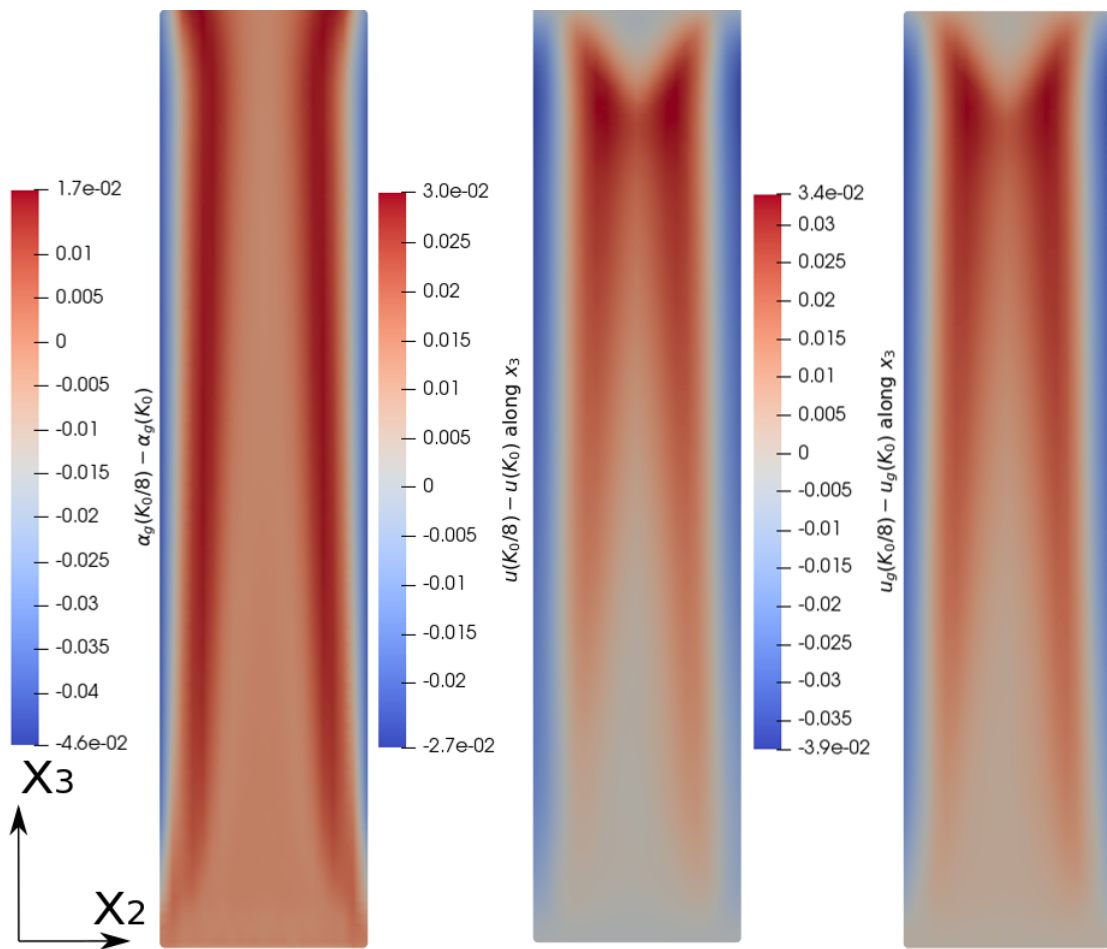


Figure 3.13 – Results in the middle of the water column at  $x_1 = 0$ . From left to right :with less diffusion, the gas volumetric ratio is lower close to the border, and more important inside. As the difference of density is more important, the circulation of the liquid velocity is increased. Due to the drag force, the same kind of difference is observed for the gas velocity.

### 3.5.6 Comparison with experimental data

The numerical velocity of compared with experimental data provided in [Gem19]. In the first part, radial profiles are compared: the model is also compared with a second experiment, that can be found in [BRJ06]. Second, comparison of the average gas ratio obtained with increasing inflow is compared with the experimental numbers.

#### Radial profile of velocity $u$ and gas volumetric ratio $\alpha_g$

The profiles obtained for the velocity  $u$  and the gas distribution  $\alpha_g$  with the default parameters are compared with experimental data in Figure 3.14, with different choices of parameters.

It can be observed that the numerical solution is not corresponding for  $\alpha_g$  close to the wall

### Chapter 3. Comparison with a water-column experiment

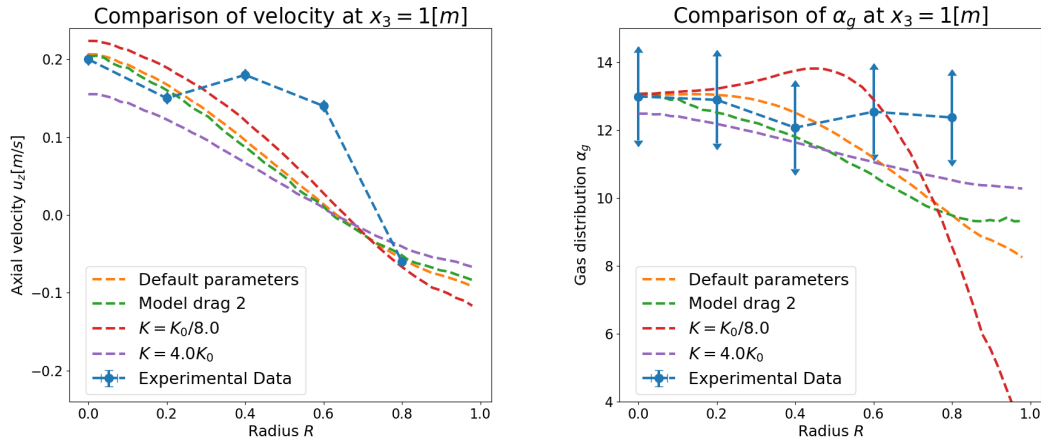


Figure 3.14 – Comparison between the model and experimental measurements from [Gem19] at  $x_3 = 1[m]$ .

and for the velocity  $\mathbf{u}$  in the middle of the column.

Notice that none of the parameters allow to reproduce the bump observed in the velocity radial profile. Regarding this case, we compared a second experiment with different water-column geometry (smaller radius), but similar conditions, found in [BRJ06]: this second study assesses the effects of the two kind of spargers on the flow, we considered the configuration with smaller spargers, closer to the settings of the first experiment. Table 3.9 summarises the parameters of the two experiments.

Figure 3.15 shows that the bump in the velocity radial profile is not observed in [BRJ06], corresponding to the results of the numerical model.

Reference	$d[mm]$	$\phi_{in}[m/s]$	$H_{cylinder}[m]$	$D_c[m]$	$H_{data}[m]$	$\bar{\alpha}_g[\%]$	$n_{sp}$	$r_{sp}[mm]$
[Gem19]	7	0.03	1.77	0.4	$1.0=2.5 D_c$	10.78	92	1
[BRJ06]	6	0.02	0.9	0.15	$0.45=3D_c$	5.5	25	2

Table 3.9 – Macroscopic characteristics of two water-columns in the homogeneous regimes with different geometries and experimental set-ups:  $n_{sp}$  is the number of spargers at the inflow,  $r_{sp}$  the radius of the spargers and  $H_{data}$  the height at which the data was measured. The mesh size for the second experiment was  $h = 0.01[m]$ .

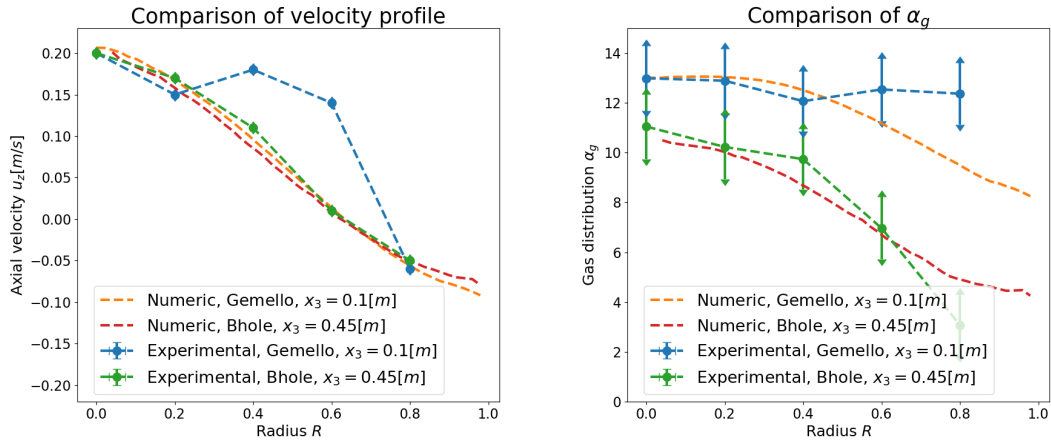


Figure 3.15 – Comparison between the model and experimental in the settings of [Gem19] with data of [BRJ06].

### Solutions with different inflows

The average gas volumetric ratio  $\bar{\alpha}_g$  is reported for different values of  $\Phi_{in}$  (defined in (3.2)). Comparisons with experiments are shown in Table 3.10. Experimental data are reported with demineralised water by default and also with tap water to illustrate the sensitivity of the results due to a parameter such as the quality of the water considered experimentally. On average, the numerical results for  $\alpha_g$  follow the same tendency than the experimental data, although for higher gas quantity, the numerical model overestimates the quantity of gas present in the column. For  $\Phi_{in} \geq 0.07$  [m/s], the numerical solution is not stationary.

$\Phi_{in}$ [m/s]	Exp 1 $\bar{\alpha}_g$ [%]	Exp 2 $\bar{\alpha}_g$ [%]	Simulation $\bar{\alpha}_g$ [%]	$N$
0.01	3.5	3.5	3.69	12
0.02	7.69	6.96	7.06	12
0.03	10.78	10.93	10.21	13
0.04	12.73	13.34	13.15	15
0.05	14.83	15.23	15.91	18
0.06	15.50	16.72	18.50	36

Table 3.10 – Average gas  $\bar{\alpha}_g$  for different values of inflow  $\Phi_{in}$ . Exp 1 corresponds to experimental data with demineralised water and Exp 2 with tap water.  $N$  is the number of iterations of the algorithm to reach a stationary solution.

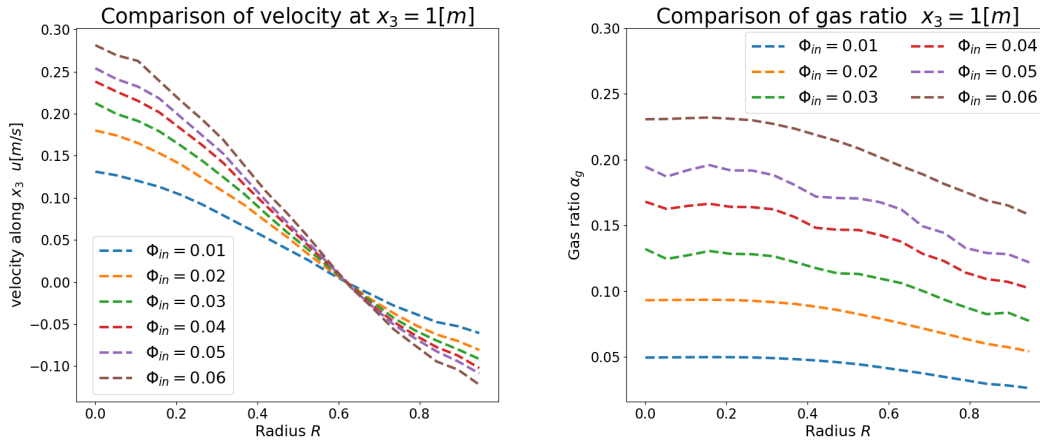


Figure 3.16 – For different gas source values  $\Phi_{in}$ : on the left the vertical velocity  $u$ , on the right values of  $\alpha_g$  along the radius  $R$  at  $x_3 = 1[m]$ .

### 3.6 Conclusion

In this section, the model has been applied to a water-column experiment. It has been shown that the mesh size does not change much the results. The influence of the drag coefficient and the diffusion of the gas has been shown to impact considerably the results. The gas viscosity  $\mu_g$  has only a secondary order effect. The Boussinesq approximation (1.7.3) and the explicit formulation for the gas velocity (1.7.1) gave results very close to the general model.

Regarding the comparison with experimental data, the model seems to reproduce approximately the average gas quantity for low and non turbulent regime. When the algorithm is used for more important gas flow, it does not converge. With regard to the radial profile measured experimentally, the behaviour of the solution does not correspond completely for the velocity  $u$  in the first experiment and is well reproduced in the second one. In both case, the experimental data are observed for the profile of the gas ratio  $\alpha_g$  are not completely reproduced close to the wall.

# 4 Application to aluminium electrolysis

In this chapter, the model detailed and analysed in previous chapters is applied to fluid flow simulations in aluminium reduction cells.

The software Alucell [Ste09] is the result of a collaboration of more than thirty years between EPFL and Rio Tinto aluminium, with purpose to model the most important phenomena related to aluminium electrolysis. The previous thesis have been dedicated to the magneto-hydrodynamics (MHD) [Ste09], models of turbulence in the fluid [Roc16], the thermal effects [Flo13; Saf05] or the alumina transport and dissolution [Hof11; Hil19]. Applications with the software Alucell corresponding to measurements in industry modelling can be found in [Ren+18].

In this thesis the modifications of the fluid flow induced due to the presence of gas is assessed. The density is changed due to the gas volumetric distribution, impacting the fluid flow. The equations describing the magneto-hydrodynamics are recalled. The equations of the gas are presented in this context. Then the weak formulations are presented. Next, the algorithm without gas is recalled and a new algorithm taking into account the gas equations is proposed.

## 4.1 The fluid flow model in aluminium electrolysis

In this section, the the magneto-hydrodynamics equations are presented in the framework of aluminium electrolysis. The interactions taking place between the fluid flow, the magnetic forces, the interface between the electrolyte and the liquid aluminium and the gas dynamics are described.

### 4.1.1 Notations

An electrolysis cell contains the fluid domain, the anodes, cathodes, conductors and ferromagnetic crates, illustrated with a middle cut view given in Figure 4.1. The fluid domain  $\Omega$  is split into the electrolytic bath denoted  $\Omega_{el}$ , the aluminium region  $\Omega_{al}$  and the bath/metal interface

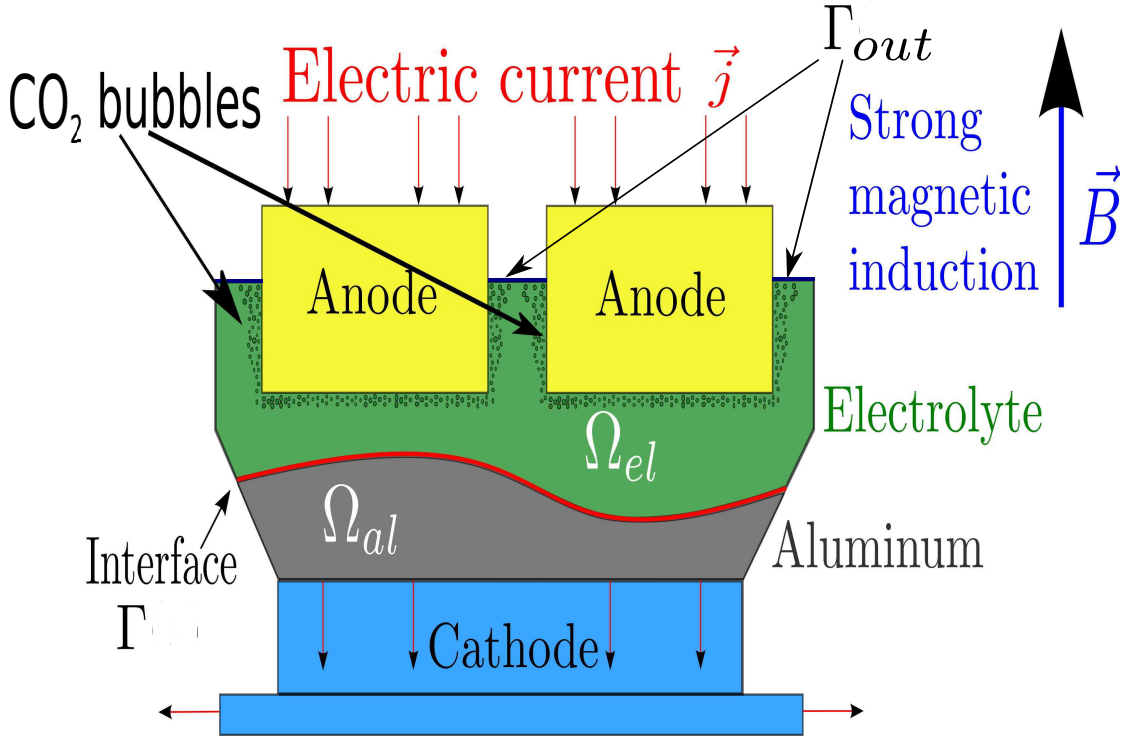


Figure 4.1 – Cut view of an aluminium reduction cell.

$\Gamma = \bar{\Omega}_{el} \cap \bar{\Omega}_{al}$ . It is assumed that the interface  $\Gamma$  can be parametrised by a continuous function  $H : (x_1, x_2) \in \Sigma \rightarrow x_3 = H(x_1, x_2) \in \mathbb{R}$ :

$$\begin{cases} \Gamma = \{(x_1, x_2, x_3) \in \Omega : x_3 = H(x_1, x_2), (x_1, x_2) \in \Sigma\}, \\ \text{If } x_3 > H \text{ then } \mathbf{x} \in \Omega_{el} \text{ and if } x_3 < H \text{ then } \mathbf{x} \in \Omega_{al}, \forall \mathbf{x} \in \Omega. \end{cases} \quad (4.1)$$

The top surface of the channels between the anodic blocs is denoted  $\Gamma_{out}$ .

Due to the important electric current density  $\mathbf{j}$ , the corresponding electromagnetic forces will put the fluid into motion. In the electrolytic bath, chemical reactions will lead to the production of different gas, mostly Carbon dioxide (see section 4.1.6).

#### 4.1.2 Hydrodynamic equations: two immiscible fluids

In this subsection, the electric density current  $\mathbf{j}$ , the induced magnetic field  $\mathbf{B}$ , as well as the distribution of the volumetric gas ratio  $\alpha_g$  are assumed to be known and the goal is to compute the velocity field  $\mathbf{u} : \Omega \rightarrow \mathbb{R}^3$ , the pressure  $p : \Omega \rightarrow \mathbb{R}$  and the interface height  $H : \Sigma \rightarrow \mathbb{R}$  between the aluminium and electrolytic bath.

The stationary problem of Navier-Stokes consists in looking for the velocity field  $\mathbf{u} : \Omega \rightarrow \mathbb{R}^3$ ,

## 4.1. The fluid flow model in aluminium electrolysis

the pressure  $p : \Omega \rightarrow \mathbb{R}$  such that

$$\begin{cases} \operatorname{div}(\rho \mathbf{u} \otimes \mathbf{u}) - \operatorname{div}(\boldsymbol{\tau}) = -\rho \mathbf{g} + \mathbf{j} \wedge \mathbf{B}, \\ \operatorname{div}(\rho \mathbf{u}) = 0, \end{cases} \quad \text{in } \Omega_{el} \cup \Omega_{al}. \quad (4.2)$$

The problem is completed with  $\mathbf{u} = \mathbf{0}$  on the whole boundary  $\partial\Omega$  to facilitate the reading of the problem. In practice partial sliding is used on the boundary (see section 4.1.4).

In (4.2), the density in the fluid domain  $\Omega$  is defined as a constant density  $\rho_{al}$  in the aluminium and as a mixture in the electrolyte between the density of the liquid electrolyte  $\rho_{el}$  and the density of the gas  $\rho_g$  ( as 1.8 ):

$$\rho [kg/m^3] = \begin{cases} \rho_{al} & \text{if } \mathbf{x} \in \Omega_{al}; \\ \alpha_g \rho_g + (1 - \alpha_g) \rho_{el} & \text{if } \mathbf{x} \in \Omega_{el}. \end{cases} \quad (4.3)$$

When the gas is not taken into account,  $\alpha_g = 0$  everywhere and  $\rho = \rho_{el}$  is constant in the electrolyte domain  $\Omega_{el}$ . The viscosity  $\mu$  follows the Smagorinski turbulent model proposed in [Roc16] (see 1.79), composed of a linear constant part respectively  $\mu_{al}$  and  $\mu_{el}$  in the aluminium and in the electrolyte, as well as a turbulent part depending on the norm of  $\epsilon(\mathbf{u})$ :

$$\mu [kg/ms] = \begin{cases} \mu_{al} + C_T \rho_{al} |\epsilon(\mathbf{u})| & \text{if } \mathbf{x} \in \Omega_{al}; \\ \mu_{el} + C_T \rho |\epsilon(\mathbf{u})| & \text{if } \mathbf{x} \in \Omega_{el}, \end{cases} \quad (4.4)$$

where the turbulent constant coefficient  $C_T = 5e - 4[m^2]^1$  in aluminium cells and  $\epsilon(\mathbf{u})$  is defined in (1.1) and  $|\epsilon(\mathbf{u})| = \sqrt{\sum_{i,j} (\epsilon_{i,j}(\mathbf{u}))^2}$ . The usual definition of the stress tensor  $\boldsymbol{\tau}$  is given with:

$$\boldsymbol{\tau} = -p\mathbf{I} - \frac{2}{3}\mu \operatorname{div}(\mathbf{u})\mathbf{I} + 2\mu\epsilon(\mathbf{u}), \quad (4.5)$$

and the external forces have been written as  $\mathbf{F} = -\rho \mathbf{g} + \mathbf{j} \wedge \mathbf{B}$ .

On the interface  $\Gamma$ , we define the jump operator  $[\cdot]$ . For any scalar field  $q$  defined in  $\Omega$ , the jump of  $q$  is the subtraction of its value in the electrolyte by its value in the aluminium:

$$[q](x_1, x_2) = \lim_{\varepsilon \rightarrow 0^+} q(x_1, x_2, H(x_1, x_2) + \varepsilon) - q(x_1, x_2, H(x_1, x_2) - \varepsilon) = q_{el} - q_{al},$$

and the notion of the jump through  $\Gamma$  can be naturally extended to a vector, by considering the jump of each of its component.

The five following conditions hold on  $\Gamma$ . First, the velocity is assumed to be continuous across the interface  $\Gamma$ :

$$[\mathbf{u}] = \mathbf{0}, \quad \text{on } \Gamma. \quad (4.6)$$

---

<sup>1</sup>In the literature,  $C_T = l^2 C_S$ , where  $l$  is a characteristic length and  $C_S$  a dimensionless constant. In the case of aluminium electrolysis, we equivalently consider  $l = 0.1$  and  $C_S = 5e - 2$ , thus  $C_T = 5e - 4$  as in [Roc16].

In addition the velocity field is assumed to be tangent to the interface  $\Gamma$ :

$$\mathbf{u} \cdot \mathbf{n} = 0, \text{ on } \Gamma, \quad (4.7)$$

otherwise the interface would be transported. Finally the jump of the viscous forces through the interface is assumed to be zero:

$$[\boldsymbol{\tau} \cdot \mathbf{n}] \cdot \mathbf{t}_i = 0, \quad i = 1, 2, \text{ on } \Gamma, \quad (4.8)$$

$$[\boldsymbol{\tau} \cdot \mathbf{n}] \cdot \mathbf{n} = 0, \text{ on } \Gamma, \quad (4.9)$$

reflecting that the forces are at equilibrium through the interface. Then the following stationary problem can be stated, regrouping (4.2) to (4.9): find the velocity  $\mathbf{u}$ , the pressure  $p$  and the interface  $\Gamma$  such that:

$$\left\{ \begin{array}{l} \text{div}(\rho \mathbf{u} \otimes \mathbf{u}) - \text{div}(\boldsymbol{\tau}) = \mathbf{F} = -\rho \mathbf{g} + \mathbf{j} \wedge \mathbf{B}, \text{ in } \Omega_k, \quad k = \{el, al\} \quad (4.10a) \\ \text{div}(\rho \mathbf{u}) = 0, \text{ in } \Omega, \quad (4.10b) \\ \mathbf{u} = \mathbf{0}, \text{ on } \partial\Omega, \quad (4.10c) \\ [\mathbf{u}] = \mathbf{0}, \text{ on } \Gamma, \quad (4.10d) \\ \mathbf{u} \cdot \mathbf{n} = 0, \text{ on } \Gamma, \quad (4.10e) \\ [\boldsymbol{\tau} \cdot \mathbf{n}] \cdot \mathbf{t}_i = 0, \quad i = 1, 2, \text{ on } \Gamma, \quad (4.10f) \\ [\boldsymbol{\tau} \cdot \mathbf{n}] \cdot \mathbf{n} = 0, \text{ on } \Gamma, \quad (4.10g) \\ \int_{\Omega_{al}} dx = V_{alu}, \quad (4.10h) \end{array} \right.$$

where the condition (4.10h) ensures the conservation of the initial volume of aluminium  $V_{alu}$ .

### 4.1.3 Principles of an algorithm to solve the hydrodynamic equations coupled to the interface

The resolution of problem (4.10a-4.10h) usually requires an iterative algorithm that split the problem into two systems: one of the four conditions (4.10d-4.10g) is usually relaxed to update the interface while the other four conditions are used to compute the velocity. For example, a classical approach consists to relax the immiscibility condition (4.10e), and solve (4.10a-4.10d)(4.10f-4.10g) for the velocity and the pressure. Then the interface is computed (for example with a time level-set transport equation with velocity  $\mathbf{u}$ ) with an equation that aims to reach iteratively condition (4.10e). Condition (4.10h) is used in post-process to conserve the volume of the fluids. This method is used in the framework of aluminium electrolysis in [Pai06; Flo13; Roc16] for example.

A method which converges faster to the stationary solution of (4.10a-4.10h) will be used. This method consists to relax the jump of the viscous force through the interface condition (4.10g)

and to consider the problem:

$$\text{For a given interface } \Gamma, \text{ find } \mathbf{u} \text{ and } p \text{ satisfying (4.10a-4.10f).} \quad (4.11)$$

The interface is then updated to reach (4.10g). At iteration  $k$ , the velocity, pressure and interface are given as  $\mathbf{u}^k$ ,  $p^k$  and  $\Gamma^k$ . A linearisation at first order between the velocity, pressure and interface solutions of (4.10a-4.10h) and the velocity and pressure solutions of (4.10a-4.10f) lead to an expression for the new interface. Details can be found in [DFF89], as well as well-posedness and convergence of this iterative method in a simplified static case. With this method, the new interface  $\Gamma^{k+1}$  is computed with:

$$H^{k+1} = H^k + \frac{([\boldsymbol{\tau}(\mathbf{u}^k, p^k)] \cdot \mathbf{n}^k) \cdot \mathbf{n}^k + C}{[\mathbf{F}_3]}, \quad (4.12)$$

where  $C$  is chosen such that the conservation of the volume of  $\Omega_{al}$  (4.10h) holds and  $\mathbf{F}_3$  is the third component of the external forces in (4.10a). Then the process can be repeated, solving iteratively the problem (4.11) and using (4.12) to update the interface, up to a solution satisfying (4.10a)-(4.10h).

**Remark 11.** The pressure is discontinuous through the interface  $\Gamma$ . As the relation (4.10f) is independent of the pressure  $p$ , a solution  $(\mathbf{u}, p)$  solution of (4.11) also admits as solution  $(\mathbf{u}, q)$ , where  $q = p + c_{el}$  in  $\Omega_{el}$  and  $q = p + c_{al}$  in  $\Omega_{al}$ , for any constant  $c_{el}, c_{al}$ . The difference between these two constants is set through (4.10h). (see later Remark 12)

### 4.1.4 Partially sliding boundary conditions for the fluid in aluminium electrolysis cells and weak formulation

In this paragraph, we introduce a different boundary condition than (4.10c) to allow sliding.

The friction coefficient  $f_{Wall}$  is introduced in [Roc16] (page 103). Notice that the dimension of  $f_{Wall}$  is  $[kg/sm^2]$ . Then the boundary conditions (4.10c) are replaced by:

$$\mathbf{u} \cdot \mathbf{n} = 0 \text{ on } \partial\Omega, \quad (4.13)$$

$$(\boldsymbol{\tau} \cdot \mathbf{n}) \cdot \mathbf{t}_i = -f_{Wall} \mathbf{u} \cdot \mathbf{t}_i, \quad i = 1, 2, \text{ on } \partial\Omega, \quad (4.14)$$

Notice that the limit when the coefficient  $f_{Wall} \rightarrow 0$  corresponds to a slip condition, while the limit  $f_{Wall} \rightarrow \infty$  corresponds together with (4.13) to the boundary condition (4.10c).

Typically the coefficient  $f_{Wall}$  varies from 0 to  $1e6$  on the boundary  $\partial\Omega$ , see section 4.4.

The calculations described in section (1.8.1) can be used. In particular, the friction terms and normal forces on the interface  $\Gamma$  come up when integrating the boundary part of the viscous forces and using  $\mathbf{u}, \mathbf{v}$  satisfying boundary conditions (4.10e)-(4.10g)(4.13)-(4.14), giving the

following relation when integrating the viscous tensor on  $\partial\Omega_{el}$  and  $\partial\Omega_{al}$  instead of (1.64):

$$\begin{aligned}
 & \int_{\partial\Omega_{el}} (\boldsymbol{\tau} \cdot \mathbf{n}) \cdot \mathbf{v} ds + \int_{\partial\Omega_{al}} (\boldsymbol{\tau} \cdot \mathbf{n}) \cdot \mathbf{v} ds = \int_{\partial\Omega} (\boldsymbol{\tau} \cdot \mathbf{n}) \cdot \mathbf{v} ds + \int_{\Gamma} [\boldsymbol{\tau} \cdot \mathbf{n}] \cdot \mathbf{n} (\mathbf{v} \cdot \mathbf{n}) ds \\
 & = \int_{\Gamma} [\boldsymbol{\tau} \cdot \mathbf{n}] \cdot \mathbf{n} (\mathbf{v} \cdot \mathbf{n}) ds + \int_{\partial\Omega} (\boldsymbol{\tau} \cdot \mathbf{n}) \cdot \mathbf{n} (\mathbf{v} \cdot \mathbf{n}) ds + \int_{\partial\Omega} (\boldsymbol{\tau} \cdot \mathbf{n}) \cdot \mathbf{t}_1 (\mathbf{v} \cdot \mathbf{t}_1) ds + \int_{\partial\Omega} (\boldsymbol{\tau} \cdot \mathbf{n}) \cdot \mathbf{t}_2 (\mathbf{v} \cdot \mathbf{t}_2) ds \\
 & = \int_{\Gamma} [\boldsymbol{\tau} \cdot \mathbf{n}] \cdot \mathbf{n} (\mathbf{v} \cdot \mathbf{n}) ds + \int_{\Gamma_{out}} (\boldsymbol{\tau} \cdot \mathbf{n}) \cdot \mathbf{n} (\mathbf{v} \cdot \mathbf{n}) ds + \sum_{i=1,2} \int_{\partial\Omega} (\boldsymbol{\tau} \cdot \mathbf{n}) \cdot \mathbf{t}_i (\mathbf{v} \cdot \mathbf{t}_i) ds \\
 & = \int_{\Gamma_{out}} \xi (\mathbf{v} \cdot \mathbf{n}) ds + \int_{\Gamma} \psi (\mathbf{v} \cdot \mathbf{n}) ds - \sum_{i=1,2} \int_{\partial\Omega} f_{wall} \mathbf{u} \cdot \mathbf{t}_i (\mathbf{v} \cdot \mathbf{t}_i) ds.
 \end{aligned} \tag{4.15}$$

In the above, we have chosen the variables  $\xi = (\boldsymbol{\tau} \cdot \mathbf{n}) \cdot \mathbf{n}$  on  $\Gamma_{out}$  and  $\psi = [\boldsymbol{\tau} \cdot \mathbf{n}] \cdot \mathbf{n}$  on  $\Gamma$ .

#### Weak formulation for the Navier-Stokes problem 4.11 with sliding conditions

In this paragraph, the weak formulation associated to (4.11) is presented, with the partially sliding boundary conditions (4.13)-(4.14) instead of  $\mathbf{u} = \mathbf{0}$ . The unknown corresponding to  $\psi = ([\boldsymbol{\tau}(\mathbf{u}, p)] \cdot \mathbf{n}) \cdot \mathbf{n}$  on the interface  $\Gamma$  is introduced, which is exactly what is required to use the algorithm to update the interface with (4.12). In addition the viscous force  $\xi = (\boldsymbol{\tau} \cdot \mathbf{n}) \cdot \mathbf{n}$  is introduced on the gas outflow surface  $\Gamma_{out}$ , which is required in the boundary condition for the gas. Consider the spaces:

$$S = \{s : \partial\Omega \rightarrow \mathbb{R} : s = 0 \text{ on } \partial\Omega \setminus \Gamma_{out}\},$$

$$Z = \{f : \Gamma \rightarrow \mathbb{R}\},$$

$$\mathbf{V} = \{\Omega \rightarrow \mathbb{R}^3 : \mathbf{v} \cdot \mathbf{n} = 0 \text{ on } \partial\Omega \setminus \Gamma_{out}\}$$

$$L_{alu} = \left\{ f : \Omega_{al} \rightarrow \mathbb{R} : \int_{\Omega_{al}} f dx = 0 \right\},$$

$$L_{el} = \left\{ f : \Omega_{el} \rightarrow \mathbb{R} : \int_{\Omega_{el}} f dx = 0 \right\}.$$

Then a weak formulation of the initial Navier-Stokes system (4.2) with boundary conditions (4.10e)-(4.10g)(4.13)-(4.14) integrated as in (4.15) consist into looking for  $(\mathbf{u}, p, \xi, \psi) \in \mathbf{V} \times$

$(L_{alu} \oplus L_{el}) \times S \times Z$  such that:

$$\begin{aligned}
& \int_{\Omega} (\rho \mathbf{u} \cdot \nabla) \mathbf{u} \cdot \mathbf{v} dx + \int_{\Omega} 2\mu \left( \epsilon(\mathbf{u}) : \epsilon(\mathbf{v}) - \frac{1}{3} \operatorname{div}(\mathbf{u}) \operatorname{div}(\mathbf{v}) \right) dx \\
& - \int_{\Omega} p \operatorname{div}(\mathbf{v}) dx - \int_{\Gamma_{out}} \xi(\mathbf{v} \cdot \mathbf{n}) ds - \int_{\Gamma} \psi(\mathbf{v} \cdot \mathbf{n}) ds + \int_{\partial\Omega} f_{wall} \mathbf{u} \cdot \mathbf{t}_1(\mathbf{v} \cdot \mathbf{t}_1) ds \\
& + \int_{\partial\Omega} f_{wall} \mathbf{u} \cdot \mathbf{t}_2(\mathbf{v} \cdot \mathbf{t}_2) ds = \int_{\Omega} (\mathbf{F} + \rho \mathbf{g}) \cdot \mathbf{v} dx, \\
& \int_{\Omega} \operatorname{div}(\rho \mathbf{u}) q dx = 0, \\
& \int_{\Gamma_{out}} \zeta_{out}(\mathbf{u} \cdot \mathbf{n}) ds = 0, \\
& \int_{\Gamma} \zeta(\mathbf{u} \cdot \mathbf{n}) ds = 0,
\end{aligned} \tag{4.16}$$

for all  $(\mathbf{v}, q, \zeta_{out}, \zeta) \in \mathbf{V} \times (L_{alu} \oplus L_{el}) \times S \times Z$ .

**Remark 12.** The definition of the space  $(L_{alu} \oplus L_{el})$  is only a way to fix the two constants  $c_{al}, c_{el}$  mentioned in remark 11. More precisely, the second constant is implicitly changed in the complete problem when fixing  $C$  in the conservation of the volume of aluminium (4.10h). Then, the second constant in the weak formulation can be imposed in an arbitrary way in (4.16) (in this case the choice of the space  $(L_{alu} \oplus L_{el})$  was made), as it will be adjusted to condition (4.16) when using the algorithm procedure to modify the interface in (4.12) with the constant  $C$ .

**Remark 13.** The pressure is often considered as a Lagrange multiplier associated with the conservation of mass  $\operatorname{div}(\rho \mathbf{u}) = 0$ . In a similar fashion,  $\xi$  and  $\psi$  can be seen as Lagrange multipliers associated with the sliding condition  $\mathbf{u} \cdot \mathbf{n} = 0$  on respectively the surface  $\Gamma_{out}$  and the interface  $\Gamma$ .

#### 4.1.5 Electromagnetic effects

This section describes the electromagnetic effects in the aluminium electrolysis process. This description and the associated methods to solve them numerically in Alucell can be found in [Ste09]. From the Maxwell equations, a model allows to compute the density of current  $\mathbf{j}$  and the induced magnetic field  $\mathbf{B}$ .

##### Maxwell equations

The electromagnetic phenomena are described through Maxwell's equations, coupling through differential equations the current density  $\mathbf{j}$ , the magnetic field  $\mathbf{B}$  and the electric field  $\mathbf{E}$ .

The first equation called Faraday's law of induction, links the circulation of an electric field  $\mathbf{E}$  to the temporal variation of the magnetic field  $\mathbf{B}$ . This temporal variation can be neglected

## Chapter 4. Application to aluminium electrolysis

---

[Ste09](page 90) and can be written under stationary form:

$$\nabla \wedge \mathbf{E} = \mathbf{0}. \quad (4.17)$$

The second law, named Ampere's law, relates the magnetic field  $\mathbf{H} = \frac{1}{\mu_0 \mu_r} \mathbf{B}$  with time variation of the electric field (this part is neglected, justification in [Mun04]). and the density of current  $\mathbf{j}$ . Under stationary form it reads:

$$\nabla \wedge \mathbf{H} = \mathbf{j}. \quad (4.18)$$

In this case  $\mu_0 = 4\pi 10^{-7} [kgm/A^2s^2]$  is the magnetic permeability of vacuum and  $\mu_r$  the relative magnetic permeability of the materials. In addition, if there are no ferromagnetic effects ( $\mu_r = 1$ ) and the equation simplifies to:

$$\nabla \wedge \mathbf{B} = \mu_0 \mathbf{j}. \quad (4.19)$$

The third law is the conservation of the magnetic field  $\mathbf{B}$ :

$$\text{div}(\mathbf{B}) = 0, \quad (4.20)$$

and lastly Ohm's law binds the density of current  $\mathbf{j}$  to the electric field  $\mathbf{E}$ , the magnetic field  $\mathbf{B}$  and the fluid velocity  $\mathbf{u}$ :

$$\mathbf{j} = \sigma (\mathbf{E} + \mathbf{u} \wedge \mathbf{B}). \quad (4.21)$$

$\sigma$  is the conductivity of the different materials. In the fluid,  $\sigma(\alpha_g)$  can depend on the volumetric gas ratio  $\alpha_g$ . Applying the divergence operator on (4.19) gives the continuity equation for the density of current  $\mathbf{j}$ :

$$\text{div}(\mathbf{j}) = 0. \quad (4.22)$$

### Electric potential

In this paragraph, the magnetic field  $\mathbf{B}$  is supposed given. Then because of the simplified equation of Faraday (4.17), there exists an electric potential  $V$  such that:

$$\mathbf{E} = -\nabla V. \quad (4.23)$$

Then Ohm's law (4.21) can be rewritten as:

$$\mathbf{j} = \sigma (-\nabla V + \mathbf{u} \wedge \mathbf{B}). \quad (4.24)$$

Applying the divergence operator on (4.21), using the fact that the divergence of  $\mathbf{j}$  is zero (4.22) and Ampere's law (4.19), one gets an elliptic equation for the potential  $V$ :

$$\text{div}(-\sigma \nabla V) = -\text{div}(\sigma \mathbf{u} \wedge \mathbf{B}), \quad (4.25)$$

in the whole aluminium reduction cell. Then, if  $V$ ,  $\mathbf{u}$ ,  $\mathbf{B}$  and  $\sigma$  are known, the density of current

$\mathbf{j}$  can be directly computed with (4.24). The numerical method to solve (4.25) with as unknown the electric potential  $V$  in the electrolysis cell will be used in the following. The details of the method in Alucell can be found in [Roc16](page 83).

### Magnetic induction

Assuming that the density of current  $\mathbf{j}$  and the velocity  $\mathbf{u}$  are given, it is possible to compute the induced magnetic field  $\mathbf{B}$  thanks to the integral formula of Biot-Savart:

$$\mathbf{B} = \frac{\mu_0}{4} \int_{\mathbb{R}^3} \mathbf{j} \wedge \frac{(\mathbf{x} - \mathbf{y})}{|\mathbf{x} - \mathbf{y}|^3} d\mathbf{y}. \quad (4.26)$$

The magnetic field  $\mathbf{B}$  depends on the current circulating in neighbouring cells, the metallic structure surrounding the cell and the current distribution through the two fluids. In addition the ferromagnetic cell shell screens partially the magnetic field. Details of the numerical model computing this magnetic field in Alucell can be found in [Ste09; Flu+10].

### 4.1.6 Gas dynamics

In this section, it is assumed that the velocity field of the mixture  $\mathbf{u}$  and the pressure  $p$  as well as the interface  $\Gamma$  are given as inputs. Then the dynamic of the gas is considered only in the electrolyte domain  $\Omega_{el}$  with appropriate boundary conditions. The purpose of the equations is to determine the gas volumetric ratio  $\alpha_g : \Omega_{el} \rightarrow \mathbb{R}$  and the gas velocity field  $\mathbf{u}_g : \Omega_{el} \rightarrow \mathbb{R}^3$ . The purpose is to reach a stationary solution, and time evolution is used as a continuation method to approach a stationary equilibrium, solving:

$$\begin{cases} \operatorname{div}(\alpha_g \rho_g \mathbf{u}_g \otimes \mathbf{u}_g) + D\alpha_g \frac{\rho}{\rho_{el}} \mathbf{u}_g - \operatorname{div}(\boldsymbol{\tau}_g) + p \nabla \alpha_g = \alpha_g \rho_g \mathbf{g} + D\alpha_g \frac{\rho}{\rho_{el}} \mathbf{u}, \\ \frac{\partial \alpha_g}{\partial t} + \operatorname{div}(\alpha_g \mathbf{u}_g - K \nabla \alpha_g) = \dot{\alpha}_{source}, \end{cases} \quad \text{in } \Omega_{el}. \quad (4.27)$$

where the density  $\rho$  is the mixture density in the electrolyte:

$$\rho = \alpha_g \rho_g + (1 - \alpha_g) \rho_{el}, \quad (4.28)$$

$D$  is the drag coefficient described in section (1.6), and  $\boldsymbol{\tau}_g$  is the gas stress tensor:

$$\boldsymbol{\tau}_g = -p \alpha_g \mathbf{I} + \mu_g \left( -\frac{2}{3} \operatorname{div}(\mathbf{u}_g) \mathbf{I} + 2\boldsymbol{\epsilon}(\mathbf{u}_g) \right), \quad (4.29)$$

with  $\mu_g = 0.5[\text{kg/ms}]$  taken as a constant similar to the values of the electrolytic viscosity (see 4.59, [DFR98]). Finally the diffusion coefficient  $K$  is also composed of a linear part and a

turbulent part:

$$K = K_L + K_T |\epsilon(\mathbf{u}_g)|, \quad K_L = 5e - 5[m^2/s] \text{ and } K_T = 5e - 4[m^2]. \quad (4.30)$$

The idea to use a turbulent coefficient comes into an analogy with the turbulent viscosity, for which the turbulent coefficient  $C_T$  (4.4) for electrolysis cells in industry is already calibrated. Finally,  $\dot{\alpha}_{source}[1/s]$  is the volumetric internal source term from chemical reduction reactions, see (4.39).

### Boundary conditions and weak formulation

Similarly to section 1.4, it is assumed that the boundary of the electrolyte can be split into the outflow  $\Gamma_{out}$  and  $\partial\Omega_{el} \setminus \Gamma_{out}$ . On  $\partial\Omega_{el} \setminus \Gamma_{out}$ , free slip boundary conditions are allowed: the gas is allowed to slide and transport  $\alpha_g$  along the channels and anodes. On the surface  $\Gamma_{out}$ , the special outflow conditions are considered. The constant  $p_0$  is defined as:

$$p_0 = \frac{\int_{\Gamma_{out}} (\boldsymbol{\tau} \cdot \mathbf{n}) \cdot \mathbf{n} ds}{\int_{\Gamma_{out}} ds}.$$

Then the boundary conditions are:

$$(\boldsymbol{\tau}_g \cdot \mathbf{n}) \cdot \mathbf{n} = \alpha_g p_0, \text{ on } \Gamma_{out}, \quad (4.31)$$

$$(\boldsymbol{\tau}_g \cdot \mathbf{n}) \cdot \mathbf{t}_i = 0, \text{ on } \partial\Omega_{el}, \quad i = 1, 2, \quad (4.32)$$

$$\mathbf{u}_g \cdot \mathbf{n} = 0, \text{ on } \partial\Omega_{el} \setminus \Gamma_{out}, \quad (4.33)$$

$$K \nabla \alpha_g \cdot \mathbf{n} = 0, \text{ on } \partial\Omega_{el}, \quad (4.34)$$

Taken into account these boundary conditions, define the space:

$$\mathbf{V}_g = \{ \mathbf{v} : \Omega_{el} \rightarrow \mathbb{R}^3 : \mathbf{v} \cdot \mathbf{n} = 0 \text{ on } \partial\Omega_{el} \setminus \Gamma_{out} \}, \quad (4.35)$$

and an equivalent formulation of the momentum equation in (4.27) with boundary conditions (4.31-4.33) is to look for  $\mathbf{u}_g \in \mathbf{V}_g$ :

$$\begin{aligned} & \int_{\Omega_{el}} (\rho_g \alpha_g \mathbf{u}_g \cdot \nabla) \mathbf{u}_g \cdot \mathbf{v}_g dx + \int_{\Omega_{el}} (\rho_g \dot{\alpha}_{source}) \mathbf{u}_g \cdot \mathbf{v}_g dx - \int_{\Gamma_{out}} \alpha_g p_0 (\mathbf{v}_g \cdot \mathbf{n}) ds \\ & + \int_{\Omega_{el}} 2\mu_g \left( \epsilon(\mathbf{u}_g) : \epsilon(\mathbf{v}_g) - \frac{1}{3} \operatorname{div}(\mathbf{u}_g) \operatorname{div}(\mathbf{v}_g) \right) dx + \int_{\Omega_{el}} D \frac{\rho}{\rho_{el}} \alpha_g \mathbf{u}_g \cdot \mathbf{v}_g dx = \int_{\Omega_{el}} \alpha_g p \operatorname{div}(\mathbf{v}_g) dx \\ & + \int_{\Omega_{el}} p \nabla \alpha_g \cdot \mathbf{v}_g dx + \int_{\Omega_{el}} \alpha_g \rho_g \mathbf{g} \cdot \mathbf{v}_g dx + \int_{\Omega_{el}} D \frac{\rho}{\rho_{el}} \alpha_g \mathbf{u} \cdot \mathbf{v}_g dx, \end{aligned} \quad (4.36)$$

## 4.1. The fluid flow model in aluminium electrolysis

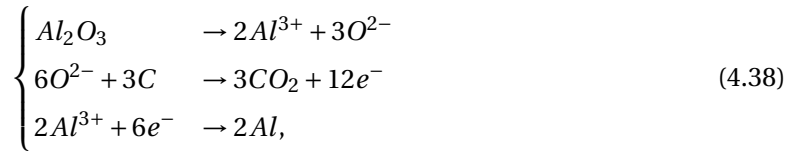
for all  $\mathbf{v}_g \in \mathbf{V}_g$ . The equivalent formulation of the advection-diffusion equation in (4.27) with boundary condition (4.34) consists into looking for  $\alpha_g : \Omega_{el} \rightarrow \mathbb{R}$  satisfying:

$$\int_{\Omega_{el}} \frac{\partial \alpha_g}{\partial t} \omega dx + \int_{\Omega_{el}} \operatorname{div}(\alpha_g \mathbf{u}_g) \omega dx + \int_{\Omega_{el}} K \nabla \alpha_g \nabla \omega dx = \int_{\Omega_{el}} \dot{\alpha}_{source} \omega dx, \quad (4.37)$$

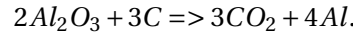
for all  $\omega : \Omega_{el} \rightarrow \mathbb{R}$ .

### Gas production

The different chemical reactions (see introduction) occurring in an aluminium electrolysis reduction cell are:



overall giving:



As a result, for every 3 molecules of Carbon Dioxide produced, 4 molecules of aluminium are obtained, and 12 electrons are exchanged in the process. Other gas are also released, but as carbon dioxide amounts to 90% of the gases present, they are neglected. An estimate of the amount of gas produced and the term  $\dot{\alpha}_{source}$  can be obtained, considering the scale of the whole electrolysis cell and the total current  $I$ :

$$\int_{\Omega_{el}} \rho_g \dot{\alpha}_{source} dx = \frac{\eta_f I M_{CO_2}}{4 q_e N_A} = \frac{\eta_f I M_{CO_2}}{4F}, \quad (4.39)$$

In this case  $I$  is the total current used in the electrolysis cell,  $M_{CO_2} = 44.009[g/mol]$  is the molar mass of carbon dioxide,  $q_e = 1.6021 \times 10^{-19}[C]$  is the charge of one electron,  $N_A = 6.0221 \times 10^{23}[1/mol]$  is Avogadro constant,  $F = 96485.33[sA/mol]$  is the Faraday constant and  $\eta_f$  is the Faraday efficiency, which is about  $\eta_f = 0.95$  for aluminium electrolysis [Cha17]. The relation (4.39) gives an indication of the total amount of the term source, but does not express its local distribution through the domain  $\Omega_{el}$ . A reasonable hypothesis consists into assuming that the production of gas is proportional to the local current density  $\mathbf{j}$  as it is the case for some aluminium dissolution models for instance [Hof11; Hil19]:

$$\dot{\alpha}_{source}(\mathbf{x}) = \frac{\eta_f I M_{CO_2}}{4F \rho_g} \frac{|\mathbf{j}(\mathbf{x})|}{\int_{\Omega_{el}} |\mathbf{j}(\mathbf{x})| dx}. \quad (4.40)$$

Finally, notice that the choice of the constant density  $\rho_g$  will scale accordingly the source term. As the gas is diluted in the fluid, it is not clear what value is the most appropriate in practice. The behaviour of carbon dioxide as a perfect gas would give  $\rho_g = 0.5[kg/m^3]$ , while the triple

point for carbon dioxide is  $\rho_g = 467[\text{kg}/\text{m}^3]$ . The lower the value of  $\rho_g$ , the greater  $\dot{\alpha}_{source}$ . By default, the gas density is set at  $\rho_g = 10[\text{kg}/\text{m}^3]$ . Section 4.6.1 shows the behaviour with different amplitude of source term.

**Remark 14.** Another method to introduce gas in the electrolytic bath is to inject it under the anodes by choosing a given gas velocity (going downwards vertically) and given value of  $\alpha_g$ , both imposed on the anodic surface. In practice, this method was found out to be unstable with our algorithm : the intuitive explanation being that the gas velocity is naturally going up vertically, and imposing a boundary condition with a velocity going down on the anodic plane lead to a thin unstable layer. Second it would require to fix two parameters. And finally, we will see that the solution of  $\alpha_g$  is not constant at all on the anodic surface, so fixing it as a constant does not seem relevant in this model.

## 4.2 Space discretization and algorithm

This section is dedicated to the space discretization in finite elements of the problem presented in section (4.1), and an algorithm consisting in solving the different physical processes one at a time, while the variables associated with the other problems are used as given inputs. The algorithm used in the Alucell software to reach a stationary solution being quite complicated, a summary of the algorithm without gas is first presented. Second, the gas model is added as an additional phase of the algorithm which will modify the density of the electrolyte  $\rho_{el}$ .

### 4.2.1 Meshes along the iterations

The initial mesh of the algorithm, see top of Figure 4.2, starts with a flat interface  $\Gamma^0$  located at  $x_3 = 0.2[\text{m}]$  above the bottom of  $\Omega$ , that is cut into triangles. We also define a fictitious interface  $\tilde{\Gamma}^0$  located at  $x_3 = 0.232[\text{m}]$  (thus the ACD=  $0.032[\text{m}]^2$ ), at the frontier between the anodes and the electrolyte. We then mesh the initial aluminium domain  $\Omega_{al}^0$  (grey region in Figure 4.2) and the initial electrolyte domain  $\Omega_{el}^0$  (red region in Figure 4.2) and denote  $\mathcal{T}_h^0$  the corresponding mesh of  $\Omega_{al}^0 \cup \Omega_{el}^0$  into tetrahedra of maximum size  $h$ .

At iteration  $k$ , given  $\Gamma^k$ ,  $\tilde{\Gamma}^k$  and the mesh  $\mathcal{T}_h^k$ , we update the vertices of the interface  $\Gamma^k$  according to (4.12) to obtain  $\Gamma^{k+1}$ . We also update the vertices of the fictitious interface to obtain  $\tilde{\Gamma}^{k+1}$  by locating them at exactly ACD=0.032[m] above those of  $\Gamma^{k+1}$ . We then move proportionally the vertices of the aluminium and electrolyte domains to obtain  $\Omega_{al}^{k+1}$  and  $\Omega_{el}^{k+1}$ , see Figure 4.2, bottom. Notice that the mesh topology remains unchanged. Details of this method can be found in [Pai06]. The electromagnetic variables are computed on a wider mesh containing the whole cell structure including the fluid mesh  $\mathcal{T}_h$ . (see [Ste09; Roc16])

---

<sup>2</sup>ACD stands for Anode Cathode Distance, and is the height between the aluminium-bath interface and the anodes.

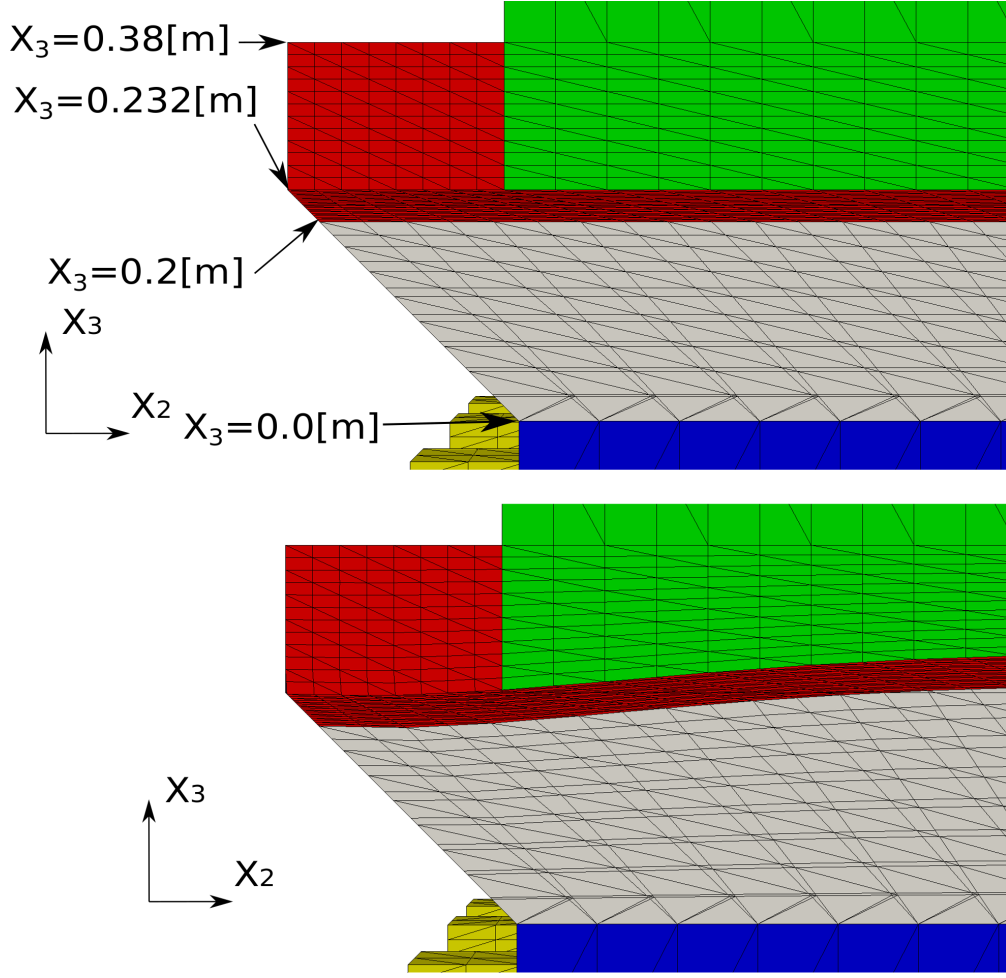


Figure 4.2 – Top: initial mesh  $\mathcal{T}_h^0$ . Bottom: deformed mesh  $\mathcal{T}_h^k$ . The grey region contains the aluminium while the red region contains the electrolytic bath. The interface  $\Gamma^0$  at initialisation is located at  $x_3 = 0.2[m]$ . An additional fictitious interface is added at  $x_3 = 0.032[m]$  above the interface in order to have a constant distance between the interface and the anodes (green).

### Finite element spaces

Define  $\mathcal{S}_h^k$  and  $\mathcal{G}_h$  as discretizations into triangles of respectively  $\Gamma^k$  and  $\Gamma_{out}$ . For the fluid domain  $\Omega$ , consider the following spaces:

$$\mathbf{V}_h^k = \left\{ \mathbf{v} \in C^0(\bar{\Omega}^k)^3 : v_1|_K, v_2|_K, v_3|_K \in \mathbb{P}^1(K), \forall K \in \mathcal{T}_h^k; \mathbf{v} \cdot \mathbf{n} = 0 \text{ on } \partial\Omega \setminus \Gamma_{out} \right\}, \quad (4.41)$$

In addition, let  $P_{pres}$  be a point of one of the vertices of the interface mesh  $\mathcal{G}_h^k$ . Then:

$$\mathcal{L}_{el}^k = \left\{ W \in C^0(\bar{\Omega}^k) : W|_K \in \mathbb{P}^1(K), \forall K \in \mathcal{T}_h^k; W = 0 \text{ in } \Omega_{al}^k \setminus \Gamma^k; W(P_{pres}) = 0 \right\}, \quad (4.42)$$

$$\mathcal{L}_{al}^k = \left\{ W \in C^0(\bar{\Omega}^k) : W|_K \in \mathbb{P}^1(K), \forall K \in \mathcal{T}_h^k; W = 0 \text{ in } \Omega_{el}^k \setminus \Gamma^k; W(P_{pres}) = 0 \right\}, \quad (4.43)$$

$$A_h^k = \left\{ W \in C^0(\bar{\Omega}_{el}^k) : W|_K \in \mathbb{P}^1(K), \forall K \in \mathcal{T}_h^k \cap \Omega_{el}^k \right\}, \quad (4.44)$$

$$\mathcal{S}_{h,fe}^k = \left\{ W \in C^0(\Gamma) : W|_T \in \mathbb{P}^1(T), \forall T \in \mathcal{T}_h^k \right\}, \quad (4.45)$$

$$\mathcal{G}_{h,fe} = \left\{ W \in C^0(\Gamma_{out}) : W|_T \in \mathbb{P}^1(T), \forall T \in \mathcal{G}_h \right\}. \quad (4.46)$$

#### 4.2.2 Iterative algorithm without gas

Let the magnetic field  $\mathbf{B}$  be given. The Alucell software successively performs the following steps [Ste09; Roc16], updating the electric potential  $V_h^k$ , the density current  $\mathbf{j}_h^k$ , the fluid velocity  $\mathbf{u}_h^k$ , the pressure  $p_h^k$ , the jump of the normal forces on the interface  $\psi_h^k$  and the height of the bath-metal interface  $H^k$  from step  $k$  to the next step  $k+1$ :

1. Compute the discretized potential  $V_h^{k+1}$  on a mesh containing the whole cell solving (4.25) as in [Roc16](page 83) and the current density  $\mathbf{j}_h^{k+1}$  with:

$$\mathbf{j}_h^{k+1} = \sigma_h^k \left( -\nabla V_h^{k+1} + \mathbf{u}_h^k \wedge \mathbf{B} \right). \quad (4.47)$$

2. Solve the Navier-Stokes system to find the numerical velocity  $\mathbf{u}_h^{k+1}$ , the pressure  $p_h^{k+1}$  and the jump on  $\Gamma_h^k$  of the normal viscous forces  $\psi_h^{k+1}$ : look for  $(\mathbf{u}_h^{k+1}, p_h^{k+1}, \psi_h^{k+1}) \in \mathbf{V}_h^k \oplus V_{bubble,h} \times \mathcal{L}_{el}^k \oplus \mathcal{L}_{al}^k \times \mathcal{S}_{h,fe}^k$  such that:

$$\begin{aligned} & \int_{\Omega} (\rho_h \mathbf{u}_h^{k+1} \cdot \nabla) \mathbf{u}_h^{k+1} \cdot \mathbf{v} dx + \int_{\Omega} 2\mu \left( \epsilon(\mathbf{u}_h^{k+1}) : \epsilon(\mathbf{v}) \right) dx \\ & + \int_{\partial\Omega} f_{wall} \mathbf{u} \cdot \mathbf{t}_1 (\mathbf{v} \cdot \mathbf{t}_1) ds + \int_{\partial\Omega} f_{wall} \mathbf{u} \cdot \mathbf{t}_2 (\mathbf{v} \cdot \mathbf{t}_2) ds \\ & - \int_{\Omega} p_h^{k+1} \operatorname{div}(\mathbf{v}) dx - \int_{\Gamma} \psi_h^{k+1} (\mathbf{v} \cdot \mathbf{n}) ds = \int_{\Omega} (\rho_h \mathbf{g} + \mathbf{j}_h^{k+1} \wedge \mathbf{B}) \cdot \mathbf{v} dx, \quad (4.48) \\ & \int_{\Omega} \operatorname{div}(\mathbf{u}_h^{k+1}) q dx = 0, \\ & \int_{\Gamma} \zeta(\mathbf{u}_h^{k+1} \cdot \mathbf{n}) ds = 0, \end{aligned}$$

$\forall (\mathbf{v}, q, \zeta) \in \mathbf{V}_h^k \oplus V_{bubble,h} \times \mathcal{L}_{el}^k \oplus \mathcal{L}_{al}^k \times \mathcal{S}_{h,fe}^k$ , where  $V_{bubble,h}$  is the same bubble space as in chapter 1 (see (1.95) and the density  $\rho_h$  follows the discretized equivalent of definition (4.3)<sup>3</sup>. The system is linearised if needed and solved with Newton's method as

<sup>3</sup>This is the case without gas, with  $\alpha_g = 0$  everywhere. Notice that at the discrete level, the discretized integrals over  $\Omega$  containing density  $\rho_h$  is performed tetrahedron after tetrahedron: therefore either a tetrahedron is above the interface  $\Gamma$  and belongs to  $\Omega_{el}$ , either it is below  $\Gamma$  and belongs to  $\Omega_{al}$ : there is no ambiguous case when computing the integrals with  $\rho_h$ .

detailed in section 1.10. Notice that the pressure  $p_h^{k+1}$  is discontinuous on the interface  $\Gamma_h^k$ , except on the point  $P_{press}$  (4.42-4.43).

3. Finally the interface is moved following (4.12), i.e the new height of the interface is given by:

$$H^{k+1} = H^k + \frac{\psi_h^{k+1} + C}{[\rho_h |g|]}, \quad (4.49)$$

which is used to parametrised the new interface  $\Gamma_h^{k+1}$ , with  $x_3 = H^{k+1}(x_1, x_2)$ . The constant  $C$  is chosen such that the volume of aluminium is conserved:

$$\int_{\Gamma} H^k(x_1, x_2) dx_1 dx_2 = \int_{\Gamma} H^{k+1}(x_1, x_2) dx_1 dx_2 = Vol(\Omega_{al}), \quad (x_1, x_2) \in \Gamma^0. \quad (4.50)$$

At the end of this stage, the fluid mesh  $\mathcal{T}_h^{k+1}$  is adapted to the new interface  $\Gamma_h^{k+1}$ , with the procedure described in [Pai06]: the nodes are moved along  $x_3$  proportionally to the value of  $H^{k+1}$ .

A repetition of steps 1. to 3. with appropriate boundary conditions converge, fortunately, to a stationary solution in terms of electric potential, current density, velocity field, pressure and interface in practice.

### 4.2.3 Iterative algorithm with gas

Now the algorithm 4.2.2 is modified to include the gas model of this thesis. The following describes how to update the unknowns of the precedent algorithm  $V_h^k, \mathbf{j}_h^k, \mathbf{u}_h^k, p_h^k, \psi_h^k, H^k$ , with in addition the normal of the viscous force on the outflow  $\Gamma_{out}$  denoted by  $\xi_h^k$ , the gas velocity  $\mathbf{u}_{g,h}^k$  and the gas distribution  $\alpha_{g,h}^k$  from step  $k$  to the next step  $k+1$ :

1. As previously described, compute the discretized potential  $V_h^{k+1}$  on on a mesh containing the whole cell solving (4.25) and the current density  $\mathbf{j}_h^{k+1}$  with:

$$\mathbf{j}_h^{k+1} = \sigma_h^k \left( -\nabla V_h^{k+1} + \mathbf{u}_h^k \wedge \mathbf{B} \right). \quad (4.51)$$

The influence of the gas modifying  $\sigma_h^k$  as depending on  $\alpha_{g,h}^k$  is also investigated (section 4.6.3).

2. At this stage, the discrete density in the electrolyte is not constant and is modified by the gas, computed as

$$\rho_h = \begin{cases} \rho_{al} & \text{if } K_j \in \Omega_{al}^k \cap \mathcal{T}_h^k; \\ \alpha_{g,h}^k \rho_g + (1 - \alpha_{g,h}^k) \rho_{el} & \text{if } K_j \in \Omega_{el}^k \cap \mathcal{T}_h^k. \end{cases} \quad (4.52)$$

for each tetrahedron  $K_j$  in  $\mathcal{T}_h^k$ . The following system with variable density is considered. Search for  $(\mathbf{u}_h^{k+1}, p_h^{k+1}, \psi_h^{k+1}, \xi_h^{k+1}) \in \mathbf{V}_h \oplus V_{bubble,h} \times \mathcal{L}_{el}^k \oplus \mathcal{L}_{al}^k \times \mathcal{S}_{h,fe}^k \times \mathcal{G}_{h,fe}^k$  such that:

$$\begin{aligned}
& \int_{\Omega} (\rho_h \mathbf{u}_h^{k+1} \cdot \nabla) \mathbf{u}_h^{k+1} \cdot \mathbf{v} dx + \int_{\Omega} 2\mu \left( \epsilon(\mathbf{u}_h^{k+1}) : \epsilon(\mathbf{v}) - \frac{1}{3} \operatorname{div}(\mathbf{u}_h^{k+1}) \operatorname{div}(\mathbf{v}) \right) dx \\
& - \int_{\Omega} p_h^{k+1} \operatorname{div}(\mathbf{v}) dx - \int_{\Gamma_{out}} \xi_h^{k+1} (\mathbf{v} \cdot \mathbf{n}) ds - \int_{\Gamma} \psi_h^{k+1} (\mathbf{v} \cdot \mathbf{n}) ds = \int_{\Omega} (\rho_h \mathbf{g} + \mathbf{j}_h^{k+1} \wedge \mathbf{B}) \cdot \mathbf{v} dx, \\
& \int_{\Omega} \operatorname{div}(\rho_h \mathbf{u}_h^{k+1}) q dx = 0, \\
& \int_{\Gamma_{out}} \zeta_{out}(\mathbf{u}_h^{k+1} \cdot \mathbf{n}) ds = 0, \\
& \int_{\Gamma} \zeta(\mathbf{u}_h^{k+1} \cdot \mathbf{n}) ds = 0,
\end{aligned} \tag{4.53}$$

$\forall (\mathbf{v}, q, \zeta_{out}, \zeta) \in \mathbf{V}_h \oplus V_{bubble,h} \times \mathcal{L}_{el}^k \oplus \mathcal{L}_{al}^k \times \mathcal{S}_{h,fe}^k \times \mathcal{G}_{h,fe}^k$ . The system is linearised if needed and solved with Newton's method as detailed in section 1.10.

3. As before, the new height of the interface is given by:

$$H^{k+1} = H^k + \frac{\psi_h^{k+1} + C}{[\rho_h |\mathbf{g}|]}, \tag{4.54}$$

the only difference being that  $\rho_h$  has changed since it depends on  $\alpha_{g,h}^k$  (4.3). The constant  $C$  is chosen to conserve the aluminium volume and the nodes of the mesh are moved with exactly the same procedure as (4.50).

4. The restriction of the variables  $\mathbf{u}_h^{k+1}$ ,  $p_h^{k+1}$  to  $\Omega_{el}^{k+1} \cap \mathcal{T}_h^{k+1}$  can be obtained directly considering their values node by node and  $\mathbf{j}_h^{k+1}$  its value element by element. The source is then defined as:

$$\dot{\alpha}_{h,source} = \frac{\eta_f IM_{CO_2}}{4F\rho_g} \frac{|\mathbf{j}_h^{k+1}|}{\int_{\Omega_{el}} |\mathbf{j}_h^{k+1}| dx}, \text{ for every element } K \text{ in } \Omega_{el}^{k+1} \cap \mathcal{T}_h^{k+1}. \tag{4.55}$$

5. First compute the constant  $p_0$  as:

$$p_0 = \frac{\int_{\Gamma_{out}} \xi_h^{k+1} ds}{\int_{\Gamma_{out}} ds}, \tag{4.56}$$

then for  $N_g$  steps, a sub-algorithm is going to be performed. The sub-sequences  $\alpha_{g,h}^{k,r}$ ,  $\mathbf{u}_{g,h}^{k,r}$  are considered where the sub-index  $r = 0, \dots, N_g$ . Of course, the initialisation is  $\alpha_{g,h}^{k,r=0} = \alpha_{g,h}^k$  and  $\mathbf{u}_{g,h}^{k,r=0} = \mathbf{u}_{g,h}^k$ . The sub-algorithm reads:

(a) Look for  $\mathbf{u}_{g,h}^{k,r+1} \in \mathbf{V}_h^{k+1} \cap \Omega_{el}^{k+1}$  such that:

$$\begin{aligned}
 & \int_{\Omega_{el}^{k+1}} (\rho_g \alpha_{g,h}^{k,r} \mathbf{u}_{g,h}^{k,r+1} \cdot \nabla) \mathbf{u}_{g,h}^{k,r+1} \cdot \mathbf{v}_{g,h} dx + \int_{\Omega_{el}^{k+1}} (\rho_g \dot{\alpha}_{h,source}) \mathbf{u}_{g,h}^{k,r+1} \cdot \mathbf{v}_g dx \\
 & - \int_{\Gamma_{out}} (\alpha_{g,h}^{k,r} p_0) (\mathbf{v}_g \cdot \mathbf{n}) ds + \int_{\Omega_{el}^{k+1}} 2\mu_g \left( \epsilon(\mathbf{u}_{g,h}^{k,r+1}) : \epsilon(\mathbf{v}_g) - \frac{1}{3} \operatorname{div}(\mathbf{u}_{g,h}^{k,r+1}) \operatorname{div}(\mathbf{v}_g) \right) dx \\
 & = \int_{\Omega_{el}^{k+1}} \alpha_{g,h}^{k,r} (p_h) \operatorname{div}(\mathbf{v}_g) dx + \int_{\Omega_{el}^{k+1}} (p_h^{k+1}) \nabla \alpha_{g,h}^{k,r} \cdot \mathbf{v}_g dx + \int_{\Omega_{el}^{k+1}} \alpha_{g,h}^{k,r} \rho_g \mathbf{g} \cdot \mathbf{v}_g dx \\
 & + \int_{\Omega_{el}^{k+1}} D \frac{\rho_h}{\rho_l} \alpha_{g,h}^{k,r} (\mathbf{u}_h^{k+1} - \mathbf{u}_{g,h}^{k,r+1}) \cdot \mathbf{v}_g dx,
 \end{aligned} \tag{4.57}$$

$\forall \mathbf{v}_g \in \mathbf{V}_h^{k+1} \cap \Omega_{el}^{k+1}$ . The linearisation (section 1.10) is applied for the non linear terms.

(b) Then perform one time step of the advection-diffusion equation, that is look for  $\alpha_{g,h}^{k,r+1} \in A_h^{k+1}$  such that:

$$\begin{aligned}
 & \int_{\Omega_{el}^{k+1}} \frac{\alpha_{g,h}^{k,r+1} - \alpha_{g,h}^{k,r}}{\Delta t} \omega dx + \int_{\Omega_{el}^{k+1}} \operatorname{div}(\alpha_{g,h}^{k,r+1} \mathbf{u}_{g,h}^{k,r+1}) \omega dx + \int_{\Omega_{el}^{k+1}} K \nabla \alpha_{g,h}^{k,r+1} \nabla \omega dx \\
 & + \frac{h C_S}{2 |\mathbf{u}_{g,h}^{k,r+1}|} \int_{\Omega_{el}^{k+1}} (\mathbf{u}_{g,h}^{k,r+1} \cdot \nabla \omega) (\operatorname{div}(\alpha_{g,h}^{k,r+1} \mathbf{u}_{g,h}^{k,r+1}) - \dot{\alpha}_{h,source}) dx = \int_{\Omega_{el}^{k+1}} \dot{\alpha}_{h,source} \omega dx,
 \end{aligned} \tag{4.58}$$

for all  $\omega \in A_h^{k+1}$ . Finally update the density  $\rho_h = \alpha_{g,h}^{k,r+1} \rho_g + (1 - \alpha_{g,h}^{k,r+1}) \rho_{el}$  in  $\Omega_{el,h}^{k+1}$ .

Repeat (4.57-4.58)  $N_g$  times.

6. At this stage,  $\alpha_{g,h}^{k+1}$  is chosen as  $\alpha_{g,h}^{k,r+1}$  and  $\mathbf{u}_{g,h}^{k+1}$  as  $\mathbf{u}_{g,h}^{k,r+1}$ . From a virtual time-flow perspective, a time  $T_g = N_g \Delta t$  has elapsed: it is important that this virtual time is not too small when aiming at a stationary state. Virtually  $\mathbf{u}_h^{k+1}$ ,  $\mathbf{u}_{g,h}^{k+1}$  and  $\alpha_{g,h}^{k+1}$  can be seen as the numerical solutions at time  $t = (k+1) \Delta t N_g$ .

Notice that if the algorithm with gas is used setting  $\dot{\alpha}_{source} = 0$ , steps 4 to 6 give for all steps  $\alpha_g = 0$  and  $\mathbf{u}_g = \mathbf{0}$ , thus giving the same results as the first algorithm 4.2.2.

#### 4.2.4 Initialisation of the algorithms

The initial values of the unknowns of both algorithms are zeros:  $\mathbf{u}_h^0 = \mathbf{0}$ ,  $\mathbf{u}_{g,h}^0 = \mathbf{0}$ ,  $\alpha_{g,h}^0 = 0$ ,  $H^0 = 0$ . System (4.53) is solved with a Newton method. The delicate part is to initialise the solution appropriately. As it is discussed in [KLS06], a good initial guess consists into solving the Stokes problem  $(\rho_h \mathbf{u}_h \cdot \nabla) \mathbf{u}_h$  neglected) with an artificial viscosity. A blind first step of the method would not be a good choice because the turbulent viscosity  $\mu_T = C_T \rho |\epsilon(\mathbf{u}_h)|$  would

be homogeneously zero. For this reason, the first iteration of Newton is computed with the following tensor viscosity, which values have been calibrated with respect to the geometric ratio of the cells in a study in [DFR98]:

$$\mu = (\mu)_{i,j} = \begin{pmatrix} 10 & 10 & 0.5 \\ 10 & 10 & 0.5 \\ 0.5 & 0.5 & 1 \end{pmatrix} [kg/ms]. \quad (4.59)$$

For the gas velocity system (4.57), the value  $\mu_g = 0.5[kg/ms]$  is set.

### 4.3 Two aluminium reduction cell domains

In this section, two aluminium reduction cells are presented. These type of cells that are considered are based on the AP technology developed by Rio Tinto. The first cells of this kind were put in service in the early 1990, and more than four thousand of them are still operating worldwide (in 2011) [Alu13]. The first cell is a so-called simplified cell containing six anodic blocks, while the real scale industrial cell called AP32 is composed of twenty anodic blocs. The two domains having a lot of similarities, a number of numerical experiments are performed with the simplified cell, in order to spare computational time.

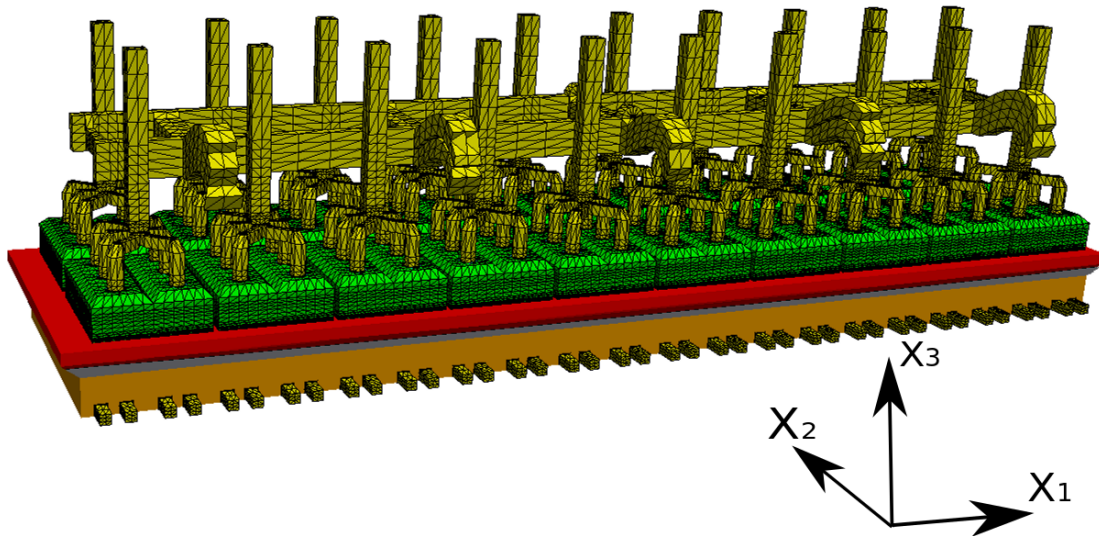


Figure 4.3 – Side view of a numerical aluminium electrolysis cells: the electric current comes through the yellow bars, then through the anodic blocks (green), the electrolytic bath (red), the aluminium liquid (grey) and finally the cathode (orange), and goes out through external bars.

An industrial AP32 cell and its mesh is illustrated in Figure 4.3: it is constituted of twenty anodic blocs<sup>4</sup> and measures 14 meters in length and 3 meters of width. The height of the aluminium liquid measures 20 centimetres and the bath up to the anode 3 centimetres, and the

<sup>4</sup>Each block being constituted of 2 anodes.

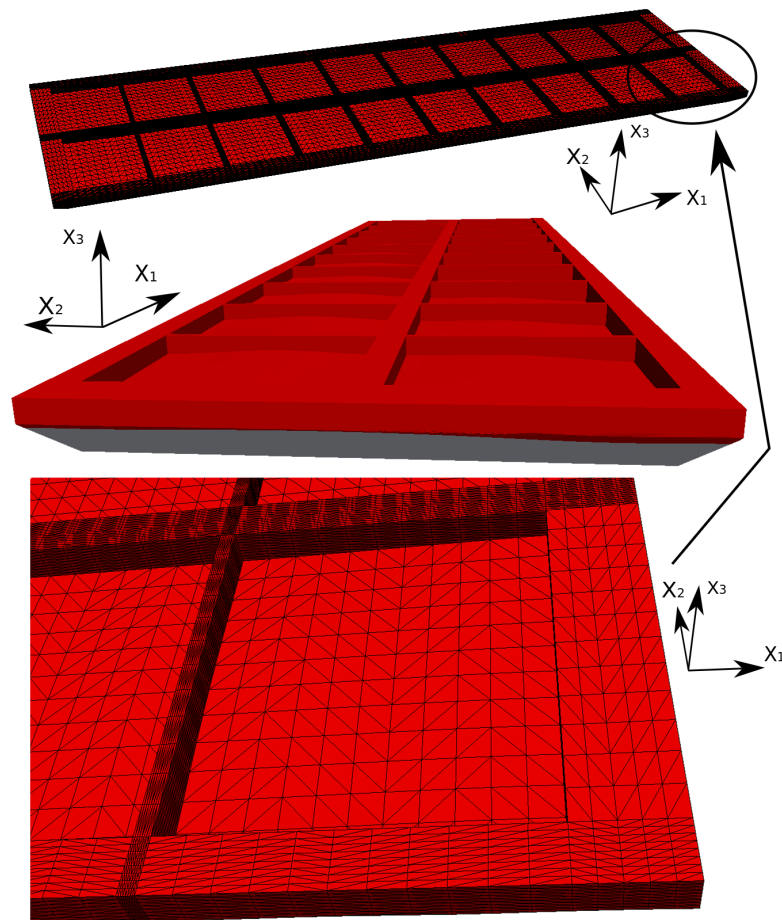


Figure 4.4 – Perspective view of the fluid domain: the electrolytic bath (red) and the aluminium liquid (grey).

liquid domain (aluminium and bath) is shown in Figure 4.4: notice that the elements density is higher in the channels, in order to capture the movement in these areas. The channels between the anodic blocs are 15 centimetres high.

The mesh of this industrial cell contains 1'569'507 vertices and 11'367'168 elements (Figure 4.3) and the fluid domain is made of 978'297 vertices and 7'273'152 elements (Figure 4.4).

In the following, in order to assess the effects of different parameters with a reasonable computational time, a smaller and simplified cell of only six anodic blocs will be used. The external forces on this cell are artificial, but we will see that the behaviour of the flow is similar with the flow of the industrial cell. This small cell is composed of 283'362 vertices and 2'076'120 elements for the complete cell, and of 171'945 vertices and 1'231'416 elements for the fluid domain. The fluid domain of this simplified cell and the surrounding blocks are shown in Figure 4.5.

Typical results are shown for both cells in Figures 4.6 and 4.7. In both cases: the velocity

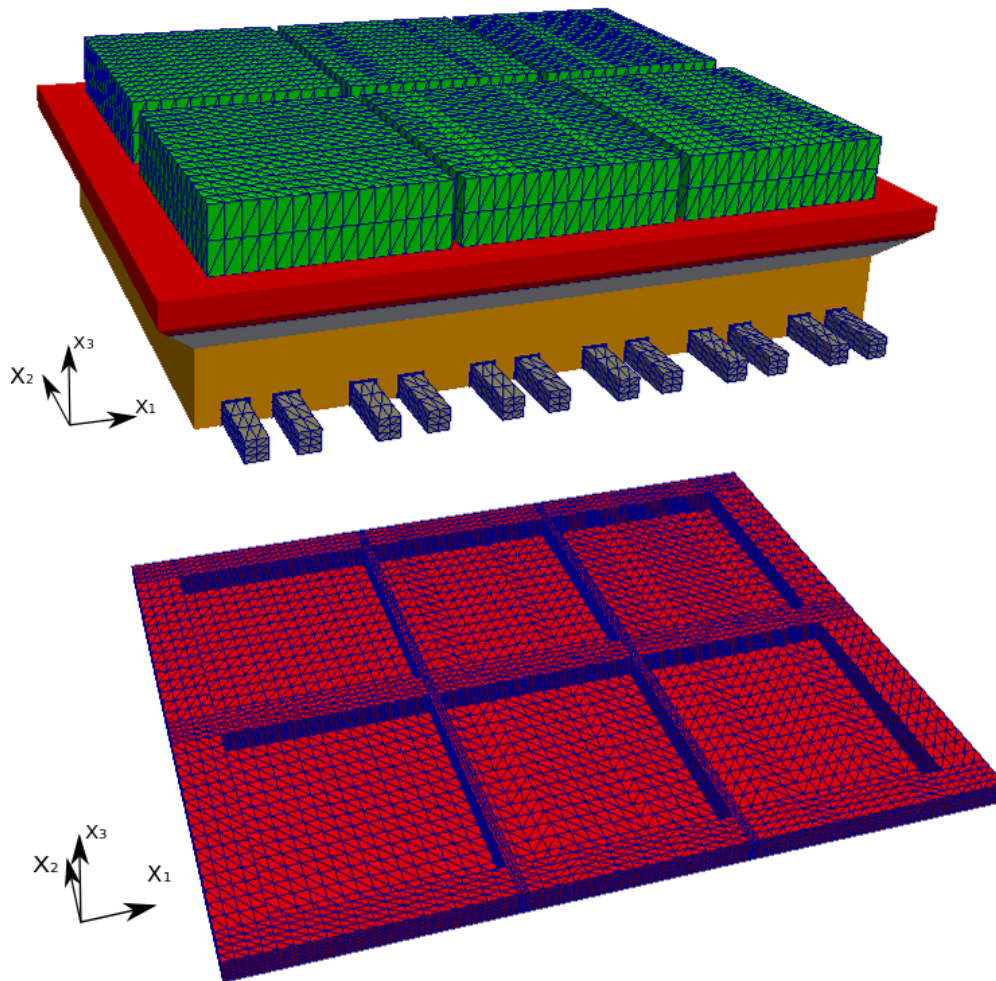


Figure 4.5 – Perspective view of the smaller simplified cell, containing only six anodic blocs, above a view of the cells with the anodes, and below only the mesh of the fluid domain viewed from the top.

field is important in the central channels and along the left and right sides of the cell, leading to eddies in these areas. The smaller lateral channels also exhibits a velocity field pointing "outwards". Because of these common behaviours, some results on the smaller domain can be reasonably assumed to be the same on the complete cell. Observe that the velocity field is on average more important in the complete cells, leading to more important differences of interface extreme values. The velocities are in the range of a few centimetres per second, up to  $10[cm/s]$ : this corresponds to experimental data available in similar reduction cells on the velocity fields [TH16].

Figure 4.7 shows the interface for both domains. The artificial cell includes a much flatter interface than the industrial case. On the industrial cell, the variations of the interface height can go up to  $6[cm]$  with respect to the average (scaled at zero), for a distance interface to

### 4.3. Two aluminium reduction cell domains

anode in the bath of only 3.2[*cm*].

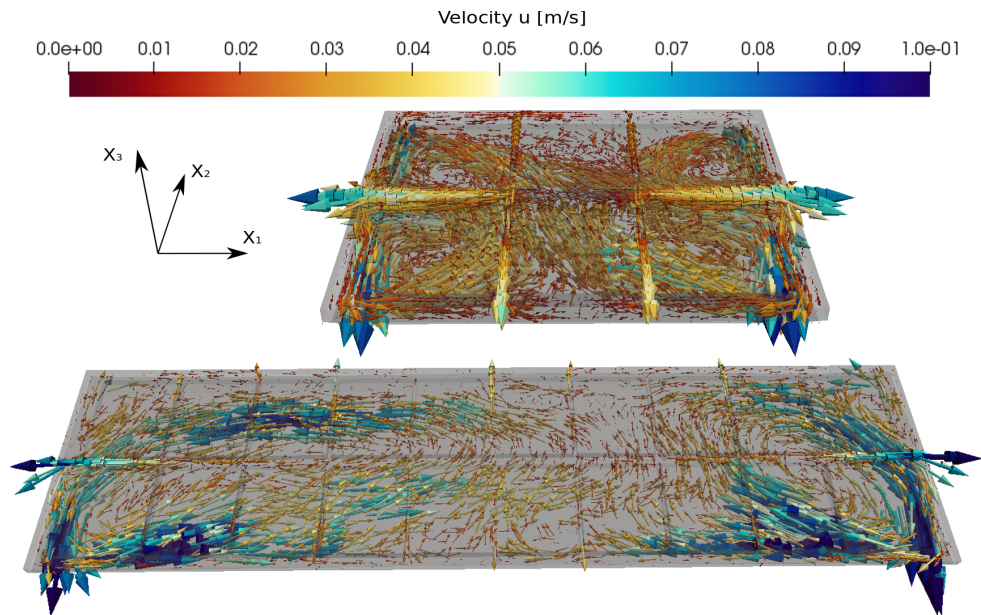


Figure 4.6 – The velocity fields without gas for both cells, top: simplified cell, bottom: industrial cell.

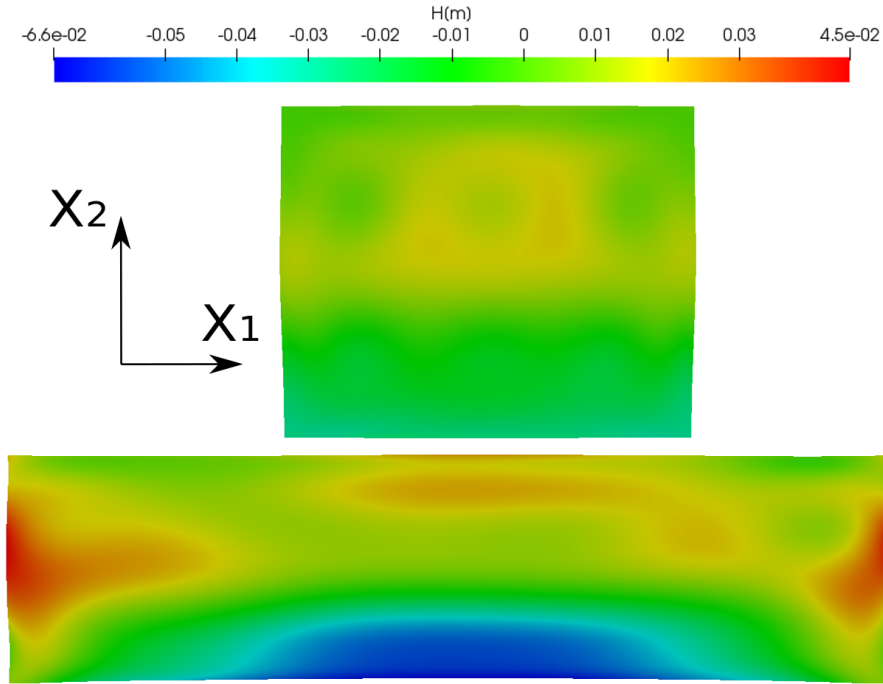


Figure 4.7 – The interface height  $H$  without gas. Top: simplified cell, bottom: industrial cell.

### 4.3.1 Reference solution

The goal is now to study the influence of different parameters on the numerical solution. For this purpose we define a reference solution  $u_{h,ref}$  (for all the relevant unknowns: the velocity, gas velocity, interface, etc). The reference parameters are those given in Table 4.1.

The following notation is used to compare the reference solution  $u_{h,ref}$  with the solution  $u_h$  with different settings:

$$\Delta_{L^2, \Omega} u_h = 100 \frac{\|u_h - u_{h,ref}\|_{L^2(\Omega)}}{\|u_{h,ref}\|_{L^2(\Omega)}}. \quad (4.60)$$

In this example, the difference for a variable is computed in the  $L^2$  norm for the fluid domain  $\Omega$ . If the gas variables are compared ( $\alpha_g, \mathbf{u}_g$ ), the integrals are computed only on the electrolyte domain  $\Omega_{el}$ . If the interface height  $H$  is investigated with this notation, the norms will be computed on  $\Gamma$ .

#### 4.4. Numerical experiments : numerical parameters

Name	Notation	Value	Cross-reference
Electrolytic bath density	$\rho_{el}$	2130 [kg/m <sup>3</sup> ]	(4.3)
Aluminium density	$\rho_{al}$	2270 [kg/m <sup>3</sup> ]	(4.3)
Gas density	$\rho_g$	10 [kg/m <sup>3</sup> ]	(4.28)
Gas viscosity	$\mu_g$	0.5 [kg/ms]	(4.29)
Laminar viscosity	$\mu_L$	0.5 [kg/ms]	section 4.5.2
Electrolytic bath viscosity	$\mu_{el}$	0.002[kg/ms]	(4.4)
Aluminium viscosity	$\mu_{al}$	0.002[kg/ms]	(4.4)
Laminar diffusion coefficient	$K_L$	$5e-5$ [m <sup>2</sup> /s]	(4.30)
Turbulent diffusion coefficient	$K_T$	$5e-4$ [m <sup>2</sup> ]	(4.30)
Turbulent viscosity coefficient	$C_T$	$5e-4$ [m <sup>2</sup> ]	(4.4)
Bubble diameter	$d$	4.0 [mm]	section 4.5.2
Drag coefficient	$D$	$18\mu_L/d^2$	section 4.5.2
Time-step	$\Delta t$	10[s]	section 4.4.3
Gas iterations	$N_g$	6	section 4.4.3
Newton iterations	$N_{Ne}$	3, then 1	(4.4.2)
Friction coefficient external wall	$f_0$	$1e6$ [kg/m <sup>2</sup> s]	section 4.5.1
Friction coefficient anode	$f_1$	$1e4$ [kg/m <sup>2</sup> s]	section 4.5.1
Friction coefficient channels	$f_2$	$1e3$ [kg/m <sup>2</sup> s]	section 4.5.1
Friction coefficient top surface	$f_3$	0[kg/m <sup>2</sup> s]	section 4.5.1
Total current for an industrial cell	$I$	320'000[A]	(4.39)
Source gas production term	$\dot{\alpha}_{source}$ [1/s]	$\frac{\eta_F IM_{CO_2}}{4F}$	(4.39), (4.40)

Table 4.1 – Parameters used to define the reference solution  $u_{h,ref}$ .

#### 4.4 Numerical experiments : numerical parameters

In this section, numerical parameters are investigated in order to reduce the computing time of the algorithm. The distribution of the computational time through one iteration of the algorithm is presented. Then it is shown that a low number of Newton iteration  $N_{Ne} = 1$  is sufficient, as well as a low number of gas iterations  $N_g$  with a parameter  $\Delta t$  between 1 and 100. Finally, results with a mesh with elements twice smaller are compared.

##### 4.4.1 Distribution of the computational time through an iteration on an industrial cell

In the following sections, numerical parameters are investigated in order to converge as fast as possible. These three parameters are the number of Newton iterations  $N_{Ne}$ , the time-step for the gas system  $\Delta t$  and the number of iterations of the gas sub-algorithm  $N_g$ . The first parameter concerns both algorithms 4.2.2 without gas and 4.2.3 with gas, while the two last only applies to the algorithm with gas 4.2.3. Table 4.2 shows the computational time is dedicated to each phase of one iteration of the algorithm with gas 4.2.3 for the industrial AP32 cell, with a machine with a processor Intel(R) Xeon(R) CPU E5-1650 v3 of 3.50GHz, where the

## Chapter 4. Application to aluminium electrolysis

number of Newton iteration and of gas iteration is the unity,  $N_{Ne} = 1$ ,  $N_g = 1$ . These numbers should be as low as possible, while preserving the convergence of the algorithm.

Label	Process in the algorithm	Time on AP32 cell [s]	Percent
A	Maxwell, step 1 and (4.47)	34	4.8%
B	Preconditioner of system (4.53)	55	7.8%
C	Assembly and solving (4.53)	475	67.6%
D	Move $\Gamma$ (4.54) and preprocess $\Omega_{el}$ (BC)	60	8.5%
E	Assembly and solving (4.57)	50	7.1%
F	Assembly and solving (4.58)	29	4.1%
A-F	Total	703	100%

Table 4.2 – Computational time spent at each iteration of (4.2.3) with  $N_g = 1$ ,  $N_{Ne} = 1$  for the industrial AP32 cell.

In the "assembly and solving" rows in Table 4.2, the solving is naturally the time consuming part of the process. In Alucell the algorithm used to solve the finite element linear system is the iterative algorithm GMRES[SS86] in the Petsc library[Abh+18].

If the number of Newton iterations  $N_{Ne} > 1$  is not unity, part C in Table 4.2 is multiplied by the corresponding factor. As it represents around 70% of an iteration of the algorithm when set to unity, it is the first parameter to investigate.

If the number of iterations of the gas sub-algorithm  $N_g > 1$  is not unity, parts E and F in Table 4.2 are multiplied accordingly. For the same reason it should be as low as possible.

Finally the time-step parameter  $\Delta t$  only impacts part F in Table 4.2. If it is too small, the algorithm would be meaningless as it would correspond to look at a very short time-scale. As long as the virtual time associated, the product  $N_g \times \Delta t$  is sufficiently important, the solution can be considered meaningful. In order to have a sufficient product  $N_g \times \Delta t$ , but also a low  $N_g$ , the time-step should be as large as possible, as long as it converges.

In the following, it is considered that an absolute tolerance of  $1e - 5$  [m/s] on velocity fields of the order of  $1e - 2$  to  $1e - 1$  [m/s] is enough. In an industrial AP32 cell, 10 iterations suffice in general to reach a discrepancy below  $1e - 5$ .

### 4.4.2 Influence of Newton iterations $N_{Ne}$ on a small cell

The effect of  $N_{Ne}$  on the discrepancy of the velocity when using algorithm 4.2.2 is shown in Figure 4.8. The number of Newton iteration does not change the rate of convergence, except at the very first step of the algorithm. As a result, the number of Newton iteration will be  $N_{Ne} = 1$  by default, except for the initialisation, where three Newton iterations are used.

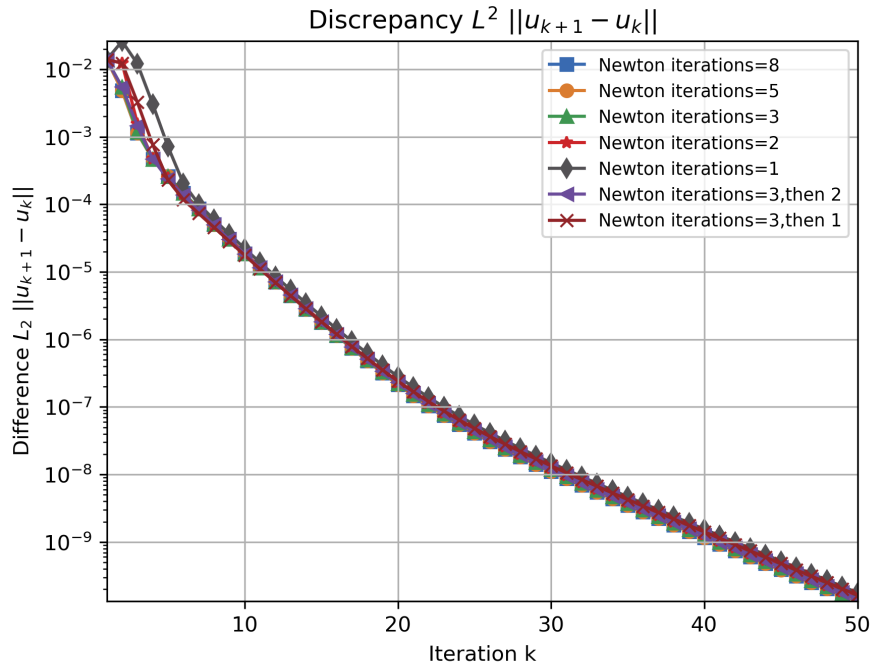


Figure 4.8 – Discrepancy of the velocity  $\mathbf{u}$  through 50 iterations of algorithm (4.2.2) for different Newton iteration  $N_{Ne}$ .

#### 4.4.3 Influence of gas iteration $N_g$ and time-step $\Delta t$ on a small cell

In algorithm (4.2.3), numerical experiments showed that the initialisation should be performed with  $\Delta t < 1000[s]$ . The discrepancy of numerical experiments with various values of  $N_g$  and  $\Delta t$  are shown in Figures 4.9 and 4.10. Figure 4.9 shows several cases where the product  $N_g \times \Delta t = 60[s]$  is constant and Figure 4.10 shows various values of  $N_g$ . In particular, it shows that  $N_g = 1$  should be avoided, as it impacts the convergence, while a virtual time  $N_g \times \Delta t = 60[s]$  gives the same convergence rate as a virtual time of  $N_g \times \Delta t = 4800[s]$ . The default values are taken as  $\Delta t = 10[s]$ ,  $N_g = 6$ .

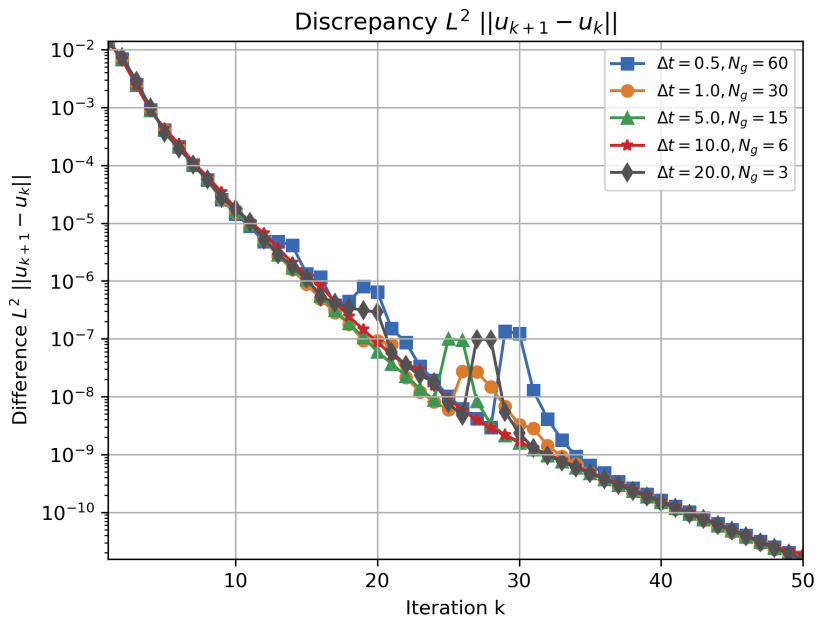


Figure 4.9 – Behaviour of the discrepancy of the velocity  $\mathbf{u}$  through fifty iterations of algorithm 4.2.3 for different values of  $\Delta t$  and  $N_g$ , while preserving the product  $N_g \times \Delta t$ .

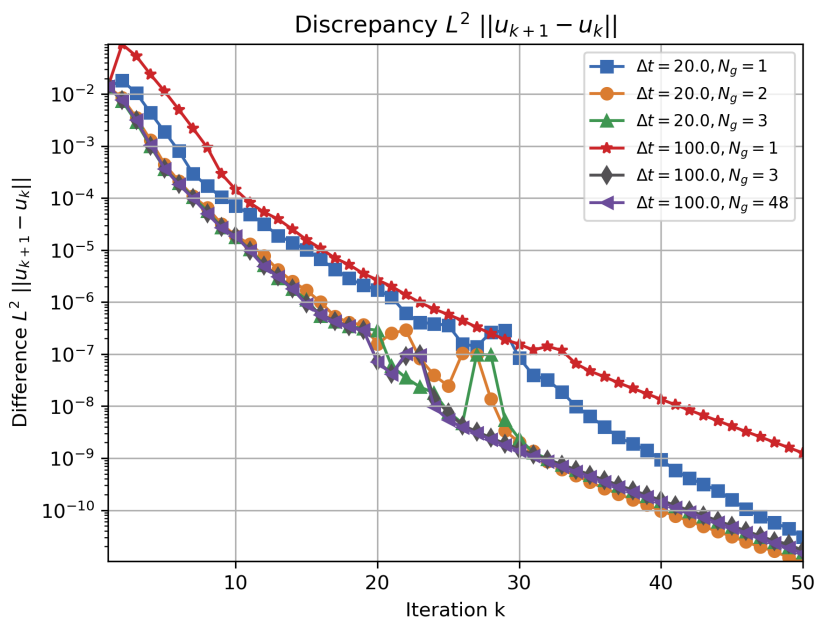


Figure 4.10 – Behaviour of the discrepancy of the velocity  $\mathbf{u}$  through fifty iterations of algorithm 4.2.3 for an increase value of the product  $N_g \times \Delta t$ .

### 4.4.4 Comparison with a fine mesh on a small cell

In this subsection, the solutions of the mesh of size  $h$  shown in section of the simplified cell are compared with solutions obtained on the same geometry, with a mesh size two times smaller  $h/2$ . Four situations are compared:

- A the solution of algorithm without gas 4.2.2 on the mesh of size  $h$ .
- B The solution of algorithm with gas 4.2.3 on the mesh of size  $h$ .
- C the solution of algorithm without gas 4.2.2 on the mesh of size  $h/2$ .
- D The solution of algorithm with gas 4.2.3 on the mesh of size  $h/2$ .

Figure 4.11 shows that the velocity field  $\mathbf{u}$  do not change much in the electrolyte between the two meshes. Figure 4.12 shows similar results, except with the finer mesh in one lateral channel. Figure 4.13 shows that the interface obtained with both meshes is similar.

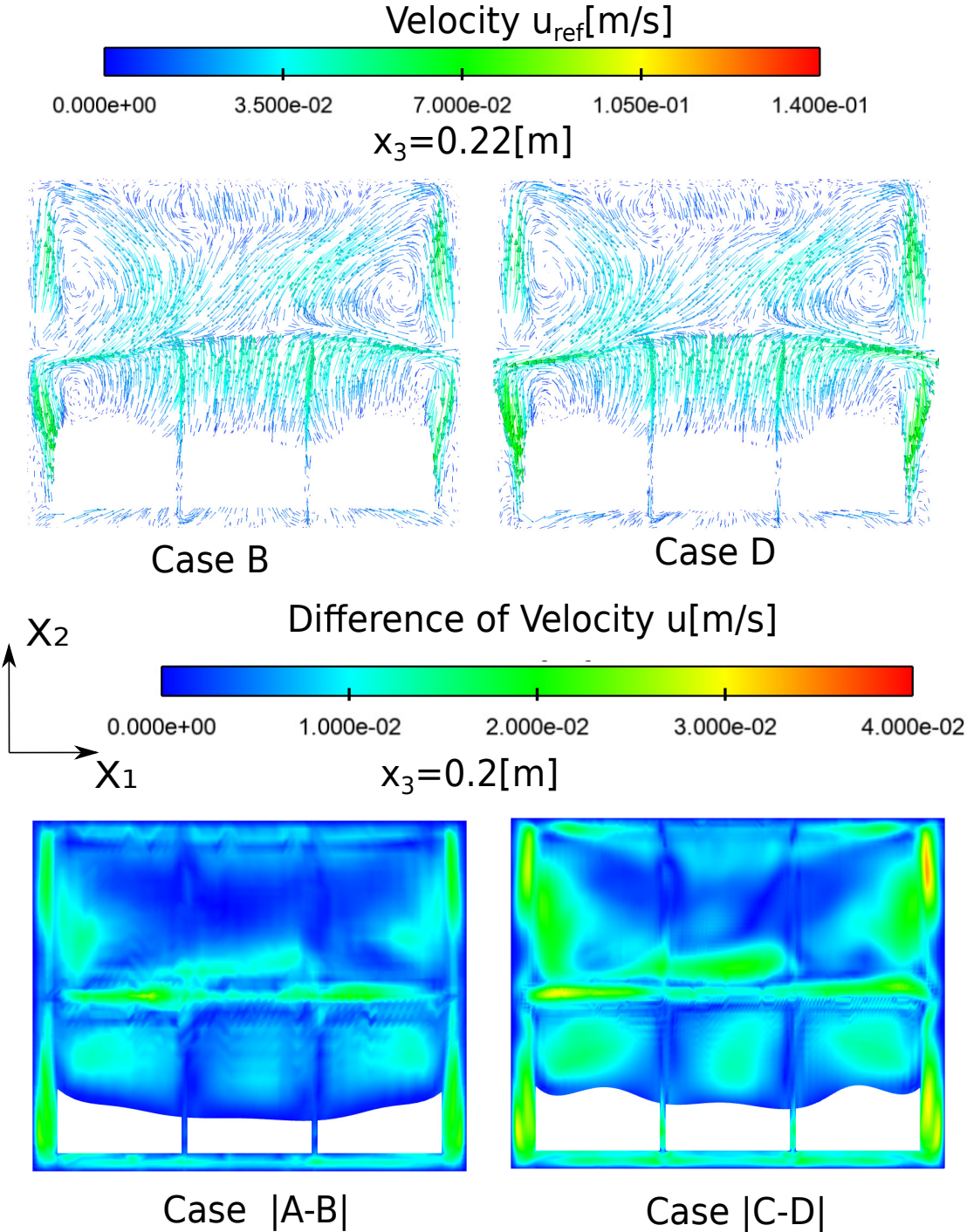


Figure 4.11 – On the left: results with mesh of size  $h$ . On the right: results with size  $h/2$ . Top: velocity field of reference solution. Bottom: Difference of amplitude of the velocity field with and without gas.

#### 4.4. Numerical experiments : numerical parameters

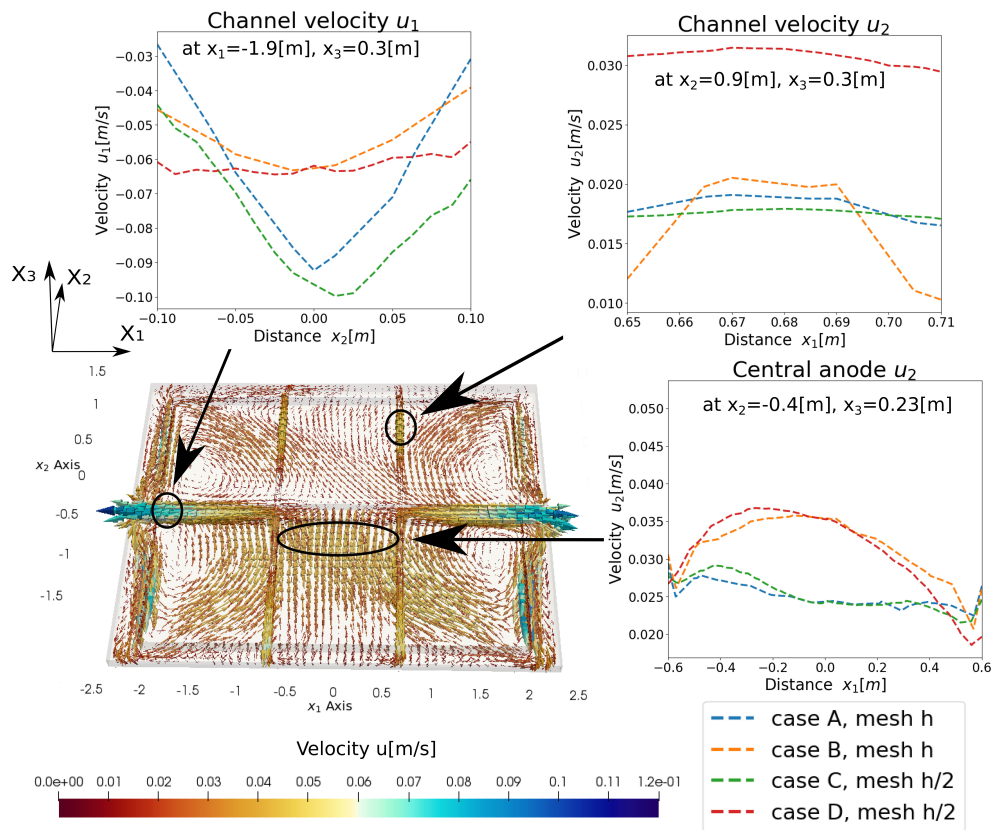


Figure 4.12 – Velocity field  $\mathbf{u}$  for cases A to D.

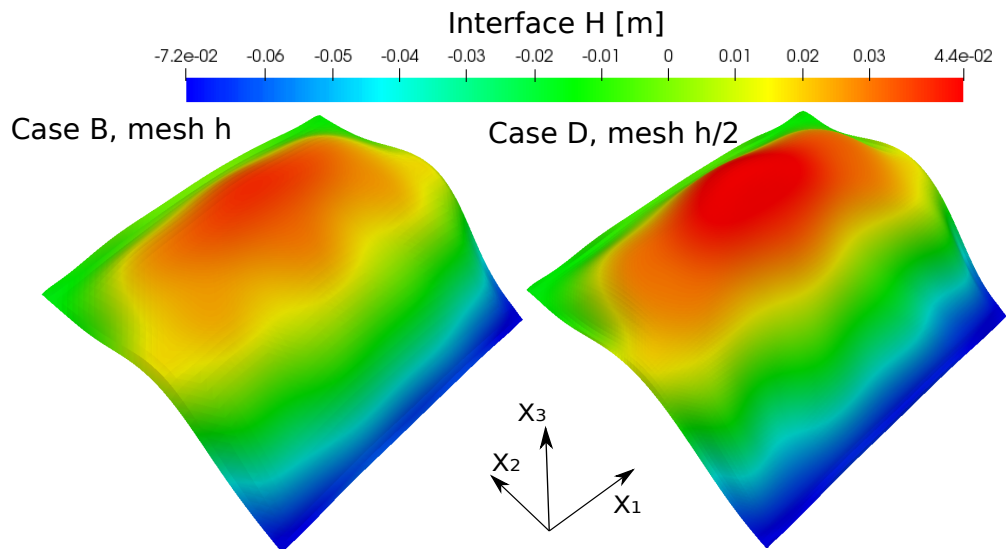


Figure 4.13 – Interface  $H$  obtained with gas, on the left with mesh of size  $h$ , on the right with mesh of size  $h/2$ .

### 4.4.5 Conclusion about the numerical parameters

The default values have been chosen as  $N_{Ne} = 1$ ,  $N_g = 6$  and  $\Delta t = 10[s]$  for the examples in the following of this thesis. With this setting, ten iterations are sufficient to reach a tolerance of  $10^{-5}$  in the algorithm without gas in the AP32 industrial cell. This result can be obtained in roughly two hours. This is a substantial improvement compared to precedent thesis [Roc16; Hil19] although the mesh of the fluid is refined in the channels, mainly due to the fact that the Newton algorithm was not converging with the optimal rate previously (remark 8, chapter 1). For this reason, the number of Newton iterations  $N_{Ne}$  chosen was higher than necessary, resulting to an important computational cost. In the following, a unique Newton iteration per surface iteration of the algorithm is sufficient. This results in a considerable reduction of the computational time.

Moreover, notice that with these values, based on the computational time in Table 4.2, for each iteration of the algorithm with gas 4.2.3, the amount of time dedicated to the gas system will be ( $N_g$  times parts E and F) 474[s], 43% of the computational time. Taking only ( $N_g = 2, \Delta t = 100$ ) will reduce this time to 158[s], in this case the gas model would only account for 20% of the computational time, while preserving the convergence.

In conclusion, the recommended setting is to take  $N_{Ne} = 1$ , a small value of  $N_g > 1$  and  $1 < \Delta t < 1000$ . If the product  $N_g \times \Delta t > 60$ , the same convergence has been observed. The mesh size does not seem to change much the solution, except in the lateral channels where the number of elements is very low.

## 4.5 Numerical experiments on the smaller simplified electrolysis cell: physical parameters

In this section, different physical parameters of the model are investigated on the simplified cell. First the effect of the boundary conditions on the velocity field is discussed through various choices of friction coefficients. Then, numerical experiments with different amplitudes of Drag forces, turbulent diffusion coefficient and gas viscosities are presented

### 4.5.1 Boundary conditions and friction coefficients

In this section the influence of the friction coefficients is investigated, when using algorithm 4.2.2 without gas. The boundary conditions used for the mixture velocity  $\mathbf{u}$  are:

$$\mathbf{u} \cdot \mathbf{n} = 0 \text{ on } \partial\Omega,$$

$$(\boldsymbol{\tau} \cdot \mathbf{n}) \cdot \mathbf{t}_i = -f_{Wall} \mathbf{u} \cdot \mathbf{t}_i, \quad i = 1, 2, \text{ on } \partial\Omega,$$

where  $f_{Wall}$  can take different values depending along the boundary  $\partial\Omega$ . In the following, we will distinguish four areas: the bottom and lateral external walls of the cell denoted  $\partial\Omega_0$ , the

#### 4.5. Numerical experiments on the smaller simplified electrolysis cell: physical parameters

anodic surface  $\partial\Omega_1$ , the side channels  $\partial\Omega_2$  and finally the top surface of the channels denoted  $\Gamma_{out}$ :

$$f_{Wall}(\mathbf{x}) = \begin{cases} f_0 & \text{if } \mathbf{x} \in \partial\Omega_0, \\ f_1 & \text{if } \mathbf{x} \in \partial\Omega_1, \\ f_2 & \text{if } \mathbf{x} \in \partial\Omega_2, \\ f_3 & \text{if } \mathbf{x} \in \Gamma_{out}. \end{cases} \quad (4.61)$$

These areas are illustrated for a small cell in Figure 4.14.

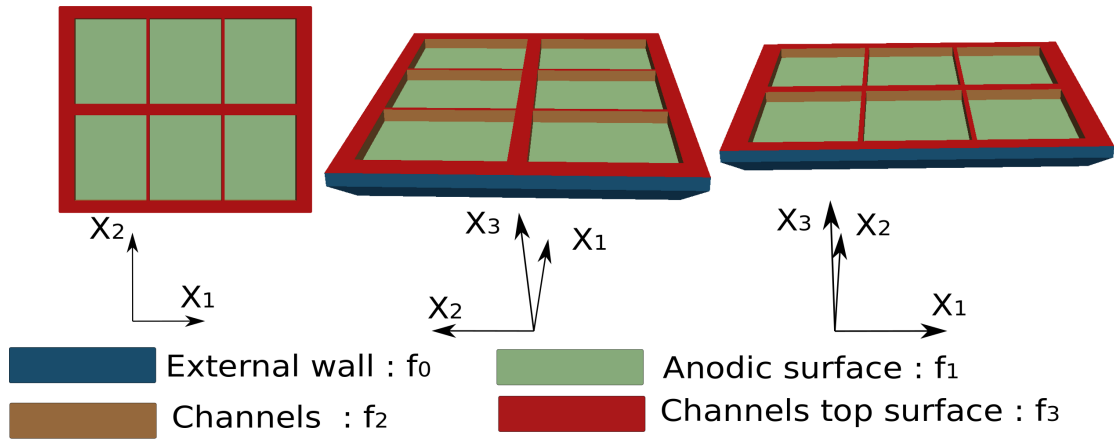


Figure 4.14 – Surfaces with possibly different friction coefficients: in blue the external walls, in green the anodic surface, in orange the channels and in red the top surface of the channels.

The velocity for different values of  $f_i$  is reported in Figure 4.18 and Figure 4.16. Depending on the value of  $f_i$ , the velocity change in the channels, as illustrated in Figure 4.17. Figure 4.19 shows that the interface is slightly modified, but the global shape remains unchanged.

Convergence with respect to  $k$  is slower for small values of  $f_i$  (Remember that the problem is ill-posed if  $f_i = 0$ ). Figure 4.15 shows the discrepancy curves for fifty iterations with different values of friction coefficients. For  $f_i = 1e2$ , the algorithm did not converge. Similarly the convergence rate of the case  $f_0 = 1e6$ ,  $f_1 = f_2 = f_3 = 0$  in Figure 4.15 is so slow that it is just enough to assume convergence.

**Remark 15.** The discrepancy between iteration  $k + 1$  and  $k$  in Figure 4.15 is not enough to ensure the convergence of  $\mathbf{u}^k$ . Notice that it is possible that  $|\mathbf{u}^{k+1} - \mathbf{u}^k|$  tends to 0 while  $\mathbf{u}^{k+1}$  does not converge to a solution  $\mathbf{u}$ . (The scalar example  $u^{k+1} - u^k = 1/k$  converges to zero as  $k \rightarrow \infty$  but the sum  $\sum_{k=1}^{\infty} u^k = \sum_{k=1}^{\infty} 1/k$  diverges.) However if  $|\mathbf{u}^{k+1} - \mathbf{u}^k| < 1/k^p$ , for any  $p > 1$ ,  $\sum_k \mathbf{u}^k$  converges. (Cauchy) For this reason, if the discrepancy curve in Figure is clearly steeper in Figure 4.15 than the curve  $f(k) = 0.01/k$ , convergence can be assumed.

In Table 4.3, numerical results are reported for the maximum velocity of the components  $u_1, u_2, u_3$  with various coefficients  $f_i$ : the velocity globally changes accordingly to the local

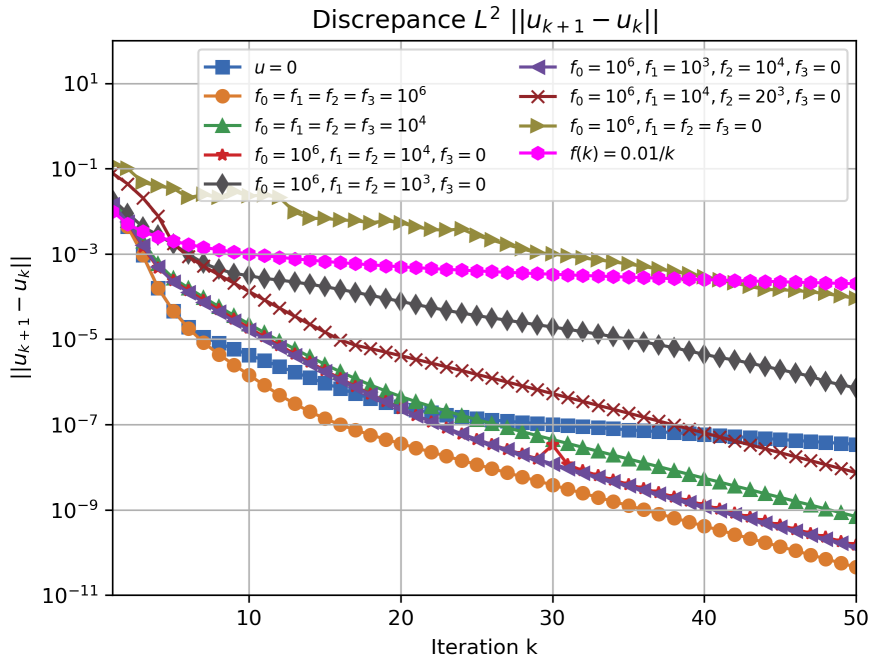


Figure 4.15 – Convergence with friction coefficients without gas. For reference the curve  $f(k) = C/k$  is plotted: a discrepancy with a rate decreasing faster implies convergence.

friction coefficient: it is increased when a lower value for the friction coefficient is taken. It should be noted that the maximum of the velocity  $\mathbf{u}$ : it is not affected friction coefficients, except when  $f_i = 1e4[kg/m^2 s]$  everywhere.

$f_{Wall}[kg/m^2 s]$				Under the anode $u[m/s]$			In the channels $u[m/s]$			All $[m/s]$
$f_0$	$f_1$	$f_2$	$f_3$	$ u_1 _{L^\infty}$	$ u_2 _{L^\infty}$	$ u_3 _{L^\infty}$	$ u_1 _{L^\infty}$	$ u_2 _{L^\infty}$	$ u_3 _{L^\infty}$	$ \mathbf{u} _{L^\infty(\Omega)}$
$\infty$	$\infty$	$\infty$	$\infty$	$3.8e-2$	$4.5e-2$	$2.5e-3$	$8.5e-2$	$5.4e-2$	$8.8e-3$	$1.43e-1$
$1e6$	$1e6$	$1e6$	$1e6$	$3.8e-2$	$4.5e-2$	$2.5e-3$	$8.6e-2$	$5.4e-2$	$9.0e-3$	$1.43e-1$
$1e4$	$1e4$	$1e4$	$1e4$	$4.8e-2$	$5.5e-2$	$3.0e-3$	$9.3e-2$	$6.2e-2$	$4.7e-2$	$1.73e-1$
$1e6$	$1e4$	$1e4$	0.0	$4.6e-2$	$5.4e-2$	$2.9e-3$	$9.9e-2$	$5.6e-2$	$1.4e-2$	$1.46e-1$
$1e6$	$1e3$	$1e3$	0.0	$6.6e-2$	$7.7e-2$	$5.1e-3$	$1.1e-1$	$7.8e-2$	$2.4e-2$	$1.53e-1$
$1e6$	$1e3$	$1e4$	0.0	$6.6e-2$	$7.1e-2$	$4.8e-3$	$1.0e-1$	$6.4e-2$	$1.7e-2$	$1.53e-1$
$1e6$	$1e4$	$1e3$	0.0	$4.7e-2$	$5.5e-2$	$2.9e-3$	$1.0e-1$	$6.4e-2$	$2.7e-2$	$1.46e-1$
$1e6$	0.0	0.0	0.0	$9.4e-2$	$1.2e-1$	$7.4e-3$	$1.3e-1$	$9.0e-2$	$3.0e-2$	$1.58e-1$

Table 4.3 – Amplitude of the velocities with simulations with various friction coefficients after convergence.

In conclusion, the velocity depends on the choice of the friction coefficients. The velocity in the channels is particularly impacted. If the friction is too low, the algorithm fails to converge. In the sequel we chose  $\mathbf{u} = \mathbf{0}$ ,  $f_1 = 1e6[kg/m^2 s]$ ,  $f_2 = 1e4[kg/m^2 s]$ ,  $f_3 = 1e3[kg/m^2 s]$ ,  $f_4 = 0[kg/m^2 s]$ .

4.5. Numerical experiments on the smaller simplified electrolysis cell: physical parameters

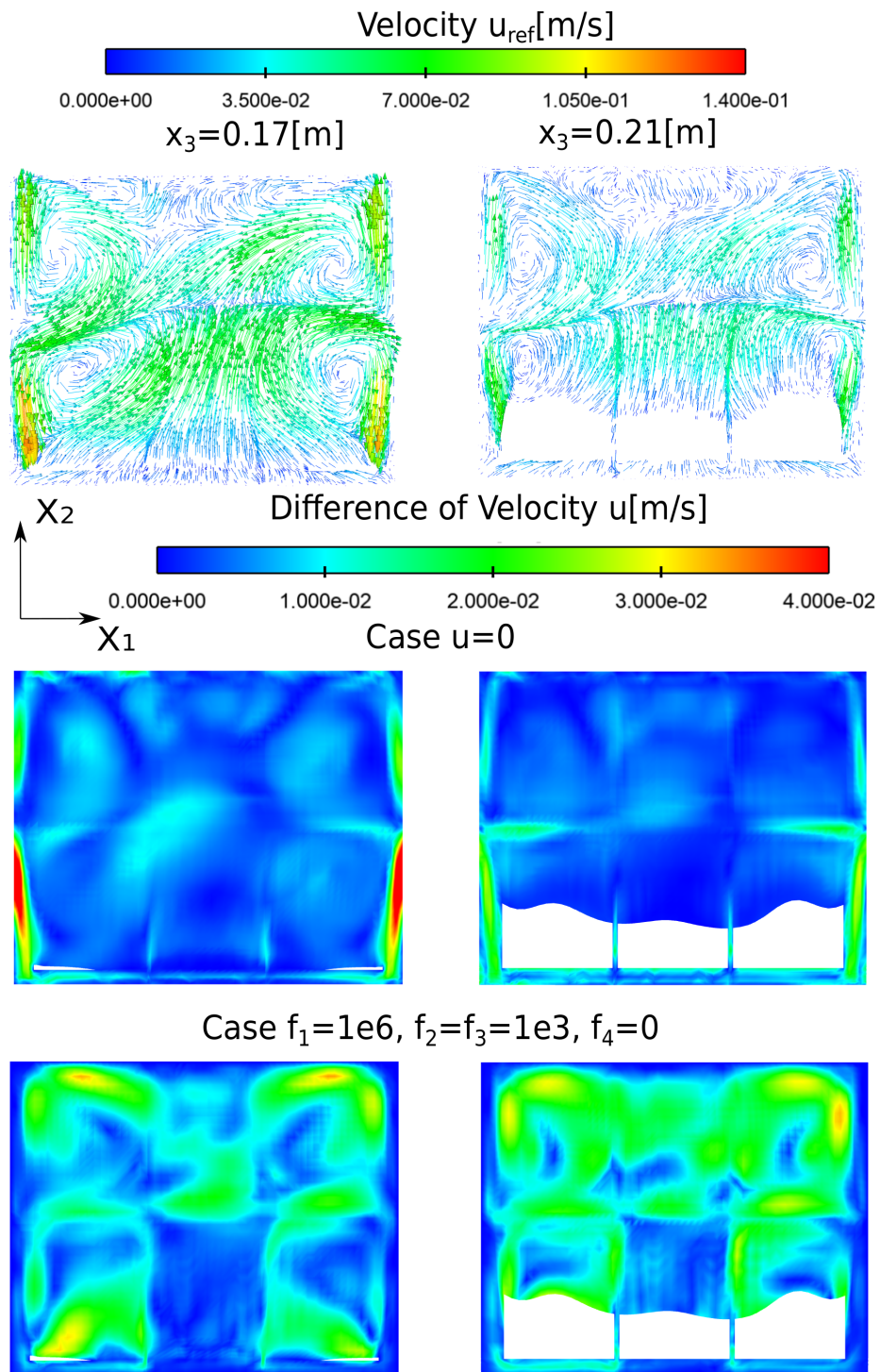


Figure 4.16 – On the left: the velocity field in the aluminium at  $x_3 = 0.17[m]$ . On the right: the velocity field in the bath at  $x_3 = 0.21[m]$ . On the top, the velocity field with the friction coefficients of Table 4.2. In the middle the difference of velocity with the case  $\mathbf{u} = \mathbf{0}$  on  $\partial\Omega$ . On the bottom, the difference of velocity when the coefficient under the anode is reduced from  $1e3$  to  $1e4$ .

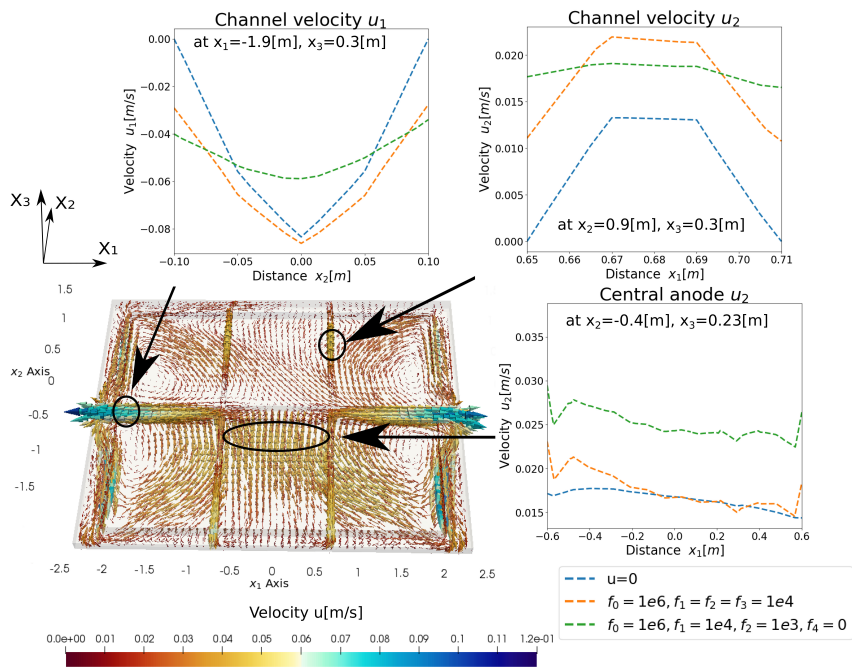


Figure 4.17 – The velocity field  $\mathbf{u}$  with different friction coefficients  $f_i$ .

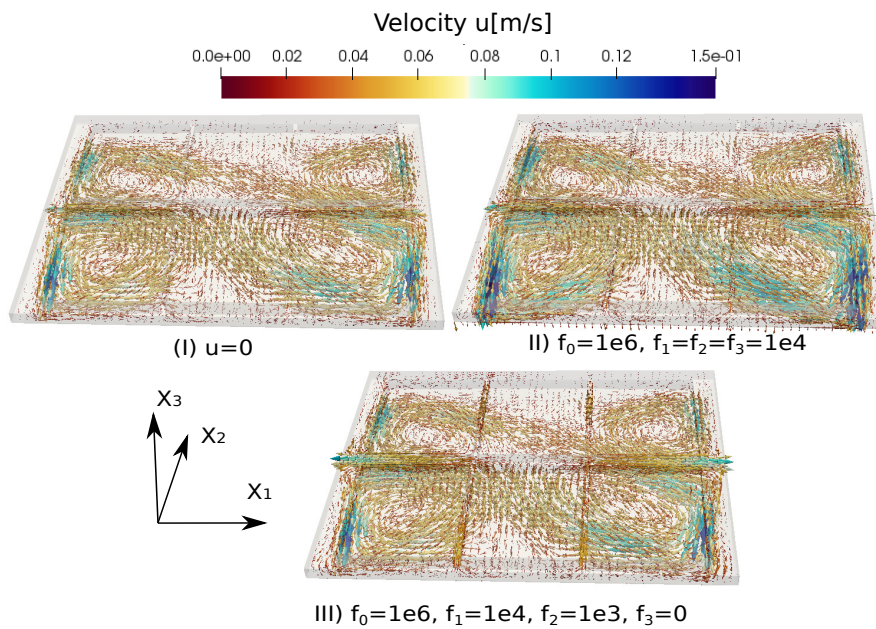


Figure 4.18 – The velocity field  $\mathbf{u}$  with different friction coefficients  $f_i$ .

4.5. Numerical experiments on the smaller simplified electrolysis cell: physical parameters

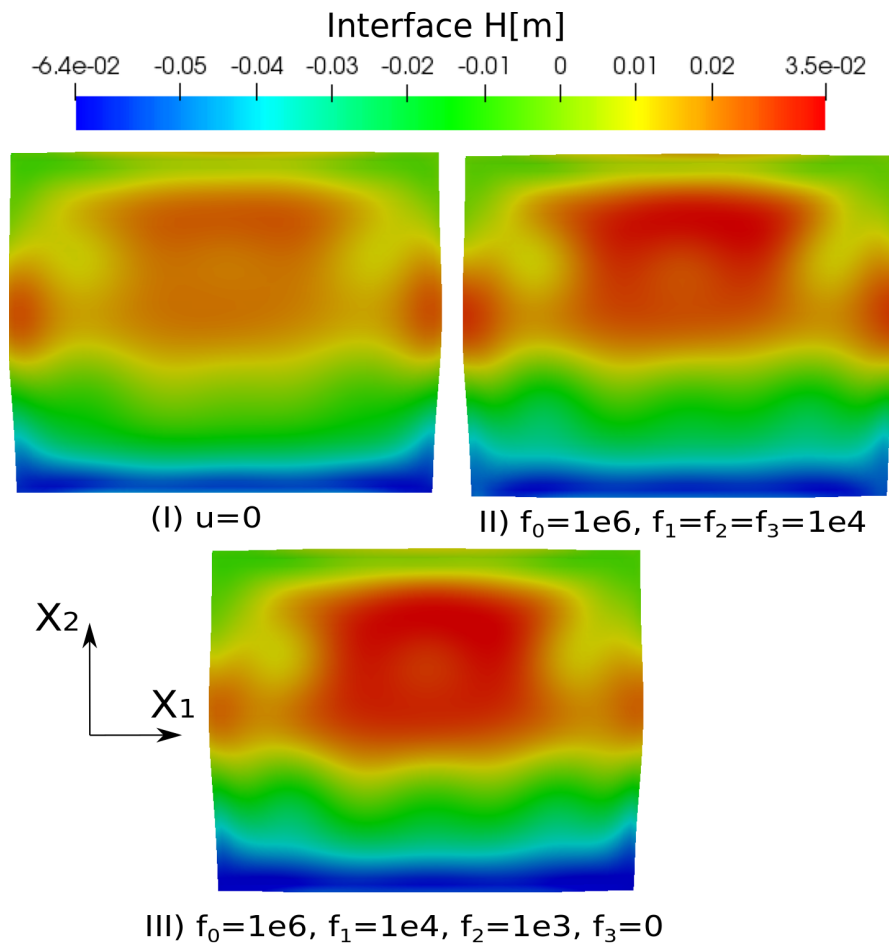


Figure 4.19 – Interface bath aluminium  $H[m]$  view with different friction boundary conditions.

### 4.5.2 Influence of the drag coefficient

Consider the algorithm 4.2.3 with the drag coefficient  $D$  is given by (1.41):

$$D = \frac{18\mu_L r}{d^2}, \text{ where } \mu_L = 0.5[\text{kg/ms}]. \quad (4.62)$$

Small diluted bubbles of diameter  $d = 4[\text{mm}]$  (see [Pon00]) are considered. On the other hand, we also compare the second non-linear drag coefficient given by (1.47):

$$D = \max\left(\left[1 + 0.15Re_b^{0.687}\right], \frac{0.44Re_b}{24}\right) \frac{18\mu_L r}{d^2}, \quad Re_b = \frac{\rho_l |\mathbf{u} - \mathbf{u}_g| d}{\mu_L}. \quad (4.63)$$

The influence of  $\mu_L$  is reported in Table 4.4 and 4.5: as expected, the changes are considerable regarding the gas velocity  $\mathbf{u}_g$ , resulting in up to 27% of change in  $L^2$  norm for  $\alpha_g$ , and 25% for the mixture velocity  $\mathbf{u}$ . For  $\mu_L = 2[\text{kg/ms}]$ , the algorithm did not converge, for both (4.62) and (4.63): the gas cannot be expelled out of the domain, similarly to the results in Chapter 3. For  $\mu_L = 0.02, 0.002[\text{kg/ms}]$ , the algorithm did not converge with (4.62). Illustrations of the different variables for two cases are reported in Figure 4.20. In particular notice that the velocity  $\mathbf{u}$  at the end of the main channels exhibits important changes.

$\mu_L[\text{kg/ms}]$	$\Delta_{L^\infty, \Omega} \mathbf{u}_h$	$\Delta_{L^\infty, \Omega_{el}} \alpha_{g,h}$	$\Delta_{L^\infty, \Omega_{el}} \mathbf{u}_{g,h}$	$\Delta_{L^2, \Omega} \mathbf{u}_h$	$\Delta_{L^2, \Omega_{el}} \alpha_{g,h}$	$\Delta_{L^2, \Omega_{el}} \mathbf{u}_{g,h}$	$\bar{\alpha}_g[\%]$
0.02	-%	-%	-%	-%	-%	-%	-%
0.125	29.9%	46.2%	39.7%	10.6%	27.8%	126.7%	1.30%
0.25	18.3%	32.9%	23.9%	6.0%	17.3%	54.8%	1.52%
0.5	0%	0%	0%	0%	0%	0%	1.84%
1.0	39.3%	34.8%	18.2%	10.8%	23.9%	39.6%	2.30%
2.0	-%	-%	-%	-%	-%	-%	-%

Table 4.4 – Comparison of drag force with (4.62) with different values of  $\mu_L$ , with the reference being  $\mu_L = 0.5[\text{kg/ms}]$ .

$\mu_L[\text{kg/ms}]$	$\Delta_{L^\infty, \Omega} \mathbf{u}_h$	$\Delta_{L^\infty, \Omega_{el}} \alpha_{g,h}$	$\Delta_{L^\infty, \Omega_{el}} \mathbf{u}_{g,h}$	$\Delta_{L^2, \Omega} \mathbf{u}_h$	$\Delta_{L^2, \Omega_{el}} \alpha_{g,h}$	$\Delta_{L^2, \Omega_{el}} \mathbf{u}_{g,h}$	$\bar{\alpha}_g[\%]$
0.002	76.0%	67.9%	88.4%	26.6%	46.3%	567.2%	1.08%
0.02	41.3%	53.2%	43.8%	16.7%	33.5%	149.7%	1.78%
0.125	52.8%	38.4%	29.2%	16.8%	21.3%	69.2%	1.41%
0.25	59.7%	25.7%	27.6%	18.2%	12.4%	32.9%	1.58%
0.5	66.9%	24.3%	30.4%	20.6%	8.06%	19.4%	1.84%
1.0	69.3%	35.7%	30.8%	26.1%	23.9%	46.6%	2.20%
2.0	-%	-%	-%	-%	-%	-%	-%

Table 4.5 – Comparison of drag force (4.63) with different values of  $\mu_L$ , with the reference being  $\mu_L = 0.5[\text{kg/ms}]$  and  $D$  given by (4.62).

#### 4.5. Numerical experiments on the smaller simplified electrolysis cell: physical parameters

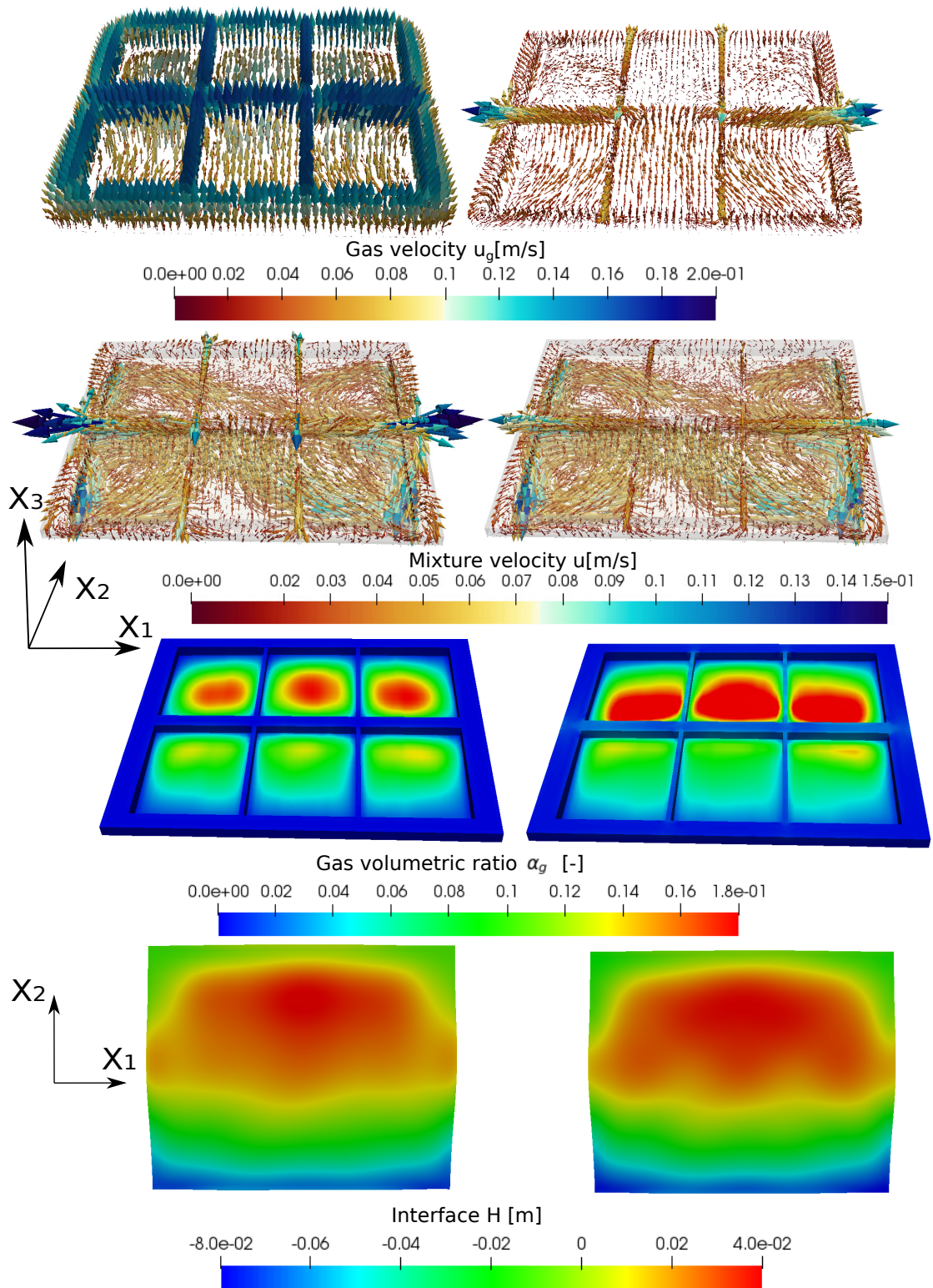


Figure 4.20 – On the left: simulations with  $\mu_L = 0.125 \text{ kg/ms}$ , and on the right with  $\mu_L = 1 \text{ kg/ms}$  in a simplified electrolysis cell.

### 4.5.3 Influence of the turbulent gas diffusion

In (4.58) we chose as default value:

$$K = K_L + K_T |\epsilon(\mathbf{u}_g)|, \text{ with } K_L = 5e - 5 [m^2/s] \text{ and } K_T = 5e - 4 [m^2]. \quad (4.30)$$

The influence of  $K_T$  is shown in Table 4.6 and Figure 4.21. Amongst the various changes, notice that under the anode, along  $x_3$ ,  $\alpha_g$  is increased when  $K_T$  is small. With  $K_T = 1.25e - 4 [m^2]$ , the algorithm failed to converge.

$K_T [m^2]$	$\Delta_{L^\infty, \Omega} \mathbf{u}_h$	$\Delta_{L^\infty, \Omega_{el}} \alpha_{g,h}$	$\Delta_{L^\infty, \Omega_{el}} \mathbf{u}_{g,h}$	$\Delta_{L^2, \Omega} \mathbf{u}_h$	$\Delta_{L^2, \Omega_{el}} \alpha_{g,h}$	$\Delta_{L^2, \Omega_{el}} \mathbf{u}_{g,h}$	$\bar{\alpha}_g [\%]$
25e-5	65.5%	61.9%	30.3%	19.6%	34.8%	17.5%	2.02%
5e-4	0%	0%	0%	0%	0%	0%	1.84%
1e-4	64.1%	48.8%	28.9%	19.9%	30.8%	17.7%	1.53%

Table 4.6 – Influence of the turbulent diffusion coefficient  $K_T$ .

In this section, we have seen that the turbulent diffusion coefficient is a key element to the numerical solutions. If its value is too low, the gas will increase under the anode without any bound and prevent convergence. The more diffusion is added, the more the profile of gas will be smoothed.

#### 4.5. Numerical experiments on the smaller simplified electrolysis cell: physical parameters

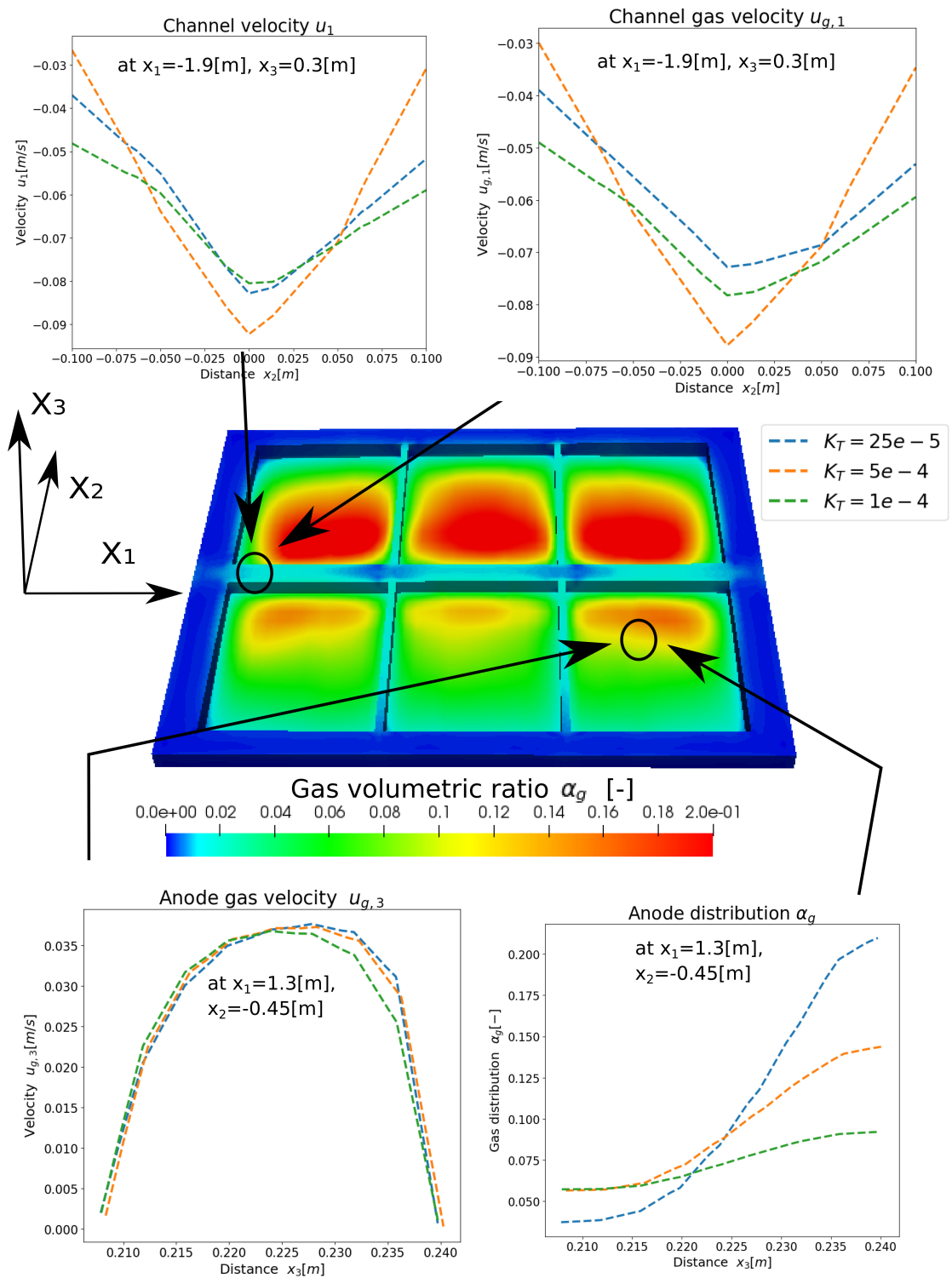


Figure 4.21 – Comparison with different value of turbulent diffusion coefficient  $K_T$  with reference value  $K_T = 5e-4$  [m<sup>2</sup>].

#### 4.5.4 Influence of the gas viscosity

Table 4.7 and Figure 4.22 show when using several values of the gas viscosity  $\mu_g$  compared to the reference case  $\mu_g = 0.5[kg/ms]$ . The algorithm did not converge for  $\mu_g = 5e-4[kg/ms]$ , as expected from theory for a very small  $\mu_g$ .

$\mu_g[kg/ms]$	$\Delta_{L^\infty, \Omega} \mathbf{u}_h$	$\Delta_{L^\infty, \Omega_{el}} \alpha_{g,h}$	$\Delta_{L^\infty, \Omega_{el}} (\mathbf{u}_{g,h})$	$\Delta_{L^2, \Omega} \mathbf{u}_h$	$\Delta_{L^2, \Omega_{el}} \alpha_{g,h}$	$\Delta_{L^2, \Omega_{el}} \mathbf{u}_{g,h}$	$\bar{\alpha}_g [\%]$
0.005	12.4%	41.0%	71.2%	4.77%	24.9%	45.9%	1.49%
0.05	9.93%	23.5%	38.0%	3.8%	16.3%	21.9%	1.60%
0.5	0%	0%	0%	0%	0%	0%	1.84%
5.0	27.3%	51.2%	17.8%	11.7%	41.8%	36.4%	2.41%

Table 4.7 – Comparison of the results with different value of the gas viscosity  $\mu_g$ .

A lower gas viscosity would mostly change the sharpness of the gas velocity profile close to the boundary: one effect of this is to increase its gradient right below the anodic surface. With our turbulent diffusion model (4.30), this result in an increased diffusion under the anode.

#### 4.5.5 Conclusion

The friction coefficients  $f_i$ , drag coefficient  $D$ , turbulent diffusion coefficient  $K_T$  and gas viscosity  $\mu_g$  have important influence on the solutions. In the gas model,  $D$  and  $K_T$  have quantitatively a stronger impact on the resulting mixture velocity  $\mathbf{u}$ . The algorithm fails to converge if the coefficient  $D$  is too high ( $\mu_L > 2[kg/ms]$ ), if the gas viscosity ( $\mu_g < 5e-4[kg/ms]$ ), turbulent diffusion coefficient ( $K_T < 1.25e-4[m^2]$ ) or the friction coefficients are too small.

#### 4.5. Numerical experiments on the smaller simplified electrolysis cell: physical parameters

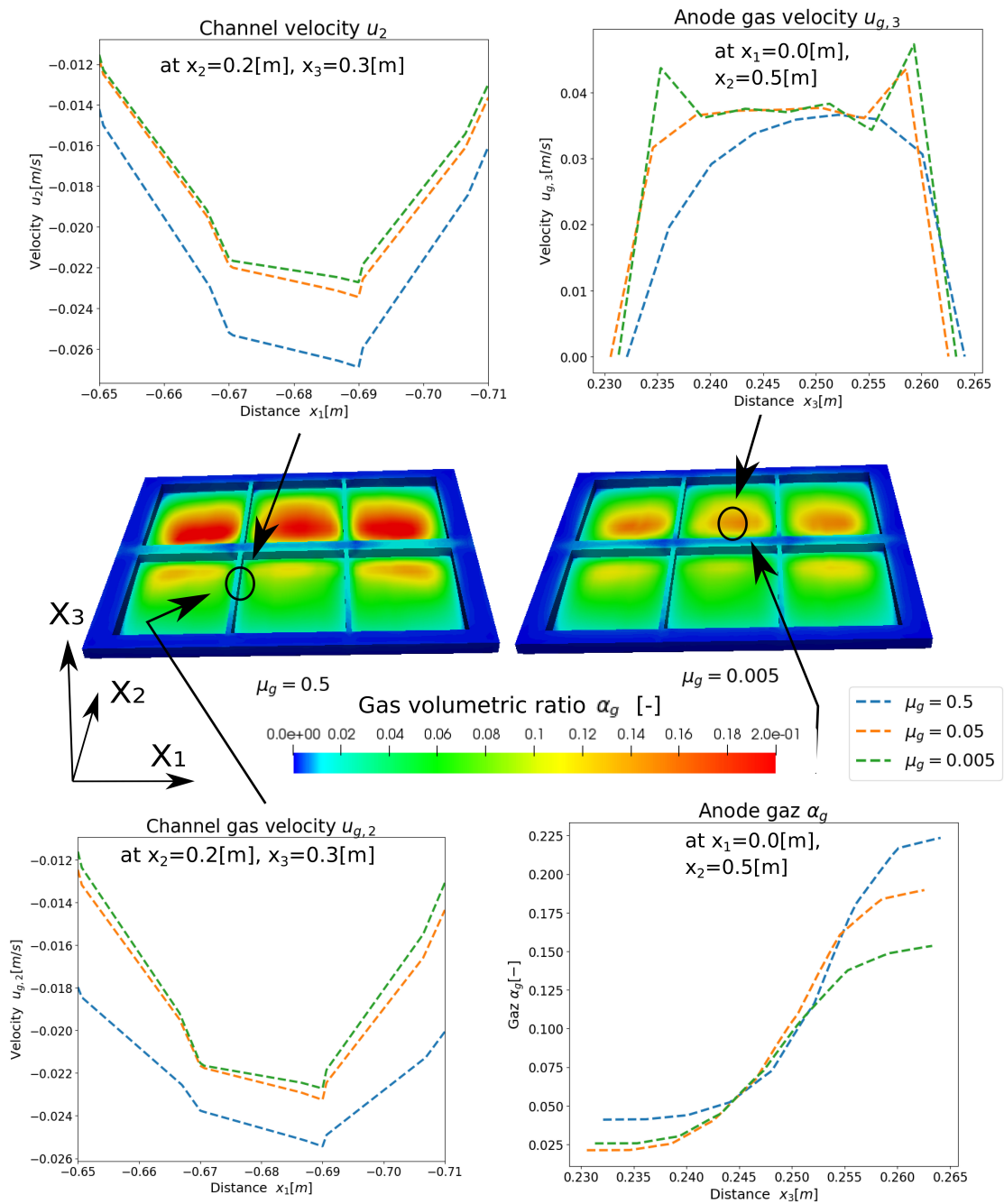


Figure 4.22 – On the left: simulations with different values of  $\mu_g$ . In particular the gas distribution at the surface is given on the left for  $\mu_g = 0.5[kg/ms]$  and on the right for  $\mu_g = 0.005[kg/ms]$ .

## 4.6 Numerical results on an industrial AP32 electrolysis cell

The AP32 industrial cell is considered in the following results : it is constituted of twenty anodic blocs and measures fourteen meters in length. The total current going through this cell amounts to  $320'000[A]$ , which corresponds to a production of carbon dioxide of  $2990[kg/day]$ . The velocity of the fluid flow obtained with the model range up to  $14[cm/s]$ .

### 4.6.1 Effects of the gas

The amount of gas injected in the system is controlled through the source term  $\dot{\alpha}_{source}$  in (4.40). In this section, we will use:

$$\dot{\alpha}_{source}(\eta) = \eta \dot{\alpha}_{source,ref}, \eta \geq 0, \quad (4.64)$$

if  $\eta = 0$ , there is no gas production, and if  $\eta = 1$ , the standard production settings are used. For values of  $\eta$  scenarii are reported in Table 4.8:  $\eta = 0.0, 0.5, 1.0, 1.5$ . For  $\eta = 2.0$ , the system did not converge to a solution. In the following the changes are discussed in more details.

$\eta[-]$	$\Delta_{L^\infty, \Omega} \mathbf{u}_h$	$\Delta_{L^\infty, \Omega_{el}} \alpha_{g,h}$	$\Delta_{L^\infty, \Omega_{el}} \mathbf{u}_{g,h}$	$\Delta_{L^2, \Omega} \mathbf{u}_h$	$\Delta_{L^2, \Omega_{el}} \alpha_{g,h}$	$\Delta_{L^2, \Omega_{el}} \mathbf{u}_{g,h}$	$\bar{\alpha}_g [\%]$
0.0	61.1%	-%	-%	29.1%	-%	-%	0.0%
0.5	20.3%	37.8%	20.3%	10.75%	40.1%	16.3%	1.32%
1.0	0.0%	0.0%	0.0%	0.0%	0.0%	0.0%	2.26%
1.5	14.9%	31.2%	20.6%	8.2%	11.8%	31.2%	3.03%

Table 4.8 – Comparison of the norms of the different unknowns with different  $\eta$  with the reference  $\eta = 1.0$ .

### Mixture velocity $\mathbf{u}$

The mixture velocity field  $\mathbf{u}$  is compared in the model with gas ( $\eta = 1$ ) and without ( $\eta = 0$ ) in Figures 4.23 and 4.23, in two vertical cuts. (The initial interface is located at  $x_3 = 0.2[m]$  and the bottom of the aluminium at  $x_3 = 0.0[m]$ ). At  $x_3 = 0.17$ , in the aluminium domain, the velocity field is not changed much, in the order of  $2[cm/s]$ , when the maximum observed in this cut is about  $10[cm/s]$ .

At  $x_3 = 0.22$ , the most noticeable changes of velocity are located under the channels, with amplitude up to  $4[cm/s]$ . The area where the velocity field is not represented corresponds to region where the solution interface  $H$  sank down to that point that the anodic plane is also below the height  $x_3$  considered.<sup>5</sup> Figure 4.25 compares results with an increasing amount of gas ( $\eta = 0, 0.5, 1.0, 1.5$ ). In particular, notice that the amplitude of the velocity at the extremity of the main channel (on the left of the figure) is increased due with a higher  $\eta$ . In the lateral channels, a systematic increase of the velocity at the extremity of the channels close to the wall is observed and illustrated in one location.

<sup>5</sup>see later Figure 4.29 showing the interface

### Gas velocity $u_g$

From Figure 4.26, the vertical gas velocity is more important close to the wall of the main channel than in the centre. At the end of lateral channels, it can be observed that increasing  $\eta$  leads to a higher vertical velocity, so that more gas can be expelled. Going along  $x_3$  under an anode from the interface aluminium-bath (initially at  $x_3 = 0.2[m]$ ) from  $x_3 = 0.22$  to  $x_3 = 0.255$ , the profile of the vertical velocity is not changed much: it always follows a parabolic profile, with a value of zero on the interface as well as on the anodic plane. The horizontal components of the gas velocity are not shown much, as they are very similar to the velocity  $u$ .

### Gas distribution $\alpha_g$

Figure 4.27 shows: in the central channel the gas is localised with a higher concentration close to the wall. In the lateral channel, the distribution does not change much, but naturally there is more gas present with a higher value of  $\eta$ . Along  $x_3$ , in the channels as well as under the anodes, the quantity of gas increases, with a particularly important accumulation under the anodic plane.

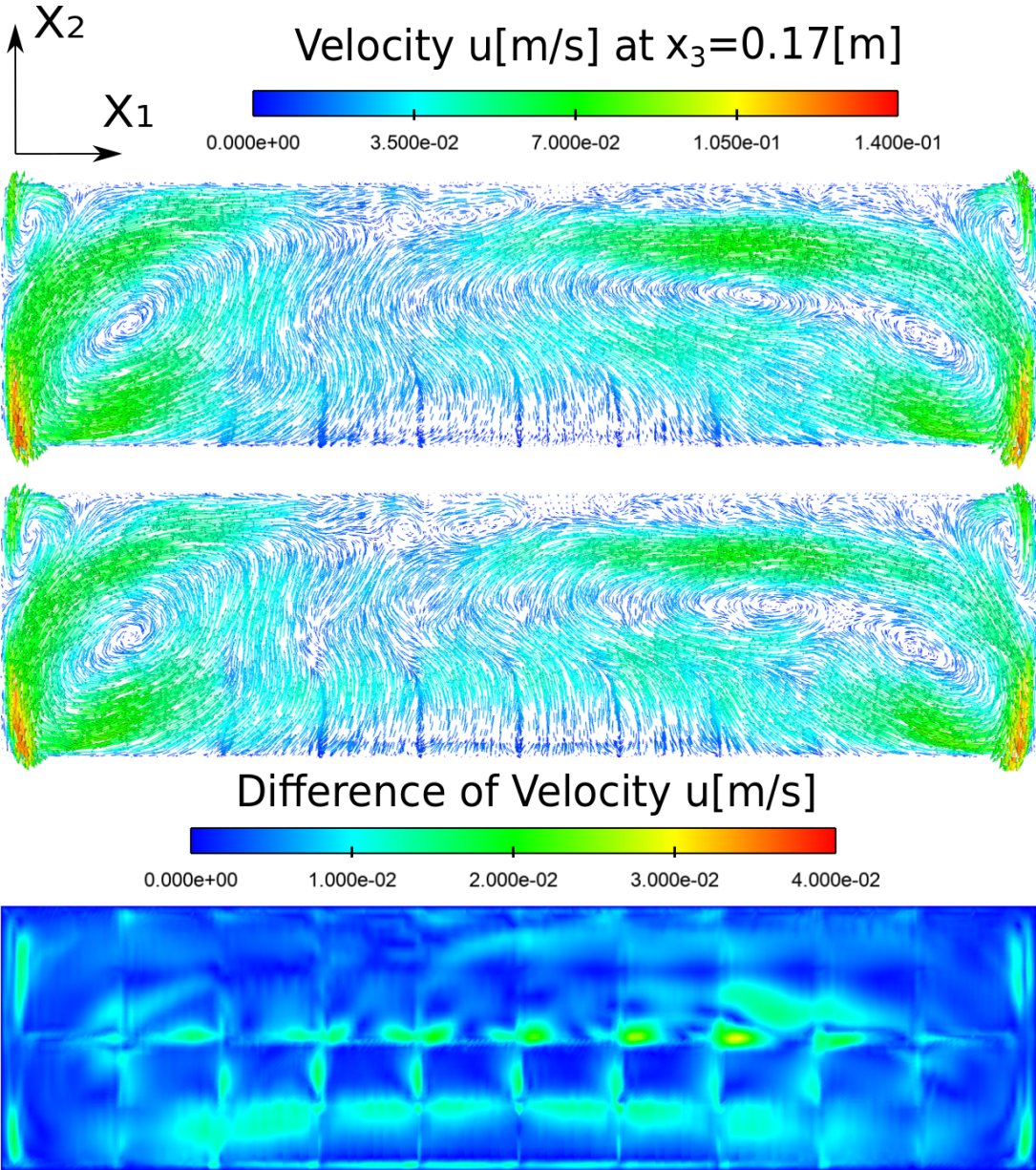


Figure 4.23 – Illustrations of the velocity field  $\mathbf{u}$  in a horizontal cut at  $x_3 = 0.17[m]$ . Top: velocity without gas  $\eta = 0$ , below:  $\eta = 1$ , bottom: difference of amplitude.

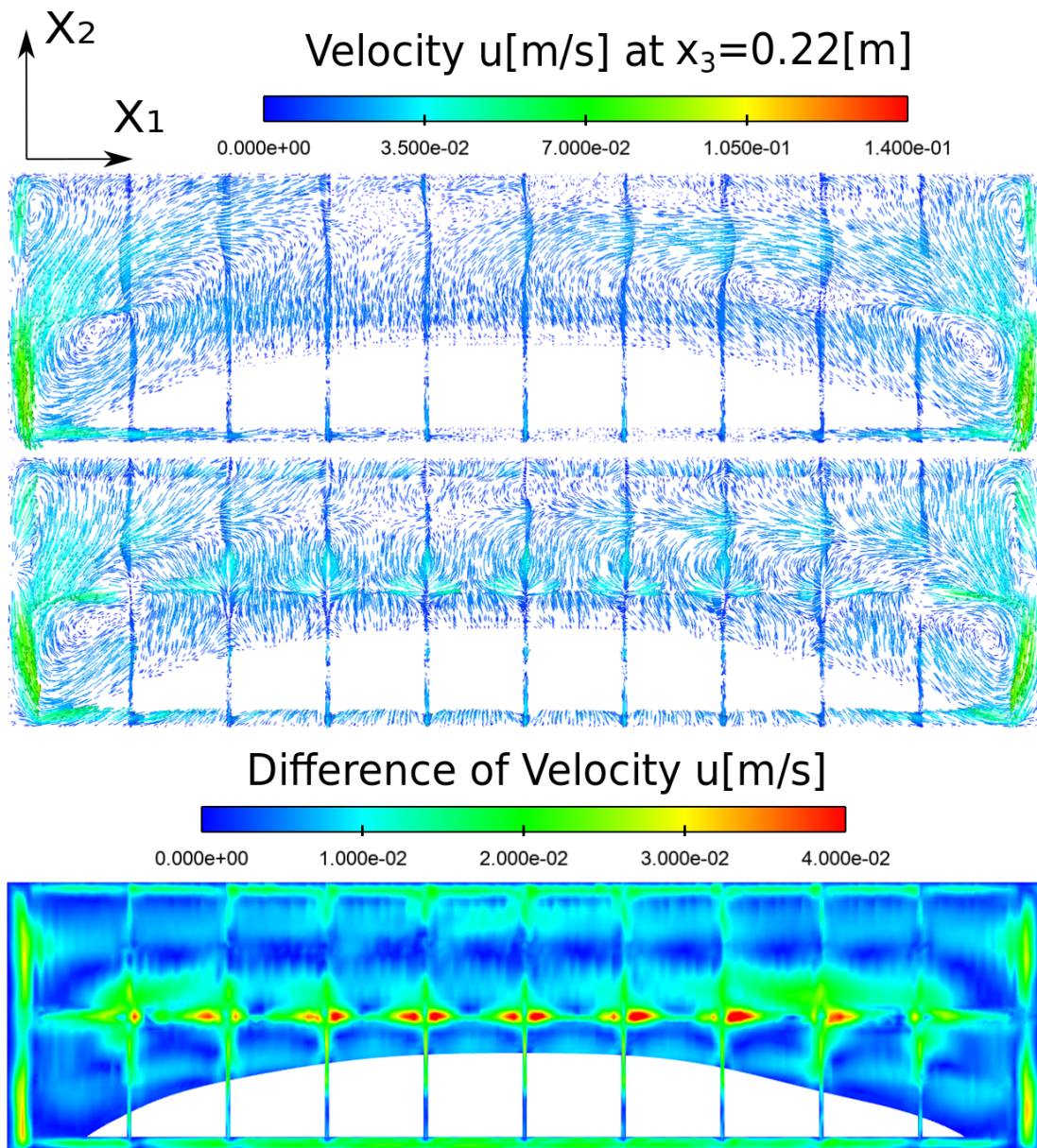


Figure 4.24 – Illustrations of the velocity field  $\mathbf{u}$  in a horizontal cut at  $x_3 = 0.22\text{ [m]}$ . Top: velocity without gas  $\eta = 0$ , below:  $\eta = 1$ , bottom: difference of amplitude.

**Chapter 4. Application to aluminium electrolysis**

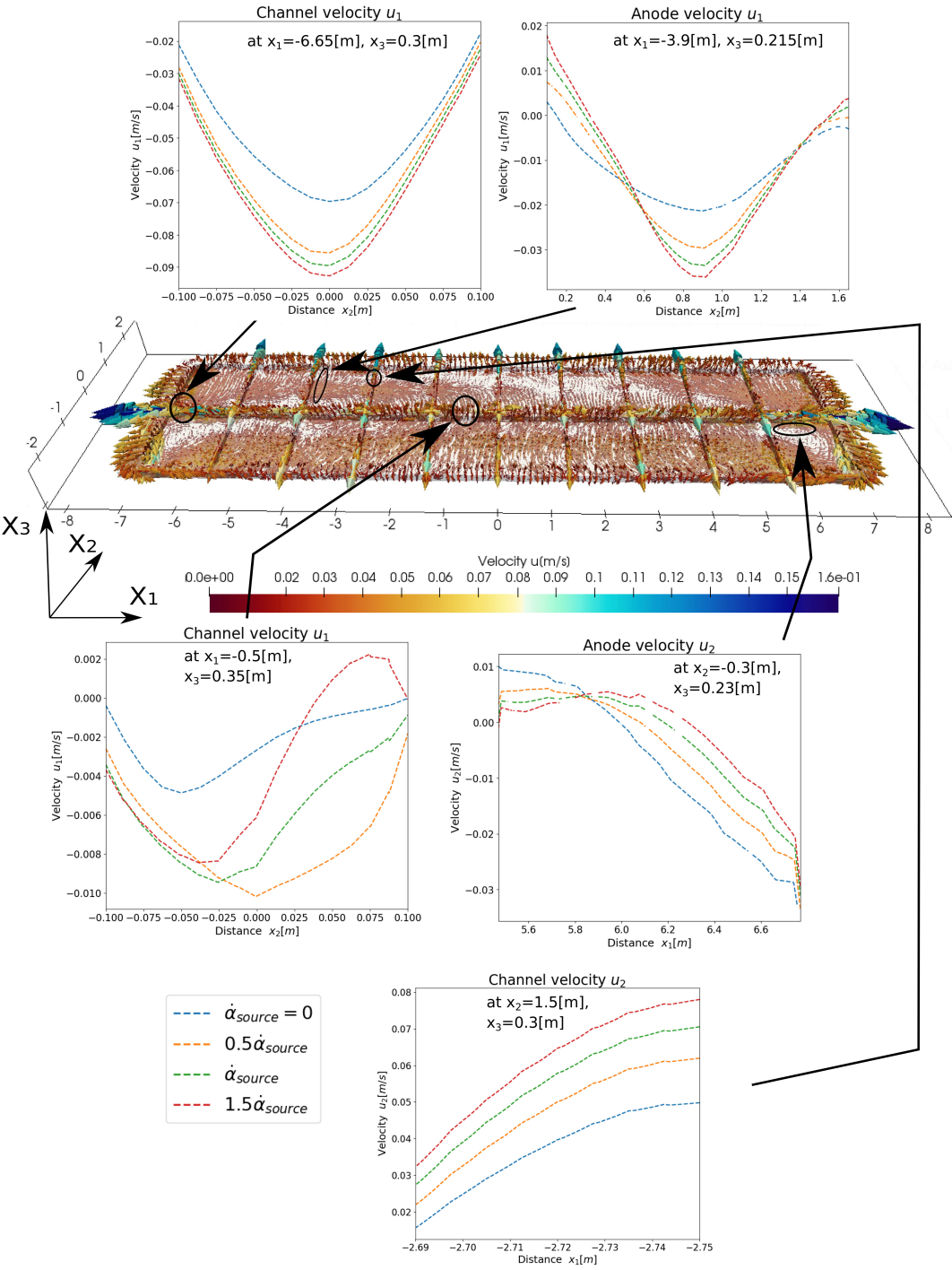


Figure 4.25 – Illustrations of the velocity field components  $u_1, u_2$  in various location of the electrolysis cells for four scenarii, with increasing gas source term.

#### 4.6. Numerical results on an industrial AP32 electrolysis cell

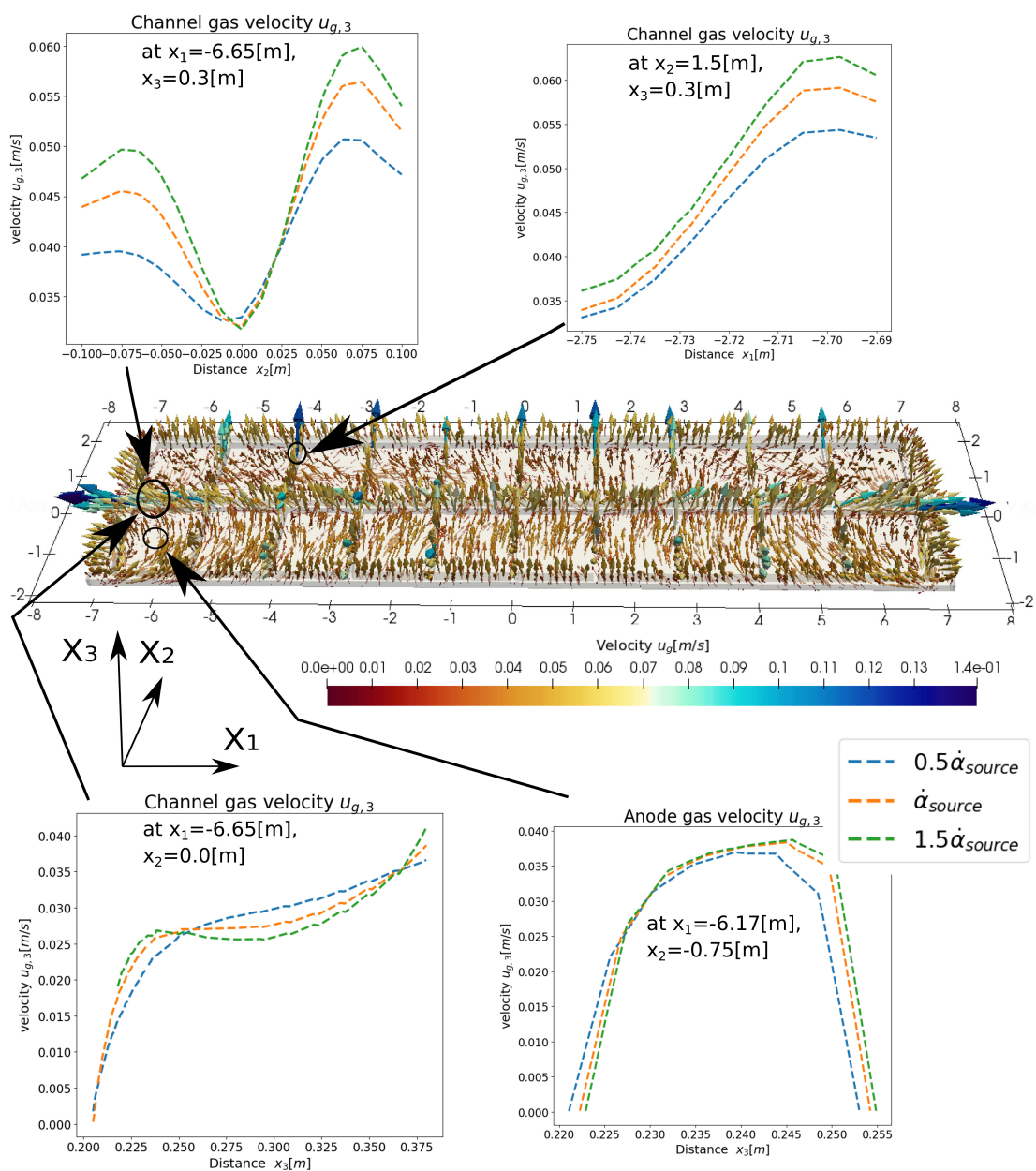


Figure 4.26 – Illustrations of the gas velocity field component  $u_{g,3}$  in various location of the electrolysis cells for four scenarii, with increasing gas source term.

Chapter 4. Application to aluminium electrolysis

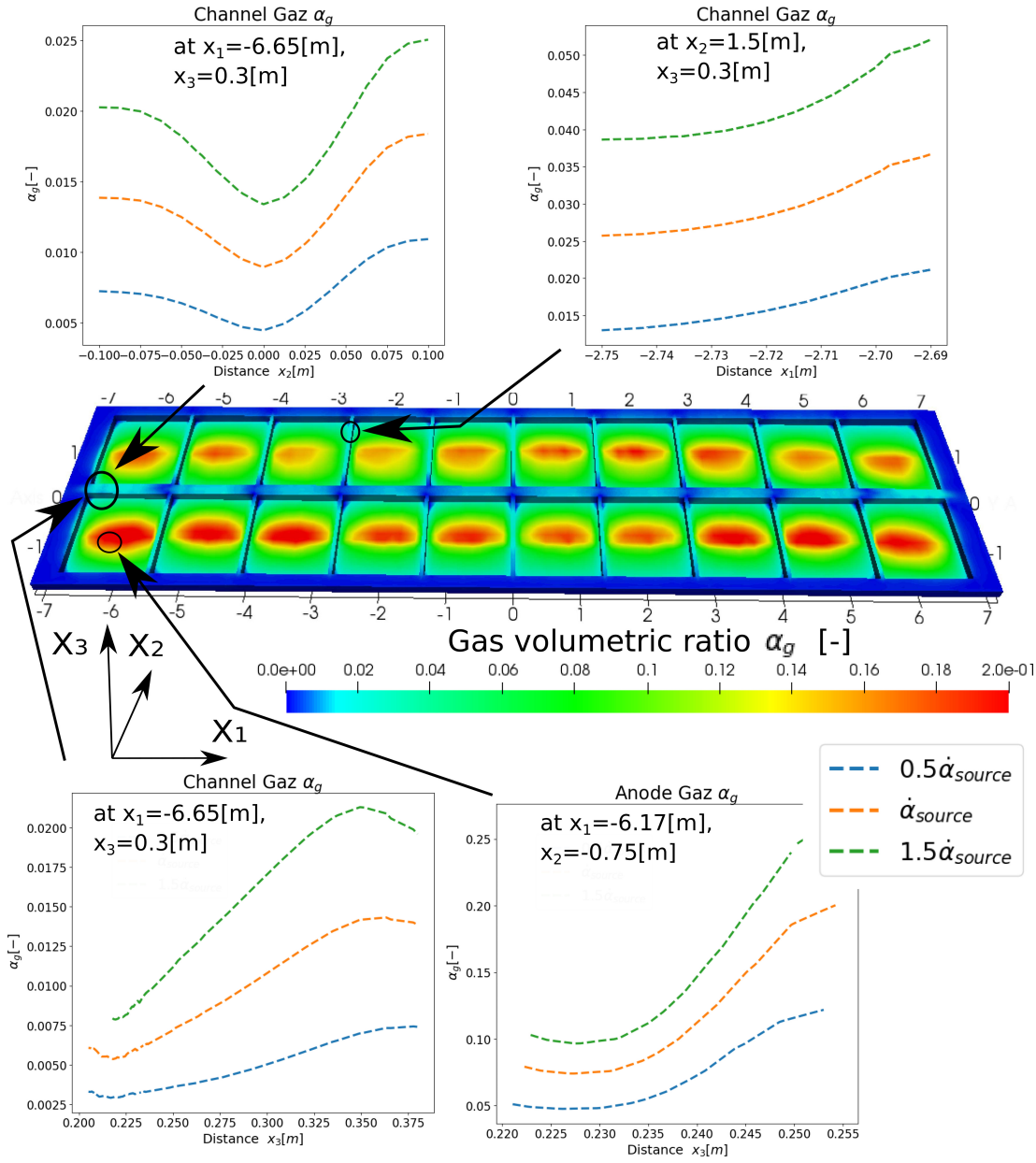


Figure 4.27 – Illustrations of the gas distribution  $\alpha_g$  in various location of the electrolysis cells for four scenarii, with increasing gas source term.

**Interface**

Figure 4.29 shows different shapes of interface. A tendency is perceptible to the naked eye: the interface is mostly changed by the gas density: in areas where a lot of gas is present, the alleviated density leads the interface to lift upwards: it is illustrated by Figure 4.28 showing the red areas correspond to a move upwards of the interface when taking into account the gas: it corresponds approximately to areas where gas distribution  $\alpha_g$  is concentrated under the anodes. (see precedent Figure 4.27 ) Table 4.9 quantifies the relative change of the interface being about 30% when taking into account the gas. The  $\|H\|_0$  norm can be seen as a way to assess how flat the interface is: on average with and without gas, it does not change much.

As a sion, it seems that the numeric interface is changed mostly due to the accumulation of gas in some specific area. In this industrial cell, in particular the highest point of the interface (left and right middle of the cell) does go down, while the lowest part (center along  $x_1$ , lower value of  $x_2$ ) of the interface is lowered even more. The change is quantified at about 30%.

$\eta[-]$	$\Delta_{L^\infty, \Gamma} H$	$\Delta_{L^2, \Gamma} H$	$\ H\ _{L^2(\Gamma)}$	$H_{max}[cm]$	$H_{min}[cm]$
0.0	0.0%	0.0%	0.16	4.4	-6.5
0.5	20.4%	24.2%	0.15	3.5	-6.6
1.0	28.7%	32.4%	0.15	3.2	-7.1
1.5	35.5%	37.9%	0.16	3.3	-7.4

Table 4.9 – Comparison of the different interfaces obtained with  $\eta = 0.0, 0.5, 1.0, 1.5$ . The reference solution  $H_{ref}$  is without gas,  $\eta = 0$ .

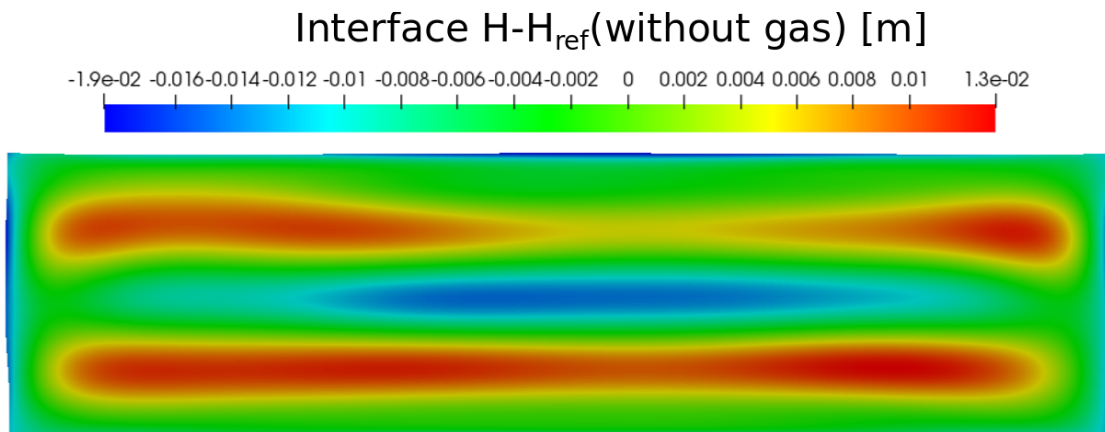


Figure 4.28 – Illustration of the difference of the reference interface with gas  $H_{ref}(\eta = 1)$  compared to the interface without gas  $H$  with  $\eta = 0$ .

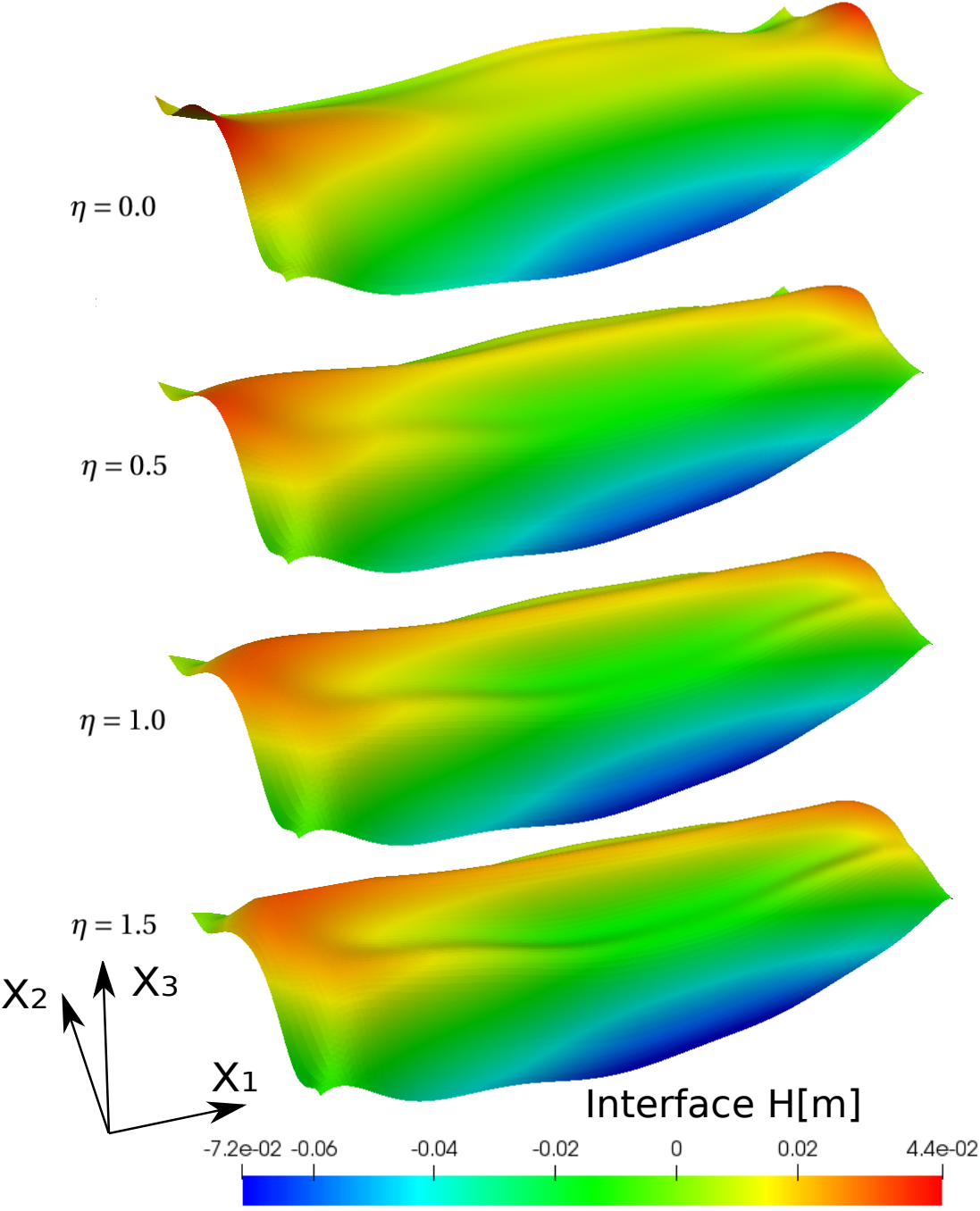


Figure 4.29 – Resulting interfaces with different quantities of gas considered in the model. The amount of gas being controlled with parameter  $\eta$ .

## 4.6. Numerical results on an industrial AP32 electrolysis cell

### 4.6.2 Source term geometry and model

In this section, two area are compared for the production region of  $\dot{\alpha}_{source}$ . The first setting considers that the source is proportional to the electric current  $\mathbf{j}$ , while the second setting considers a homogeneous production in the upper half volume of the electrolytic bath under the anode. Table 4.10 a change of about 18% in the gas distribution  $\alpha_g$ , and change the fluid dynamics through the velocity  $\mathbf{u}$  of about 9%.

$\Delta_{L^\infty, \Gamma} H$	$\Delta_{L^\infty, \Omega} \mathbf{u}_h$	$\Delta_{L^\infty, \Omega_{el}} \alpha_{g,h}$	$\Delta_{L^\infty, \Omega_{el}} \mathbf{u}_{g,h}$	$\Delta_{L^2, \Gamma} H$	$\Delta_{L^2, \Omega} \mathbf{u}_h$	$\Delta_{L^2, \Omega_{el}} \alpha_{g,h}$	$\Delta_{L^2, \Omega_{el}} \mathbf{u}_{g,h}$
5.8%	7.9%	17.4%	60.3%	5.5%	4.3%	18.1%	27.4%

Table 4.10 – Comparison of solutions with two settings of source terms  $\dot{\alpha}_{source}$ .

Figure 4.30 shows the two source profiles, as well as some example of the gas distribution  $\alpha_g$  under an anode and the gas velocity in a neighbour channel: under this specific anode, to regroup all the production under the anode (and not a part of the production in the channels) globally increases the local production, and consequently the gas present. Notice that even though the gas is produced in the upper half of the anode, some gas is diffused/transported to the lower part. In sion, if the source term is chosen to be limited to the anode, the solution is changed mostly in the following way: the quantity of gas is increased under the anodes, although it is still diffused through the thin layer of the bath (height of 3.2[cm]).

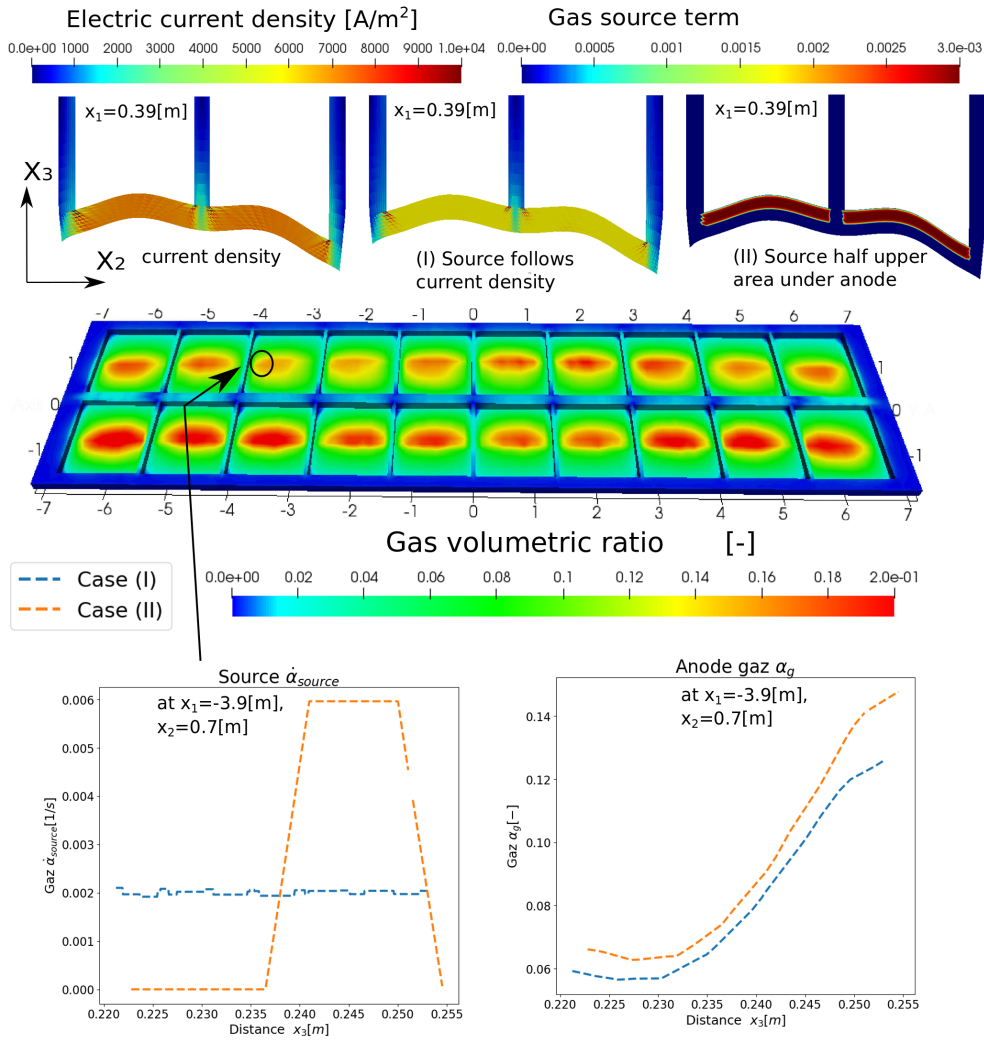


Figure 4.30 – Resulting interfaces with different gas source geometries.

#### 4.6.3 Influence of the gas with variable conductivity

It is investigated if the fact that the electric conductivity  $\sigma$  in the bath is changed due to the presence of gas also changes the solutions of the fluid problem. The gas can be considered as an insulator, thus the conductivity in the Maxwell equations can be modified:

$$\sigma = (1 - \alpha_g)\sigma_{el}, \text{ in } \Omega_{el}, \quad (4.65)$$

where  $\sigma_{el}$  is the constant conductivity of the electrolytic bath.

$$\mathbf{j} = \sigma(-\nabla V + \mathbf{u} \wedge \mathbf{B}), \quad (4.24)$$

$$\text{div}(-\sigma \nabla V) = -\text{div}(\sigma \mathbf{u} \wedge \mathbf{B}) \text{ in } \Theta, \quad (4.25)$$

## 4.6. Numerical results on an industrial AP32 electrolysis cell

As it can be seen in Table 4.11, this influence is very low and negligible compared to other effects.

$\Delta_{L^\infty, \Gamma} H$	$\Delta_{L^\infty, \Omega} \mathbf{u}_h$	$\Delta_{L^\infty, \Omega_{el}} \alpha_{g,h}$	$\Delta_{L^\infty, \Omega_{el}} \mathbf{u}_{g,h}$	$\Delta_{L^2, \Gamma} H$	$\Delta_{L^2, \Omega} \mathbf{u}_h$	$\Delta_{L^2, \Omega_{el}} \alpha_{g,h}$	$\Delta_{L^2, \Omega_{el}} \mathbf{u}_{g,h}$
0.9%	6.0%	2.2%	19.4%	1.9%	3.4%	2.2%	1.6%

Table 4.11 – Comparison of solutions of the solution when  $\sigma' = (1 - \alpha_g)\sigma$ , with the reference solution when  $\sigma$  is constant in  $\Omega_{el}$ .

### 4.6.4 Comparison with simplified gas velocity model

Recall the simplified model (1.50) described in the first chapter where the gas velocity is given with:

$$\mathbf{u}_g = \mathbf{u} - \frac{d^2 \rho_l}{18 \mu_L r \rho} (\nabla p - \rho_g \mathbf{g}) = \mathbf{u} - \lambda (\nabla p - \rho_g \mathbf{g}). \quad (4.66)$$

This model is rewritten here with parameter  $\lambda$ . When  $\lambda = \frac{d^2 \rho_l}{18 \mu_L r \rho}$ , the resulting gas velocity  $\mathbf{u}_g$  is the same as the mixture velocity  $\mathbf{u}$  with an additional vertical component. Of course, in order to respect the boundary conditions,  $\lambda$  should be zero on the anodic surface (otherwise  $\mathbf{u}_g \cdot \mathbf{n} \neq 0$  on the anodic surface). Two models are considered:

- I A first case when  $\lambda = 0$  under all the anode and on all the interface  $\Gamma$ .
- II A second case when  $\lambda = 0$  only on the nodes on the anodic surface and on all the interface  $H$ .

Table 4.12 quantifies these two choices of models and compare them with the standard formulation, as reference. As it could be expected the second model is closer to the standard formulation.

Model	$\Delta_{L^\infty, \Omega} \mathbf{u}_h$	$\Delta_{L^\infty, \Omega_{el}} \alpha_{g,h}$	$\Delta_{L^\infty, \Omega_{el}} \mathbf{u}_{g,h}$	$\Delta_{L^2, \Omega} \mathbf{u}_h$	$\Delta_{L^2, \Omega_{el}} \alpha_{g,h}$	$\Delta_{L^2, \Omega_{el}} \mathbf{u}_{g,h}$	$\bar{\alpha}_g$ [%]
Standard	0.0%	0.0%	0.0%	0.0%	0.0%	0.0%	2.21%
$\lambda$ (I)	80.8%	62.2%	44.9%	20.1%	50.6%	55.9%	2.45%
$\lambda$ (II)	16.3%	22.3%	22.3%	7.8%	20.8%	45.2%	1.95%

Table 4.12 – Comparison of the explicit model for gas velocity and reference model

In Figure 4.31, the gas velocity vertical component represents well the three models under one anode: a parabolic curve for the standard model, a constant close to zero for the  $\lambda - (I)$  model and a Heaviside-like behaviour for the  $\lambda - (II)$  model with value zero on the interface and on the anode. Under this anode, it results into a constant  $\alpha_g$  profile when the gas velocity is the

same as the mixture velocity  $\mathbf{u}$  along  $x_3$ . Regarding the velocities, the  $\lambda - (I)$  model results for instance in a slight increase of amplitude in a lateral channel, and to a decrease in the main channel on the left.

As a conclusion, we have seen that this simplified model is not very well suited for the application with horizontal anodes, as it implies important difference. The second model  $\lambda - (II)$  is more appropriate, but results in a very sharp change of  $\mathbf{u}_g$  close to the boundaries, which leads to change up to 16% to the velocity field  $\mathbf{u}$ . This explicit model is advantageous when the number of times the gas velocity system needs to be solved is important. It is not the case for the numerical experiments presented. However, if a high number of iterations  $N_g$  would be require for another numerical experiment, the model  $\lambda(II)$  should be considered as it gives similar results.

### 4.6.5 Conclusion

In this section, it has been shown that the influence of the gas modifies the fluid velocities, with order of magnitude of 30%. The boundary conditions of the problem also change the flow. Partially sliding conditions converge as fast as the strong condition  $\mathbf{u} = \mathbf{0}$ , and are appropriate with the gas algorithm. The algorithm with gas converges with a similar rate to a stationary solution, with a similar computational cost, than the algorithm without gas. The behaviour of the model has been shown, when the different parameters of the model are modified, indicating the default settings as reasonable. The most impacting parameters of the gas model are the the drag coefficient  $D$  and the amplitude of the turbulent diffusion  $K_T$ .

Furthermore, the velocity field numerically predicted is globally increased in amplitude in the channels, when taking the gas into account: this can explain differences between numerical predictions of previous models without gas and experimental observations by Rio Tinto engineers. In addition, the distribution of the gas, through its density and the modified fluid flow, changes the shape of the interface. On the other hand, the effect of the gas on the conductivity is negligible.

#### 4.6. Numerical results on an industrial AP32 electrolysis cell

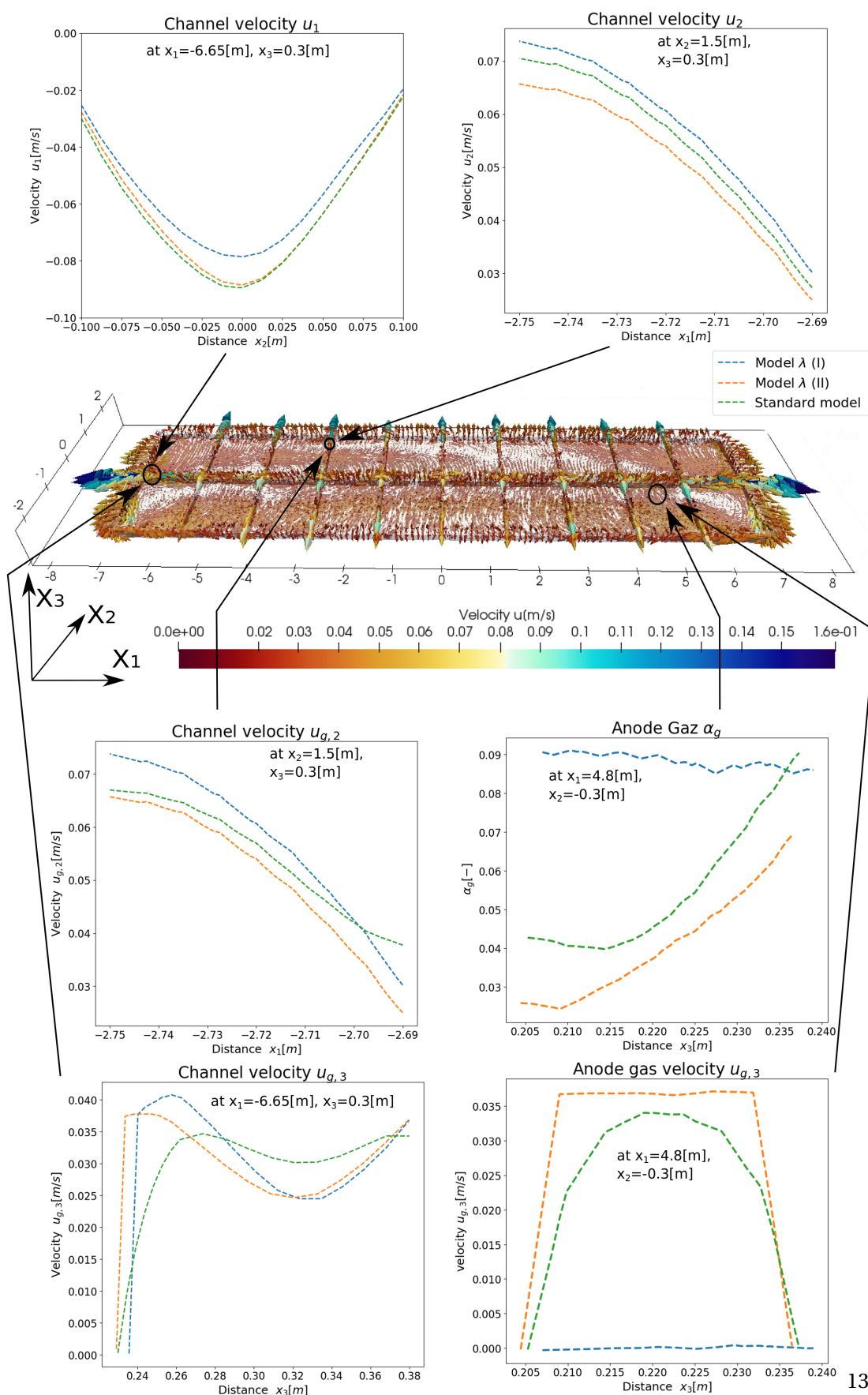


Figure 4.31 – Comparison between the two explicit models and the standard model for  $u_g$ .



## 5 Conclusion

The goal of this thesis was the study of a mixture model of liquid and diluted gas, to evaluate how the the liquid flow is modified in the aluminium electrolysis process.

A model with a single pressure was developed in chapter 1, in which the main unknowns of the problem are the mixture velocity, the pressure, the gas velocity, and the gas ratio. An algorithm was proposed to solve the stationary problem associated with a finite element approximation. The significant conclusions of this work are the following:

- In a closed domain, the theoretical analysis of a Stokes problem shows that as long as the gas ratio  $\alpha_g$  is sufficiently small, the problem is well-posed.
- The gas problem is particularly sensitive to the drag force. Two models are compared. The first model is linear with respect to the gas velocity, while the second one is non-linear. The advantage of the second model is that it is compatible with a wider range of viscosities (parameter).
- A simplified model is compared to compute explicitly the gas velocity as the sum of the fluid velocity and the component due to Archimedes force. This model is accurate with respect to the complete model in a domain such as a water-column, but is inadequate in a domain like an aluminium reduction cell, where some geometric obstacles are present in the  $x_3$  direction.
- Numerical recommendations have been given, resulting in an algorithm that converges to a solution on an AP32 aluminium electrolysis cell in about two hours. With the recommended parameters, the module to take into account the gas amounts to 20% of the computational time.
- The effects of the gas on the liquid flow is measured at about 30% of change. The most important modifications of the velocity field in an aluminium reduction cell take place in the channels. However, these velocities also strongly depend on the boundary conditions, through the friction coefficients that are considered.

## Chapter 5. Conclusion

---

- The stationary volumetric rate of gas is large mostly under the anodes, and escapes up quickly once in the channels. This distribution seems to be at the origin of the change on the interface, modified of about 30%, which tends to be higher under the anodes, compared to a model without any gas.
- The effect of the gas on the electric density current  $\mathbf{j}$  through the conductivity  $\sigma$  is small in this model. The resulting force  $\mathbf{j} \wedge \mathbf{B}$  does not change much the fluid flow.

Regarding the applications of the model, we would do the following recommendations :

- From the theory and practice, the model is done to perform well when the gas ratio  $\alpha_g$  is small. The model computing  $\alpha_g$  could be modified obtain an adequate  $\alpha_g$  by another constitutive law, as long as it ensure that  $\alpha_g$  is bounded correctly.
- Measurements are necessary to validate and calibrate further the coefficients of the model. Measurements of the gas velocity at the outflow would allow to calibrate accurately the amplitude of the drag coefficient  $D$ .
- Computation of models of alumina dissolution [Hof11; Hil19] with the modified velocity fields are to be investigated and confronted with real observations.

## Bibliography

- [Abh+18] Shrirang Abhyankar et al. “PETSc/TS: A modern scalable ODE/DAE solver library”. *arXiv preprint arXiv:1806.01437* (2018). URL: <https://arxiv.org/abs/1806.01437>.
- [Aln+15] Martin Alnæs et al. “The FEniCS Project Version 1.5”. *Archive of Numerical Software* 3.100 (2015), pp. 9–23. DOI: 10.11588/ans.2015.100.20553.
- [Alu13] Rio Tinto Aluminium. “AP30/ AP40 The world’s benchmark reduction technologies” (2013). URL: [https://www.ap-technology.com/wp-content/uploads/2019/02/AP\\_Factsheet\\_AP30-AP40.pdf](https://www.ap-technology.com/wp-content/uploads/2019/02/AP_Factsheet_AP30-AP40.pdf).
- [BD88] Franco Brezzi and Jim Douglas. “Stabilized mixed methods for the Stokes problem”. *Numerische Mathematik* 53 (1988), pp. 225–235. DOI: 10.1007/BF01395886.
- [BE15] Valdis Bojarevics and James Evans. “Mathematical modelling of Hall-Héroult pot instability and verification by measurements of anode current distribution” (2015), pp. 783–788. DOI: 10.1007/978-3-319-48248-4\_132.
- [Ber+92] Christine Bernardi et al. “Finite element approximation of viscous flow with varying density”. *SIAM Journal of Numerical Analysis* 29.5 (1992), pp. 1203–1243. DOI: 10.1137/0729073.
- [Bor+16] Chenna Borra et al. “Recovery of rare earths and other valuable metals from bauxite residue (red mud): a review”. *Journal of Sustainable Metallurgy* 2.4 (2016), pp. 365–386. DOI: 10.1007/s40831-016-0068-2.
- [Bou77] Joseph Boussinesq. “Essai sur la théorie des eaux courantes , Comptes rendus de l’Académie des Sciences”. 23 (1877), pp. 1–680.
- [BRJ06] Manish Bhole, Swarnendu Roy, and Jyeshtharaj Joshi. “Laser doppler anemometer measurements in bubble column: effect of sparger”. *Industrial & engineering chemistry research* 45.26 (2006), pp. 9201–9207. DOI: 10.1021/ie060745z.
- [BW90] Randolph Bank and Bruno Welfert. “A comparison between the mini-element and the Petrov-Galerkin formulations for the generalized Stokes problem”. *Computer methods in applied mechanics and engineering* 83.1 (1990), pp. 61–68. DOI: 10.1016/0045-7825(90)90124-5.
- [Cha17] Robert Chahine. “Production journalière de CO<sub>2</sub>, Intern communication” (2017).
- [Cia02a] Philippe Ciarlet. “Finite Element Method for Elliptic Problems” (2002), pp. 36–55.

## Bibliography

---

- [Cia02b] Philippe Ciarlet. “Finite Element Method for Elliptic Problems” (2002), p. 113.
- [Clé75] Philippe Clément. “Approximation by finite element functions using local regularization”. *ESAIM: Mathematical Modelling and Numerical Analysis - Modélisation Mathématique et Analyse Numérique* 9.R2 (1975), pp. 77–84. DOI: 10.1051/m2an/197509r200771.
- [CR97] Gabriel Caloz and Jacques Rappaz. “Numerical analysis for nonlinear and bifurcation problems”. *Handbook of numerical analysis* 5 (1997), pp. 487–637. DOI: 10.1016/S1570-8659(97)80004-X.
- [Das12] Subodh Das. “Achieving Carbon Neutrality in the Global Aluminum Industry”. *Journal of the Minerals* 64 (Feb. 2012). DOI: 10.1007/s11837-012-0237-0.
- [DFF89] Jean Descloux, Roberto Frosio, and Michel Flueck. “A two fluids stationary free boundary problem”. *Computer Methods in Applied Mechanics and Engineering* 77 (Dec. 1989), pp. 215–226. DOI: 10.1016/0045-7825(89)90076-5.
- [DFR98] Jean Descloux, Michel Flueck, and Michel Romerio. “A modelling of the stability of aluminium electrolysis cells”. *Pitman research notes in mathematics series* (1998), pp. 117–133.
- [Ein+17] Kristian Etienne Einarsrud et al. “Towards a coupled multi-scale, multi-physics simulation framework for aluminium electrolysis”. *Applied Mathematical Modelling* 44 (2017), pp. 3–24. DOI: 10.1016/j.apm.2016.11.011.
- [Ern96] Alexandre Ern. “Vorticity-velocity formulation of the Stokes problem with variable density and viscosity”. *Mathematical Models and Methods in Applied Sciences* 8 (1996), pp. 203–218. DOI: 10.1142/S021820259800010X.
- [Flo13] Stéphane Flotron. “Simulations numériques de phénomènes MHD-thermiques avec interface libre dans l’électrolyse de l’aluminium”. *Thèse No 5738 EPFL* (2013). DOI: 10.5075/epfl-thesis-5738.
- [Flu+10] Michel Flueck et al. “Numerical Methods for Ferromagnetic Plates”. *Computational Methods in Applied Sciences* 15 (2010), pp. 169–182. DOI: 10.1007/978-90-481-3239-3\_13.
- [Gat+21] Gabriel N Gatica et al. “Banach spaces-based analysis of a fully-mixed finite element method for the steady-state model of fluidized beds”. *Computers and Mathematics with Applications* 84 (2021), pp. 244–276. DOI: 10.1016/j.camwa.2021.01.001.
- [GBL03] Jean-Frédéric Gerbeau, Claude Bris, and Tony Lelièvre. “Simulations of MHD flows with moving interfaces”. *Journal of Computational Physics* 184.1 (2003), pp. 163–191. DOI: 10.1093/acprof:oso/9780198566656.001.0001.
- [Gem+18] Luca Gemello et al. “CFD-based scale-up of hydrodynamics and mixing in bubble columns”. *Chemical Engineering Research and Design* 136.69 (2018), pp. 846–858. ISSN: 02638762. DOI: 10.1016/j.cherd.2018.06.026.

- [Gem19] Luca Gemello. “Modelling of the hydrodynamics of bubble columns using a two-fluid model coupled with a population balance approach”. Université de Lyon; Politecnico di Milano (2019). URL: <https://tel.archives-ouvertes.fr/tel-02006754/document>.
- [GM11] Elisabeth Guazzelli and Jeffrey Morris. *A physical introduction to suspension dynamics*. Vol. 45. Cambridge University Press, 2011.
- [GR09] Christophe Geuzaine and Jean-François Remacle. “Gmsh: A 3-D finite element mesh generator with built-in pre-and post-processing facilities”. *International journal for numerical methods in engineering* 79.11 (2009), pp. 1309–1331. DOI: <https://doi.org/10.1002/nme.2579>.
- [GR86] Vivette Girault and Pierre-Arnaud Raviart. “Finite Element Methods for Navier-Stokes Equations: Theory and Algorithms” (1986). DOI: 10.1007/978-3-642-61623-5.
- [Grj+77] Kai Grjotheim et al. “Aluminum Electrolysis. The Chemistry of the Hall-Heroult Process”. *Aluminium- Verlag GmbH, Dusseldorf, Germany*. 1977 (1977).
- [Hau13] Warren E. Haupin. “Principles of Aluminum Electrolysis” (Apr. 2013), pp. 1–11. DOI: 10.1002/9781118647851.ch1.
- [Hil19] Thomas Frédéric Hilke. “Méthodes numériques liées à la distribution d’alumine dans une cuve d’électrolyse d’aluminium”. *Thèse No 8682 EPFL* (2019). DOI: 10.5075/epfl-thesis-8682.
- [Hof11] Thomas Hofer. “Numerical simulation and optimization of the alumina distribution in an aluminium electrolysis pot”. *Thèse No 5023 EPFL* (2011). DOI: 10.5075/epfl-thesis-5023.
- [Hyd21] Hydro. *Aluminium Life cycle*. <https://www.hydro.com/en/aluminium/about-aluminium/>. Accessed on 2021-28-07. Mar. 2021.
- [KHP19] Kitungwa Kabezya, Tom Hara, and Randall Paton. “A review of primary aluminium tapping models”. *SN Applied Sciences* 1.8 (2019), pp. 1–9. DOI: 10.1007/s42452-019-0869-6.
- [KLS06] Sang Dong Kim, Yong Hun Lee, and Byeong Chun Shin. “Newton’s method for the Navier-Stokes equations with finite-element initial guess of stokes equations”. *Computers and Mathematics with Applications* 51.5 (2006), pp. 805–816. DOI: <https://doi.org/10.1016/j.camwa.2006.03.007>.
- [Kuz10] Dmitri Kuzmin. “A guide to numerical methods for transport equations”. Friedrich Alexander Universität Erlangen Nürnberg (2010), pp. 43–46. URL: <http://www.mathematik.tu-dortmund.de/~kuzmin/Transport.pdf>.
- [Lau16] Viljami Laurmaa. “An octree-based adaptive semi-Lagrangian free surface flow solver”. *Thèse No 7011 EPFL* (2016). DOI: 10.5075/epfl-thesis-7011.
- [LL59] Lev Davidovitch Landau and Evgueni Mikhaïlovitch Lifshitz. “Fluid Mechanics”. 45 (1959), p. 180.

## Bibliography

---

- [MR96] Philippe Maillard and Michel Romerio. “A stability criterion for an infinitely long Hall-Héroult cell”. *Journal of Computational and Applied Mathematics* 71.1 (1996), pp. 47–65. ISSN: 0377-0427. DOI: [https://doi.org/10.1016/0377-0427\(95\)00217-0](https://doi.org/10.1016/0377-0427(95)00217-0).
- [Mun04] David Munger. “Simulation numérique des instabilités magnétohydrodynamiques dans les cuves de production de l’aluminium”. Université de Montréal (2004). URL: [https://papyrus.bib.umontreal.ca/xmlui/bitstream/handle/1866/14764/Munger\\_David\\_2004\\_memoire.pdf?sequence=1&isAllowed=y](https://papyrus.bib.umontreal.ca/xmlui/bitstream/handle/1866/14764/Munger_David_2004_memoire.pdf?sequence=1&isAllowed=y).
- [Pai06] Sonia Pain. “Simulation numérique du mouvement des fluides dans une cellule de Hall-Héroult”. *Thèse No 3497 EPFL* (2006). DOI: 10.5075/epfl-thesis-3497.
- [Pan06] Florentina Panescu. “Modélisation Eulerienne d’écoulements diphasiques à phase dispersée et simulation numérique par une méthode volumes - éléments finis”. Université de Nice Sophia Antipolis (2006). URL: <http://www-sop.inria.fr/smash/personnel/Roxana.Panescu/These.pdf>.
- [Pon00] Sandor Poncsák. “Formation et évolution des bulles de gaz au-dessous de l’anode dans une cuve d’électrolyse d’aluminium”. *Thèse UCAQ* (2000), pp. 127–128. DOI: <https://doi.org/10.1522/12270309>.
- [Pop01] Stephen B Pope. “Turbulent Flows”. *Measurement Science and Technology* 12.11 (Oct. 2001). DOI: 10.1088/0957-0233/12/11/705.
- [QV08] Alfio Quarteroni and Alberto Valli. *Numerical approximation of partial differential equations*. Vol. 23. Springer Science & Business Media, 2008.
- [Ren+18] Steeve Renaudier et al. “Alucell: A unique suite of models to optimize pot design and performance”. In: *TMS Annual Meeting & Exhibition*. Springer. 2018, pp. 541–549. DOI: 10.1007/978-3-319-72284-9\_71.
- [RL16] Ricardo Ruiz-Baier and Ivan Lunati. “Mixed finite element – discontinuous finite volume element discretization of a general class of multicontinuum models”. *Journal of Computational Physics* 322 (2016), pp. 666–688. DOI: 10.1016/j.jcp.2016.06.054.
- [Roc16] Jonathan Rochat. “Approximation numérique des écoulements turbulents dans des cuves d’électrolyse de l’aluminium”. *Thèse No 7113 EPFL* (2016). DOI: 10.5075/epfl-thesis-7113.
- [Saf05] Yasser Safa. “Simulation numérique des phénomènes thermiques et magnétohydrodynamiques dans une cellule de Hall-Héroult”. *Thèse No 3185 EPFL* (2005). DOI: 10.5075/epfl-thesis-3185.
- [Sch33] Links Schiller. “A drag coefficient correlation”. *Zeit. Ver. Deutsch. Ing.* 77 (1933), pp. 318–320.
- [Sch97] Joachim Schöberl. “NETGEN An advancing front 2D/3D-mesh generator based on abstract rules”. *Computing and visualization in science* 1.1 (1997), pp. 41–52. DOI: 10.1007/s007910050004.

- [SLL19] Meijia Sun, Baokuan Li, and Linmin Li. “Multiscale Simulation of Bubble Behavior in Aluminum Reduction Cell Using a Combined Discrete-Bubble-Model-Volume-of-Fluid-Magnetohydrodynamical Method”. *Industrial and Engineering Chemistry Research* 58.8 (2019), pp. 3407–3419. DOI: 10.1021/acs.iecr.8b05109.
- [Sne85] Alfred David Sneyd. “Stability of fluid layers carrying a normal electric current”. *Journal of Fluid Mechanics* 156 (1985), pp. 223–236. DOI: 10.1017/s0022112085002063.
- [SRP21] Emile Soutter, Jacques Rappaz, and Marco Picasso. “A mixture model for a dilute dispersion of gas in a liquid flow: Mathematical analysis and application to aluminium electrolysis”. *Computers and Mathematics with Applications* 90 (2021), pp. 55–65. DOI: 10.1016/j.camwa.2021.03.007.
- [SS86] Youcef Saad and Martin H Schultz. “GMRES: A generalized minimal residual algorithm for solving nonsymmetric linear systems”. *SIAM Journal on scientific and statistical computing* 7.3 (1986), pp. 856–869. DOI: 10.1137/0907058.
- [Ste09] Gilles Steiner. “Simulation numérique de phénomènes MHD: Application à l'électrolyse de l'aluminium”. *Thèse No 4469 EPFL* (2009). DOI: 10.5075/epfl-thesis-4469.
- [Sto51] George Gabriel Stokes. “On the Effect of the Internal Friction of Fluids on the Motion of Pendulums” (1851), pp. 1–10. DOI: 10.1017/cbo9780511702266.002.
- [TH16] Alton Tabereaux and Raymond Hester. “Metal pad velocity measurements in prebake and soderberg reduction cells” (2016), pp. 240–250. DOI: 10.1007/978-3-319-48156-2\_35.
- [Yas+20] AS Yasinskiy et al. “An update on inert anodes for aluminium electrolysis”. *Non Ferr. Met* 48 (2020), pp. 15–23. DOI: 10.17580/nfm.2020.01.03.
- [Zha+17] Shuiqing Zhan et al. “3D Numerical Simulations of Gas-Liquid Two-Phase Flows in Aluminum Electrolysis Cells with the Coupled Model of Computational Fluid Dynamics-Population Balance Model”. *Industrial and Engineering Chemistry Research* 56.30 (2017), pp. 8649–8662. DOI: 10.1021/acs.iecr.7b01765.



# A Appendix

## A.1 Proof of the independence of the gas velocity with respect to the choice of the constant for the pressure $p$

In this annex, the demonstration that the boundary conditions (1.28-1.31) make sense are explicitly demonstrated in the following sense : assume that the pressure  $p$  is defined up to a constant. Whatever the way the constant  $C$  is chosen, the solution  $\mathbf{u}_g$  will be the same, i.e it is the same for  $p = P$  or  $p = P + C$ . The proof can be done with a more general condition instead of (1.29), that is :

$$(\boldsymbol{\tau}_g \cdot \mathbf{n}) \cdot \mathbf{n} = \alpha_g (\boldsymbol{\tau} \cdot \mathbf{n}) \cdot \mathbf{n}, \text{ on } \Gamma_{out}, \quad (\text{A.1})$$

**Proposition 7.** *The boundary conditions(1.28)(1.31)(A.1) and equation (1.15) result in the following weak form (see (1.74)) : we are looking for  $\mathbf{u}_g \in \mathbf{V}$  such that :*

$$\begin{aligned} & \int_{\Omega} (\rho_g \alpha_g \mathbf{u}_g \cdot \nabla) \mathbf{u}_g \cdot \mathbf{v}_g dx + \int_{\Omega} (\rho_g \dot{\alpha}_{source}) \mathbf{u}_g \cdot \mathbf{v}_g dx - \int_{\Gamma_{out}} \alpha_g \xi (\mathbf{v}_g \cdot \mathbf{n}) ds \\ & + \int_{\Omega} 2\mu_g \left( \epsilon(\mathbf{u}_g) : \epsilon(\mathbf{v}_g) - \frac{1}{3} \text{div}(\mathbf{u}_g) \text{div}(\mathbf{v}_g) \right) dx + \int_{\Omega} D \frac{\rho}{\rho_l} \alpha_g \mathbf{u}_g \cdot \mathbf{v}_g dx = \int_{\Omega} \alpha_g p \text{div}(\mathbf{v}_g) dx \\ & + \int_{\Omega} p \nabla \alpha_g \cdot \mathbf{v}_g dx + \int_{\Omega} \alpha_g \rho_g \mathbf{g} \cdot \mathbf{v}_g dx + \int_{\Omega} D \frac{\rho}{\rho_l} \alpha_g \mathbf{u} \cdot \mathbf{v}_g dx, \end{aligned} \quad (\text{A.2})$$

for all  $\mathbf{v}_g \in \mathbf{V}$ , with  $\xi = (\boldsymbol{\tau} \cdot \mathbf{n}) \cdot \mathbf{n} = -p + ((-2/3\mu \text{div}(\mathbf{u})\mathbf{I} + 2\mu\epsilon(\mathbf{u})) \cdot \mathbf{n}) \cdot \mathbf{n}$ . The solution  $\mathbf{u}_g$  of (A.2) does not change, taking  $p = P$  or  $p = P + C$ , for any constant  $C$ , and  $P \in L$ .

*Proof.* In order to do so, let us compute the subtraction of (A.2) with  $p = P$  and with  $p = P + C$  resulting in :

$$\int_{\Gamma_{out}} \alpha_g C (\mathbf{v}_g \cdot \mathbf{n}) ds = \int_{\Omega} \alpha_g C \text{div}(\mathbf{v}_g) dx + \int_{\Omega} C \nabla \alpha_g \cdot \mathbf{v}_g dx, \quad (\text{A.3})$$

## Appendix A. Appendix

---

and observe the following equality integrating by part :

$$\int_{\Omega} \alpha_g C \operatorname{div}(\mathbf{v}_g) dx = - \int_{\Omega} \nabla(\alpha_g C) \cdot (\mathbf{v}_g) dx + \int_{\partial\Omega} \alpha_g C (\mathbf{v}_g \cdot \mathbf{n}) ds. \quad (\text{A.4})$$

As on  $\partial\Omega$ ,  $\mathbf{v}_g \in V$  is zero everywhere except on  $\Gamma_{out}$ , and as  $C$  is a constant, one can write:

$$- \int_{\Omega} \nabla(\alpha_g C) \cdot (\mathbf{v}_g) dx + \int_{\partial\Omega} \alpha_g C (\mathbf{v}_g \cdot \mathbf{n}) ds = - \int_{\Omega} C \nabla(\alpha_g) \cdot (\mathbf{v}_g) dx + \int_{\Gamma_{out}} \alpha_g C (\mathbf{v}_g \cdot \mathbf{n}) ds \quad (\text{A.5})$$

Thus the contribution of the terms expressed in (A.3) is zero :

$$- \int_{\Gamma_{out}} \alpha_g C (\mathbf{v}_g \cdot \mathbf{n}) ds - \int_{\Omega} \alpha_g C \operatorname{div}(\mathbf{v}_g) dx - \int_{\Omega} C \nabla \alpha_g \cdot \mathbf{v}_g dx = 0, \quad (\text{A.6})$$

for all  $\mathbf{v}_g \in V$ , proving that the solution does not change for any constant  $C$ . ■

**Remark 16.** The same reasoning holds when considering the average (see (1.29), (1.30) ) of  $\boldsymbol{\tau} \cdot \mathbf{n} \cdot \mathbf{n}$  on  $\Gamma_{out}$  :

$$\xi = p_0 = \frac{\int_{\Gamma_{out}} (\boldsymbol{\tau} \cdot \mathbf{n}) \cdot \mathbf{n} ds}{\int_{\Gamma_{out}} ds}, \quad (\text{A.7})$$

which is the condition used by default in this thesis.

**Remark 17.** The property that the solution is independent of the choice of the constant  $C$  can also be satisfied taking only  $\xi = -p$ . However, the pressure  $p$  in itself belongs to  $L_2(\Omega)$  and is not well-defined on  $\partial\Omega$  : therefore the mathematical analysis of the problem is impossible, unless assuming extra regularity on the pressure  $p$ . (if  $p \in H^1(\Omega)$ ) The specific choice of boundary condition presented in this thesis allows to compute a problem that is naturally independent of the constant and also well-defined. Moreover, observe that using  $\xi = -p$  in (A.2) can be further simplified, as :

$$\begin{aligned} & - \int_{\Gamma_{out}} \alpha_g \xi (\mathbf{v}_g \cdot \mathbf{n}) ds - \int_{\Omega} \alpha_g p \operatorname{div}(\mathbf{v}_g) dx - \int_{\Omega} p \nabla \alpha_g \cdot \mathbf{v}_g dx \\ & = \int_{\Gamma_{out}} \alpha_g p (\mathbf{v}_g \cdot \mathbf{n}) ds - \int_{\Omega} \alpha_g p \operatorname{div}(\mathbf{v}_g) dx - \int_{\Omega} p \nabla \alpha_g \cdot \mathbf{v}_g dx \\ & = \int_{\Omega} \operatorname{div}(\alpha_g p) \cdot \mathbf{v}_g dx - \int_{\Omega} p \nabla \alpha_g \cdot \mathbf{v}_g dx \\ & = \int_{\Omega} \alpha_g \nabla p \cdot \mathbf{v}_g dx \end{aligned} \quad (\text{A.8})$$

Of course, in order to use (A.8),  $p$  needs to be at least  $H^1(\Omega)$ . The results can also be obtained directly from the strong formulation of the gas momentum equation (1.15), giving a term with

the gradient of the pressure. Then looking for  $\mathbf{u}_g \in \mathbf{V}$ , with  $\nabla p$  defined, such that :

$$\begin{aligned} & \int_{\Omega} (\rho_g \alpha_g \mathbf{u}_g \cdot \nabla) \mathbf{u}_g \cdot \mathbf{v}_g dx + \int_{\Omega} (\rho_g \dot{\alpha}_{source}) \mathbf{u}_g \cdot \mathbf{v}_g dx \\ & + \int_{\Omega} 2\mu_g \left( \epsilon(\mathbf{u}_g) : \epsilon(\mathbf{v}_g) - \frac{1}{3} \text{div}(\mathbf{u}_g) \text{div}(\mathbf{v}_g) \right) dx + \int_{\Omega} D \frac{\rho}{\rho_l} \alpha_g \mathbf{u}_g \cdot \mathbf{v}_g dx = \\ & - \int_{\Omega} \alpha_g \nabla p \cdot \mathbf{v}_g dx + \int_{\Omega} \alpha_g \rho_g \mathbf{g} \cdot \mathbf{v}_g dx + \int_{\Omega} D \frac{\rho}{\rho_l} \alpha_g \mathbf{u} \cdot \mathbf{v}_g dx, \end{aligned} \quad (\text{A.9})$$

for all  $\mathbf{v}_g \in \mathbf{V}$ , corresponds to the strong form (1.15), together with boundary conditions (1.28) and (1.31), and an implicit third boundary condition :

$$(\boldsymbol{\tau}_g \cdot \mathbf{n}) \cdot \mathbf{n} = -\alpha_g p, \text{ on } \Gamma_{out}. \quad (\text{A.10})$$

Weak formulation (A.9) has the advantage of being easy to implement and gives good results in practice (chapter 3). A typical example of applications where the use of (A.9) could not be applicable is if the finite element approximation  $p_h$  of  $p$  is a constant per element.

## A.2 Gmsh simple code to generate a cylinder

This is the typical code used to generate the cylinder column. In this example, the parameters considered are an element size of  $h = 0.02$ ,  $\Phi = 0.03[m/s]$  giving the final mixture height  $h' = 1.77248[m]$  and a radius  $r = 0.2[m]$  in the file `mesh.geo` and the mesh was generated with `gmsh 4.6.0` with the following command line :

```
gmsh -3 mesh.geo -o mesh.msh -format msh2
```

The mesh format is the old mesh format (msh2) for compatibility with our finite element code.

```
SetFactory("OpenCASCADE");
radius= 0.20000000E+00;
height= 0.17724800E+01;
px0=0.0;
px1=0.0;
px2=0.0;
hsize= 0.02;
cylinder1=newv;
Cylinder(cylinder1)=
{
  px0,
  px1,
  px2,
  0.0,
```

## Appendix A. Appendix

---

```
    0.0,  
    heigth,  
    radius  
};  
//Define length  
Mesh.CharacteristicLengthMin=hsize/ 0.20000000E+01;  
Mesh.CharacteristicLengthMax=hsize;  
Mesh.Algorithm = 6;  
Mesh.Algorithm3D = 4;
```

### A.3 Python code for chapter 2 : Stokes experiment

The two codes are performed with Python 3.6.9 and Fenics 2019.1.0. The code is available on github for download : <https://github.com/etpsoutt/StokesCode.git>.



# Emile Soutter

---

CONTACT INFORMATION	Emile Soutter, Chemin du Languedoc 24 Chemin du Languedoc 24 1007 Lausanne, Switzerland	✉E-mail: <a href="mailto:emile92soutter@gmail.com">emile92soutter@gmail.com</a> Phone: +41 78 603 97 71
RESEARCH BACKGROUND	<ul style="list-style-type: none"><li>• <b>Physics:</b> Aluminium electrolysis (MHD, fluids), plasma physics.</li><li>• <b>Mathematics:</b> numerical analysis, finite elements, algorithms.</li></ul>	
EDUCATION	<b>Ecole Polytechnique Fédérale de Lausanne (EPFL)</b>	2017-2021 (December)
	<ul style="list-style-type: none"><li>• Ph.D. in <i>Section of mathematics</i>, title "A mixture model to take into account diluted gas in liquid flow applied to aluminium electrolysis"</li><li>• Advisors: Prof. Jacques Rappaz and Prof. Marco Picasso .</li></ul>	
	<b>Institut für Plasma Physik (IPP)</b> , Garching.	2016-2017
	<ul style="list-style-type: none"><li>• Master thesis "Plasma Physics : FIDA spectroscopy in presence of large fast-ion populations"</li></ul>	
	<b>EPFL</b>	2011-2016
	<ul style="list-style-type: none"><li>• Bachelor and master in physics.</li></ul>	
	<b>Gymnase Auguste Piccard</b>	2008-2011
	<ul style="list-style-type: none"><li>• Diploma in math physics, diploma thesis "Les énergies renouvelables dans le canton de Vaud"</li></ul>	
IT SKILLS	<ul style="list-style-type: none"><li>• <i>Programming Languages (strong):</i> C/C++, Python, bash(ubuntu), MATLAB</li><li>• <i>Technical Softwares (strong):</i> Fenics (open source finite element), paraview (3D visualisation).</li><li>• <i>Others :</i> svn, git, fortran (notions), machine learning (tensorflow), all standard desk tools (latex for instance)</li></ul>	
JOB EXPERIENCE	<ul style="list-style-type: none"><li>• <b>Internship os sox months during master at Hydro SA exploitation</b></li></ul>	2016-2017
	Development of a risk analysis software through matlab.	
	<ul style="list-style-type: none"><li>• <b>Teaching</b></li></ul>	2009-2021
	Repeater, and later teaching assistant at EPFL for various courses during studies and PhD : advanced physics, advanced analysis, numerical analysis	
ASSOCIATIVE	<ul style="list-style-type: none"><li>• <b>AIIESEC</b> Two months in Peru, teaching english and maths in spanish in Piura, 2016.</li><li>• <b>Les polyssons</b> Theater group at university, president of the association for two years, 2014-2015.</li><li>• <b>PhD-student representative</b> Discuss the school policies and represent the right of the PhDs at university.</li></ul>	
LANGUAGES	French (mother-tongue), english (fluent), spanish (around B2-), german (around B2-)	
INTERESTS	Kitesurf, (beach-)volleyball, biking, ski, theater, machine learning, algorithms, challenge about the current crisis that includes global warming, extinction of biodiversity and the issue of energy production/consumption "as clean as possible"	